THE UNIVERSITY
of ADELAIDE

Plaque Rupture Prediction in Human Arteries

By

Alireza Gholipour

A thesis submitted for the degree of Doctor of Philosophy at the

School of Mechanical Engineering

The University of Adelaide

Australia

November, 2019

Abstract

According to the World Health Organisation (WHO), coronary artery disease (CAD) and stroke are the two leading causes of death globally, with more than 15.2 million deaths in 2016. In 2017, there were: 18,000 and 10,000 deaths in Australia due to CAD and cerebrovascular diseases, respectively. Atherosclerosis is the predominant cause for both coronary and cerebrovascular diseases with acute events usually caused by plaque rupture which releases thrombogenic material into the artery lumen leading to clot formation. Identification of the most at risk plaques for rupture, known as the 'vulnerable plaque', remains an important pursuit in the treatment of patients with CAD.

The aim of this thesis was to model and simulate the nonlinear fluid-structure interaction (FSI) dynamics of atherosclerotic coronary arteries, based on clinical data, as a tool to recognise vulnerable locations and hence to predict the initiation of heart attack. This thesis consists of four peer-reviewed journal papers, two published and two submitted for publication.

- Paper 1: A dynamic, three-dimensional (3D), visco/hyperelastic, FSI model of an atherosclerotic coronary artery was developed via the finite element method (FEM) to examine the risk of high shear/von Mises stresses, incorporating: physiological pulsatile blood flow; tapered shape of the artery; viscoelasticity and hyperelasticity of the artery wall; effect of the motion of the heart; active artery muscle contraction; the lipid core inside the plaque; three layers of the artery wall; non-Newtonian characteristics of the blood flow; and micro-calcification. The paper has been published in the International Journal of Engineering Science (Q1; Impact Factor = 9.052; journal rank: 1 out of 88 in Multidisciplinary Engineering).

- Paper 2: One of the highest risk locations of plaque growth and rupture initiation and hence occurrence of heart attack is the first main *bifurcation* of the left main (LM) coronary artery. Hence, this investigation aimed to analyse the nonlinear, three-dimensional biomechanics of the bifurcated, atherosclerotic LM coronary artery. The artery tree was modelled using FSI incorporating three-dimensionality, nonlinear geometric and material properties, asymmetry, viscosity, and hyperelasticity. The

paper has been published in the International Journal of Engineering Science (Q1; Impact Factor = 9.052; journal rank: 1 out of 88 in Multidisciplinary Engineering)

- Paper 3: Clinical data measurement was conducted at the Royal Adelaide Hospital (RAH) for two patients who underwent *in vivo* coronary angiography, optical coherence tomography (OCT) imaging, and electrocardiography (ECG). These clinically measured data were analysed using image processing techniques to obtain realistic geometries of the coronary arteries, heart motion measurements, and corresponding heart rate characteristics. A 3D FSI model was then developed using FEM, based on the measured clinical data for determination of high-risk locations. Validation of the model/simulations with clinical data was also performed.

- Paper 4: *In vivo* OCT, ECG, angiography, and time-dependent blood pressure measurements were conducted for a patient at the RAH and the obtained data were analysed using image processing techniques. Fatigue-life and crack-analysis FEM models were developed and simulations were performed based on clinical obtained data for *crack propagation*, fatigue *crack growth* and *plaque life* analyses.

Declaration

I certify that this work contains no material which has been accepted for the award of any other degree or diploma in my name, in any university or other tertiary institution and, to the best of my knowledge and belief, contains no material previously published or written by another person, except where due reference has been made in the text. In addition, I certify that no part of this work will, in the future, be used in a submission in my name, for any other degree or diploma in any university or other tertiary institution without the prior approval of the University of Adelaide and where applicable, any partner institution responsible for the joint-award of this degree. I acknowledge that copyright of published works contained within this thesis resides with the copyright holder(s) of those works. I also give permission for the digital version of my thesis to be made available on the web, via the University's digital research repository, the Library Search and also through web search engines, unless permission has been granted by the University to restrict access for a period of time.

I acknowledge the support I have received for my research through the provision of an Australian Government Research Training Program Scholarship.

I acknowledge the support I have received for my research through The University of Adelaide and Faculty of Engineering, Computer & Mathematical Sciences, The University of Adelaide.

Alireza Gholipour

Date: 07/10/2019

Acknowledgements

Life is full of challenges, one of the most inspiring challenges for me was my PhD journey. I honestly know that without help of special individuals I could not finish my journey.

First and foremost, I would like to express my deepest gratitude to my supervisors Dr. Mergen Ghayesh, Prof. Anthony C. Zander, and A/Prof. Peter J. Psaltis. Dr. Mergen Ghayesh, I want to thank you for your precious support in technical aspects of my thesis, providing me with excellent research atmosphere, kindness, friendship, valuable and meticulous feedback, and for being with me in each minute of this journey. Prof. Anthony C. Zander and A/Prof. Peter J. Psaltis I am grateful for your precious support, insightful comments, and helpful feedback.

I acknowledged assistance provided by Dr. Daisuke Shishikura and Mr. Giuseppe Di Giovanni from the Atherosclerosis Imaging Core Laboratory at South Australian Health and Medical Research Institute (SAHMRI), Mrs Trudy Patrick from Abbott Pty Ltd and doctors and nurses from the Cardiovascular Investigation Unit at the Royal Adelaide Hospital (RAH). The supports provided for this investigation from The University of Adelaide, RAH, and SAHMRI are highly acknowledged.

Many thanks to my friend Harry James Carpenter for his help and support.

I am deeply thankful to my parents (Reza and Shahdokht), including my in-laws (Farhad and Fereshteh), and my sisters (Fatemeh, Mahsa, and Fateme) and my brother (Mohammad Reza) for being beside me timelessly.

Special thanks to my amazing sister Fatemeh, her memory, her encouragements, her laughs are always with me.

At last I would like to truly thank my love, my friend and my wife Elnaz; thanks for being with me every second of this journey and the journey of life.

List of publications

(i) **A. Gholipour**, M. H. Ghayesh, A. Zander, R. Mahajan, "Three-dimensional biomechanics of coronary arteries", International *Journal of Engineering Science* 130 (2018): 93-114. (Q1; Impact Factor = 9.052; journal rank: 1 out of 88 in multidisciplinary engineering)

(ii) **A. Gholipour**, M. H. Ghayesh, A. Zander, "Nonlinear biomechanics of bifurcated atherosclerotic coronary arteries", International *Journal of Engineering Science* 133 (2018): 60-83. (Q1; Impact Factor = 9.052; journal rank: 1 out of 88 in multidisciplinary engineering)

(iii) **A. Gholipour**, M. H. Ghayesh, A. Zander, P. J. Psaltis, "Clinical in vivo based biomechanics of right and left coronary arteries", submitted.

(iv) **A. Gholipour**, M. H. Ghayesh, A. Zander, P. J. Psaltis, "Plaque rupture prediction for an atherosclerotic coronary artery via use of in vivo clinical data", submitted.

Following journal article and refereed conference papers/posters are not included in the main body of the thesis; however, they have been conducted on the research topic during my candidature.

(v) H. J. Carpenter, **A. Gholipour**, M. H. Ghayesh, A. Zander, P. J. Psaltis, "A review on the biomechanics of coronary arteries ", submitted.

(vi) **A. Gholipour**, M. H. Ghayesh, A. Zander, S. J. Nicholls, and P. J. Psaltis, "Shear stress field of an atherosclerotic coronary artery", 2018 South Australian Health and Medical Research Institute (SAHMRI) Annual meeting, 25-26 October 2018, Adelaide, Australia.

(vii) **A. Gholipour**, M. H. Ghayesh, A. Zander, S. J. Nicholls, P. J. Psaltis, "Plaque shear stress distribution in an atherosclerotic coronary artery", The 2018 South Australian Cardiovascular Research Showcase, 2 November 2018, Adelaide, Australia.

(viii) **A. Gholipour**, M. H. Ghayesh, A. Zander, S. J. Nicholls, P. J. Psaltis, “Plaque shear stress in bifurcated coronary arteries”, The 2018 Annual Scientific Meeting of the Australian Atherosclerosis Society (AAS), the Australian Vascular Biology Society (AVBS) and the High Blood Pressure Research Council of Australia (HBPRCA), 27-30 November 2018, Adelaide, South Australia, Australia.

(ix) **A. Gholipour**, M. H. Ghayesh, A. Zander, S. J. Nicholls, P. J. Psaltis, “Fluid-structure analysis of an atherosclerotic coronary artery”, 21st Australasian Fluid Mechanics Conference, 10-13 December 2018, Adelaide, Australia.

(x) **A. Gholipour**, M. H. Ghayesh, A. Zander, S. J. Nicholls, P. J. Psaltis, “Shear stress and effective structural stress fields of an atherosclerotic coronary artery”, ICABTB 2019 : International Conference on Advanced Biomedical Technologies and Biomechanics, 1-2 February 2019, Melbourne, Australia.

(xi) H. J. Carpenter, **A. Gholipour**, M. H. Ghayesh, A. Zander, P. J. Psaltis, "In vivo OCT-based plaque rupture prediction in atherosclerotic coronary artery”, Australian Atherosclerosis Society ASM, 16-19 October 2019, Melbourne, Australia.

(xii) **A. Gholipour**, H. J. Carpenter, M. H. Ghayesh, A. Zander, P. J. Psaltis, "Effect of blood flow models on the flow-induced vibrations of coronary arteries", The 18th Asian Pacific Vibration Conference (APVC 2019), 18-21 November 2019, Sydney, Australia.

(xiii) H. J. Carpenter, **A. Gholipour**, M. H. Ghayesh, A. Zander, P. J. Psaltis, "Flow-induced dynamics of bifurcated coronary arteries”, The 18th Asian Pacific Vibration Conference (APVC 2019), 18-21 November 2019, Sydney, Australia.

Table of Contents

Abbreviations and Nomenclature

IVUS – Intravascular Ultrasound

US – Ultrasound

MRI – Magnetic Resonance Imaging

hrMRI – high resolution Magnetic Resonance Imaging

CT – Computerised Tomography

OCT – Optical Coherence Tomography

CFD – Computational Fluid Dynamics

FSI – Fluid-Structure Interaction

2D – 2-Dimensional

3D – 3-Dimensional

RAH – Royal Adelaide Hospital

SAHMRI – South Australian Health and Medical Research Institute

WHO – World Health Organisation

CAD – Coronary Artery Disease

FEM – Finite Element Method

XFEM – Extended Finite Element Method

FVM – Finite Volume Method

ECG – Electrocardiography

LM – Left Main

LAD – Left Anterior Descending

LCx – Left Circumflex

RCA – Right Coronary Artery

OM – Obtuse Marginal

AM – Acute Marginal

PDA – Posterior Descending Artery

PLV – Posterolateral Ventricular

STEMI – ST-segment Elevation Myocardial Infarction

NSTEMI – Non-ST segment Elevation Myocardial Infarction

LDL – Low-Density-Lipoprotein

MEMS – Micro Electro-Mechanical Systems

SSE – Shear Strain Elastography

WSS – Wall Shear Stress

WSSs – Wall Shear Stresses

VMS – von Mises Stress

VMSs – von Mises Stresses

FFR – Fractional Flow Reserve

RAO – Right Anterior Oblique

LAO – Left Anterior Oblique

CAU – Caudal

CRA – Cranial

SIF – Stress Intensity Factor

Chapter 1

Introduction

1.1 Coronary arteries

Responsibility of coronary arteries is to supply oxygen-rich blood to the heart. As seen in **Figure 1-1**, there are two main coronary arteries arising from the aortic root, namely the left main (LM) and the right coronary artery (RCA), where the LM typically divides into two branches, the left anterior descending (LAD) and the left circumflex (LCx), although occasionally it trifurcates into the LAD, LCx and ramus intermedius arteries. Responsibility of the LAD is to deliver blood to the anterior wall and apex of the left ventricle, which is the main pumping chamber of the heart. The LAD gives rise to diagonal branches, which deliver blood to the antero-lateral left ventricular myocardium; from proximally to distally the diagonal branches are labelled numerically as D1, D2, and so on. The LAD also provides septal branches (with blood) that supply the anterior aspect of the interventricular septum. The LCx provides blood to the left atrium and lateral wall of the left ventricle via its obtuse marginal (OM) branches, which are

designated OM1, OM2, and so on, proximally to distally. The RCA supplies the right atrium and ventricle with blood; different branches are the posterior descending artery (PDA), conus (arteriosus), sinoatrial, acute marginal (AM), and posterolateral ventricular (PLV) arteries. The PDA supplies left ventricle's inferior wall and the posterior two thirds of the interventricular septum. Provision of the PDA defines which coronary artery is designated as being "dominant". The majority of individuals have a dominant RCA, although in approximately 10% the PDA arises from the distal LCx, while 5% have a co-dominant coronary circulation, meaning that PDA branches come from both the RCA and LCx [1] (**Figure 1-1**).

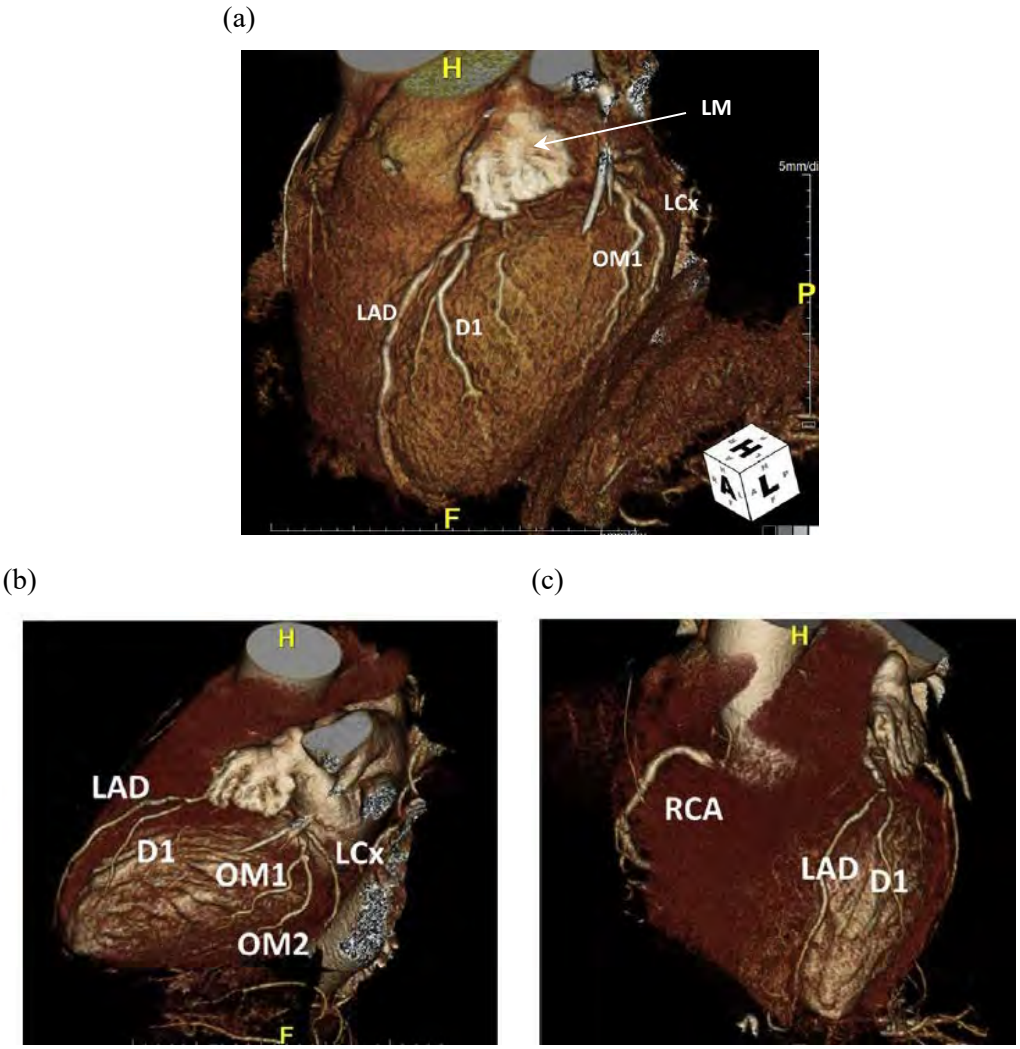

Figure 1-1. Computerised Tomography (CT) images showing different branches of the coronary arteries on the heart from different angles [2].

Like other blood vessels, the wall of coronary arteries has of three layers, the tunica adventitia (outermost layer), media (middle) and intima (inner layer). The innermost or luminal surface of the intima contains the endothelium layer, a thin layer of endothelial cells responsible for preventing blood from coagulating along the artery surface and, hence, is a critical location for disease initiation [3]. The media consists mainly of smooth muscle cells capable of active contraction to assist in maintaining vascular tone and blood pressure, while the external layer, the adventitia, is a network of connective tissues, including collagen and elastin, and small blood vessels (*vasa vasorum*) nourish the wall of the artery. All three layers play a crucial role in maintaining vessel wall structure, function and homeostasis, making the study of disease initiation and progression challenging.

1.2 Significance of coronary heart diseases

According to the World Health Organisation (WHO) coronary heart diseases and strokes are the *two leading* causes of death globally, with more than 15.2 million deaths in 2016 [4]. In Australia, approximately 18,000 deaths are attributed to coronary artery disease (CAD) annually, the largest single cause of death, while a further 10,000 deaths are caused by cerebrovascular diseases, ranking it the third largest cause in 2017 [5]. Both of these diseases reflect situations in which the blood supply for the heart or brain is affected in some way. Among the various causes, *atherosclerosis* is the most common for obstructing the supply of fresh, oxygenated blood to the heart. **Figure 1-2** depicts an angiographic image of an atherosclerotic, stenotic LAD coronary artery taken from a patient at the Royal Adelaide Hospital (RAH) with the diseased artery causing the patient to present with a non-ST segment elevation myocardial infarction (NSTEMI).

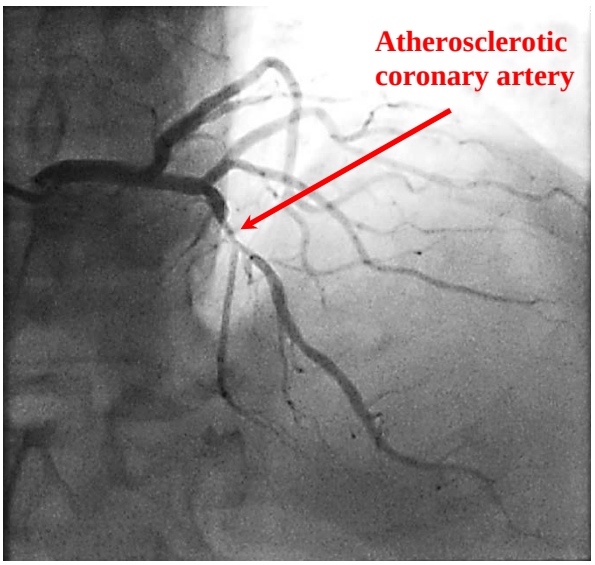

Figure 1-2. Angiographic image taken in antero-posterior (AP) cranial projection of LAD showing atherosclerotic narrowing in the mid segment.

1.3 Obstruction of arteries and plaque formation

Although it is accepted that increasing low-density-lipoprotein (LDL) is responsible for shaping and growth of plaque and hence atherosclerotic arteries, the primary cause of this disease is a damaged endothelium-lined intimal layer. Disruption of the endothelial layer by a crack or injury in addition to a large amount of LDL could initiate the process of atherosclerosis and as a result, atherosclerosis has the potential to be initiated at an early age when arteries are being shaped [6]. According to clinical and experimental investigations atherosclerosis is a result of complex molecular and cellular mechanisms caused by inflammation [7]. Plaque growth in the inner layer of the arteries produces increased stenosis over time. The main problem with the plaque begins at rupture or erosion (where rupture accounts for about 60-65% of athero-thrombotic events, while erosion accounts for another 30%) when the materials inside the plaque (such as lipids and calcium) are released and a thrombus is produced by platelets in the blood. The thrombus obstructs the artery and blood flow to the corresponding region of the patients' myocardium, causing myocardial infarction (heart attack). **Figure 1-3** shows cross-sections of atherosclerotic coronary arteries

with sub-figures (a) & (b) without any rupture and sub-figures (c) & (d) after plaque rupture and thrombus shaping.

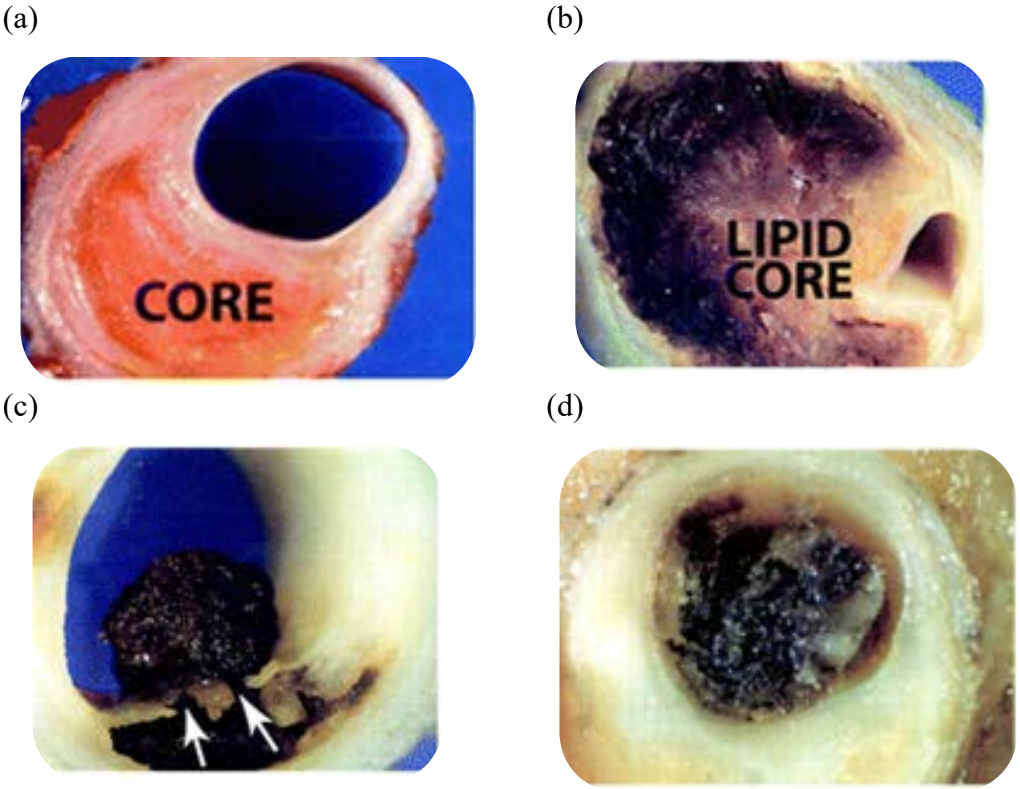

Figure 1-3. Atherosclerosis and thrombus [8]: (a) cholesterol deposition; (b) enlarged plaque; (c) plaque rupture and thrombus formation; (d) artery obstruction.

Various imaging techniques, such as OCT imaging shown in **Figure 1-4**, are employed to probe narrowed coronary arteries, however, it is almost impossible to predict rupture since plaque growth is dependent on many other haemodynamic factors including blood pressure, LDL, and calcium. According to experiments, most of the ruptures occur in the stenosis range of 45-50% [9, 10] implying that rupture is very likely to occur even when the stenosis level is smaller than half of the cross-section of the artery. As atherosclerotic plaques grow, they are typically asymptomatic. The vessel remodels, often positively or outward, in the early stages of atherogenesis to accommodate the growing plaque and symptoms do not occur until a severe enough stenosis is caused to restrict blood flow to the heart (i.e. cause ischaemia) or an acute thrombotic event occurs due to plaque rupture or erosion, to cause infarction. This highlights the need for the development of a

computer model for plaque growth and rupture simulation capable of predicting the risk factors associated with heart attack. The biomechanics of atherosclerotic plaque rupture has not been fully determined in the literature and establishing reliable models/simulations for rupture prediction is highly needed. This thesis attempts to address this challenge.

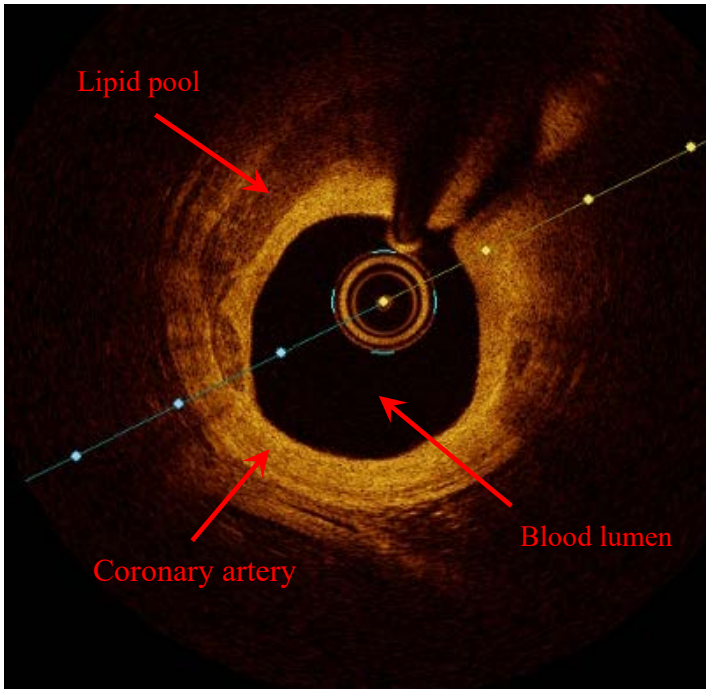

Figure 1-4. *In vivo* OCT images for an atherosclerotic coronary artery of a patient obtained at the RAH.

1.4 Aim and objectives of the thesis

The goal of this thesis was to model and simulate the nonlinear fluid-structure interaction (FSI) behaviour of atherosclerotic coronary arteries, using clinical data, as a tool to predict heart attack; clinical data were measured at the RAH and post-processed at South Australian Health and Medical Research Institute (SAHMRI) and School of Mechanical Engineering, The University of Adelaide and finite element models were developed and simulated to predict heart attack.

The primary objective of this thesis was obtaining stress fields in atherosclerotic coronary arteries and examining the influences of different

parameters by considering all contributing factors using the finite element method (FEM). This is currently the main challenge in predicting plaque rupture due to the nonlinear nature of the biomechanical system, making it critical to consider the effects of different contributing parameters such as: the physiological pulsatile blood flow; tapered shape of the artery; viscoelasticity and hyperelasticity of the artery wall; effect of the motion of the heart; active artery muscle contraction; the lipid core inside the plaque; three layers of the artery wall; non-Newtonian characteristics of the blood flow; and micro-calcification along with the fully coupled fluid (blood) - structure (artery/plaque) interactions. As a result, a dynamic model of a coronary artery has been developed to predict the vulnerable atherosclerotic plaque that is at high risk of rupturing. This model could result in the identification of patients who are at high risk of myocardial infarction and allow interventions to stabilise the plaque, hence, preventing myocardial infarction.

The second objective of this thesis was to model/simulate the biomechanical behaviour of the highest risk location for plaque growth and rupture initiation, and hence occurrence of heart attack, which is the *first main bifurcation* of the LM coronary artery; i.e., a branch of arteries was considered. In order to consider all contributing factors and their influences, an idealised, nonlinear, three-dimensional, geometry has been biomechanically modelled/simulated using FSI. Three plaques of varying geometry and material properties were located inside the three branches of the LM, the LAD, and the LCx arteries and were modelled incorporating three-dimensionality, nonlinear geometric and material properties, asymmetry, viscosity, and hyperelasticity. The effect on the stress field (shear and structural) of varying different system features such as the degree of stenosis, the curved shape of the artery, the plaque location, and the fibrous cap thickness has also been examined.

As the third objective, a set of clinical data was measured at the RAH for two patients who underwent *in vivo* optical coherence tomography (OCT), angiography, and electrocardiography (ECG). Then, the measured data were post-processed, using image processing techniques, at the SAHMRI and the School of Mechanical Engineering, the University of Adelaide so as to determine realistic

geometric/haemodynamic characteristics used to develop a 3D FSI model by means of FEM. The developed model was simulated to determine stress/strain fields, plaque rupture high-risk locations, deflections, and stiffness of atherosclerotic coronary arteries. Validations were performed by comparing the simulated and clinically-obtained artery motions.

As the fourth objective, *in vivo* ECG, angiography, OCT, and time-varying blood pressure measurements were performed for a patient at the RAH and measured clinical data were post-processed for the purpose of development of a *fatigue-life* and *crack-analysis* FEM biomechanical model and investigating *crack propagation*, *fatigue crack growth*, and *plaque life* and *prediction of plaque rupture initiation*/*progression*. The developed rupture/fatigue model took into account all of the realistic/important patient-specific parameters, and hence it is considered reliable for prediction of plaque rupture and resulting heart attack.

1.5 Structure of the thesis

As shown in **Figure 1-5**, Chapter 1 of the thesis provides introductory remarks about the importance of coronary heart diseases and the general objectives to be addressed in the prevention of heart attack and hence deaths, as well as a brief introductory to the theoretical method. Chapter 2 is devoted to a detailed literature review on the biomechanics of coronary arteries and plaque rupture. The subsequent four chapters are four manuscripts that either are published or submitted as journal papers. Chapter 3 presents the three-dimensional biomechanics of coronary arteries combining different nonlinear parameters of the biomechanical system. In Chapter 4, the nonlinear biomechanics of *bifurcated* atherosclerotic arteries has been investigated by considering plaques in each artery branch. Using different *in vivo* clinical data obtained at the RAH, Chapter 5 develops the modelling/simulation of the biomechanics of the left and right coronary arteries based on OCT, angiography, and ECG. The focus of Chapter 6 is on plaque rupture prediction for an atherosclerotic coronary artery based on *in vivo* clinical data using *fracture* biomechanics. Chapter 7 provides a summary of the thesis together with concluding remarks.

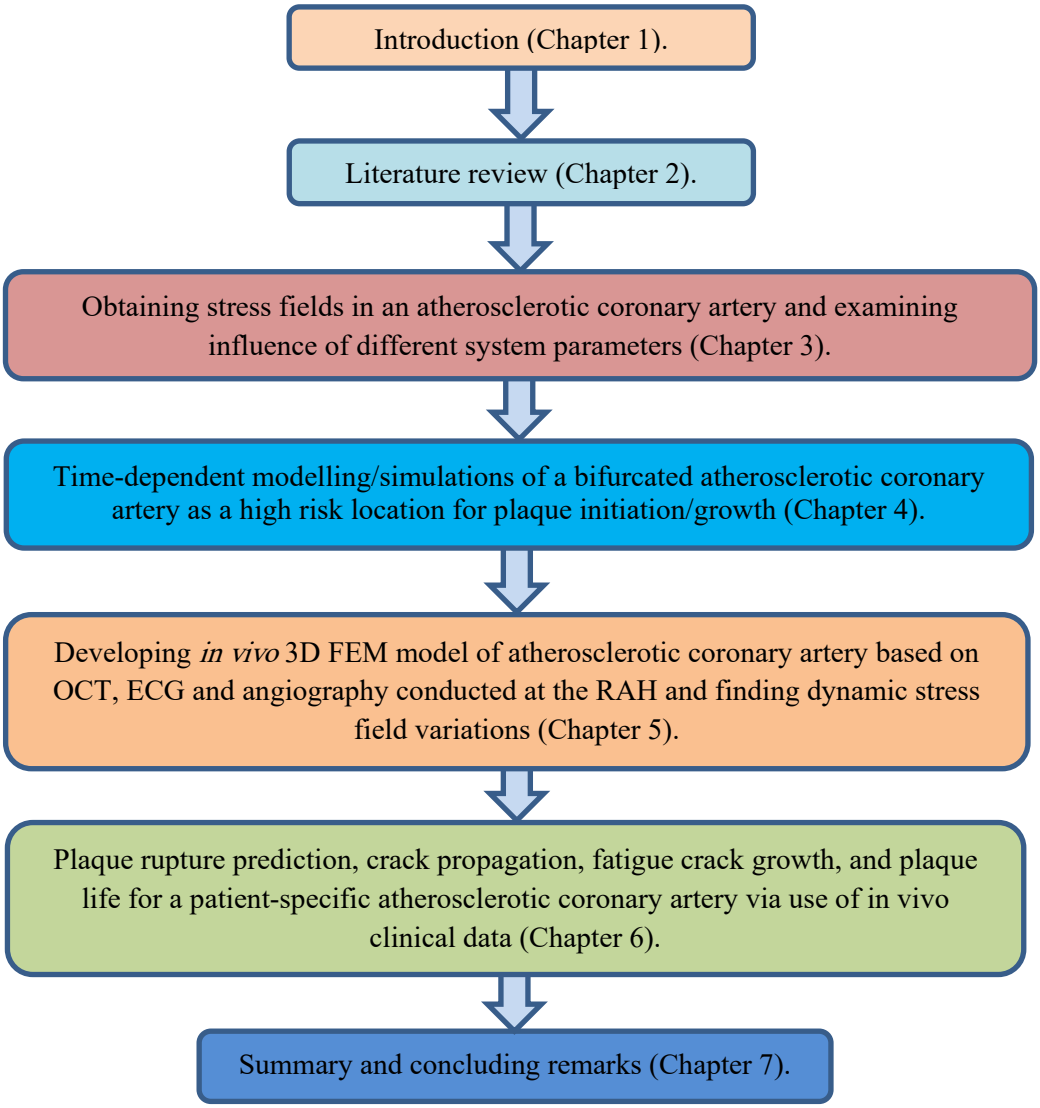

Figure 1-5. Thesis structure.

1.6 A brief introduction to the theoretical method

The fundamental theoretical methodology employed in this thesis is described briefly in this section to give an insight on why this method is chosen and what are the benefits/limitations of the various techniques; the advanced and detailed version of the methodology employed in each chapter is given in the corresponding chapter.

A theoretical analysis in engineering usually involves development of a theoretical model of a system based on system parameters and to simulate/solve the model, via different numerical/analytical techniques, and extract

understandings from the simulations. The FEM has widely been applied in simulations of arteries and plaques since this technique is capable of handling mechanical systems with complex geometries and properties. In addition, different material models such as hyperelasticity and viscoelasticity can be applied to the problem as well as various boundary conditions and forces. FEM is currently considered to be the best available numerical technique to model biomechanical systems. In the following, the fundamentals of the FEM for solid, fluid, and FSI are outlined to give a better insight to the methodology employed.

1.6.1 Fundamentals of the FEM

The FEM was introduced by Turner (reported from [11]) for obtaining the stiffness coefficient of a complicated shell-like structure. After nearly 60 years it has now become one of the most common methods in modelling, simulating and predicting complex properties of physical and engineering systems [12, 13]. Due to the complicated physical nature of both the material and boundary conditions of biomechanical systems, the FEM is the most powerful numerical technique as it divides the system into a finite number (but many) of domains (called meshes) and convinces compatibilities. Continuum mechanics is the basis for the FEM. As fluid and solid mechanics both have their own continuity/moment/energy equations and since the FEM works with a finite number of nodes on the continuous system, both fluid and solid domains in addition to their interaction can be modelled/simulated.

The basic concept of the FEM comes from considering an elastic spring and applying Hooke's law between two points such that [11]

$$F = k\,\delta, \tag{1.1}$$

where F is the force between nodes (points), k shows the stiffness of the spring, and δ is the displacement between two nodes. By defining a finite number of 3D nodes in the physical domain the stiffness equations can be obtained:

$$\{F\} = [K]\{\delta\}, \tag{1.2}$$

in which $[K]$ is the stiffness matrix between the 3D nodes. By having boundary conditions of a continuum domain, the unknown parameters such as

displacements and inter-nodal forces can be determined. Irregular domains of initial, boundary, and eigenvalue problems can be discretised and solved by the FEM which makes it powerful and practical numerical method in engineering.

The approach to solve the FEM of the biomechanical system of a coronary artery in this thesis is shown in **Figure 1-6**. As the first step, the mathematical model of the biomechanical system according to the mechanical laws can be obtained. Then using the FEM, the nonlinear biomechanical system can be discretised into a finite number of equations and unknowns. In the next step, the equations obtained from discretisation are solved through use of various numerical techniques. In the numerical discretisation, different factors such as stability, accuracy, robustness, ability to handle complex geometry, and speed of execution are considered for each biomechanical system.

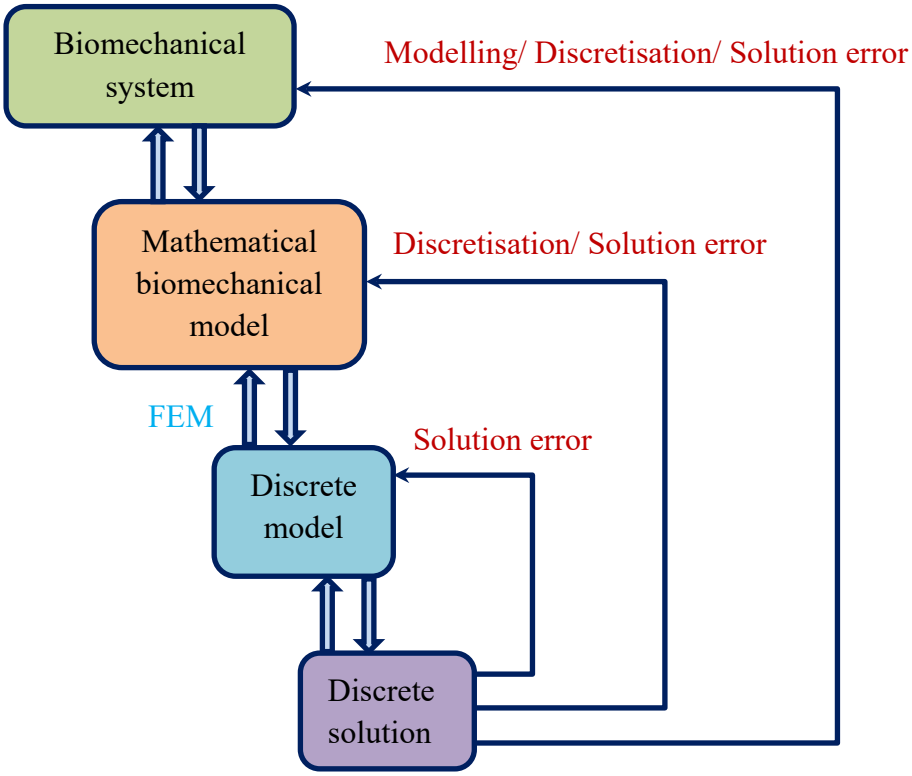

Figure 1-6. Computational biomechanics model used in this thesis.

1.6.2 Fundamentals for bio-solid equations

Considering infinitesimal element sizes on the solid part of the biomechanical system as shown in **Figure 1-7**, the three-dimensional stress components can be obtained as [14]:

$$\begin{aligned}
&\left[\frac{\partial \sigma_{yy}}{\partial y}+\frac{\partial \sigma_{xy}}{\partial x}+\frac{\partial \sigma_{zy}}{\partial z}\right]+b_y=\rho \ddot{v},\\
&\left[\frac{\partial \sigma_{xx}}{\partial x}+\frac{\partial \sigma_{yx}}{\partial y}+\frac{\partial \sigma_{zx}}{\partial z}\right]+b_x=\rho \ddot{u},\\
&\left[\frac{\partial \sigma_{zz}}{\partial z}+\frac{\partial \sigma_{yz}}{\partial y}+\frac{\partial \sigma_{xz}}{\partial x}\right]+b_z=\rho \ddot{w},
\end{aligned} \tag{1.3}$$

in which σ_{ij} are the stress components; the first index is normal to the stress plane and the second index shows the direction of the stress; b_i represents the body force for unit volume where the index shows body force's direction; ρ is the density of the element; v, w, u denote displacement components of the element, respectively, in the y, z, *and* x directions.

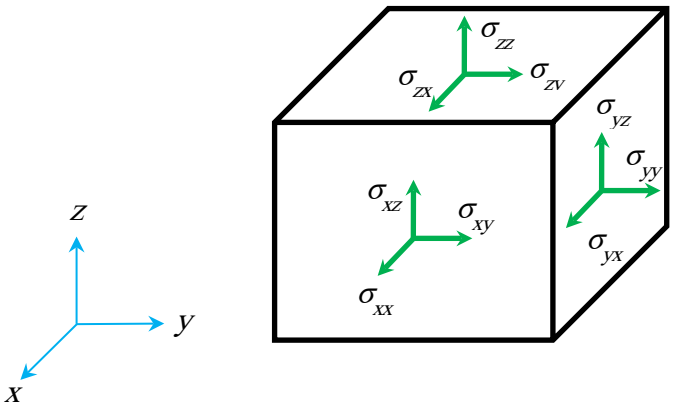

Figure 1-7. Stress components on infinitesimal solid element.

The stress field can be related to the strain field based on finite strain theory [15] (known as large deformation theory) by constitutive equations which consider the internal work within the element. The kinematic equations are the relations between strain and displacement in the model. In the bio-solid solution process, the aforementioned equations, namely the stiffness equations, dynamic

equilibrium equations, kinematic equations, and the constitutive equations relate force, displacements, strains, and stresses (**Figure 1-8**).

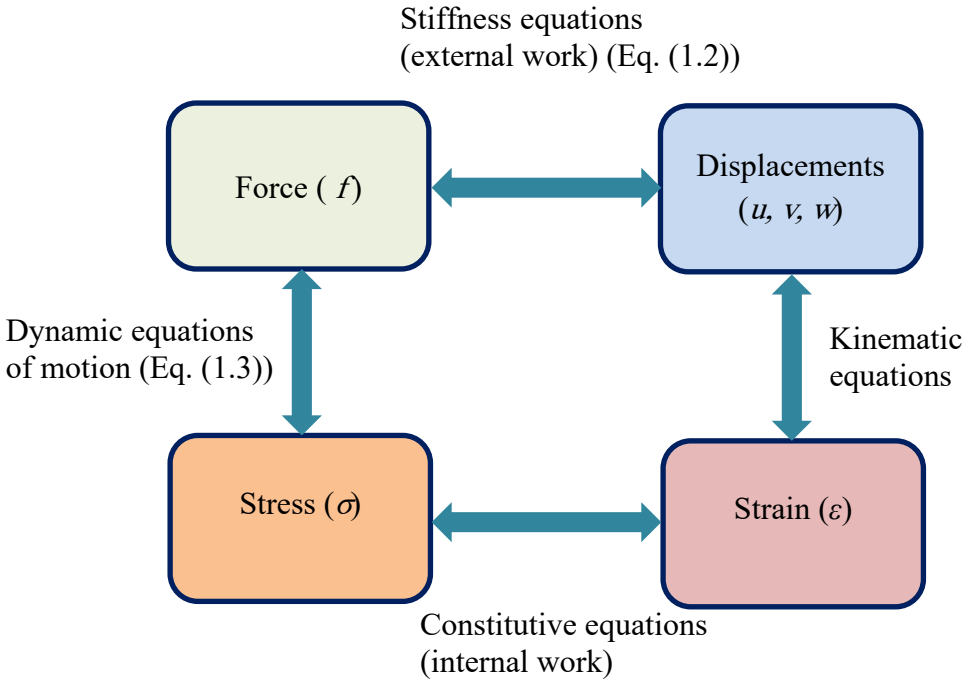

Figure 1-8. Bio-solid solution process [16].

In order to analyse the failure of the solid part of coronary arteries, von Mises stress (VMS) is used as an effective 3D stress, and is calculated as [17]

$$\sigma = \sqrt{\frac{6\left[\sigma_{xy}{}^2 + \sigma_{yz}{}^2 + \sigma_{zx}{}^2\right] + \left(-\sigma_{zz} + \sigma_{yy}\right)^2 + \left(-\sigma_{xx} + \sigma_{zz}\right)^2 + \left(-\sigma_{yy} + \sigma_{xx}\right)^2}{2}} \quad (1.4)$$

1.6.3 Fundamentals for bio-fluid equations

The same general concept of discretisation of the bio-solid is applied for the fluid discretisation to obtain elements and nodes, however, there are two different fundamental equations in bio-fluid analysis for the discretised element. First, the continuity equation which conserves the mass for the fluid element [16]:

$$\frac{\partial \rho}{\partial t} + \left[\frac{\partial\left(\rho V_x\right)}{\partial x} + \frac{\partial\left(\rho V_y\right)}{\partial y} + \frac{\partial\left(\rho V_z\right)}{\partial z}\right] = 0, \quad (1.5)$$

where V_x, V_y, and V_z are velocity components of the element in the x, y, and z directions, respectively; ρ is the fluid density. The next equations in the bio-fluid is the conservation of momentum (Navier-Stokes equations). Again by considering an infinitesimal element in the bio-fluid domain, the equations can be obtained [16]:

$$\begin{aligned}
\rho\left(\frac{\partial V_y}{\partial t}+V_x\frac{\partial V_y}{\partial x}+V_y\frac{\partial V_y}{\partial y}+V_z\frac{\partial V_y}{\partial z}\right)&=\frac{\partial \tau_{yy}}{\partial y}-\frac{\partial p}{\partial y}+\frac{\partial \tau_{xy}}{\partial x}+\frac{\partial \tau_{zy}}{\partial z}+f_y,\\
\rho\left(\frac{\partial V_x}{\partial t}+V_x\frac{\partial V_x}{\partial x}+V_y\frac{\partial V_x}{\partial y}+V_z\frac{\partial V_x}{\partial z}\right)&=\frac{\partial \tau_{xx}}{\partial x}-\frac{\partial p}{\partial x}+\frac{\partial \tau_{yx}}{\partial y}+\frac{\partial \tau_{zx}}{\partial z}+f_x,\\
\rho\left(\frac{\partial V_z}{\partial t}+V_x\frac{\partial V_z}{\partial x}+V_y\frac{\partial V_z}{\partial y}+V_z\frac{\partial V_z}{\partial z}\right)&=\frac{\partial \tau_{zz}}{\partial z}-\frac{\partial p}{\partial z}+\frac{\partial \tau_{xz}}{\partial x}+\frac{\partial \tau_{yz}}{\partial y}+f_z,
\end{aligned} \tag{1.6}$$

in which p is pressure, τ_{ij} is a stress tensor on the element's control volume, and f_i shows the body force on the element for each direction. Computational fluid dynamics (CFD) based on discretisation is employed to solve the aforementioned differential equations [18].

1.6.4 Fundamentals for bio fluid-structure interaction (FSI)

In bio-FSI the interaction and coupling motions of the bio-solid and the bio-fluid are analysed. Dynamic motion of the coronary artery and its interaction with the dynamic pressure and velocity of the blood is the main source of bio-FSI. Due to the time-dependent and nonlinear nature of biomechanical systems, the coupling simulations are incorporated using the same computational approach of discretisation. In the bio-FSI, the differential equations and boundary conditions of the bio-solid and the bio-fluid should be satisfied at the same time. As the bio-solid boundary conditions and forces from the bio-fluid deform the geometry of the biomechanical system, a new geometry for the fluid part is generated according to the FSI interference surface; the discretisation of the new geometry is taken into account based on the moving mesh (remeshing) method [19].

Generally, FSI problems can be considered as either a one problem domain (monolithic approach) or two separate problem domains with interactions (partitioned approach). The first approach is more complicated all equations should be solved simultaneously and it needs more time and resources; however,

the result is more accurate. Using the second approach, each domain of the bio-solid and the bio-fluid should be solved separately and then their results should be linked using different algorithms. For the partitioned approach, there are two ways of incorporating boundary interferences between the bio-solid and bio-fluid; one is to consider the boundary interference effect on the solution procedure and the other is to consider it on the equations of the model. In the first approach, the boundary interference is considered as a physical boundary condition, and hence is considered as a part of the solution procedure. In this way, discretisation (mesh) of the domain needs to follow the change in the boundary interference (conforming method), or in other words, remeshing is required. The Arbitrary Lagrangian Eulerian (ALE) method is the most applicable technique to consider remeshing boundary interferences between the bio-solid and bio-fluid. The other way of considering boundary interferences is to apply them to the equations of the model; in this method the remeshing of the problem during solution is not necessary (non-conforming method), however, this method is only applicable for small deflections between the bio-solid and bio-fluid. The fictitious domain method is the most popular one for non-conforming meshing method. In conclusion, according to the nature of the coronary artery and the large mesh distortions induced by large displacements, rotations, or deformations, ALE is considered to be the best method to approach the biomechanical system such as coronary arteries [20].

References

[1] F. Faletra, N. Pandian, S.Y. Ho, Anatomy of the heart by multislice computed tomography, John Wiley & Sons, 2009.
[2] D. Tousoulis, Coronary Artery Disease: From Biology to Clinical Practice, Academic Press, 2017.
[3] C.R. Edwards, I.A.D. Bouchier, C. Haslett, E. Chilvers, Davidson's principles and practice of medicine, 16 ed., Churchill Livingstone Edinburgh, 1991.
[4] World Health Organisation (WHO), The top 10 causes of death, https://www.who.int/en/news-room/fact-sheets/detail/the-top-10-causes-of-death, (2019).
[5] Australian Institute of Health and Welfare (AIHW), Leading causes of death, https://www.aihw.gov.au/reports/life-expectancy-death/deaths-in-australia/contents/leading-causes-of-death, (2019).
[6] R. Ross, Atherosclerosis—an inflammatory disease, New England Journal of Medicine, 340 (1999) 115-126.
[7] P. Libby, P.M. Ridker, A. Maseri, Inflammation and atherosclerosis, Circulation, 105 (2002) 1135-1143.
[8] T.M. Doherty, L.A. Fitzpatrick, D. Inoue, J.-H. Qiao, M.C. Fishbein, R.C. Detrano, P.K. Shah, T.B. Rajavashisth, Molecular, endocrine, and genetic mechanisms of arterial calcification, Endocrine Reviews, 25 (2004) 629-672.
[9] E. Falk, P.K. Shah, V. Fuster, Coronary plaque disruption, Circulation, 92 (1995) 657-671.
[10] S. Sorof, Intravascular Atheroma Monitoring: Past, Present and Future of identifying Vulnerable Plaques, Applications in Imaging-Cardiac Interventions, (2004) 34-39.
[11] E. Madenci, I. Guven, The finite element method and applications in engineering using ANSYS®, Springer, 2015.
[12] G. Dhatt, E. Lefrançois, G. Touzot, Finite element method, John Wiley & Sons, 2012.
[13] O.C. Zienkiewicz, R.L. Taylor, P. Nithiarasu, J. Zhu, The finite element method, McGraw-hill London, 1977.
[14] A.F. Bower, Applied mechanics of solids, CRC press, 2009.
[15] K. Hashiguchi, Y. Yamakawa, Introduction to finite strain theory for continuum elasto-plasticity, John Wiley & Sons, 2012.
[16] M. Tanaka, S. Wada, M. Nakamura, Computational Biomechanics: Theoretical Background and Biological/Biomedical Problems, Springer Science & Business Media, 2012.
[17] R. von Mises, Mechanik der plastischen Formänderung von Kristallen, ZAMM - Journal of Applied Mathematics and Mechanics/Zeitschrift für Angewandte Mathematik und Mechanik, 8 (1928) 161-185.
[18] S. Jamshed, Using HPC for Computational Fluid Dynamics: A Guide to High Performance Computing for CFD Engineers, Academic Press, 2015.
[19] Y. Bazilevs, K. Takizawa, T.E. Tezduyar, Computational fluid-structure interaction: methods and applications, John Wiley & Sons, 2013.
[20] H. Mohammadi, Developing a global fluid-structure interaction model of the aortic root, McGill University Libraries, 2015.

Chapter 2

Literature review

There are a number of studies on the biomechanics of coronary arteries and plaque rupture from various disciplines including medicine and engineering; the main focus in this literature review is on the biomechanics aspects of the problem. The literature on the topic of the biomechanics of coronary arteries can be divided into two groups: (i) theoretical investigations; and (ii) combined theoretical and experimental/clinical investigations. The theoretical investigations can be grouped into: structure; fluid; and fluid-structure interaction (FSI). Combined theoretical/experimental investigations can be categorised as *in vitro* and *in vivo* where each again has three sub-classes of structural, fluid, and FSI. There are also a number of investigations in the literature on plaque rupture (crack) growth/propagation and fatigue/life analysis, which are reviewed separately in Section 2.3.

2.1 Theoretical investigations

The first section of the literature review focusses on the *theoretical modelling* of coronary arteries and plaques; in this part, the arteries and plaques have been considered as simplified shapes and were analysed in three sub-sections; structure, fluid, and FSI.

Theoretical studies from the literature are categorised into three parts, *structure* (i.e. only artery and plaques), *fluid* (i.e. only blood inside artery), and *FSI analyses* (i.e. coupled artery/plaque and blood), as discussed in the following sub-sections.

2.1.1 Structural analysis (considering only artery and plaque)

In the structural analysis studies undertaken to date, the model has usually been idealised for two reasons. In some investigations, the idealised model has been used in order to take into account the effect of *each segment of the plaque* on the stress and the critical situation for the threshold of the plaque rupture [1-4]. However, the other group of studies used an idealised model for simplifying the problem so as to investigate the effect of different parameters on the stress field, for instance, hyperelasticity in 3D space [5], inward and outward vascular growth in plaque shaping [6], considering microcalcification [7], applying fatigue crack propagation [8], fiber-reinforced and anisotropic material [9-11] and viscoelastic material model [12]. Table 2-1 summarises the theoretical studies involving structural modelling of arteries and plaque. In conclusion, while these precious studies contributed to the understanding of coronary arteries and plaques and examined the effects of different parameters on the plaque and artery in the structural part; however, they did not consider the flowing fluid (blood) effect, in addition to considering simplified model for the artery and plaque.

In order to model the large deformation of the artery and plaque, different hyperelastic models can be used such as the Neo-Hookean model [13] with

$$W = (-1+J)^2 \frac{1}{d} + (-3+\bar{I}_1)c_{10}, \tag{2.1}$$

the Mooney-Rivlin (5-parameter) hyperelastic model [14] with

$$W = \frac{1}{d}\left(-1+J\right)^2 + c_{01}\left(-3+\overline{I}_2\right) + c_{11}\left(-3+\overline{I}_1\right)\left(-3+\overline{I}_2\right) + c_{20}\left(-3+\overline{I}_1\right)^2 + c_{10}\left(-3+\overline{I}_1\right) + c_{02}\left(-3+\overline{I}_2\right)^2, \tag{2.2}$$

and the Holzapfel model [15] with

$$W = \frac{1}{d}\left(-\ln(J) + \frac{-1+J^2}{2}\right) + c_{10}(-3+\overline{I}_1) + \frac{k_1}{2k_2}\sum_{a=1}\{\exp[k_2[(-3\kappa+1)(-1+\overline{I}_{4_{(aa)}}) + \kappa(-3+\overline{I}_1)]^2 - 1]\}, \tag{2.3}$$

where W represents the strain energy potential, J represents the determinant of the elastic deformation gradient, $\overline{I}_1$ denotes the first deviatoric strain invariant, $\overline{I}_2$ denotes the second deviatoric strain invariant, d denotes the material incompressibility parameter, and c_{10}, c_{01}, c_{11}, c_{20}, and c_{02} can be obtained via curve fitting the experimental data [16] to the formulation; κ, $\overline{I}_{4_{(aa)}}$, k_1 and k_2 are also the anisotropic material constants [15, 17].

Different theoretical formulations for viscoelasticity (such as Maxwell and Kelvin-Voigt), as an internal energy dissipation mechanism have been introduced, among which the Prony Shear Relaxation formulation has been used extensively where [18]

$$\sigma = I\int_0^t \frac{\mathrm{d}\Delta}{\mathrm{d}\tau}K\left(-\tau+t\right)\mathrm{d}\tau + \int_0^t 2\frac{\mathrm{d}e}{\mathrm{d}\tau}G\left(-\tau+t\right)\mathrm{d}\tau, \tag{2.4}$$

in which t is time, σ represents the Cauchy stress, Δ denotes the volumetric strain, I denotes the identity tensor, e represents the deviatoric strain; also $K(t)$ and $G(t)$ denote the bulk-relaxation moduli and the Prony series shear, respectively and are defined as

$$G\left(t\right) = \left[\left(\sum_{i=1}^{n_G}\alpha_i^G e^{-\frac{t}{\tau_i^G}}\right) + \alpha_\infty^G\right]G_0, \tag{2.5}$$

and

$$K(t)=\left[\left(\sum_{i=1}^{n_K}\alpha_i^K e^{-\frac{t}{\tau_i^K}}\right)+\alpha_\infty^K\right]K_0, \tag{2.6}$$

in which K_0 and G_0 denote the relaxation moduli at $t = 0$ and the bulk-relaxation moduli at $t = 0$, α_i^G and α_i^K show relative moduli, n_G and n_K denote the number of Prony terms, and τ_i^K and τ_i^G represent the relaxation time [19].

2.1.2 Fluid analysis (considering only blood inside artery)

Blood is an important component of the arteries and plays a critical role in plaque rupture, progression and establishing thrombus in the arteries. In the theoretical modelling of blood there are different factors that need to be addressed including its characterisation as being pulsatile [20], either Newtonian and non-Newtonian [21, 22], and 2-dimensional (2D) or 3-dimensional (3D) [23-26]. Table 2-2 summaries the theoretical studies on the analysis of the fluid inside arteries and around plaques; while these precious studies contributed to the understanding of coronary arteries and plaques the limitation of this class is as the artery/plaque is considered rigid, the body stresses cannot be determined.

The nonlinear nature of the viscosity of the blood can be modelled through use of different models such as Carreau model [27] where

$$\mu=\left[\left(\dot{\gamma}\lambda\right)^2+1\right]^{\frac{(n-1)}{2}}\left(-\mu_\infty+\mu_0\right)+\mu_\infty, \tag{2.7}$$

in which $n = 0.3568$, $\lambda = 3.313$ s, $\mu_\infty = 0.00345$ Pa·s and $\mu_0 = 0.056$ Pa·s, the Power Law model [27] with

$$\mu=\left(\dot{\gamma}\right)^{n-1}\mu_0, \tag{2.8}$$

in which $\mu_0 = 0.035$ (Pa·s) and $n = 0.6$, and the Generalised Power Law model [28] with

$$\lambda(\dot{\gamma}) = \Delta\mu\, e^{\left[-\left(\frac{|\dot{\gamma}|}{a}+1\right)e^{\left(-\frac{b}{|\dot{\gamma}|}\right)}\right]} + \mu_\infty,$$
$$n(\dot{\gamma}) = -\Delta n\, e^{\left[-\left(\frac{|\dot{\gamma}|}{c}+1\right)e^{\left(-\frac{d}{|\dot{\gamma}|}\right)}\right]} + n_\infty, \qquad (2.9)$$
$$\mu = |\dot{\gamma}|^{n-1}\lambda,$$

in which $n_\infty = 1.0$, $\mu_\infty = 0.0035$ (Pa·s), $\Delta\mu = 0.25$, $\Delta n = 0.45$, $b = 3$, $a = 50$, $d = 4$, and $c = 50$.

Comparing the different models with experimental data for blood viscosity, Johnston et al. [29] showed that the Generalised Power Law is the best as it matches perfectly with experimental data.

2.1.3 Fluid-structure analysis (considering coupled artery/plaque and blood)

In this section, studies involving the FSI model of arteries and plaques are introduced. None of the structure and fluid analyses are able to individually describe the artery characteristics precisely. Due to the dynamic nature of the system, the boundaries and FSI forces between these two media do not remain constant. Therefore, use of FSI is inevitable for accurately modelling the arteries and plaque. In a primary study by Tang et al. [30], the solid material has been considered hyperelastic, homogenous and isotropic and the fluid characteristics were defined as Newtonian, laminar, viscous, and incompressible in a 3D FSI model which was solved for thick and thin arterial walls. Other factors such as nonlinear time-dependent fluid model [31], microcalcification [32], and pulsatile flow [33] were taken into account in the literature for 2D and 3D analyses [34-36]. In Table 2-3, studies on the theoretical fluid-structure analysis of arteries and plaques are summarised. To summarise, while these precious studies contributed to the understanding of coronary arteries and plaques, these studies did not consider the realistic conditions of the atherosclerotic artery by assuming idealised geometric/haemodynamic conditions and other simplifications. In addition, none of them model the plaque considering all the aforementioned effective factors in combination.

2.2 Combined theoretical and experimental/clinical investigations

In this section of the literature review, studies based on both theory and experimental/clinical investigations are discussed. In all of them, experimental data have been used in theoretical modelling in order to examine the mechanical behaviour of arteries and plaque in a more realistic way [37, 38]. This section is divided into two main groups, *in vitro* studies and *in vivo* investigations. In *in vitro* studies, experimental/clinical investigations were performed on arteries and plaques after harvesting them from the body. Hence, the arteries and plaques can be tested through different methods to extract their mechanical/geometric properties. This, however, presents two problems inherent in *in vitro* experiments. Firstly, the tissues in the arteries and plaques are no longer alive and thus subject to degradation and change, and secondly, the boundary conditions of their working space are not consistent with those in the body, which may affect the obtained results. *In vivo* testing, either invasive or non-invasive, is therefore essential in determining the behaviour of arteries and plaques.

2.2.1 In vitro modelling

The literature review on the *in vitro* modelling is categorised into three different parts regarding the modelling domain, namely structure, fluid, and FSI.

2.2.1(a) Structural analysis (considering only artery and plaques)

In the structural analysis (i.e. in the absence of blood), studies have been conducted based on histology, Intravascular Ultrasound (IVUS), high resolution Magnetic Resonance Imaging (hrMRI), Magnetic Resonance Imaging (MRI), and Optical Coherence Tomography (OCT) of the arteries; they used realistic artery geometries for their theoretical modelling and investigated other features in arteries such as acoustic analysis and prediction of strains [39], sensitivity to material properties [40] via isotropic nonlinear and anisotropic [41] linear methods, cracks and fracture analysis based on MRI *in vitro* [42], IVUS [43], initial stress in the arteries [44], viscoelastic and hyperelastic analysis, and nonlinear isotropic and piecewise

homogeneous material modelling. A summary of these studies is given in Table 2-4 for comparison [45-51]. While these precious studies contributed to the understanding of coronary arteries and plaques, there is still the major gap of modelling the shear stress on the plaque walls in these investigations, as the blood is absent.

2.2.1(b) Fluid analysis (considering only blood inside artery)

There is just one study in which a theoretical and experimental model of fluid micro-haemodynamic properties and flow reversal of an artificial artery vessel was examined using a thermal MEMS sensor [52]. This study did highlight the importance of low wall shear stress (WSS) and flow recirculation regions as areas of disease progression; however, this fluid analysis could not consider the structural stresses on the artery. It is inevitable that the FSI analysis is needed to fill this gap and the gap identified in the preceding section.

2.2.1(c) Fluid-structure analysis (considering coupled artery/plaque and blood)

Prominent investigations have been conducted considering hyperelastic solids and Newtonian fluid models using different characteristics such as MRI-based imaging [53-55], IVUS-based imaging [56], anisotropic vessel properties [57], IVUS-based modelling, and histology-based modelling. Table 2-5 summarises these studies. In conclusion, *in vitro* studies could be useful for obtaining estimations for material properties and other biomechanical parameters, while these precious studies contributed to the understanding of coronary arteries and plaques; however, to provide reliable results it is necessary to model atherosclerosis disease based on realistic working conditions and parameters.

2.2.2 In vivo modelling

Establishing theoretical models based on *in vivo* experimental/clinical data is considered to be the best possible way to model coronary arteries. Since experimental/clinical data are obtained under realistic working conditions of the arteries and plaques, the models/simulations are considered to be more reliable than all the *in vitro* based models/simulations. Again, the three different paradigms of *in vivo* modelling are structural, fluid and FSI analyses, as detailed as follows.

2.2.2(a) Structural analysis (considering only artery and plaques)

Structural analyses were possible via different methods of imaging modality such as MRI, IVUS, ultrasound (US) elastography, and micro-computer tomography (micro CT). Coronary arteries and plaques were the subject of *in vivo* measurements in different studies, where mechanical properties [58, 59], heterogeneous Young's modulus distribution [60], micro calcification [61], and residual stress [62] based on 2D modelling were examined. Table 2-6 presents a summary of these investigations; despite considering different techniques for extracting the *in vivo* behaviour of the artery/plaque and while these precious studies contributed to the understanding of coronary arteries and plaques, they simply eliminated the effect of blood flow on plaque rupture.

Liang et al. [63] examined the 2D radial and circumferential strains on the coronary artery wall based on IVUS imaging from the left anterior descending (LAD) coronary artery; it was showed how to use *in vivo* clinical IVUS data for measurement of the strain field by incorporating cardiac motion. Using elastography from IVUS, Baldewsing et al. [60] obtained the heterogeneous material elasticity of coronary arteries via modelling thin cap fibroatheroma based on *in vivo* IVUS images and assessed rupture; twelve patients were examined by shear strain elastography (SSE) to recognise vulnerable plaques. The first investigation to use OCT images was by Chau et al. [64], who determined the 2D stress/strain distributions in coronary arteries by comparing OCT and

histology-based geometry and analysing sensitivity of the stress and strain. Dynamic optimisation of IVUS-based segmentation was performed by Floc'h et al. [59] to reconstruct atherosclerotic coronary plaque elasticity; they applied their method to seven IVUS images and obtained Young's modulus. Ohayon et al. [65] investigated the arterial wall strain and stress caused by myocardial contraction and examined the stiffness of the bifurcated coronary artery and its correlation with plaque location; both the MRI and CT techniques were also used to determine the geometry and motion of the coronary artery.

2.2.2(b) Fluid analysis (considering only blood inside artery)

Different imaging methods have been used to examine the fluidic behaviour inside arteries and around plaques; the artery wall is assumed to be rigid. Most examinations chose Newtonian and incompressible fluid properties for blood modelling. Unsteady and pulsatile flow, 3D shear stress distributions [66], turbulence models, and haemodynamic parameters [67, 68] are the characteristics of blood flow which have been examined. Table 2-7 highlights these studies [69-71] on *in vivo* fluid analysis of arteries and plaques. While these precious studies contributed to the understanding of coronary arteries and plaques, they cannot provide the whole picture as the wall flexibility and motion of the artery were neglected.

Berthier et al. [72] examined the effect of physiological parameters on a 3D realistic model of a coronary artery; they highlighted the geometry has a large influence on pressure, WSS, and fluid velocity in the coronary arteries. The angulation effect on the haemodynamic parameters of a left coronary artery was examined by modelling both realistic and simulated coronary arteries [73]; they compared WSS, pressure, WSS gradient, and velocity profile and found that a correlation existed between angulation and haemodynamic parameters.

Gijsen et al. [74] reconstructed 3D models of bifurcations of coronary arteries in order to calculate shear stress distribution; they used IVUS and multislice computer tomography (MSCT) to generate their *in vivo* models

with results from these two methods, showing similarities in predicting regions of low and high shear stress values. Li et al. [75] studied the effect of modelling side branches by using OCT and angiograms to obtain coronary artery tree models and to compare them to traditional single-conduit models; they found that considering side branches results in more accurate estimation of the local shear stress. Johnston et al. [29] examined effect of non-Newtonian viscous blood modelling on the artery geometry extracted from bi-plane angiograms. They found that to obtain better approximations of shear stress, Generalised Power Law model for blood flow needs to be employed, and is important because shear stress plays a crucial role in plaque formation and rupture.

Katranas et al. [76] used coronary CT scans and angiography to investigate WSS, vascular stiffness, and plaque volume; they realised that WSSs on the upstream part of plaques are higher than the mid part. Melchionna et al. [71] assessed the risk factors in the atherosclerotic left main (LM) by examining haemodynamic factors such as pressure. They used CT scan images to obtain the geometry and employed the Lattice Boltzmann technique to model the blood flow. Soulis et al. [77] simulated the 3D left coronary artery tree to study haemodynamic parameters (pressure and WSS as well as their gradients); they considered the LCx, LAD and major branches in their simulation, concluding that haemodynamic factors and their gradients showed low values around artery bifurcations.

In another study based on IVUS and angiography of the right coronary artery (RCA), a medium correlation between WSS and low-density-lipoprotein (LDL) was found [78]. Progression of coronary artery disease (CAD) and WSS were examined by Timmins et al. [79] by studying five patients with CAD over two visits; i.e. baseline and a six-month follow-up. Using IVUS and angiogram images they obtained the artery geometry with differences between WSS and CAD progression observed, showing the need to consider other variables in the study or having larger clinical data sets. These studies show the importance of factors such as cardiac motion,

pulsatile blood flow and non-Newtonian fluid models, however, they cannot accurately assess plaque or artery characteristics without including structural analysis.

2.2.2(b) Fluid-structure analysis (considering coupled artery/plaque and blood)

3D FSI models for coronary plaque bifurcations have been developed by means of the previously mentioned imaging approaches. Different artery and plaque features were examined in different studies, for example, investigating microcalcifications [80], comparing wall-only and fluid-only models by FSI modelling [81], modelling 3D anisotropic FSI cyclic bending [82, 83] and by establishing a stress-based computational plaque vulnerability index [84]. Table 2-8 summarises these studies and their distinct features [85]. While these valuable investigations contributed significantly to the knowledge development in the field, they have not incorporated simultaneously all the important and influential parameters together, and hence are not yet able to predict plaque rupture accurately.

Liu et al. [86] studied plaque progression inside a coronary artery based on CT angiography taken at baseline and at a 12-month follow-up; WSS, von Mises stress (VMS), and lumen area were obtained through FSI simulations. Coupled FSI of the LM bifurcation was examined by Dong et al. [87], and analysed the effect of bifurcation angulation on the stress field using a CT based *in vivo* model; it was concluded that angulation significantly changes the mechanical stress distribution.

Fan et al. [88] analysed the correlation between the thickness of a plaque and the wall stresses via IVUS-based simulations for 10 patients; their findings suggested that a larger thickness of plaque's wall increases flow shear stress and decreases the plaque wall stress. An *in vivo,* IVUS-based patient follow-up was performed by Wang et al. [83], who analysed coronary WSS and plaque wall strain and stress; they examined different factors such as depth of lipid, cap thickness, and wall thickness in correlation with shear and plaque wall stress. Tang et al. [84] defined an

index for plaque vulnerability in atherosclerotic coronary arteries; they analysed the 2D MRI images of coronary arteries to determine a stress-based computational index for the plaque. Guo et al. [89] developed an IVUS-based computational model of coronary arteries to investigate the stress and strains on plaques and arteries; they investigated the effect of material stiffness variation on stress/strain variations and compared *ex vivo* and *in vivo* data, revealing that material properties obtained from *in vivo* vessels are significantly softer than the *ex vivo* material properties.

2.3 Plaque rupture progression (crack extension)

Different *in vitro* investigations [90-92] revealed that atherosclerotic human arteries generally start to fracture at certain stress values; it is, therefore, reasonable to use maximum stress as a predictor for plaque rupture initiation. Plaque rupture (crack) progression prediction requires development of models/simulations for fatigue analysis.

Crack propagation inside coronary arteries has been investigated in the following investigations: Bank et al. [93] discussed fatigue failure as a mechanism causing plaque rupture and proved that this hypothesis is in broad agreement with epidemiologic and physiologic data. Versluis et al. [94] analysed the fatigue mechanism for different blood pressures, anatomy, and tissue properties using a 2D idealised model of a diseased artery; it was found that the crack starts at stress concentrations on the lumen wall of the artery and fatigue occurs at low stress levels. Histological images of eight atherosclerotic coronary artery cross-sections were analysed by Rezvani-Sharif et al. [95], who found that lipid pool stiffness influences crack propagation rate and the location of crack initiation. Ferrara et al. [42] modelled/simulated a 3D crack based on *in vitro* MRI using cohesive fracture mechanics; their findings showed that crack development starts at the internal wall of an artery and was in agreement with experimental findings. Furthermore, they claim that the possibility of plaque rupture for high levels of stenosis is less than in low stenosis levels. Paritala et al. [96] used the extended finite element method (XFEM) as well as OCT to develop a 2D model of plaque rupture, demonstrating that high pulse pressure results in to low plaque life.

As a general conclusion, whilst structural-and-fluid based investigations have provided much needed information for atherosclerosis formation and plaque rupture, they cannot fully provide all the critical information to assess plaque rupture in *real life* situations. Hence, developing an accurate FSI model to investigate plaque rupture by including all the important and patient specific data such as realistic geometry, cardiac motion, pulsatile blood velocity profile, non-Newtonian blood model, both viscoelastic and hyperelastic material, microcalcification, fracture mechanisms and accurate plaque composition is essential; this is the key gap in the literature in relation to the aim and objective of this study.

Table 2-1: Theoretical studies on arteries and plaque (structure analysis)

Theoretical study	Imaging modality	Material property	Vessel type	*In vivo/ in vitro*	Number of samples	Description
[1]	---	Hyperelastic	Coronary artery	---	---	FEM/calcification/2D
[2]	---	Linear elastic	Artery	---	---	Rupture at low nominal loads occurred by the calcification/2D
[3]	---	Anisotropic hyperelastic material models	Coronary artery	---	---	FEM/parametric analysis/2D
[4]	---	Isotropic and linear elastic	Coronary artery	---	---	FEM/ parametric analysis/2D
[5]	---	Hyperelastic	Coronary artery	---	---	Axial and circumferential residual stresses/ FEM/3D
[6]	---	Hyperelastic and nonlinear	Coronary artery	---	---	Role of vascular growth/ positive and negative morphology
[7]		Hyperelastic	Coronary artery	---	---	Microcalcification/FEM/2D
[8]	---	Linear elastic	Arterial cross section	---	---	Fatigue crack propagation/FEM/2D
[9]	---	Orthotropic and hyperelastic	Coronary artery	---	---	Young's modulus and geometry of calcification/FEM/2D
[10]	---	Fiber-reinforced/ anisotropic and hyperelastic	Coronary artery	---	---	FEM/2D
[13]		Hyperelastic and nonlinear	Coronary artery	---	---	FEM/ microcalcification/3D
[11]	---	Hyperelastic	Coronary artery	---	---	FEM/2D
[12]	---	Viscoelastic		---		FEM/inversion algorithm/3D

Table 2-2: Theoretical studies on blood (fluid analysis)

Theoretical study	Imaging modality	Fluid type	Vessel type	*In vivo/ in vitro*	Number of samples	Description
[20]	---	Newtonian	Coronary arteries	---	---	Steady and pulsatile flow
[21]	---	Non-Newtonian	Artery wall	---	---	Navier-Stokes/2D
[22]	---	Laminar flow/ Newtonian/ non-Newtonian blood	Coronary arteries	---	---	Wall shear stress (WSS) and velocity distribution patterns/Pulsatile blood flow/2D
[23]	---	Viscous/ homogeneous/ Newtonian	LM coronary artery	---	---	Pulsatile flow/curved tapered artery/full Navier-Stokes equations/secondary flow/ WSS/3D
[24]	---	Newtonian/ laminar/viscous	Coronary artery	---	---	Steady & pulsatile flow/WSS/platelet aggregation/activation/surface roughness/2D
[25]	---	Laminar & turbulent/ viscous	LM coronary artery	---	---	Pulsatile flow/shear stress/velocity distribution/3D
[26]	---	Non-Newtonian/ homogeneous	Coronary artery	---	---	Steady flow/helical stenosis lesion/irrotational flow

Table 2-3: Combined theoretical studies on arteries/plaques and blood (coupled fluid-structure analysis)

Theoretical study	Imaging modality	Material property/fluid type	Vessel type	*In vivo/ in vitro*	Number of samples	Description
[30]	---	Laminar/Newtonian/viscous and incompressible/elastic	Artery wall	---	---	Thick-wall/FSI/3D
[32]	---	Isotropic hyperelastic/incompressible/ Newtonian/homogeneous/ viscous	Artery wall	---	---	FSI/microcalcification/3D
[34]	---	Hyperelastic/viscoelastic microfilaments/ incompressible/Mooney-Rivilin/Voigt viscoelastic microfibers/Newtonian/ viscous/laminar	LM/LAD/ LCx	---	---	FSI/cell scale model/endothelial cell morphology
[35]	---	Isotropic/homogeneous, hyperelastic/Mooney-Rivilin model/incompressible/single layer/Newtonian/viscous	LM/LAD/ LCx	---	---	FSI/endothelial cell alignment/ secondary plaque formation/unsteady blood flow
[36]	---	Hyperelastic/homogeneous/ viscous/laminar/Newtonian	Coronary artery	---	---	Normal and hyperaemic flow/2D

Table 2-4: Combined theoretical and experimental/clinical studies on arteries and plaques (structure analysis/ *in vitro*)

Study	Imaging modality	Material property	Vessel type	*In vivo/ in vitro*	Number of samples	Description
[39]	IVUS	Linear	Diseased coronary artery	*In vitro*	1	Acoustic analysis/prediction of strains
[40]	Histology	Isotropic non-linear/ anisotropic linear	Coronary artery	*In vitro*	1	FEM/solid/ sensitivity to material properties/2D
[41]	Histology	Anisotropic hyperelastic	Human abdominal aorta	*In vitro*	2	Residual stresses/ FEM/ solid/2D
[42]	MRI	Hyperelastic two-fiber anisotropic	Damaged artery	*In vitro*	1	FEM/ solid/ Cracks and fracture in human arteries/3D
[43]	IVUS	Hyperelastic	Coronary artery	*In vitro*	1	Hydrostatic pressure/3D/2D
[44]	Histology	Hyperelastic	Coronary arteries	*In vitro*	50	Initial stress/ Backward Incremental method /FEM/solid/2D/
[45]	Histology	Linear elastic isotropic	Mice's aorta and human's coronary arteries	*In vitro*	34+42+ 49	FEM/solid/2D
[46]	Histology	Hyperelastic	Coronary arteries	*In vitro*	23	FEM/solid/2D/ 3D
[47]	Histology	Hyperelastic	Coronary arteries	*In vitro*	1	FEM/solid/2D
[48]	Histology	Hyperelastic	Coronary arteries	*In vitro*	4	Comparison of 3D with 2D/FEM/solid
[49]	OCT		Coronary arteries	*In vitro*	6	Wall motion analysis
[50]	Histology	Hyperelastic, homogeneous and incompressible	Coronary arteries	*In vitro*	7	FEM/solid/2D
[51]	Histology	Isotropic/hyperelastic	Coronary lesions	*In vitro*	77	2D modelling

Table 2-5: Combined theoretical and experimental/clinical studies on arteries/plaques and blood (fluid-structure analysis/ *in vitro*)

Study	Imaging modality	Material property/Fluid type	Vessel type	*In vivo*/ *in vitro*	Number of samples	Description
[53]	MRI	Hyperelastic/laminar/ Newtonian/viscous/ incompressible/	Coronary plaque	*In vitro*	64	FSI/3D
[54]	MRI	Hyperelastic/laminar/ Newtonian/viscous/ incompressible/	Coronary plaque	*In vitro*	36	FSI/3D
[55]	MRI	Hyperelastic/laminar/ Newtonian/viscous/ incompressible	Coronary artery	*In vitro*	12	FSI/3D
[56]	IVUS	Hyperelastic	Diseased coronary Specimens	*In vitro*	1	FSI/3D

Table 2-6: Combined theoretical and experimental/clinical studies on arteries and plaques (structure analysis/ *in vivo*)

Study	Imaging modality	Material property	Vessel type	*In vivo*/ *in vitro*	Number of samples	Description
[58]	IVUS	Isotropic/ elastic	Coronary artery	*In vivo*/*in vitro*	1	Mechanical properties
[59]	IVUS	Linear elastic	Coronary artery	*In vivo*	1	Mechanical properties/idealised cross-sectional plaque morphologies
[60]	IVUS	Linear elastic	Coronary plaques	*In vivo*/*in vitro*	1	Heterogeneous Young's modulus distribution/different methods
[61]	High resolution microCT	Hyperelastic/ isotropic/homo geneous	Coronary arteries	*In vivo*	1	Micro Calcification
[62]	IVUS	Hyperelastic	Coronary arteries	*In vivo*	1	Residual stress/axial shrinkage/circumferential shrinkage/2D
[63]	IVUS	Linear elastic	Coronary plaques	*In vivo*	1	2D

Table 2-7: Combined theoretical and experimental/clinical studies on blood (fluid analysis/ *in vivo*)

Study	Imaging modality	Fluid type	Vessel type	*In vivo*/ *in vitro*	Number of samples	Description
[66]	IVUS	Newtonian	Coronary artery	Inspired from *in vivo*	1	Volume PIV method/3D shear stress distributions
[68]	IVUS	Newtonian/ incompressible	Coronary plaques	*In vivo*	42	Haemodynamic parameters are strongly dependent on the plaque shape
[69]	IVUS/ angiogram	Newtonian/viscous/ laminar	RCA coronary artery	*In vivo*/ idealised model	7	Stent restenosis/ WSS /wall growth instability
[70]	Angiogram	Non-Newtonian/ laminar	LM coronary artery & bifurcations	In-vivo/ idealised model	1	Artery centreline & radius reconstruction/steady flow/ WSS variation
[71]	CT/angiogram /FFR	Newtonian/viscous	Left coronary artery tree	In-vivo/ idealised model	1	Flow of suspended particles in stenosis/FFR sensitivity to stenosis severity
[73]	CT/angiogram	Newtonian/viscous/ laminar	LM coronary artery and bifurcations	In-vivo/ idealised model	4	Variation in bifurcation angle effects on haemodynamic parameters/ WSS and gradient, pulsatile flow

Table 2-8: Combined theoretical and experimental/clinical studies on arteries/plaque and blood (coupled fluid-structure analysis/ *in vivo*)

Study	Imaging modality	Material property/fluid type	Vessel type	*In vivo*/ *in vitro*	Number of samples	Description
[80]	Micro-CT	Hyperelastic	Coronary specimen	*In vivo*	1	FSI/ microcalcifications (micro-Cal)/embedded in the vulnerable plaques fibrous cap/3D
[81]	MRI	Hyperelastic/isotropic/ homogeneous/ incompressible/ laminar/ non-Newtonian/viscous /incompressible	Atherosclerotic plaques	*In vivo*	1	FSI/comparing Newtonian and non-Newtonian/comparing wall-only/fluid-only models/3D
[82]	IVUS/X-ray angiogram	Hyperelastic/laminar/ Newtonian	Coronary artery stenosis	*In vivo*	10	anisotropic FSI/effect by heart contraction/3D
[83]	IVUS	Hyperelastic/laminar/ Newtonian/ incompressible	Coronary arteries	*In vivo*	3	FSI/Patient follow-up/cyclic bending/3D
[84]	MRI	Hyperelastic/laminar/ Newtonian/viscous/ incompressible	Coronary plaque	*In vivo*	34	FSI/computational plaque vulnerability index are proposed/3D
[85]	IVUS	Hyperelastic	Coronary plaque	*In vivo*	20	FSI models/patient-specific vessel material properties/slice-specific circumferential shrinkage rates/3D

References

[1] T. Hoshino, L.A. Chow, J.J. Hsu, A.A. Perlowski, M. Abedin, J. Tobis, Y. Tintut, A.K. Mal, W.S. Klug, L.L. Demer, Mechanical stress analysis of a rigid inclusion in distensible material: a model of atherosclerotic calcification and plaque vulnerability, American Journal of Physiology-Heart and Circulatory Physiology, 297 (2009) H802-H810.
[2] C.M. Nguyen, A.J. Levy, The mechanics of atherosclerotic plaque rupture by inclusion/matrix interfacial decohesion, Journal of Biomechanics, 43 (2010) 2702-2708.
[3] A.C. Akyildiz, L. Speelman, H. van Brummelen, M.A. Gutiérrez, R. Virmani, A. van der Lugt, A.F. van der Steen, J.J. Wentzel, F.J. Gijsen, Effects of intima stiffness and plaque morphology on peak cap stress, Biomedical Engineering Online, 10 (2011) 1.
[4] W.J.S. Dolla, J.A. House, S.P. Marso, Stratification of risk in thin cap fibroatheromas using peak plaque stress estimates from idealized finite element models, Medical Engineering & Physics, 34 (2012) 1330-1338.
[5] M. Cilla, E. Pena, M. Martinez, 3D computational parametric analysis of eccentric atheroma plaque: influence of axial and circumferential residual stresses, Biomechanics and Modeling in Mechanobiology, 11 (2012) 1001-1013.
[6] M. Cilla, E. Peña, M. Martínez, D. Kelly, Comparison of the vulnerability risk for positive versus negative atheroma plaque morphology, Journal of Biomechanics, 46 (2013) 1248-1254.
[7] M. Cilla, D. Monterde, E. Peña, M.A. Martinez, Does microcalcification increase the risk of rupture?, Proceedings of the Institution of Mechanical Engineers, Part H: Journal of Engineering in Medicine, (2013) 0954411913479530.
[8] X. Pei, B. Wu, Z.-Y. Li, Fatigue crack propagation analysis of plaque rupture, Journal of Biomechanical Engineering, 135 (2013) 101003.
[9] C.M. Buffinton, D.M. Ebenstein, Effect of calcification modulus and geometry on stress in models of calcified atherosclerotic plaque, Cardiovascular Engineering and Technology, 5 (2014) 244-260.
[10] H. Mohammadi, K. Mequanint, Effect of stress intensity factor in evaluation of instability of atherosclerotic plaque, Journal of Mechanics in Medicine and Biology, 14 (2014) 1450072.
[11] W. Lee, G.J. Choi, S.W. Cho, Numerical study to indicate the vulnerability of plaques using an idealized 2D plaque model based on plaque classification in the human coronary artery, Medical & Biological Engineering & Computing, 1-9.
[12] L. Thomas-Seale, L. Hollis, D. Klatt, I. Sack, N. Roberts, P. Pankaj, P. Hoskins, The simulation of magnetic resonance elastography through atherosclerosis, Journal of Biomechanics, 49 (2016) 1781-1788.
[13] L. Cardoso, A. Kelly-Arnold, N. Maldonado, D. Laudier, S. Weinbaum, Effect of tissue properties, shape and orientation of microcalcifications on vulnerable cap stability using different hyperelastic constitutive models, Journal of Biomechanics, 47 (2014) 870-877.
[14] ANSYS® (version 18.0, ANSYS Inc., Canonsburg, PA, US), ANSYS® Academic Research Mechanical, Release 18.0, Help System, ANSYS Documentation/ Mechanical Applications/ Explicit Dynamics Analysis Guide

Overview/ Material Models Used in Explicit Dynamics Analysis/ Hyperelasticity/ 5-Parameter Mooney-Rivlin Model, ANSYS, Inc.
[15] G.A. Holzapfel, T.C. Gasser, R.W. Ogden, A new constitutive framework for arterial wall mechanics and a comparative study of material models, Journal of Elasticity and the Physical Science of Solids, 61 (2000) 1-48.
[16] G.A. Holzapfel, G. Sommer, C.T. Gasser, P. Regitnig, Determination of layer-specific mechanical properties of human coronary arteries with nonatherosclerotic intimal thickening and related constitutive modeling, American Journal of Physiology-Heart and Circulatory Physiology, 289 (2005) H2048-H2058.
[17] T. Belzacq, S. Avril, E. Leriche, A. Delache, A numerical parametric study of the mechanical action of pulsatile blood flow onto axisymmetric stenosed arteries, Medical engineering & physics, 34 (2012) 1483-1495.
[18] A. Karimi, A. Shojaei, R. Razaghi, Viscoelastic mechanical measurement of the healthy and atherosclerotic human coronary arteries using DIC technique, Artery Research, 18 (2017) 14-21.
[19] ANSYS® (version 19.0, ANSYS Inc., Canonsburg, PA, US), ANSYS® Academic Research Mechanical, Release 19.0, ANSYS Product Help, Documentation, Material Reference, Nonlinear Material Properties, Viscoelasticity, ANSYS, Inc.
[20] L. Chua, S. Yu, Q. Xue, Scaling laws for wall shear stress through stenoses under steady and pulsatile flow conditions, Proceedings of the Institution of Mechanical Engineers, Part H: Journal of Engineering in Medicine, 215 (2001) 503-514.
[21] T. Deepa, L. Binu, A.K. Sukesh, Modelling blood flow and analysis of atherosclerotic plaque rupture under G-force, 2009 3rd International Conference on Bioinformatics and Biomedical Engineering, IEEE, 2009, 1-4.
[22] S.M.J.M. Akherat, M. Kimiaghalam, A numerical investigation on pulsatile blood flow through consecutive axi-symmetric stenosis in coronary artery, ASME 2010 10th Biennial Conference on Engineering Systems Design and Analysis, American Society of Mechanical Engineers, 2010, 757-765.
[23] K. Perktold, R.M. Nerem, R.O. Peter, A numerical calculation of flow in a curved tube model of the left main coronary artery, Journal of biomechanics, 24 (1991) 175-189.
[24] D.L. Bark, D.N. Ku, Wall shear over high degree stenoses pertinent to atherothrombosis, Journal of Biomechanics, 43 (2010) 2970-2977.
[25] S.K. Shanmugavelayudam, D.A. Rubenstein, W. Yin, Effect of Geometrical Assumptions on Numerical Modeling of Coronary Blood Flow Under Normal and Disease Conditions, Journal of Biomechanical Engineering, 132 (2010) 061004-061004-061008.
[26] K. Wong, J. Mazumdar, B. Pincombe, S.G. Worthley, P. Sanders, D. Abbott, Theoretical modeling of micro-scale biological phenomena in human coronary arteries, Medical and Biological Engineering and Computing, 44 (2006) 971-982.
[27] Y.I. Cho, K.R. Kensey, Effects of the non-Newtonian viscosity of blood on flows in a diseased arterial vessel. Part 1: Steady flows, Biorheology, 28 (1991) 241-262.
[28] P. Ballyk, D. Steinman, C. Ethier, Simulation of non-Newtonian blood flow in an end-to-side anastomosis, Biorheology, 31 (1994) 565-586.

[29] B.M. Johnston, P.R. Johnston, S. Corney, D. Kilpatrick, Non-Newtonian blood flow in human right coronary arteries: steady state simulations, Journal of Biomechanics, 37 (2004) 709-720.
[30] D. Tang, C. Yang, S. Kobayashi, D.N. Ku, Steady flow and wall compression in stenotic arteries: a three-dimensional thick-wall model with fluid–wall interactions, Journal of Biomechanical Engineering, 123 (2001) 548-557.
[31] Z.-Y. Li, J.H. Gillard, Simulation of the interaction between blood flow and atherosclerotic plaque, 2007 29th Annual International Conference of the IEEE Engineering in Medicine and Biology Society, IEEE, 2007, 1699-1702.
[32] J.F. Wenk, P. Papadopoulos, T.I. Zohdi, Numerical modeling of stress in stenotic arteries with microcalcifications: a micromechanical approximation, Journal of Biomechanical Engineering, 132 (2010) 091011.
[33] L. Pu, H. Xiong, X. Liu, H. Zhang, Y.-T. Zhang, Quantifying effect of blood pressure on stress distribution in atherosclerotic plaque, The International Conference on Health Informatics, Springer, 2014, 216-219.
[34] H.A. Pakravan, M.S. Saidi, B. Firoozabadi, A multiscale approach for determining the morphology of endothelial cells at a coronary artery, International journal for numerical methods in biomedical engineering, 33 (2017) e2891.
[35] R. Jahromi, H.A. Pakravan, M.S. Saidi, B. Firoozabadi, Primary stenosis progression versus secondary stenosis formation in the left coronary bifurcation: A mechanical point of view, Biocybernetics and Biomedical Engineering, 39 (2019) 188-198.
[36] O.M. Rotman, U. Zaretsky, A. Shitzer, S. Einav, Pressure drop and arterial compliance–Two arterial parameters in one measurement, Journal of biomechanics, 50 (2017) 130-137.
[37] T.C. Lin, Y. Tintut, A. Lyman, W. Mack, L.L. Demer, T.K. Hsiai, Mechanical response of a calcified plaque model to fluid shear force, Annals of Biomedical Engineering, 34 (2006) 1535-1541.
[38] J. Ji, S. Toubaru, S. Kobayashi, H. Morikawa, D. Tang, D.N. Ku, Flow and deformation in a multi-component arterial stenosis model, Journal of Biomechanical Science and Engineering, 6 (2011) 79-88.
[39] A.I. Veress, J.A. Weiss, G.T. Gullberg, D.G. Vince, R.D. Rabbitt, Strain measurement in coronary arteries using intravascular ultrasound and deformable images, Journal of Biomechanical Engineering, 124 (2002) 734-741.
[40] S. Williamson, Y. Lam, H. Younis, H. Huang, S. Patel, M. Kaazempur-Mofrad, R. Kamm, On the sensitivity of wall stresses in diseased arteries to variable material properties, Journal of Biomechanical Engineering, 125 (2003) 147-155.
[41] D. Balzani, J. Schröder, D. Gross, Simulation of discontinuous damage incorporating residual stresses in circumferentially overstretched atherosclerotic arteries, Acta Biomaterialia, 2 (2006) 609-618.
[42] A. Ferrara, A. Pandolfi, Numerical modelling of fracture in human arteries, Computer Methods in Biomechanics and Biomedical Engineering, 11 (2008) 553-567.
[43] V. Pazos, R. Mongrain, J.-C. Tardif, Mechanical characterization of atherosclerotic arteries using finite-element modeling: feasibility study on mock arteries, IEEE Transactions on Biomedical Engineering, 57 (2010) 1520-1528.

[44] L. Speelman, A. Akyildiz, B. Den Adel, J. Wentzel, A. Van der Steen, R. Virmani, L. Van der Weerd, J.W. Jukema, R. Poelmann, E. van Brummelen, Initial stress in biomechanical models of atherosclerotic plaques, Journal of Biomechanics, 44 (2011) 2376-2382.
[45] I.C. Campbell, D. Weiss, J.D. Suever, R. Virmani, A. Veneziani, R.P. Vito, J.N. Oshinski, W.R. Taylor, Biomechanical modeling and morphology analysis indicates plaque rupture due to mechanical failure unlikely in atherosclerosis-prone mice, American Journal of Physiology-Heart and Circulatory Physiology, 304 (2013) H473-H486.
[46] A. Karimi, M. Navidbakhsh, S. Faghihi, A. Shojaei, K. Hassani, A finite element investigation on plaque vulnerability in realistic healthy and atherosclerotic human coronary arteries, Proceedings of the Institution of Mechanical Engineers, Part H: Journal of Engineering in Medicine, 227 (2013) 148-161.
[47] A. Mangalaprakash, R.K. Kumar, K.R. Balakrishnan, Effect of calcification on plaque stresses and vulnerability: A finite element study, Mechanics of Advanced Materials and Structures, 20 (2013) 309-315.
[48] H. Nieuwstadt, A. Akyildiz, L. Speelman, R. Virmani, A. van der Lugt, A. van der Steen, J. Wentzel, F. Gijsen, The influence of axial image resolution on atherosclerotic plaque stress computations, Journal of Biomechanics, 46 (2013) 689-695.
[49] C. Robertson, A.E. Heidari, Z. Chen, S.C. George, Mechanical analysis of arterial plaques in native geometry with OCT wall motion analysis, Journal of Biomechanics, 47 (2014) 755-758.
[50] A.M. Kok, L. Speelman, R. Virmani, A.F. Steen, F.J. Gijsen, J.J. Wentzel, Peak cap stress calculations in coronary atherosclerotic plaques with an incomplete necrotic core geometry, Biomedical Engineering Online, 15 (2016) 1.
[51] A.C. Akyildiz, L. Speelman, H.A. Nieuwstadt, H. van Brummelen, R. Virmani, A. van der Lugt, A.F. van der Steen, J.J. Wentzel, F.J. Gijsen, The effects of plaque morphology and material properties on peak cap stress in human coronary arteries, Computer Methods in Biomechanics and Biomedical Engineering, 19 (2016) 771-779.
[52] L. Ai, L. Zhang, W. Dai, C. Hu, K.K. Shung, T.K. Hsiai, Real-time assessment of flow reversal in an eccentric arterial stenotic model, Journal of Biomechanics, 43 (2010) 2678-2683.
[53] D. Tang, C. Yang, J. Zheng, P.K. Woodard, G.A. Sicard, J.E. Saffitz, C. Yuan, 3D MRI-based multicomponent FSI models for atherosclerotic plaques, Annals of Biomedical Engineering, 32 (2004) 947-960.
[54] D. Tang, C. Yang, J. Zheng, P.K. Woodard, J.E. Saffitz, G.A. Sicard, T.K. Pilgram, C. Yuan, Quantifying effects of plaque structure and material properties on stress distributions in human atherosclerotic plaques using 3D FSI models, Journal of Biomechanical Engineering, 127 (2005) 1185-1194.
[55] X. Huang, C. Yang, J. Zheng, R. Bach, D. Muccigrosso, P.K. Woodard, D. Tang, Higher critical plaque wall stress in patients who died of coronary artery disease compared with those who died of other causes: a 3D FSI study based on ex vivo MRI of coronary plaques, Journal of Biomechanics, 47 (2014) 432-437.

[56] M.H. Kural, M. Cai, D. Tang, T. Gwyther, J. Zheng, K.L. Billiar, Planar biaxial characterization of diseased human coronary and carotid arteries for computational modeling, Journal of Biomechanics, 45 (2012) 790-798.
[57] D. Tang, C. Yang, S. Kobayashi, J. Zheng, P.K. Woodard, Z. Teng, K. Billiar, R. Bach, D.N. Ku, 3D MRI-based anisotropic FSI models with cyclic bending for human coronary atherosclerotic plaque mechanical analysis, Journal of Biomechanical Engineering, 131 (2009) 061010.
[58] R.A. Baldewsing, J.A. Schaar, F. Mastik, C.W. Oomens, A.F. van der Steen, Assessment of vulnerable plaque composition by matching the deformation of a parametric plaque model to measured plaque deformation, IEEE Transactions on Medical Imaging, 24 (2005) 514-528.
[59] S. Le Floc'h, J. Ohayon, P. Tracqui, G. Finet, A.M. Gharib, R.L. Maurice, G. Cloutier, R.I. Pettigrew, Vulnerable atherosclerotic plaque elasticity reconstruction based on a segmentation-driven optimization procedure using strain measurements: theoretical framework, IEEE Transactions on Medical Imaging, 28 (2009) 1126-1137.
[60] R.A. Baldewsing, M.G. Danilouchkine, F. Mastik, J.A. Schaar, P.W. Serruys, A.F. van der Steen, An inverse method for imaging the local elasticity of atherosclerotic coronary plaques, IEEE Transactions on Information Technology in Biomedicine, 12 (2008) 277-289.
[61] N. Maldonado, A. Kelly-Arnold, L. Cardoso, S. Weinbaum, The explosive growth of small voids in vulnerable cap rupture; cavitation and interfacial debonding, Journal of Biomechanics, 46 (2013) 396-401.
[62] L. Wang, J. Zhu, H. Samady, D. Monoly, J. Zheng, X. Guo, A. Maehara, C. Yang, G. Ma, G.S. Mintz, Effects of Residual Stress, Axial Stretch, and Circumferential Shrinkage on Coronary Plaque Stress and Strain Calculations: A Modeling Study Using IVUS-Based Near-Idealized Geometries, Journal of Biomechanical Engineering, 139 (2017) 014501.
[63] Y. Liang, H. Zhu, T. Gehrig, M.H. Friedman, Measurement of the transverse strain tensor in the coronary arterial wall from clinical intravascular ultrasound images, Journal of Biomechanics, 41 (2008) 2906-2911.
[64] A.H. Chau, R.C. Chan, M. Shishkov, B. MacNeill, N. Iftimia, G.J. Tearney, R.D. Kamm, B.E. Bouma, M.R. Kaazempur-Mofrad, Mechanical analysis of atherosclerotic plaques based on optical coherence tomography, Annals of Biomedical Engineering, 32 (2004) 1494-1503.
[65] J. Ohayon, A.M. Gharib, A. Garcia, J. Heroux, S.K. Yazdani, M. Malvè, P. Tracqui, M.-A. Martinez, M. Doblare, G. Finet, Is arterial wall-strain stiffening an additional process responsible for atherosclerosis in coronary bifurcations?: an in vivo study based on dynamic CT and MRI, American Journal of Physiology-Heart and Circulatory Physiology, 301 (2011) H1097-H1106.
[66] J. Brunette, R. Mongrain, J. Laurier, R. Galaz, J. Tardif, 3D flow study in a mildly stenotic coronary artery phantom using a whole volume PIV method, Medical Engineering & Physics, 30 (2008) 1193-1200.
[67] M. Cummins, J.S. Rossmann, Hemodynamics of Ulcerated Plaques: Before and After, Journal of Biomechanical Engineering, 132 (2010) 104503.
[68] K. Bhaganagar, C. Moreno, Modeling of Stenotic coronary artery and implications of plaque morphology on blood flow, Modelling and Simulation in Engineering, 390313 (2013) 1-14.

[69] J. García, A. Crespo, J. Goicolea, M. Sanmartín, C. García, Study of the evolution of the shear stress on the restenosis after coronary angioplasty, Journal of Biomechanics, 39 (2006) 799-805.
[70] J.V. Soulis, T.M. Farmakis, G.D. Giannoglou, G.E. Louridas, Wall shear stress in normal left coronary artery tree, Journal of Biomechanics, 39 (2006) 742-749.
[71] S. Melchionna, G. Amati, M. Bernaschi, M. Bisson, S. Succi, D. Mitsouras, F.J. Rybicki, Risk assessment of atherosclerotic plaques based on global biomechanics, Medical Engineering & Physics, 35 (2013) 1290-1297.
[72] B. Berthier, R. Bouzerar, C. Legallais, Blood flow patterns in an anatomically realistic coronary vessel: influence of three different reconstruction methods, Journal of Biomechanics, 35 (2002) 1347-1356.
[73] T. Chaichana, Z. Sun, J. Jewkes, Computation of hemodynamics in the left coronary artery with variable angulations, Journal of Biomechanics, 44 (2011) 1869-1878.
[74] F.J. Gijsen, J.C. Schuurbiers, A.G. van de Giessen, M. Schaap, A.F. van der Steen, J.J. Wentzel, 3D reconstruction techniques of human coronary bifurcations for shear stress computations, Journal of Biomechanics, 47 (2014) 39-43.
[75] Y. Li, J.L. Gutiérrez-Chico, N.R. Holm, W. Yang, L. Hebsgaard, E.H. Christiansen, M. Mæng, J.F. Lassen, F. Yan, J.H. Reiber, Impact of side branch modeling on computation of endothelial shear stress in coronary artery disease: coronary tree reconstruction by fusion of 3D angiography and OCT, Journal of the American College of Cardiology, 66 (2015) 125-135.
[76] S.A. Katranas, A.P. Antoniadis, A.L. Kelekis, G.D. Giannoglou, Insights on atherosclerosis by non-invasive assessment of wall stress and arterial morphology along the length of human coronary plaques, The International Journal of Cardiovascular Imaging, 31 (2015) 1627-1633.
[77] J.V. Soulis, G.D. Giannoglou, G.E. Parcharidis, G.E. Louridas, Flow parameters in normal left coronary artery tree. Implication to atherogenesis, Computers in Biology and Medicine, 37 (2007) 628-636.
[78] J.V. Soulis, D.K. Fytanidis, V.C. Papaioannou, G.D. Giannoglou, Wall shear stress on LDL accumulation in human RCAs, Medical Engineering & Physics, 32 (2010) 867-877.
[79] L.H. Timmins, D.S. Molony, P. Eshtehardi, M.C. McDaniel, J.N. Oshinski, H. Samady, D.P. Giddens, Focal association between wall shear stress and clinical coronary artery disease progression, Annals of Biomedical Engineering, 43 (2015) 94-106.
[80] S. Rambhia, X. Liang, M. Xenos, Y. Alemu, N. Maldonado, A. Kelly, S. Chakraborti, S. Weinbaum, L. Cardoso, S. Einav, Microcalcifications increase coronary vulnerable plaque rupture potential: a patient-based micro-CT fluid–structure interaction study, Annals of Biomedical Engineering, 40 (2012) 1443-1454.
[81] C. Yang, D. Tang, C. Yuan, T.S. Hatsukami, J. Zheng, P.K. Woodard, In vivo/ex vivo MRI-based 3D non-Newtonian FSI models for human atherosclerotic plaques compared with fluid/wall-only models, Computer Modeling in Engineering & Sciences: CMES, 19 (2007) 233.
[82] R. Fan, D. Tang, C. Yang, J. Zheng, R. Bach, L. Wang, D. Muccigrosso, K. Billiar, J. Zhu, G. Ma, Human coronary plaque wall thickness correlated

positively with flow shear stress and negatively with plaque wall stress: an IVUS-based fluid-structure interaction multi-patient study, Biomedical Engineering Online, 13 (2014) 1.
[83] L. Wang, Z. Wu, C. Yang, J. Zheng, R. Bach, D. Muccigrosso, K. Billiar, A. Maehara, G.S. Mintz, D. Tang, IVUS-based FSI models for human coronary plaque progression study: components, correlation and predictive analysis, Annals of Biomedical Engineering, 43 (2015) 107-121.
[84] D. Tang, C. Yang, J. Zheng, P.K. Woodard, J.E. Saffitz, J.D. Petruccelli, G.A. Sicard, C. Yuan, Local maximal stress hypothesis and computational plaque vulnerability index for atherosclerotic plaque assessment, Annals of Biomedical Engineering, 33 (2005) 1789-1801.
[85] X. Guo, J. Zhu, A. Maehara, D. Monoly, H. Samady, L. Wang, K.L. Billiar, J. Zheng, C. Yang, G.S. Mintz, Quantify patient-specific coronary material property and its impact on stress/strain calculations using in vivo IVUS data and 3D FSI models: a pilot study, Biomechanics and Modeling in Mechanobiology, (2016) 1-12.
[86] X. Liu, G. Wu, C. Xu, Y. He, L. Shu, Y. Liu, N. Zhang, C. Lin, Prediction of coronary plaque progression using biomechanical factors and vascular characteristics based on computed tomography angiography, Computer Assisted Surgery, 22 (2017) 286-294.
[87] J. Dong, Z. Sun, K. Inthavong, J. Tu, Fluid–structure interaction analysis of the left coronary artery with variable angulation, Computer Methods in Biomechanics and Biomedical Engineering, 18 (2015) 1500-1508.
[88] R. Fan, D. Tang, C. Yang, J. Zheng, R. Bach, L. Wang, D. Muccigrosso, K. Billiar, J. Zhu, G. Ma, Human coronary plaque wall thickness correlated positively with flow shear stress and negatively with plaque wall stress: an IVUS-based fluid-structure interaction multi-patient study, Biomedical Engineering Online, 13 (2014) 32.
[89] X. Guo, J. Zhu, A. Maehara, D. Monoly, H. Samady, L. Wang, K.L. Billiar, J. Zheng, C. Yang, G.S. Mintz, Quantify patient-specific coronary material property and its impact on stress/strain calculations using in vivo IVUS data and 3D FSI models: a pilot study, Biomechanics and Modeling in Mechanobiology, 16 (2017) 333-344.
[90] C.L. Lendon, M. Davies, G. Born, P.D. Richardson, Atherosclerotic plaque caps are locally weakened when macrophages density is increased, Atherosclerosis, 87 (1991) 87-90.
[91] H. Huang, R. Virmani, H. Younis, A.P. Burke, R.D. Kamm, R.T. Lee, The impact of calcification on the biomechanical stability of atherosclerotic plaques, Circulation, 103 (2001) 1051-1056.
[92] G.C. Cheng, H.M. Loree, R.D. Kamm, M.C. Fishbein, R.T. Lee, Distribution of circumferential stress in ruptured and stable atherosclerotic lesions. A structural analysis with histopathological correlation, Circulation, 87 (1993) 1179-1187.
[93] A. Bank, A. Versluis, S. Dodge, W.H. Douglas, Atherosclerotic plaque rupture: a fatigue process?, Medical Hypotheses, 55 (2000) 480-484.
[94] A. Versluis, A.J. Bank, W.H. Douglas, Fatigue and plaque rupture in myocardial infarction, Journal of Biomechanics, 39 (2006) 339-347.

[95] A. Rezvani-Sharif, M. Tafazzoli-Shadpour, D. Kazemi-Saleh, M. Sotoudeh-Anvari, Stress analysis of fracture of atherosclerotic plaques: crack propagation modeling, Medical & biological engineering & computing, 55 (2017) 1389-1400.
[96] P.K. Paritala, P.K. Yarlagadda, J. Wang, Y. Gu, Z. Li, Numerical investigation of atherosclerotic plaque rupture using optical coherence tomography imaging and XFEM, Engineering Fracture Mechanics, 204 (2018) 531-541.

Chapter 3

Three-dimensional biomechanics of coronary arteries

Statement of Authorship

Title of Paper	Three-dimensional biomechanics of coronary arteries
Publication Status	☑ Published ☐ Accepted for Publication ☐ Submitted for Publication ☐ Unpublished and Unsubmitted work written in manuscript style
Publication Details	International Journal of Engineering Science Volume 130, September 2018, Pages 93-114

Principal Author

Name of Principal Author (Candidate)	Alireza Gholipour
Contribution to the Paper	Performed all analyses and wrote the manuscript.
Overall percentage (%)	75
Certification:	This paper reports on original research I conducted during the period of my Higher Degree by Research candidature and is not subject to any obligations or contractual agreements with a third party that would constrain its inclusion in this thesis. I am the primary author of this paper.
Signature	Date 19/8/2019

Co-Author Contributions

By signing the Statement of Authorship, each author certifies that:

i. the candidate's stated contribution to the publication is accurate (as detailed above);

ii. permission is granted for the candidate in include the publication in the thesis; and

iii. the sum of all co-author contributions is equal to 100% less the candidate's stated contribution.

Name of Co-Author	Dr. Mergen H. Ghayesh
Contribution to the Paper	Helped in modelling/simulations, checked the results, and assisted in the preparation of the manuscript.
Signature	Date 19/8/2019

Name of Co-Author	Prof. Anthony Zander
Contribution to the Paper	Checked the results and assisted in the preparation of the manuscript.
Signature	Date 19/08/2019

Name of Co-Author	Dr. Rajiv Mahajan		
Contribution to the Paper	Checked the results and assisted in the preparation of the manuscript.		
Signature		Date	20/08/2019

Please cut and paste additional co-author panels here as required.

International Journal of Engineering Science 130 (2018) 93–114

Contents lists available at ScienceDirect

International Journal of Engineering Science

journal homepage: www.elsevier.com/locate/ijengsci

Three-dimensional biomechanics of coronary arteries

Alireza Gholipour[a], Mergen H. Ghayesh[a,*], Anthony Zander[a], Rajiv Mahajan[b]

[a] School of Mechanical Engineering, University of Adelaide, South Australia 5005, Australia
[b] Centre for Heart Rhythm Disorders, South Australian Health and Medical Research Institute, University of Adelaide and Royal Adelaide Hospital, Adelaide, SA 5000, Australia

ARTICLE INFO

Article history:
Received 2 March 2018
Accepted 12 March 2018
Available online 14 June 2018

Keywords:
Nonlinear mechanics
biomechanics
arteries
stenosis

ABSTRACT

The focus of this paper is to model and simulate the nonlinear dynamics of atherosclerotic coronary arteries as a tool to predict the initiation of heart attack. A dynamic three-dimensional visco/hyperelastic fluid–structure interaction model of an atherosclerotic coronary artery is developed by means of the finite element method (FEM) using ANSYS. Simulations are undertaken using the model to examine the risk of plaque rupture with the following parameters taken into account with varying levels of stenosis: physiological pulsatile blood flow; tapered shape of the artery; viscoelasticity and hyperelasticity of the artery wall; effect of the motion of the heart; active artery muscle contraction; the lipid core inside the plaque; three layers of the artery wall; non-Newtonian characteristics of the blood flow; and micro-calcification; this paper is the first to incorporate all these effects. The generated model can potentially be used as a predictive tool for plaque rupture to identify the conditions that are high risk for atherosclerosis plaque rupture.

1. Introduction

1.1. Impact of this investigation

According to the World Health Organization (WHO), coronary heart disease (CAD) and stroke are the *two leading* causes of death globally with more than 15 million deaths in 2015 (WHO, 2017). This situation has been reported to be similar in Australia with CAD and cerebrovascular diseases being ranked as the first and third most important causes of death respectively with approximately 20,000 and 10,000 deaths attributed to them in 2014 (AIHW, 2017). Atherosclerosis is the predominant cause for both coronary and cerebrovascular diseases. The acute events are usually caused by plaque rupture which releases thrombogenic material into the artery lumen leading to clot formation. Identification of the vulnerable plaque, at high risk for rupturing, remains the Holy Grail in the field.

This study aims at developing a dynamic model for coronary arteries to predict the vulnerable atherosclerotic plaque that is at high risk for rupturing. This model could result in identification of patients who are at high risk of myocardial infarction and allow interventions to stabilise the plaque and prevent myocardial infarction.

Although it is accepted that increasing low-density-lipoprotein (LDL) is responsible for shaping and growing plaque and hence atherosclerotic arteries, the primary cause for plaque formation is disruption of the endothelial layer (which is the inner layer of arteries consisting of one layer of cells). A very small crack or injury in the endothelium in addition to

* Corresponding author.
E-mail address: mergen.ghayesh@adelaide.edu.au (M.H. Ghayesh).

https://doi.org/10.1016/j.ijengsci.2018.03.002
0020-7225/

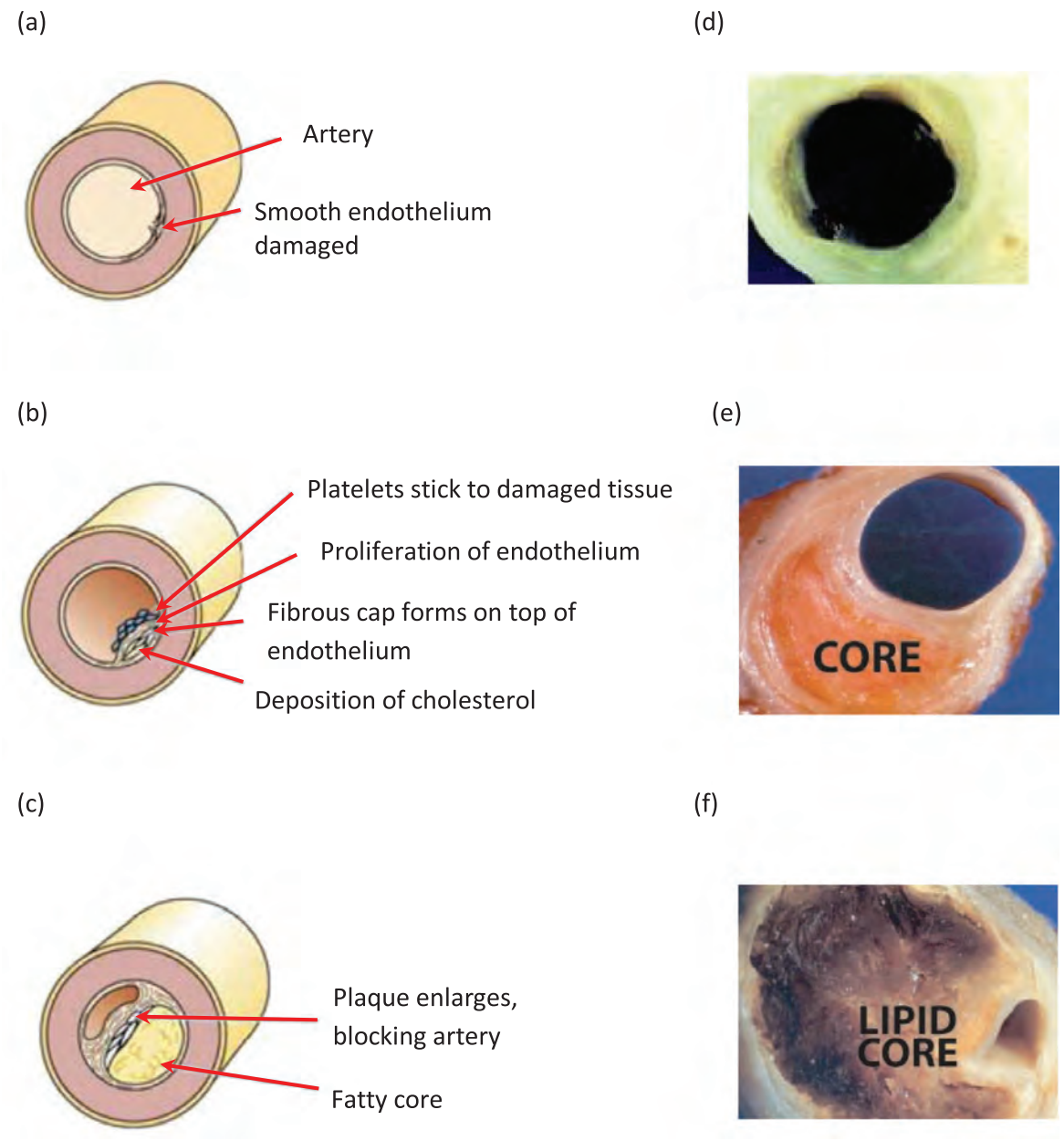

Fig. 1. Different stages of an atherosclerosis (Purves, Purves, Orians, Sadava, & Heller, 2003); (a) damaged endothelium; (b) cholesterol deposition; (c) enlarged plaque; (d–f) are the experimental (Doherty et al., 2004) counterparts of (a–c), respectively.

circulating LDL lipoprotein is thought to initiate the process of atherosclerosis. As a result, fatty streaks are seen as early as 6 months of age (Ross, 1999). These fatty streaks accumulate lipids and grow into a plaque, enlarging into the inner layer of the arteries in the course of time, and producing stenosis in the arteries. The myocardial infarction occurs due to the plaque rupture. As such, the thrombogenic materials (such as lipid and calcium) inside the plaque is released leading to thrombus formation by platelets in the blood. The thrombus obstructs the artery and the blood flow is cut from that part of the heart which causes a heart attack. Fig. 1 shows the different stages of atherosclerosis involving (a) the damaged endothelium (b) cholesterol deposition, and (c) the enlarged plaque.

1.2. Contribution of the current study to the field

Different imaging techniques are employed to investigate coronary plaques; however, it is almost impossible to predict the vulnerable plaque that is more likely to rupture. According to experiments (Falk, Shah, & Fuster, 1995), most of the ruptures occur in the stenosis range of 45–50%; this implies that the rupture is very likely to occur even when the stenosis is less than half of the cross-section of the artery. This indicates the need for the development of a computer model which simulates atherosclerosis in coronary arteries to predict the risk factors associated with the plaque rupture and resultant acute myocardial infarction. Being asymptotic is the main problem of the plaque composition which could be related to the

re-shaping capability of arteries. The dynamic fluid–structure interaction biomechanics of atherosclerotic coronary arteries (taking into account three-dimensionality the plaque and the artery, viscoelasticity, and hyperelasticity of the artery wall, the tapered shape of the artery, active artery muscle contraction, three layers of the artery, lipid core inside the plaque, effect of the heart motion, micro-calcification, non-Newtonian characteristics of the blood flow and blood pulsation due to heart beat) for several levels of stenosis is developed in this paper *for the first time*; the stress field developed in the artery and the plaque surface and the core are obtained numerically using the finite element method (FEM) and the regions with high risk of rupture (and hence the initiation of heart attack) are determined. The developed model and simulations have first been verified with simulations available in the literature are showed excellent agreement.

The innovation of this investigation is to develop a comprehensive model of an atherosclerotic coronary artery by taking into account all the following factors in the three-dimensional nonlinear fluid–structure dynamical analysis of the system: (1) the blood physiological pulsation; (2) the tapered shape of the artery; (3) the motion of the artery due to the heart motion; (4) media layer muscle contraction; (5) the lipid pool inside the plaque; (6) non-Newtonian flow for the blood; (7) the three layers of the artery wall, i.e., adventitia, media, and intima; and (8) the micro-calcification of the plaque. The developed model and the resulting simulations are the most comprehensive to date.

2. Literature on coronary artery investigations

There are several studies from different disciplines including medicine and engineering on the biomechanics of atherosclerotic coronary arteries. In the first section, the *experimental* efforts have been reviewed including both in-vivo and in-vitro studies; their main focus was on either imaging or extracting mechanical properties. The second group of the literature is concerned with *theoretical and numerical modelling* of the atherosclerotic coronary arteries. In this part, arteries and plaques have been considered as simplified shapes and were analysed in three sections of structure, fluid, and fluid–structure interaction.

2.1. Experimental investigations

A number of experimental studies have focused on the mechanical behaviour or material properties of atherosclerotic plaques. The complex behaviour of the arteries and plaque results from the nonlinear geometry and material properties (Doraiswamy, Criscione, & Srinivasa, 2016; Soares, Pasta, Vorp, & Moore Jr, 2010) as well as different forces and boundary conditions exerted on the plaque. In the process of rupture prediction, the first step is to obtain the mechanical properties of the arteries and plaques. Some attempts in replicating mechanical behaviour of the plaque utilised idealised geometric models based on histology (Ji et al., 2011). However, these studies could not sufficiently model the plaque and its characteristics. Another way to extract mechanical characteristics is to conduct experiments on in-vitro plaques and arteries. In this regard, researchers harvested samples from human carotid arteries (Teng et al., 2015). The afore-mentioned studies investigated the problem by means of different methods such as histology, electron microscopy, and particle image velocimetry (PIV) and examined fluid shear stress, circumferential and axial ultimate strength as well as adhesive strength between the plaque and the arterial wall. Although these studies provide information about the characteristics of the artery (Karšaj, Sorić, & Humphrey, 2010) and plaque, they could not fully investigate the problem to yield information about the causes without the use of numerical modelling which can consider all these influencing factors together for predicting plaque rupture.

2.2. Theoretical models

In this class of investigations, theoretical models based on system parameters are developed and the resultant model is simulated via various numerical techniques (Ghayesh, Farokhi, & Amabili, 2013; Ghayesh, Amabili, & Farokhi, 2013; Gholipour, Farokhi, & Ghayesh, 2015). As a result, the numerical approach of FEM (Haddad & Samani, 2017a; Khakalo, Balobanov, & Niiranen, 2018; Shahverdi & Barati, 2017; Trofimov, Abaimov, Akhatov, & Sevostianov, 2017) is used widely in simulating arteries and plaques since this technique is capable of handling mechanical systems with complex geometries and properties. In addition, different constitutive schemes such as hyperelasticity (Gizzi et al., 2014; Il'ichev & Fu, 2014) and viscoelasticity can be applied to the problem. Moreover, various boundary conditions and forces can be exerted on the system model. In conclusion, FEM is considered to currently be the best numerical technique to model biomechanical systems (Freed & Einstein, 2013; Ganghoffer & Sokolowski, 2014; Goda & Ganghoffer, 2015; Goda, Rahouadj, Ganghoffer, Kerdjoudj, & Siad, 2016; Joshi & Walton, 2013; Shirazi & Ayatollahi, 2014; Švihlová, Hron, Málek, Rajagopal, & Rajagopal, 2016). Theoretical studies from the literature are categorised into three parts, *structure*, *fluid*, and *fluid–structure* analyses. The differences between these parts arise from the solution approach as well as the theory they are built on.

Structural analysis: In the structural analysis studies undertaken to date, the model has usually been idealised for two reasons. In one gap of investigations, an idealised model has been used to take into account the effect of *each segment of the plaque* on the stress and the critical situation for the threshold of the plaque rupture (Dolla, House, & Marso, 2012). However, another group of studies used an idealised model for simplifying the problem so as to investigate the effect of different parameters on the plaque growth and the rupture threshold including being hyperelastic in 3D space, inward and outward vascular growth in plaque shaping, considering microcalcification, and viscoelastic material model (Thomas-Seale et al., 2016). In conclusion, these studies analysed the influences of different parameters on the plaque and artery

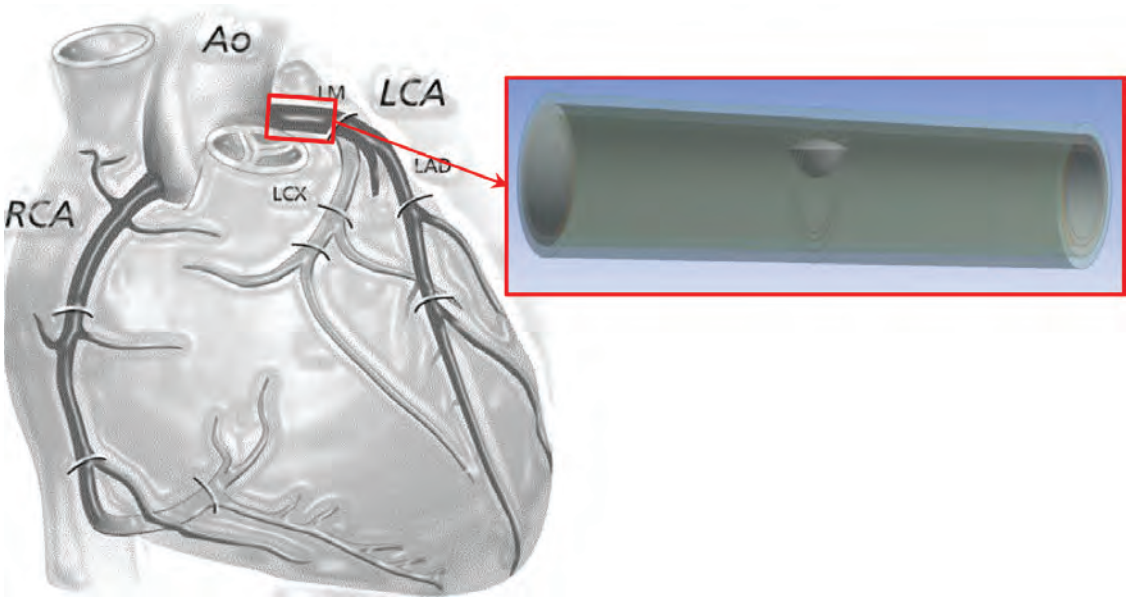

Fig. 2. The location of the modelled coronary artery in the heart with different artery segments (Habets et al., 2012).

involving the structural part; however, in considering a simplified model for the artery and plaque they did not additionally consider the fluid effect.

Fluid analysis: Blood is an important part of the arteries (Anand, Kwack, & Masud, 2013; Cyron & Humphrey, 2014) and plays a critical role in plaque rupture, progression and establishing thrombus in the arteries. In the theoretical modelling of the blood, there are different important factors to be addressed; these are characterised as either Newtonian and non-Newonian (Akherat & Kimiaghalam, 2010), as well as being pulsatile (Tambasco & Steinman, 2003), and whether 2-dimensional or 3-dimensional modelling is employed. As a result, to date the studies have focused solely on the fluid, hence are not able to determine the stress and strain in the solid parts of the atherosclerotic artery.

Fluid–structure interaction analysis: In this section, studies regarding the fluid–structure-interaction (FSI) model of arteries and plaques are introduced. None of the existing structure and fluid analyses are able to individually describe the artery characteristics precisely. Due to the dynamic nature of the system, the boundaries and the fluid–structure interaction forces between these two media do not remain constant. Therefore, the need for FSI modelling seems inevitable for the arteries (El Baroudi, Razafimahéry, & Rakotomanana, 2014) and plaque. In the primary studies by Tang, Yang, Kobayashi, and Ku (2001), the solid material has been considered hyperelastic (Gou & Walton, 2014), homogenous and isotropic and the fluid characteristics were defined as Newtonian, laminar, viscous, and incompressible, and a 3D FSI model has been solved for thick and thin arterial walls. Other factors such as nonlinear time-dependent fluid model (Li & Gillard, 2007), microcalcification (Wenk, Papadopoulos, & Zohdi, 2010), and pulsatile flow (Xiong et al., 2014) have also been taken into account in the literature for 2D and 3D analyses. To sum up, these studies did not consider representative conditions of the atherosclerotic artery due to their employing an idealised model and various simplifications. In addition, none of the previous studies modelled the plaque considering all these effective factors combined. The innovation of the current paper is to incorporate all of the different parameters combined in a three-dimensional dynamic model of an atherosclerotic coronary artery.

3. Development of the atherosclerotic coronary artery

3.1. Geometry

In order to develop a geometric model for an atherosclerotic coronary artery, an idealised model of the coronary artery with plaque has been adopted from Chen (2016) and modified using clinical data (Holzapfel, Sommer, Gasser, & Regitnig, 2005). This model is considered to be the left main (LM) coronary artery (Fig. 2) rooted from the aortic root. As depicted in Fig. 3, the artery is modelled as 3D, tapered, and three-layered (intima, media, and adventitia) and the plaque is modelled as 3D, asymmetric, and with an elliptic shape. In the solid part there are five different parts: intima, media, adventitia, plaque, and lipid (see Fig. 3(c)). The inner diameter of the artery at cross-section *A–A* is 2.8 mm. The shoulder of the plaque is set to 2 mm and the stenosis is defined as

$$Stenosis = \frac{D_{in} - D_{min}}{D_{in}} \times 100. \tag{1}$$

The stenosis is considered to be 45% (plaque height: 1.26 mm) according to the most high-risk stenosis (Sorof, 2004). Based on the tapered shape of the artery examined in Chakravarty and Mandal (2000), a taper of 1° is assumed. The outer

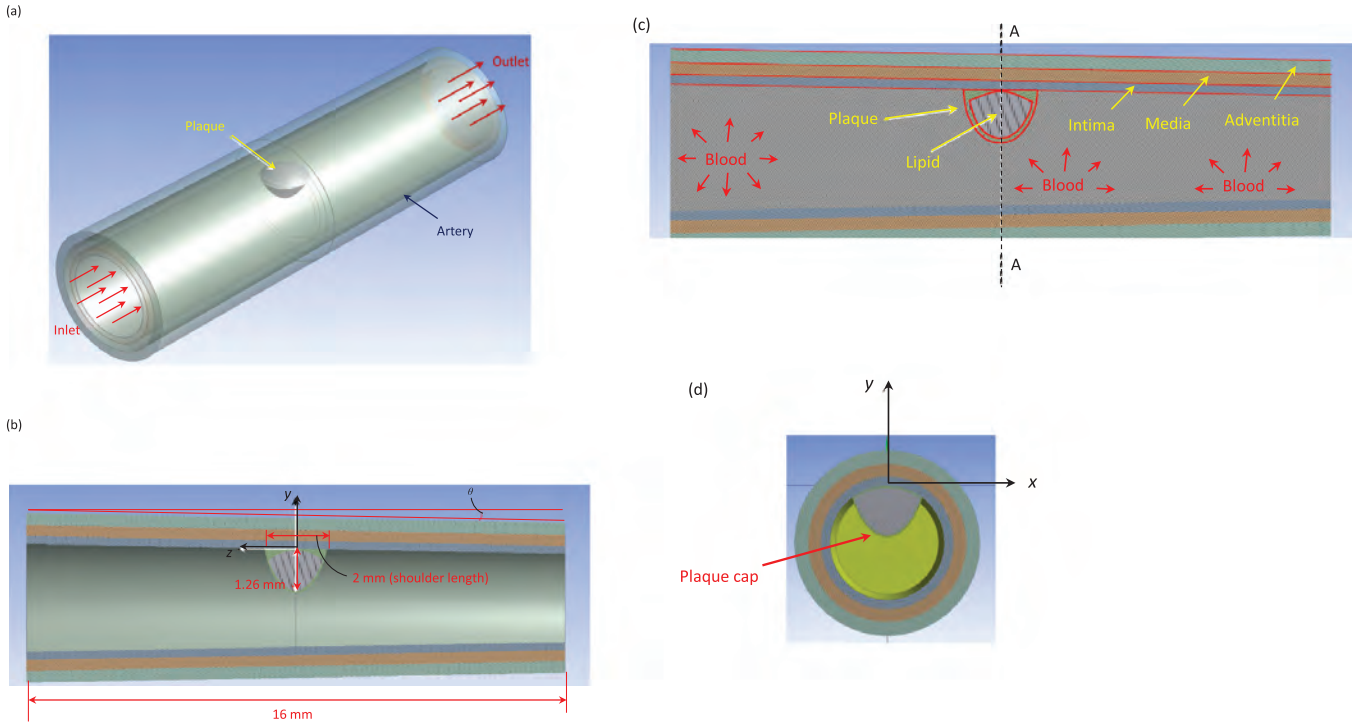

Fig. 3. Schematic model of the artery and a plaque with lipid core: (a) 3D model with inlet, outlet, plaque and artery; (b) transverse three-layered cross-section showing the tapered shape of artery; (c) transverse cross-section showing different parts of the plaque, lipid, intima, media, adventitia and the blood; (d) circumferential cross-section.

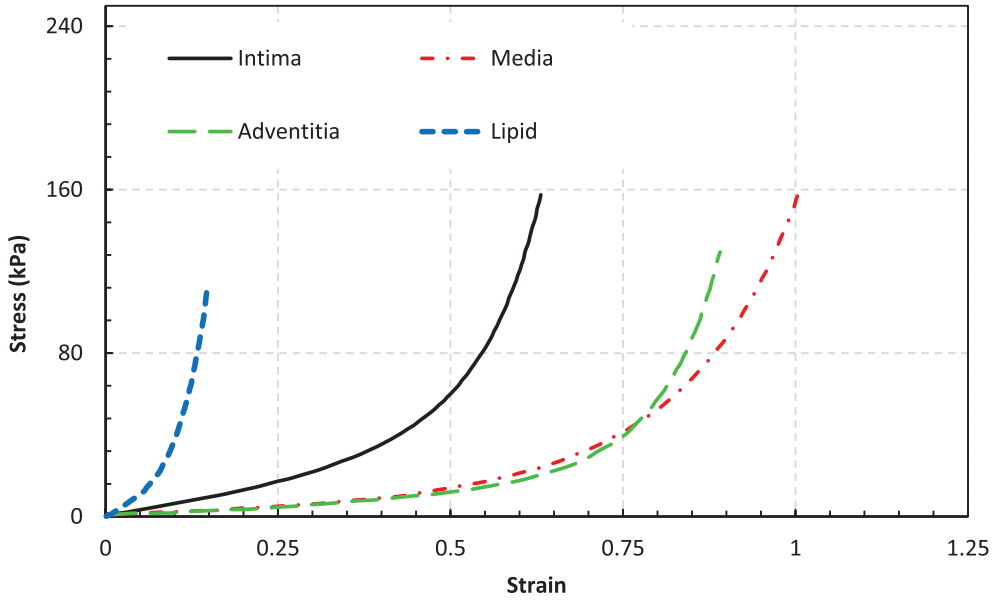

Fig. 4. Stress-strain experimental data of different layers of the artery (intima, media, and adventitia) (Holzapfel et al., 2005) and lipid (Versluis et al., 2006).

diameter, thickness of intima, thickness of media, and thickness of adventitia are set to 4.5, 0.23, 0.31, and 0.34 mm, respectively (Holzapfel et al., 2005). The length of the artery is 16 mm and the fibrous cab thickness is chosen to be 0.05 mm (Cilla, Borrás, Pena, Martínez, & Malve, 2015).

3.2. Material: solid characteristics

In the modelling the material of the system, the experimental data for three different layers has been adopted from Holzapfel et al. (2005), the material properties of plaque has been chosen to be the same as the intima layer. Fig. 4 shows the experimental data which have been used in the model for different layers of the artery and lipid (Versluis, Bank, & Douglas, 2006).

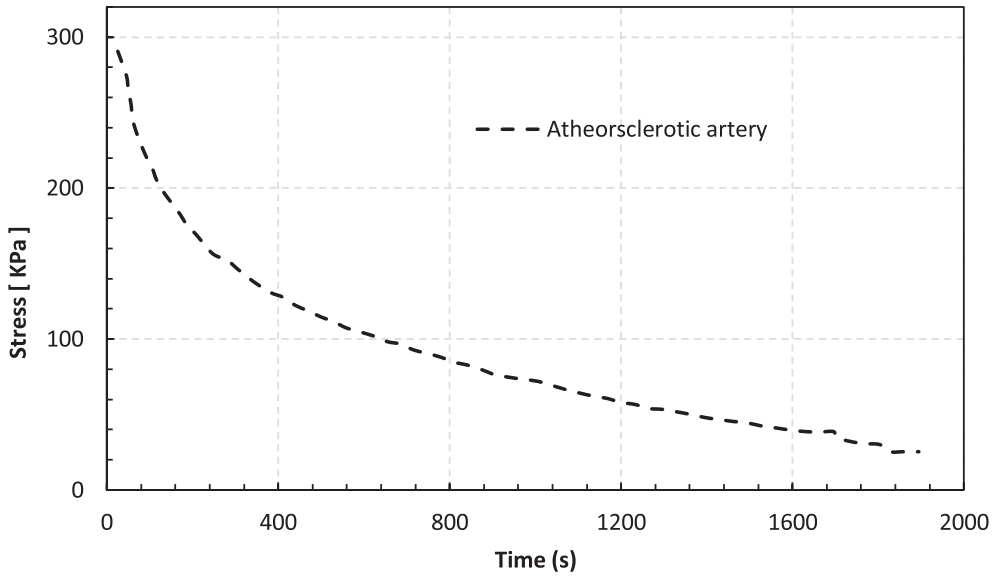

Fig. 5. Stress-time diagram of the atherosclerotic human coronary arteries data from Karimi et al. (2017).

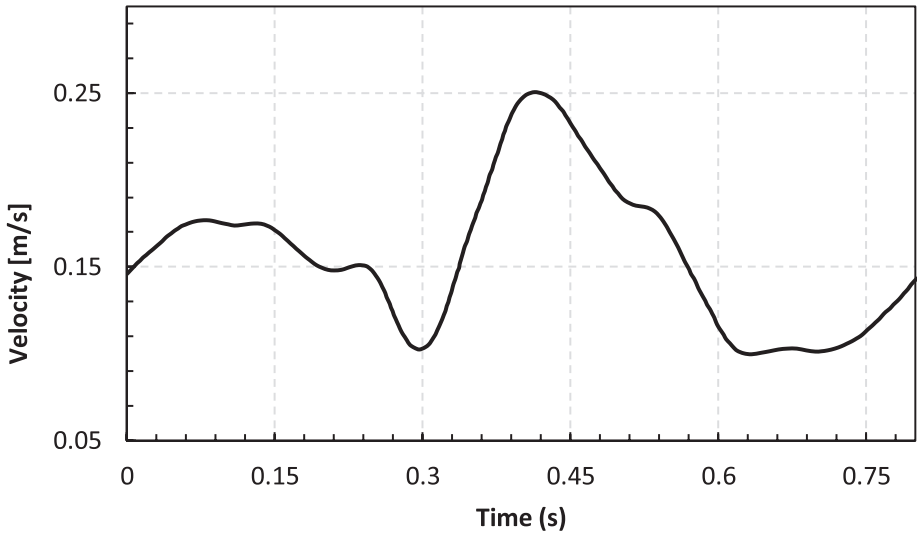

Fig. 6. Velocity pulsation in the left coronary artery (LCA) (Chabi et al., 2015).

The hyperelasticity (Bhattacharyya, Sarangi, & Samantaray, 2015; Chebbi, Wali, & Dammak, 2016; Gou & Walton, 2014; Ramírez-Torres et al., 2017) of the materials is modelled using the formulation given by Mooney–Rivlin, which is a 5-parameter hyperelastic model as Roelse, de Ruijter, Vrouwe, and Jongsma (2013) where due to the macro size of the structure, the small-size influences (Farokhi & Ghayesh, 2015; Farokhi, Ghayesh, & Amabili, 2013; Farokhi, Ghayesh, Gholipour, & Hussain, 2017; Ghayesh, Farokhi, & Alici, 2016; Ghayesh, Farokhi, & Amabili, 2014; Ghayesh, Farokhi, & Gholipour, 2017) have been neglected.

$$W = -c_{01}\left(3-\bar{I}_2\right) - c_{10}\left(3-\bar{I}_1\right) + c_{11}\left(3-\bar{I}_1\right)\left(3-\bar{I}_2\right) + \frac{1}{d}(1-J)^2 + c_{20}\left(3-\bar{I}_1\right)^2 + c_{02}\left(3-\bar{I}_2\right)^2 \tag{2}$$

in which W denotes the strain energy potential, $\bar{I}_1$ denotes the first deviatoric strain invariant, $\bar{I}_2$ represents the second deviatoric strain invariant, J is the determinant of the elastic deformation gradient, d is the material incompressibility parameter, and c_{10}, c_{01}, c_{11}, c_{20}, and c_{02} are the material constants obtained by curve fitting the above mentioned experimental data to the formulation. The material constants resulted from the curve fitting are depicted in Table 1. The density of all the material has been set to 1000 kg/m^3 (Chan, Ding, & Tu, 2007).

Viscoelasticity (Attia & Abdel Rahman, 2018; Bakhshi Khaniki and Hosseini-Hashemi, 2017; Fallah, Ahmadian, & Mohammadi Aghdam, 2017; Ghayesh, Farokhi, & Hussain, 2016), as an internal energy dissipation mechanism (Ebrahimi & Barati, 2016; Seyedkavoosi et al., 2017), has been taken into account from Karimi, Shojaei, and Razaghi (2017) using the method of Prony Shear Relaxation in ANSYS Workbench. In Fig. 5, the experimental data for the atherosclerotic artery has

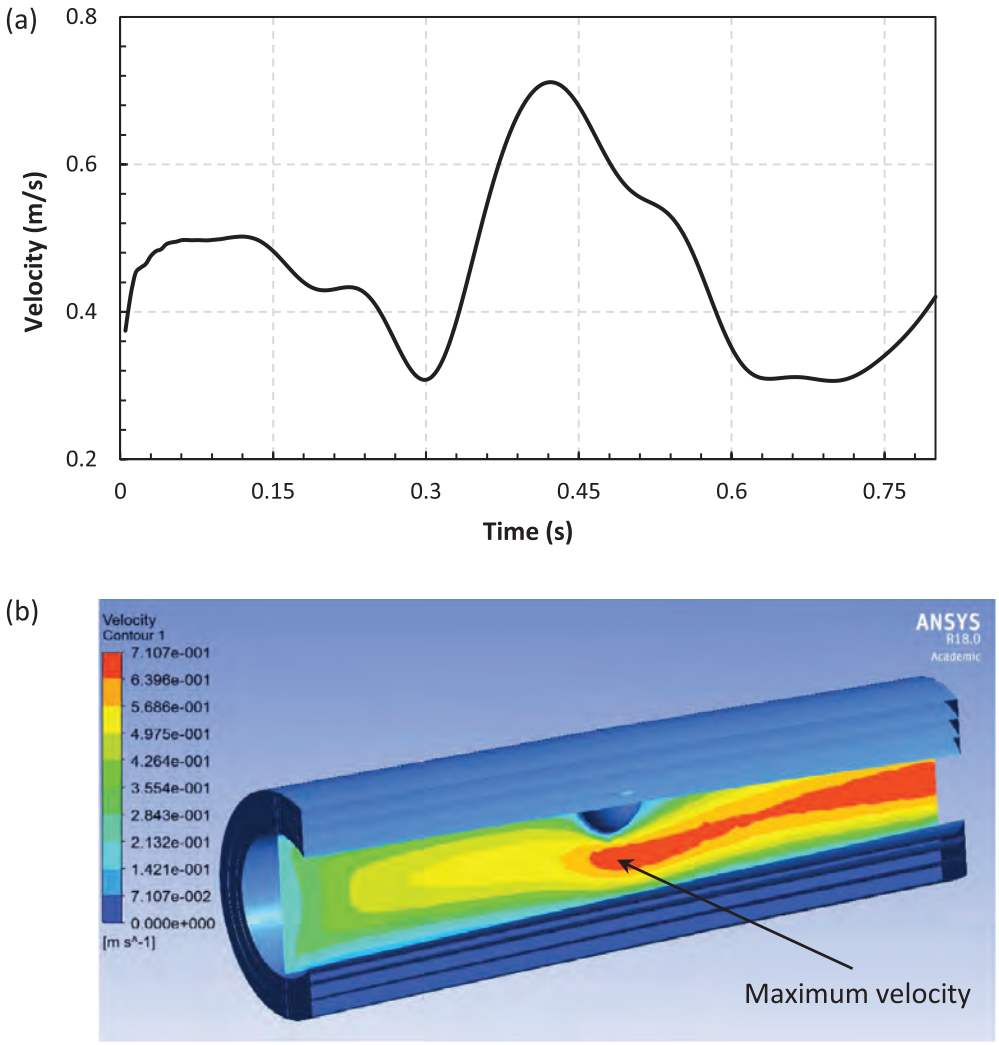

Fig. 7. (a) Variations of the velocity with time and (b) the velocity field for the cap of the plaque at $t = 0.42$ s ($x = 0.07$ mm, $y = -1.81$ mm, $z = -0.32$ mm).

Table 1
Material coefficient of Mooney–Rivlin 5-parameter model.

Material	Model	C_{10} (Pa)	C_{01} (Pa)	C_{11} (Pa)	C_{20} (Pa)	C_{02} (Pa)
Intima	Mooney–Rivlin	-2.04×10^5	2.23×10^5	-3.71×10^6	1.37×10^6	2.67×10^6
Media	Mooney–Rivlin	-1.17×10^5	1.28×10^5	-6.72×10^5	2.24×10^5	5.69×10^5
Adventitia	Mooney–Rivlin	-1.89×10^5	2.02×10^5	-1.38×10^6	4.59×10^5	1.34×10^6
Lipid	Mooney–Rivlin	5.68×10^5	-5.45×10^5	-5.86×10^5	2.85×10^7	-2.41×10^7

been adopted to obtain the viscoelastic parameters as

$$\sigma = \int_0^t 2G(t-\tau)\frac{de}{d\tau}d\tau + I\int_0^t K(t-\tau)\frac{d\Delta}{d\tau}d\tau, \tag{3}$$

in which σ represents the Cauchy stress; Δ denotes the volumetric strain; e represents the deviatoric strain; t is time; I denotes the identity tensor; $G(t)$ denotes the Prony series shear; $K(t)$ is the bulk-relaxation moduli.

$$G(t) = G_0\left[\alpha_\infty^G + \sum_{i=1}^{n_G}\alpha_i^G \exp\left(-\frac{t}{\tau_i^G}\right)\right] \tag{4}$$

and

$$K(t) = K_0\left[\alpha_\infty^K + \sum_{i=1}^{n_K}\alpha_i^K \exp\left(-\frac{t}{\tau_i^K}\right)\right] \tag{5}$$

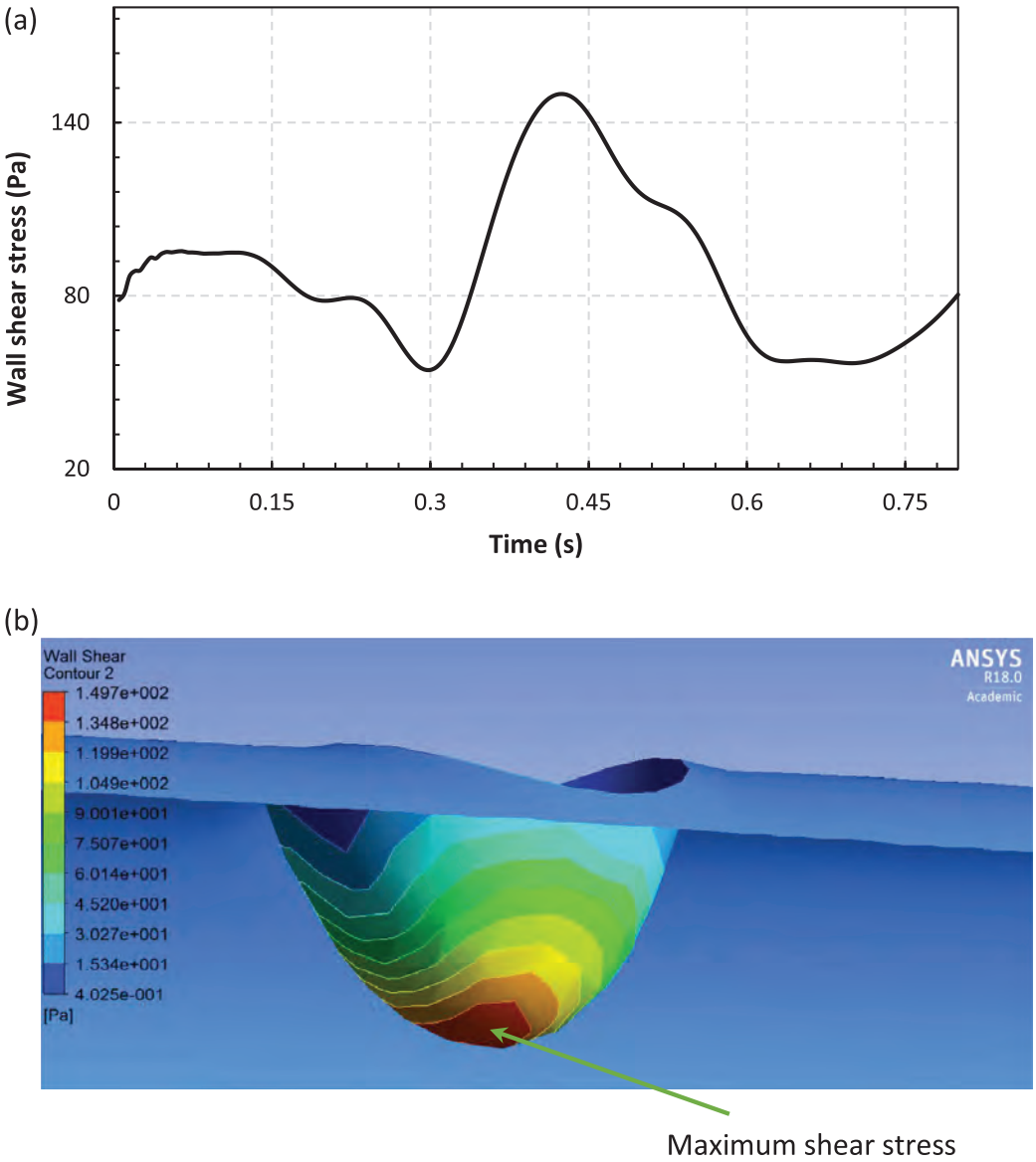

Fig. 8. (a) Variations of the wall shear stress with time and (b) the wall shear stress field for the cap of the plaque at $t = 0.42$ s ($x = 0.10$ mm, $y = -1.16$ mm, $z = 0.19$ mm).

Table 2
Material coefficient of Prony Shear Relaxation 5-terms model.

Terms	$i = 1$	$i = 2$	$i = 3$	$i = 4$	$i = 5$
Relative moduli	2.30×10^{-16}	0.39	3.16×10^{-17}	9.46×10^{-11}	0.61
Relaxation time (s)	727.7	127.88	711.52	747.68	1018.3

with G_0 and K_0 denoting the relaxation moduli at $t = 0$; n_G and n_K denoting the number of Prony terms; ${\alpha_i}^G$ and ${\alpha_i}^K$ being relative moduli; and ${\tau_i}^G$ and ${\tau_i}^K$ representing the relaxation time. A five-term relaxation model is developed by means of curve-fitting in ANSYS; the results are shown in Table 2.

3.3. Material: fluid characteristics

The blood has been modelled as turbulent, incompressible, and non-Newtonian (Perkowska, Piccolroaz, Wrobel, & Mishuris, 2017); as the blood flow is the main reason for shear stress and hence the plaque initiation, it is necessary to model it realistically (Janela, Moura, & Sequeira, 2010; Wu, Aubry, Massoudi, & Antaki, 2017). In this regard, non-Newtonian flow with the following governing formulation is considered (Mandal, 2005)

$$\eta = \eta_0 \dot{\gamma}^{n-1}, \tag{6}$$

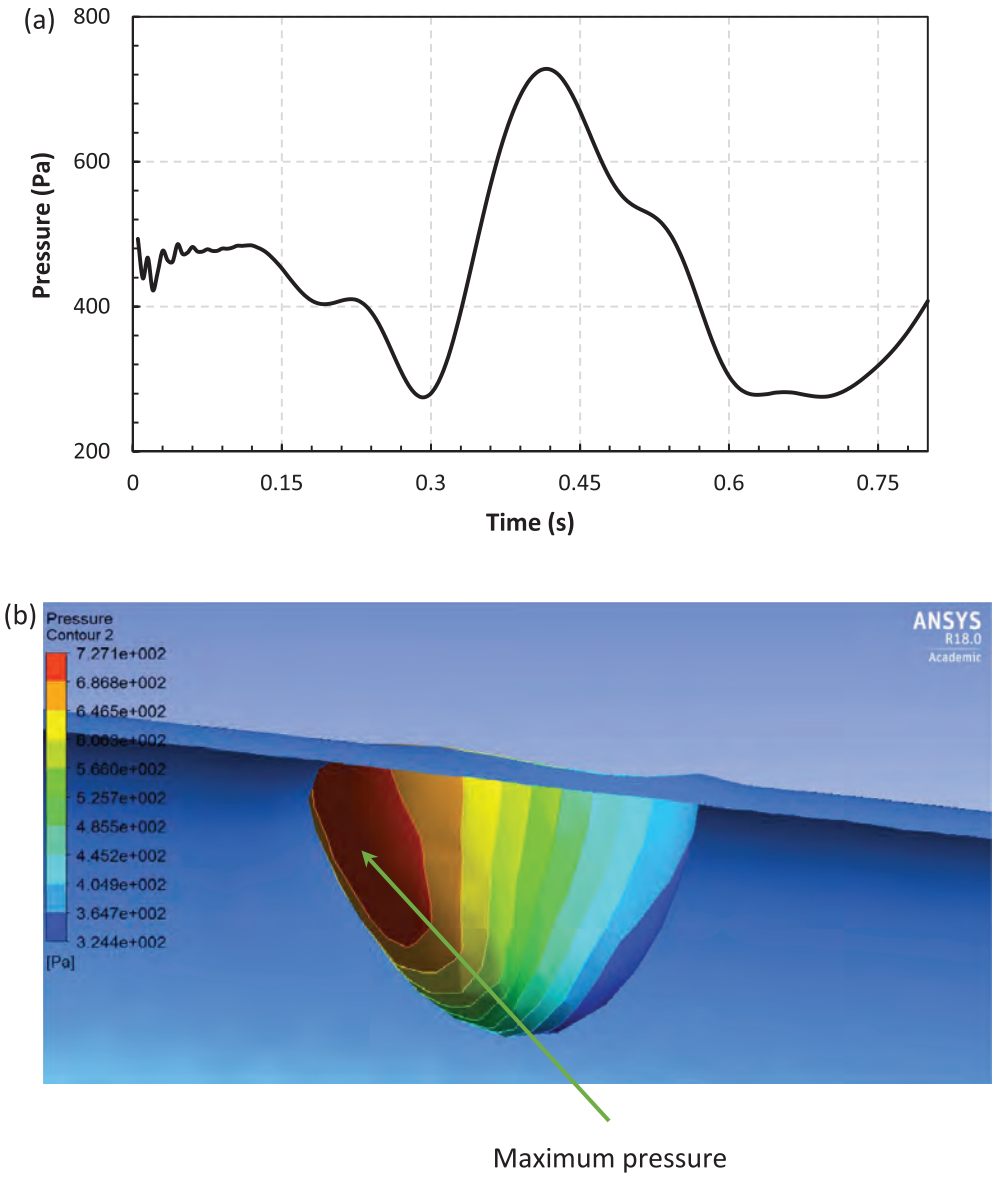

Fig. 9. (a) Variations of the pressure with time and (b) the pressure field for the plaque at $t = 0.42$ s ($x = 0.01$ mm, $y = -0.49$ mm, $z = 0.76$ mm).

in which η denotes the viscosity of the fluid, $\dot{\gamma}$ is the strain rate, $\eta_0 = 0.035$ and $n = 0.6$ are the minimum viscosity limit and power-law index, respectively (Johnston, Johnston, Corney, & Kilpatrick, 2004). The blood density is set to 1050 kg/m^3 (Cilla et al., 2015).

3.4. Physiological blood pulsation

A *pulsatile* blood flow exerts dynamic stresses on the artery and plaque (Kachanov & Abedian, 2015; Mandal, Mukhopadhyay, & Layek, 2012; Mekheimer & El Kot, 2015; Švihlová, Hron, Málek, Rajagopal, & Rajagopal, 2017; Taelman, Degroote, Swillens, Vierendeels, & Segers, 2014). The pulsatile blood flow model of the left coronary artery (LCA) is employed (Chabi, Champmartin, Sarraf, & Noguera, 2015) and plotted in Fig. 6; this figure shows the variations of the blood flow velocity over one heart beat (0.8 s).

3.5. Motion of the artery due to the heart motion

The coronary arteries are located on the heart; the motion of the heart may potentially affect the biomechanical behaviour of the artery and plaque and the blood inside it. The effect of the heart motion is included in the analysis via exerting a 3D displacement on the coronary artery (Yang, Liu, Zheng, & Liu, 2017). Sine waves of the following form are

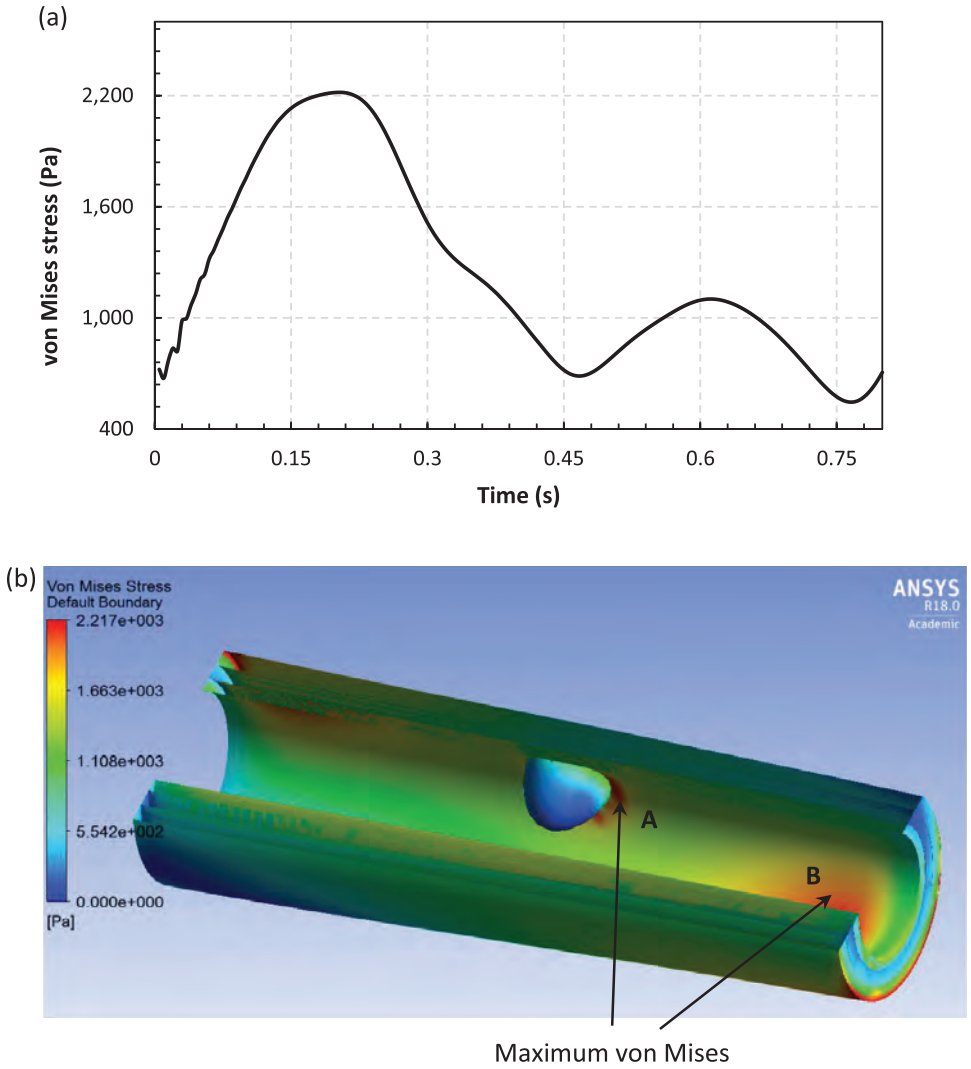

Fig. 10. (a) Variations of the von Mises with time and (b) the von Mises field for the plaque and artery at $t = 0.20$ s ($x = 1.50$ mm, $y = 0.07$ mm, $z = -1.01$ mm).

considered to model the heart motion in 3D space

$$\begin{aligned} x &= 0.30\ \sin(2\pi \cdot t/0.8)\ \text{mm} \\ y &= 0.15\ \sin(2\pi \cdot t/0.8)\ \text{mm} \\ z &= 0.15\ \sin(2\pi \cdot t/0.8)\ \text{mm} \end{aligned} \tag{7}$$

3.6. Contraction of media layer

In arteries, there is a muscular layer called the media which is responsible for pushing blood toward the capillaries. This active contraction (Haddad & Samani, 2017b) results in dynamic stresses on the artery wall and plaque. This contraction has been modelled based on the formulation

$$P = 200\ \sin(2^{*}\pi^{*}z/0.016 - t)\ \text{Pa}. \tag{8}$$

This formulation implies that the pressure varies with both time and location.

3.7. Micro-calcification of the plaque

In most recent studies, it is shown that the plaque initiates to rupture due to stress concentration around areas of the plaque with micro-calcification (Maldonado et al., 2012). As a result, micro-calcification is recognised as one of the stress concentration factors inside the plaque of the atherosclerotic artery. As a result, this important parameter has been considered via modelling it as a small sphere in the fibrous cap with a radius of 0.01 mm.

In the numerical results (Section 5) the system parameters given in Section 3 (except Section 3.7) are used, unless otherwise mentioned.

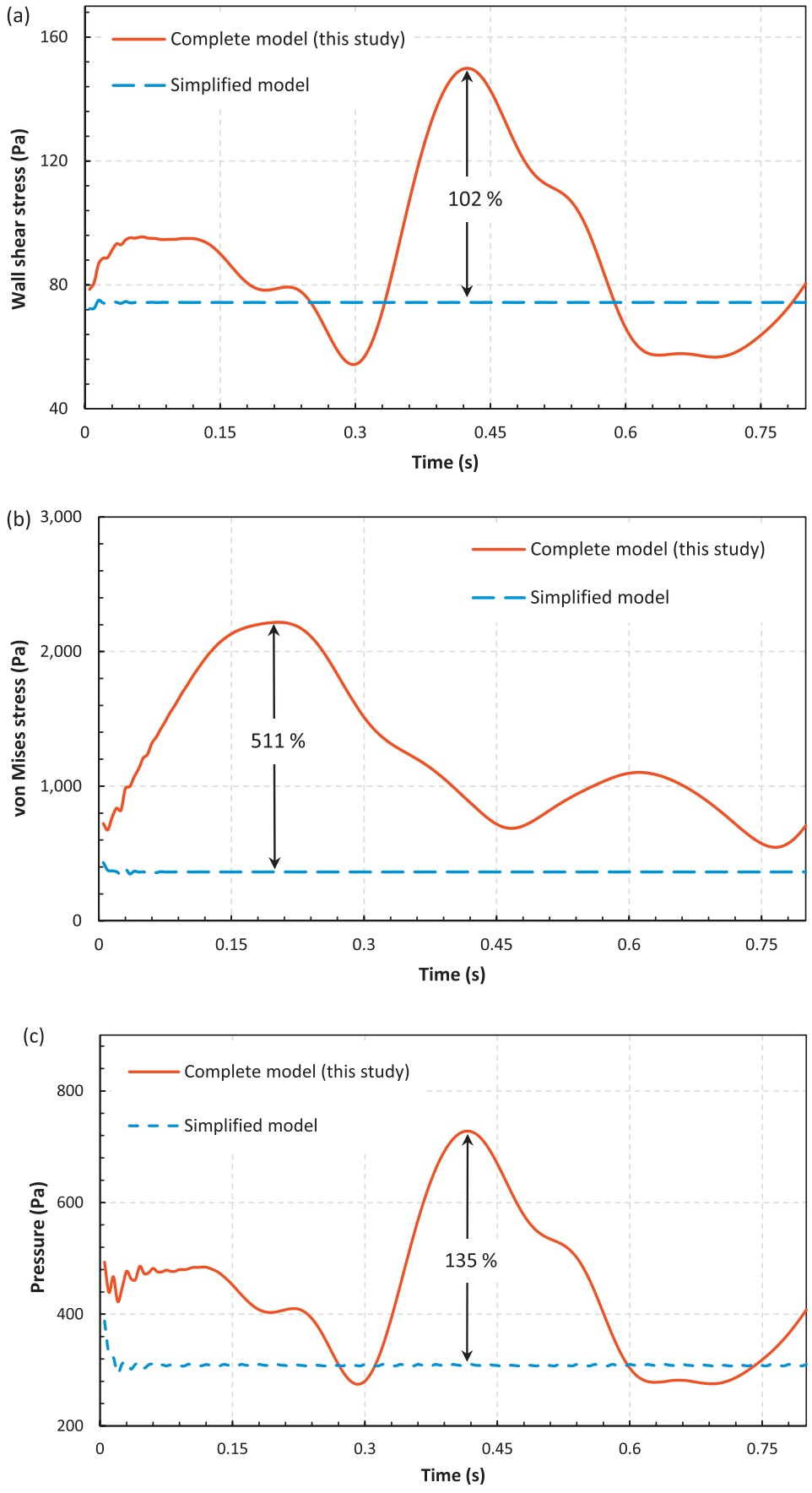

Fig. 11. (a) Comparison of wall shear stress on the plaque in the two model of atherosclerotic artery: complete model (this study) and simplified model; (b) Comparison of von Mises stress in artery in the two model of atherosclerotic artery: complete model (this study) and simplified model (c) Comparison of fluid pressure on plaque in the two model of atherosclerotic artery: complete model (this study) and simplified model.

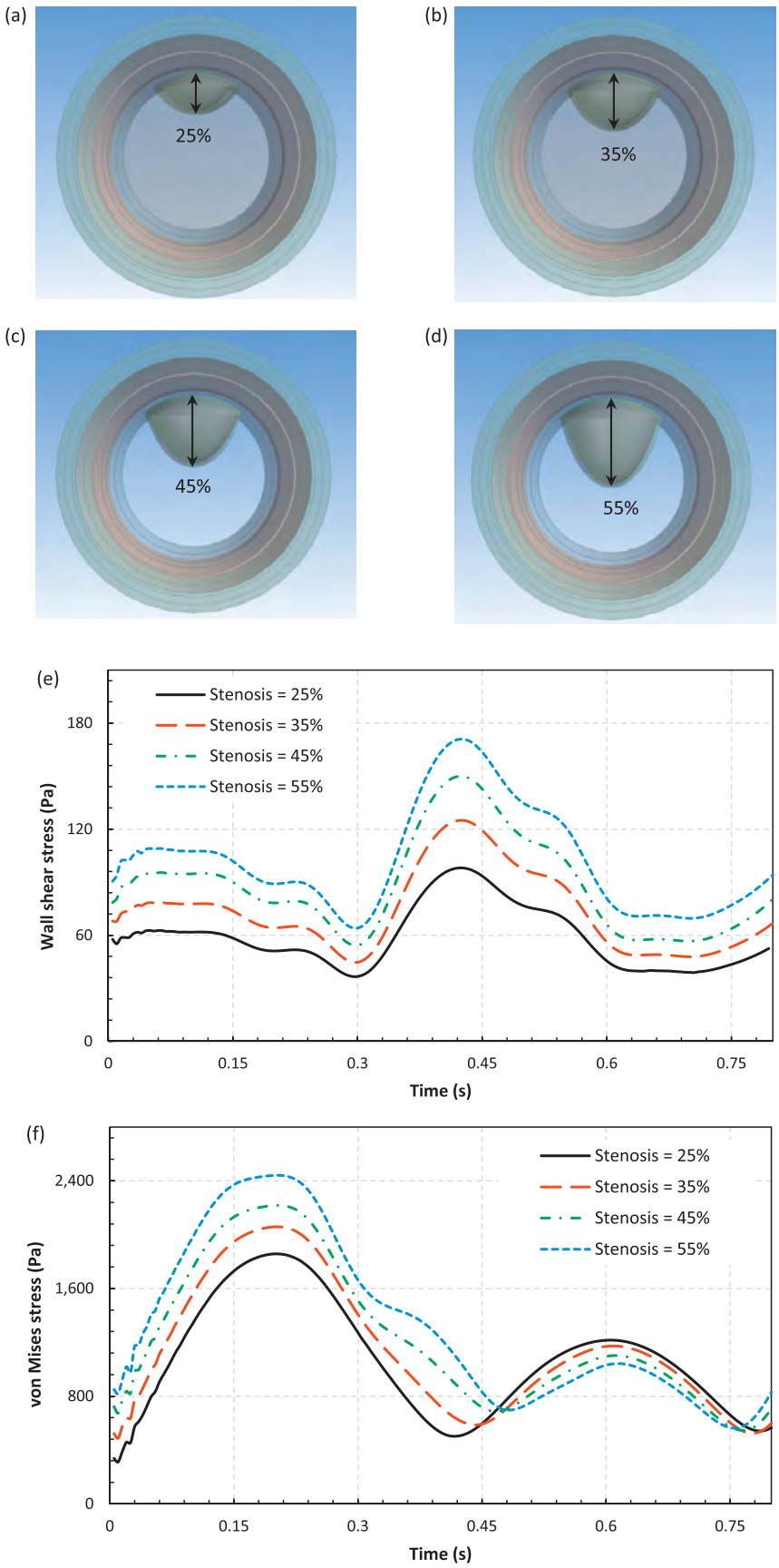

Fig. 12. The effect of different stenosis on the atherosclerotic artery: (a) schematic of stenosis 25%; (b) schematic of stenosis 35%; (c) schematic of stenosis 45%; (d) schematic of stenosis 55%; (e) wall shear stress on plaque; (f) von Mises stress.

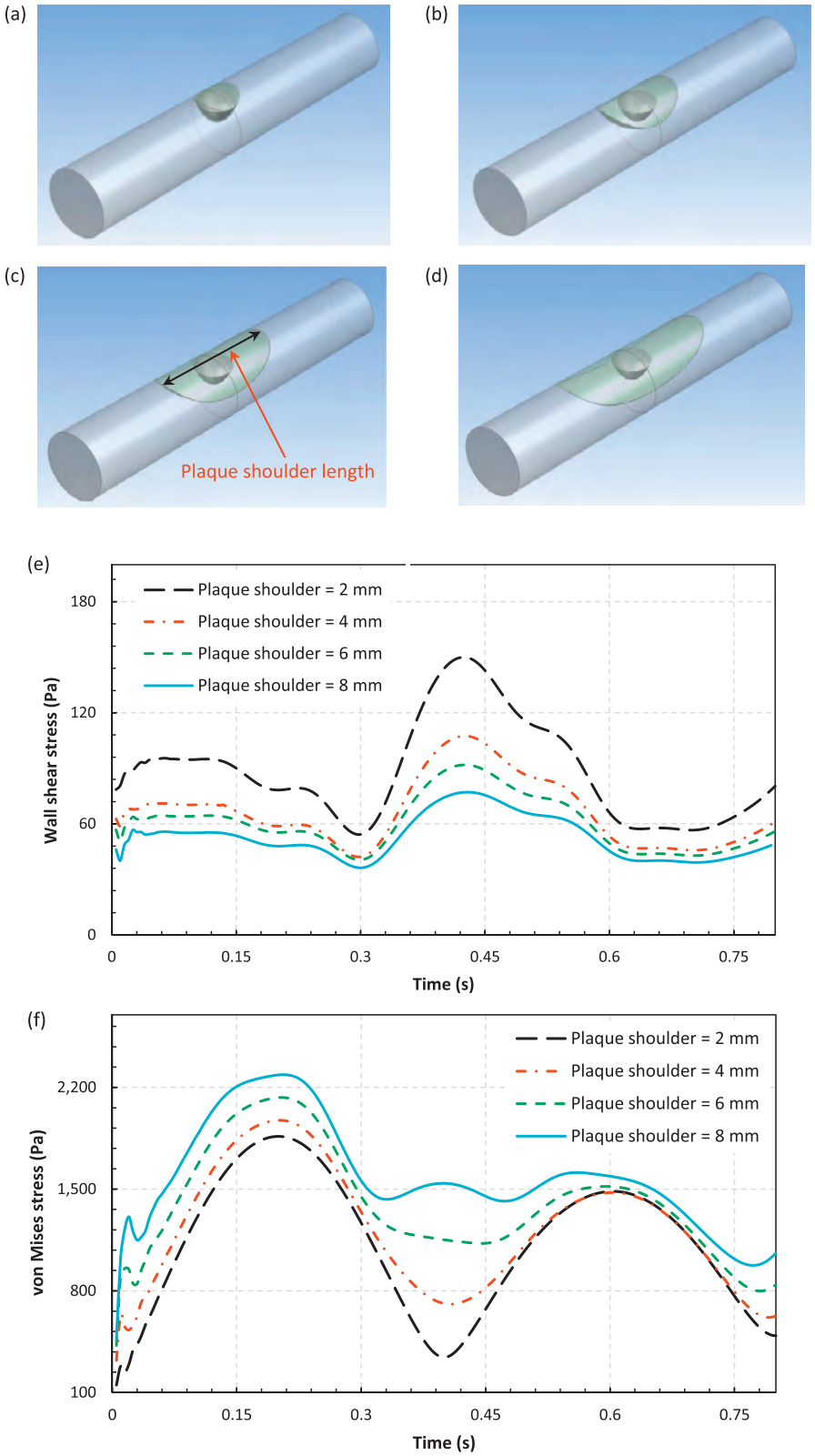

Fig. 13. The effect of different shoulder on the atherosclerotic artery: (a) schematic of shoulder length 2 mm; (b) schematic of shoulder length 4 mm; (c) schematic of shoulder length 6 mm; (d) schematic of shoulder length 8 mm; (e) wall shear stress on plaque; (f) von Mises stress.

4. Solution method

The atherosclerotic artery is modelled in ANSYS using two-way fluid–structure interaction (FSI) in the 3D space. At each time step in the solution process the four different convergencies of Transient Structural, Fluid Flow (Fluent), data transfer from Fluid Flow (Fluent) to Transient Structural, and data transfer from Transient Structural to Fluid Flow (Fluent) have been obtained. In the contact between solid and fluid “Dynamic Mesh” with “Remeshing” options have been set to investigate the

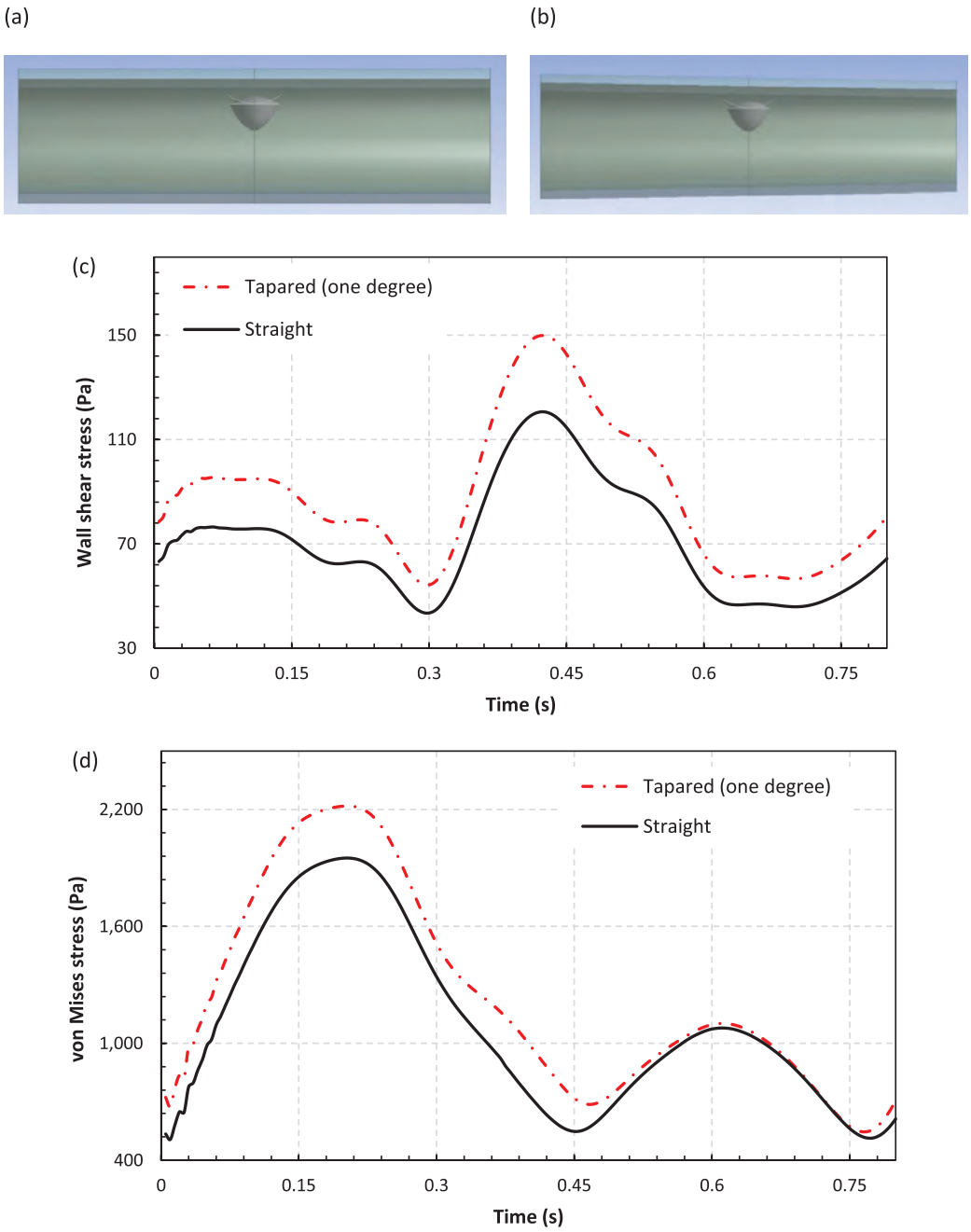

Fig. 14. The effect of different tapered degree on the atherosclerotic artery: (a) straight; (b) tapered (one degree); (c) wall shear stress on plaque; (d) von Mises stress.

interaction between the solid and the fluid. The mesh is hybrid, having both tetrahedral and hexahedral elements, with most elements of the hexahedral type and the time step is set to 0.005 s.

5. Numerical results

Since blood flow pulsation as well as heart motion are considered in the analysis, the system dynamical characteristics around the plaque such as the blood flow velocity, the wall shear stress, the pressure distribution, and the wall displacement vary with time. Fig. 7 shows the variations of the velocity with time (sub-figure (a)) and the velocity field (sub-figure (b)) for the cap of the plaque ($x = 0.07$ mm, $y = -1.81$ mm, $z = -0.32$ mm; see Fig. 3). As is expected the maximum velocity occurs at a time corresponding to the maximum pulsation velocity and at the location with the greatest constriction of the artery due to the presence of the plaque (at $t = 0.42$ s where the value for the velocity is 0.71 m/s).

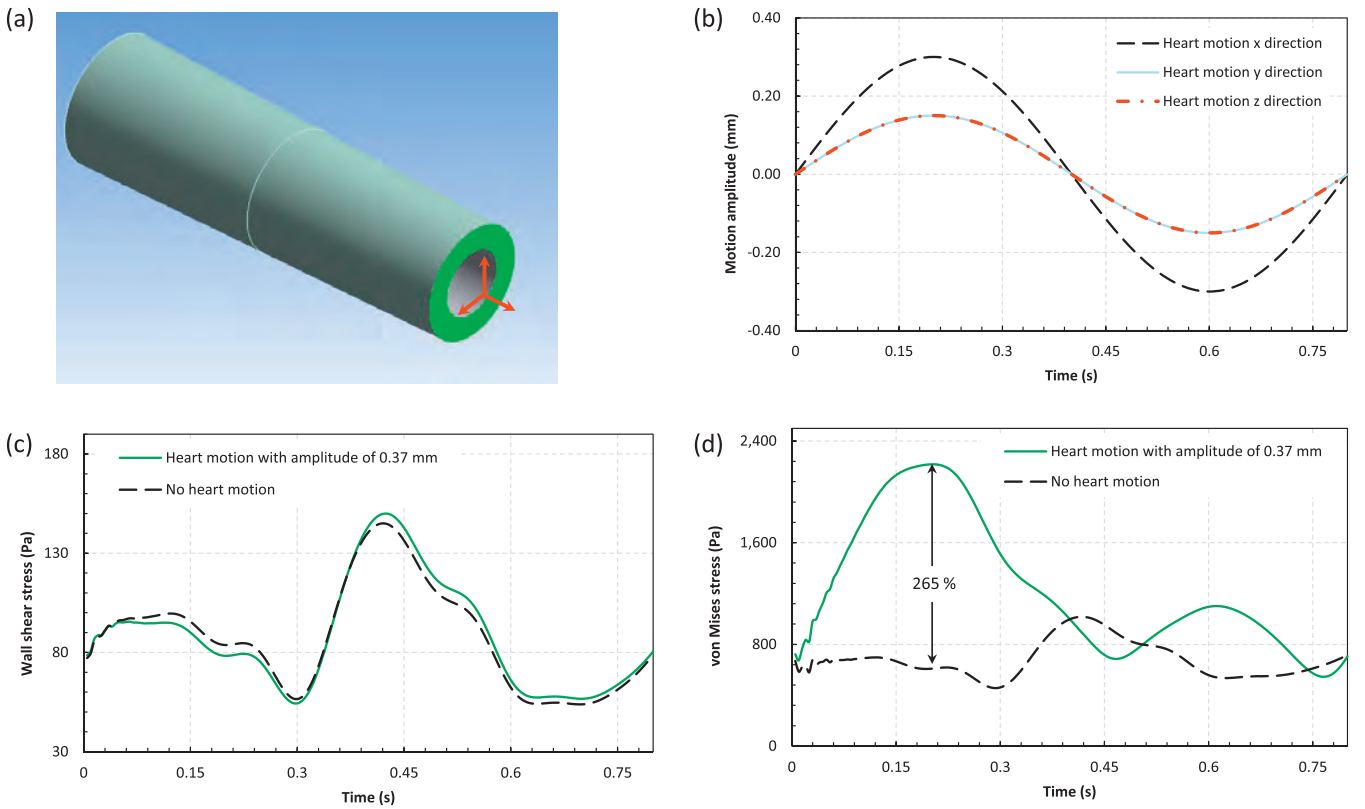

Fig. 15. The effect of different heart motion amplitude on the atherosclerotic artery: (a) location of exerted motion; (b) the time-dependent heart motion (amp. x direction = 0.3 mm; amp. y direction = 0.15 mm; amp. z direction = 0.15 mm and frequency = 0.8 Mekheimer & El Kot, 2015) (c) wall shear stress on plaque; (d) von Mises stress.

Shear stresses on the wall of the artery are as important as those on the plaque since they may cause dissection. Fig. 8 demonstrates the variations of the shear stress at the cap of the plaque surface ($x = 0.10$ mm, $y = -1.16$ mm, $z = 0.19$ mm; see Fig. 3) as a function of time. The shear stress pattern is similar to the pattern of the velocity variation but with different amplitudes. Sub-figure (b) shows that the maximum value for the shear stress corresponds to the cap area of the plaque. However, it does not exactly occur at the cap; it is slightly shifted to the left (upstream) with the location shown in sub-figure (b). It is interesting to note that even though the geometry of the plaque is symmetric, the distribution of the stress, due to the motion of the system, is asymmetric.

The temporal and spatial distributions of the pressure on the plaque surface are shown in sub-figures (a) and (b) of Fig. 9, respectively. It can be seen in sub-figure (a) that the pattern in the time domain is again similar to the pattern of the velocity, but with different amplitudes. The largest pressure distribution occurs on the left of the plaque (upstream side), as seen in sub-figure (b); the spatial distribution of the pressure (as the representative of *normal* stress) is different from that of the shear stress (compare sub-figure (b) of Fig. 9 with Fig. 8). The main cause for the initiation of rupture on the plaque is shear stresses rather than normal stresses (the pressure field).

The time-dependent variation of the von Mises stress at point A (with the location of $x = 1.50$ mm, $y = 0.07$ mm, $z = -1.01$ mm) is shown in sub-figure (a) of Fig. 10; sub-figure (b) illustrates the spatial distribution. As seen in sub-figure (a), the variation pattern is different from that of the velocity, shear stress, and the pressure (Figs. 7–9, respectively). Another max value of the stress occurs at point B (sub-figure (b)) which is far from the plaque location; this may be responsible for the initiation of the dissection.

5.1. The complete model (of this study) versus a simplified model

The completeness of the model developed in this study, which takes into account being tapered and three-layered, having lipid core inside the plaque, flow pulsation of the blood, active muscle contraction of the media layer, the heart motion, and being viscoelastic (Farokhi, Ghayesh, Gholipour, & Tavallaeinejad, 2017; Ghayesh, 2018; Hashemi, 2016; Sevostianov, Levin, & Radi, 2016), is highlighted by comparing it to a model which ignores all the above-mentioned parameters. The comparison is shown in Fig. 11; from all the sub-figures, it can be concluded that all the shown characteristics (the stresses and the pressure) possess a time-varying nature; the simplified model (dashed lines) is not able to predict this. Moreover, sub-

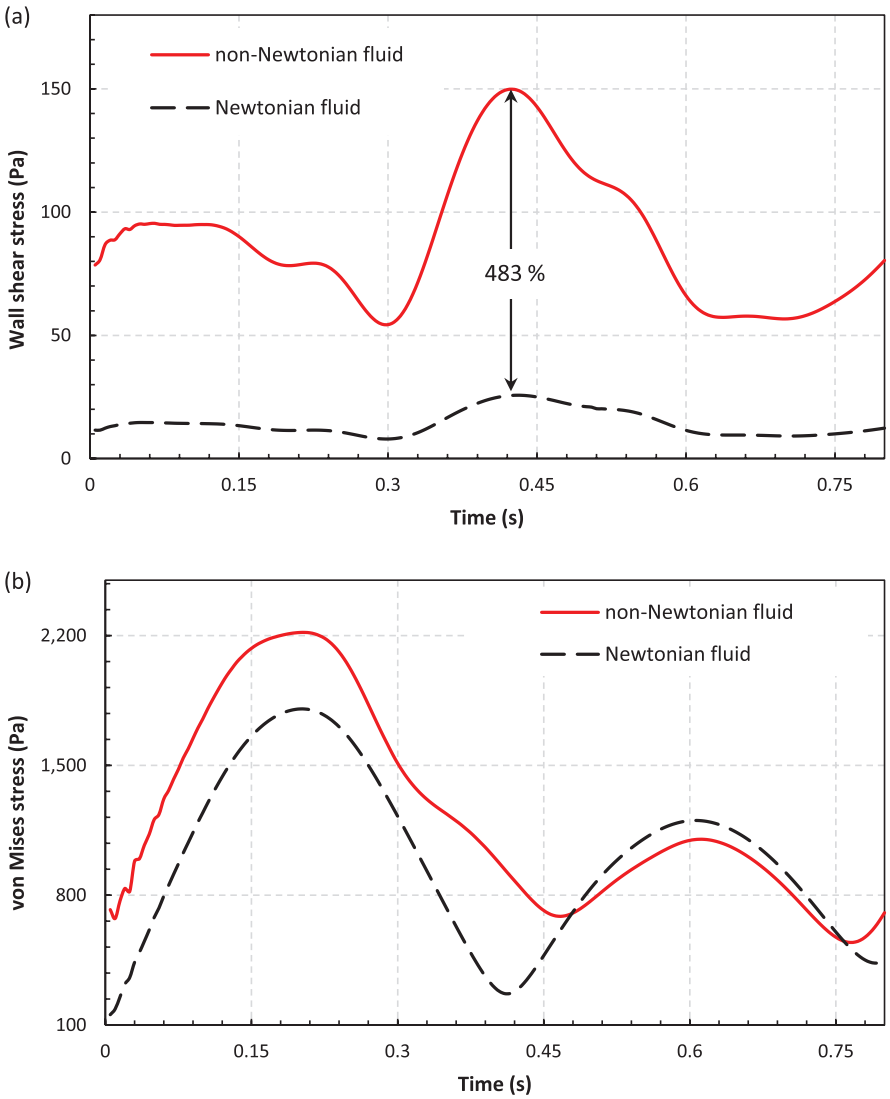

Fig. 16. The effect of Newtonian and non-Newtonian fluid on the atherosclerotic artery: (a) wall shear stress on plaque; (b) von Mises stress.

figures (a) and (c) highlight that both the wall shear stress and the pressure on the plaque follow the same pattern as the blood-flow pulsation; however, the von Mises stress follows different pattern due to the heart-motion. The maximum amplitude for the shear stress in the vicinity of $t = 0.42$ s sub-figure (a) is 149.7 Pa which shows a difference of 102% in comparison to the prediction based on the simplified model. Likewise the maximum amplitude of von Mises stress (sub-figure (b)) increases to around 511% of the simplified model value. The same trend is observed for the pressure, with a 135% increase compared to the simplified model (sub-figure (c)).

5.2. Stress distributions for different values of stenosis

The distributions of the shear and von Mises stresses on the surface and inside the plaque (where these values are maximum) are plotted in Fig. 12 for stenosis levels of 25%, 35%, 45%, and 55% shown in sub-figures (a–d), respectively. Sub-figure (e) shows that for different stenosis levels, the curves (time traces) follow more or less the same trend, while the larger the stenosis the larger the wall shear stress becomes. Sub-figure (f) highlights that the influence of the stenosis level on the variations of the von Mises stress; sub-figures (e) and (f) show that if the shoulder (bottom) area of the plaque remains constant and only the height of the plaque is increased, the maximum value of the von Mises stress and the maximum value of the shear stress increase.

5.3. Plaque shoulder effect on stress distribution

For a fixed stenosis level of 45%, the effect of increasing the length of the shoulder of the plaque is shown in Fig. 13; sub-figures (a–d) show different shoulder lengths of 2, 4, 6 and 8 mm. Sub-figure (e) shows a larger shear stress for the smallest

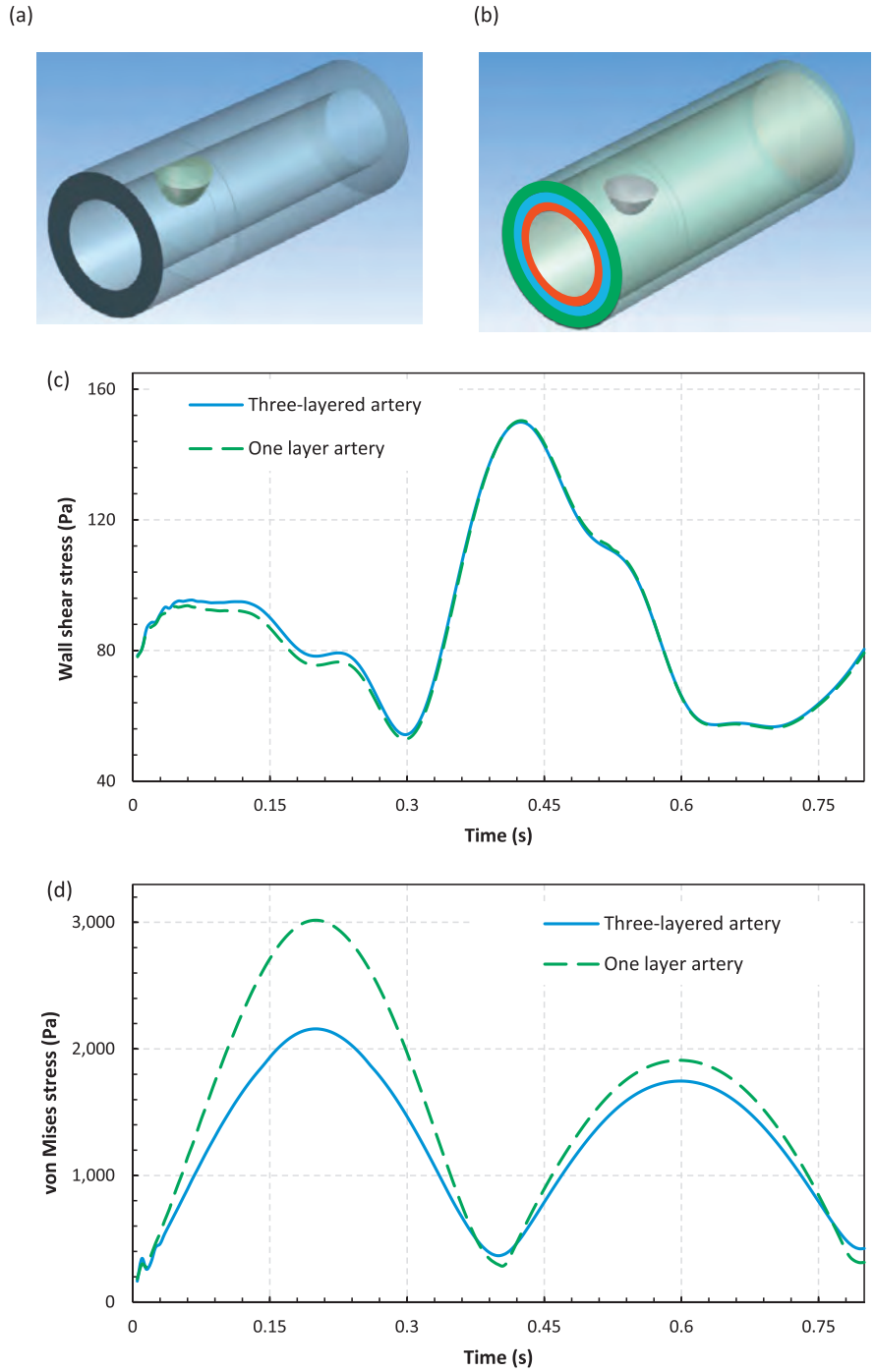

Fig. 17. The effect of three-layered modelling on the atherosclerotic artery: (a) one layer modelling; (b) three-layered modelling; (c) wall shear stress on plaque; (d) von Mises stress.

shoulder length (2 mm); the rate of decrease in the shear stress is smaller for larger values of the shoulder length. An opposite trend is observed for the case of von Mises stress, as shown in sub-figure (f). Experimental results (Richardson et al., 1989) showed that the initiation of the rupture occurs most of the time at the shoulder; hence the von Mises stress governs the plaque rupture initiation (sub-figure (f)).

5.4. Effect of tapered shape

The tapered shape of the artery plays a critical role in the initiation of the plaque-rupture (Chakravarty & Mandal, 2000). Fig. 14 highlights the effect of taking into account the tapered shape of the artery on the maximum values of the von

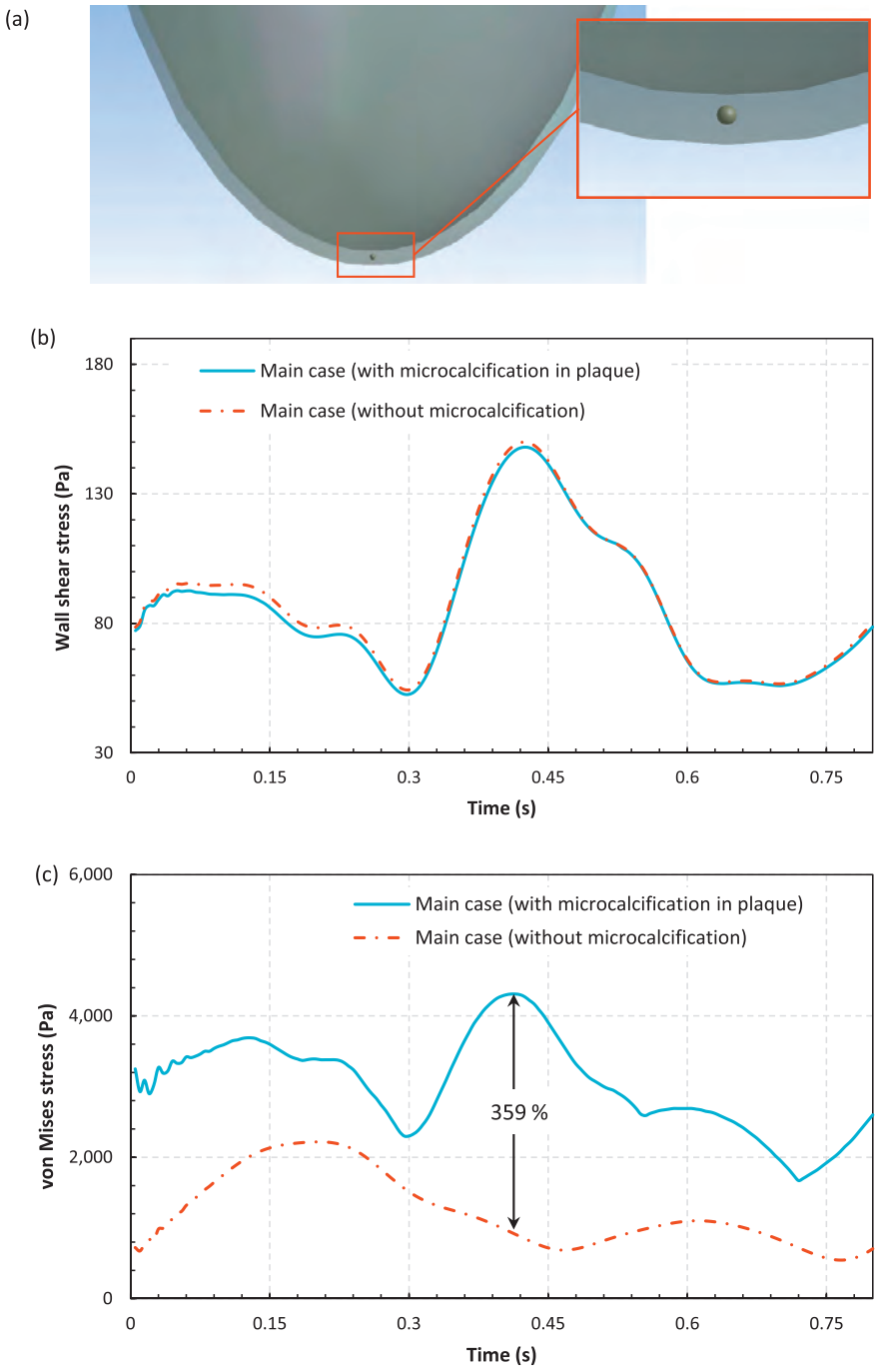

Fig. 18. The effect of micro-calcification on the atherosclerotic artery: (a) geometry of micro-calcification modelling; (b) wall shear stress on plaque; (d) von Mises stress.

Mises and wall shear stress. The shear stress and von Mises stress are larger for a tapered model sub-figures (c) and (d). For both the shear and von Mises stresses, the trend (time trace) for both the tapered and straight arteries is the same.

5.5. Effect of artery motion

The heart-beat causes the coronary artery to move back and forth; this section highlights the effect of this motion on the stress field. The heart motion is introduced as a simple sinusoidal wave at the inlet of the artery. This motion can play a fundamental role in the dynamical behaviour of the plaque and the initiation of the rupture. Fig. 15 sub-figures (a) and (b) show the location and the function of the heart motion (with the amplitude of 0.37 mm and the frequency of 0.8) (Yang et al., 2017).

5.6. Non-Newtonian blood flow

A comparison between the shear stress field when the blood is modelled as a Newtonian and non-Newtonian fluid is made in Fig. 16, showing that the shear stress increases substantially by the amount of up to 483% when the blood is considered to be non-Newtonian. The von Mises stress increases slightly.

5.7. Three-layered artery versus single-layered

The coronary artery consists of three different layers which have different properties (Tricerri, Dedè, Gambaruto, Quarteroni, & Sequeira, 2016). For instance, the adventitia has collagen material for large deformation and reshaping the artery, the media layer is active muscular tissue which supports the active pumping of the blood, and intima layer is in contact with the blood which helps the blood to move with less friction. Fig. 17 shows that taking into account the three layers do not change the shear stress while it decreases the predicted von Mises stress; for the single layer model the properties of the intima are used for comparison.

5.8. Micro-calcification effect

Stress concentration in the fibrous cap caused by micro-calcification can be considered as a rupture initiation. Considering this fact, micro-calcification has been modelled in the intima layer of the plaque (Fig. 18); this model demonstrates the maximum von Mises stress increases by 359% in comparison with model without micro-calcification. However, the shear stress of the atherosclerotic artery remains the same.

6. Conclusions

In this paper, a numerical dynamical model of an atherosclerotic coronary artery has been developed to examine the effect of different factors on a diseased coronary artery. In order to obtain a reliable model for the artery and plaque that is capable of predicting the initiation of heart attack accurately, it is vital to consider all the following parameters in the model and simulations. Therefore, taking into account (1) the blood physiological pulsation, (2) tapered shape of the artery, (3) the motion of the artery due to the heart motion, (4) media layer muscle contraction, (5) the lipid pool inside the plaque, (6) non-Newtonian flow for the blood, (7) the three layers of the artery wall, i.e. adventitia, media, and intima, and (8) the micro-calcification of the plaque, are essential for accurate prediction of plaque rupture. These factors and their influences on the atherosclerotic coronary artery can be considered as a realistic representation of the plaque behaviour that can provide accurate and reliable prediction of the plaque rupture in arteries. It was shown that:

(1) In the analysis of atherosclerotic arteries considering both solid and fluid and their interactions are essential to determine the risk of the plaque rupture. CFD and FEM by themselves predict different locations and time for high risk situations which are far from experimental results. However, FSI results developed here give accurate results.
(2) The presence of the plaque imposes higher blood velocities, higher shear stresses, higher pressure, and higher structural stresses on the artery when compared to arteries without plaques.
(3) Many simplifications in the modelling and simulations of arteries, such as ignoring being tapered and three-layered, flow pulsation of the blood, active muscle contraction of the media layer, the heart motion, having lipid core inside the plaque, and being viscoelastic, results in inaccurate predictions of the stress field, and hence the rupture.
(4) Modelling the progression of plaque by increasing the stenosis level from 25% to 55% (high risk stenosis level) shows the increase in both shear and von Mises stress. This conclusion matches with the clinically obtained data.
(5) As opposed to the previous conclusion (item 4) an increasing plaque-shoulder length increases the structural stress, while decreases the shear stress.
(6) The asymmetric 3D heart motion, incorporated in the model of this study has significant effects on the artery stress field by increasing the structural stress by 265%.
(7) Taking into account the three layers of the artery, when compared to an analysis based on a single layer artery, decreases the structural stress; however, does not alter much the shear stress.
(8) Incorporating a micro calcification in the model generates stress concentrations and hence it is very likely to encounter failure in those area.
(9) The shear stress on the plaque increases substantially (by the amount of up to 483%) when the blood is considered non-Newtonian rather than Newtonian; however, the von Mises stress increases slightly.
(10) Incorporating the tapered shape of the artery increases the shear stress, however, does not affect the von Mises stress much. Moreover, there is no phase lag in the time-domain variation between the straight and tapered arteries.

Appendix A: validation

A simple model of the coronary artery was developed by Cilla et al. (2015) in which the effects of being tapered and three-layered, having lipid core inside the plaque, active muscle contraction of the media layer, the heart motion, and being

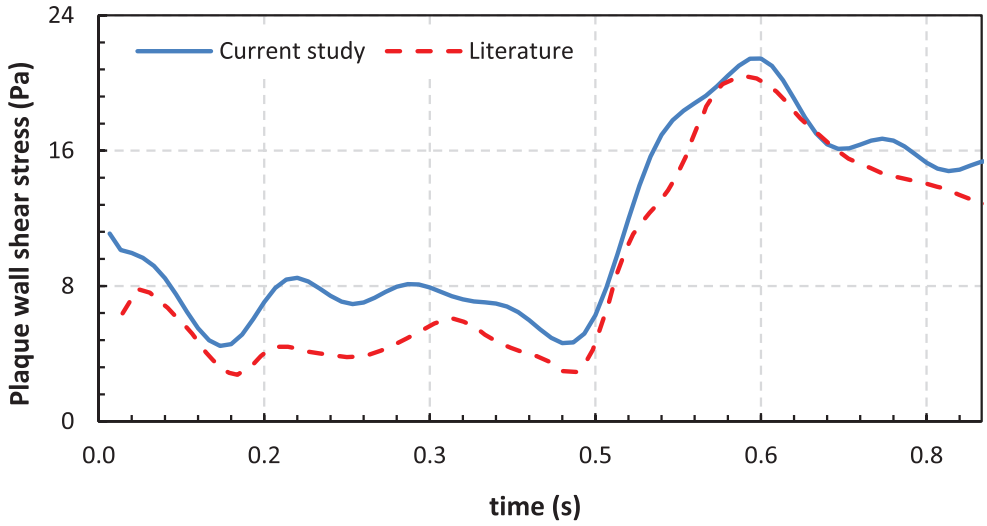

Fig. A1. Wall shear stress validation with Cilla et al. (2015).

viscoelastic and hyperelastic were not considered. We produced a simplified model and simulation results by neglecting these effects and compared our results with those given by Cilla et al. (2015). As shown in Fig. A1, the shear stress variation based on our simulations shows very good agreement with that of Cilla et al. (2015), proving the validity of our simulations.

References

A.I.o.H.a.W. AIHW.. *Leading causes of death* https://www.aihw.gov.au/reports/life-expectancy-death/deaths-in-australia/contents/leading-causes-of-death.
Akherat, S. M. J. M., & Kimiaghalam, M. (2010). A numerical investigation on pulsatile blood flow through consecutive axi-symmetric stenosis in coronary artery. In *Proceedings of the ASME 2010 tenth biennial conference on engineering systems design and analysis* (pp. 757–765). American Society of Mechanical Engineers.
Anand, M., Kwack, J., & Masud, A. (2013). A new generalized Oldroyd-B model for blood flow in complex geometries. *International Journal of Engineering Science, 72*, 78–88.
Attia, M. A., & Abdel Rahman, A. A. (2018). On vibrations of functionally graded viscoelastic nanobeams with surface effects. *International Journal of Engineering Science, 127*, 1–32.
Bakhshi Khaniki, H., & Hosseini-Hashemi, S. (2017). Dynamic response of biaxially loaded double-layer viscoelastic orthotropic nanoplate system under a moving nanoparticle. *International Journal of Engineering Science, 115*, 51–72.
Bhattacharyya, R., Sarangi, S., & Samantaray, A. K. (2015). Effect of stress-softening on the ballooning motion of hyperelastic strings. *International Journal of Engineering Science, 96*, 19–33.
Chabi, F., Champmartin, S., Sarraf, C., & Noguera, R. (2015). Critical evaluation of three hemodynamic models for the numerical simulation of intra-stent flows. *Journal of Biomechanics, 48*, 1769–1776.
Chakravarty, S., & Mandal, P. K. (2000). Two-dimensional blood flow through tapered arteries under stenotic conditions. *International Journal of Non-Linear Mechanics, 35*, 779–793.
Chan, W., Ding, Y., & Tu, J. (2007). Modeling of non-Newtonian blood flow through a stenosed artery incorporating fluid–structure interaction. *Anziam Journal, 47*, 507–523.
Chebbi, E., Wali, M., & Dammak, F. (2016). An anisotropic hyperelastic constitutive model for short glass fiber-reinforced polyamide. *International Journal of Engineering Science, 106*, 262–272.
Chen, C. X. (2016). Modelling of atherosclerotic plaque growth using fluid–structure interaction. *Bulletin of the Australian Mathematical Society, 93*, 170–172.
Cilla, M., Borrás, I., Pena, E., Martínez, M., & Malve, M. (2015). A parametric model for analysing atherosclerotic arteries: On the FSI coupling. *International Communications in Heat and Mass Transfer, 67*, 29–38.
Cyron, C., & Humphrey, J. (2014). Vascular homeostasis and the concept of mechanobiological stability. *International Journal of Engineering Science, 85*, 203–223.
Doherty, T. M., Fitzpatrick, L. A., Inoue, D., Qiao, J.-H., Fishbein, M. C., Detrano, R. C., et al. (2004). Molecular, endocrine, and genetic mechanisms of arterial calcification. *Endocrine Reviews, 25*, 629–672.
Dolla, W. J. S., House, J. A., & Marso, S. P. (2012). Stratification of risk in thin cap fibroatheromas using peak plaque stress estimates from idealized finite element models. *Medical Engineering & Physics, 34*, 1330–1338.
Doraiswamy, S., Criscione, J. C., & Srinivasa, A. R. (2016). A technique for the classification of tissues by combining mechanics based models with Bayesian inference. *International Journal of Engineering Science, 106*, 95–109.
Ebrahimi, F., & Barati, M. R. (2016). A nonlocal higher-order refined magneto-electro-viscoelastic beam model for dynamic analysis of smart nanostructures. *International Journal of Engineering Science, 107*, 183–196.
El Baroudi, A., Razafimahéry, F., & Rakotomanana, L. (2014). Fluid–structure interaction within three-dimensional models of an idealized arterial wall. *International Journal of Engineering Science, 84*, 113–126.
Falk, E., Shah, P. K., & Fuster, V. (1995). Coronary plaque disruption. *Circulation, 92*, 657–671.
Fallah, A., Ahmadian, M. T., & Mohammadi Aghdam, M. (2017). Rate-dependent behavior of connective tissue through a micromechanics-based hyper viscoelastic model. *International Journal of Engineering Science, 121*, 91–107.
Farokhi, H., & Ghayesh, M. H. (2015). Thermo-mechanical dynamics of perfect and imperfect Timoshenko microbeams. *International Journal of Engineering Science, 91*, 12–33.
Farokhi, H., Ghayesh, M. H., & Amabili, M. (2013). Nonlinear dynamics of a geometrically imperfect microbeam based on the modified couple stress theory. *International Journal of Engineering Science, 68*, 11–23.
Farokhi, H., Ghayesh, M. H., Gholipour, A., & Hussain, S. (2017). Motion characteristics of bilayered extensible Timoshenko microbeams. *International Journal of Engineering Science, 112*, 1–17.
Farokhi, H., Ghayesh, M. H., Gholipour, A., & Tavallaeinejad, M. (2017). Nonlinear oscillations of viscoelastic microplates. *International Journal of Engineering Science, 118*, 56–69.

Freed, A. D., & Einstein, D. R. (2013). An implicit elastic theory for lung parenchyma. *International Journal Engineering Science, 62*, 31–47.
Ganghoffer, J.-F., & Sokolowski, J. (2014). A micromechanical approach to volumetric and surface growth in the framework of shape optimization. *International Journal of Engineering Science, 74*, 207–226.
Ghayesh, M. H., Amabili, M., & Farokhi, H. (2013). Three-dimensional nonlinear size-dependent behaviour of Timoshenko microbeams. *International Journal of Engineering Science, 71*, 1–14.
Ghayesh, M. H., Farokhi, H., & Amabili, M. (2013). Nonlinear dynamics of a microscale beam based on the modified couple stress theory. *Composites Part B: Engineering, 50*, 318–324.
Ghayesh, M. H., Farokhi, H., & Amabili, M. (2014). In-plane and out-of-plane motion characteristics of microbeams with modal interactions. *Composites Part B: Engineering, 60*, 423–439.
Ghayesh, M. H., Farokhi, H., & Alici, G. (2016). Size-dependent performance of microgyroscopes. *International Journal of Engineering Science, 100*, 99–111.
Ghayesh, M. H., Farokhi, H., & Hussain, S. (2016). Viscoelastically coupled size-dependent dynamics of microbeams. *International Journal of Engineering Science, 109*, 243–255.
Ghayesh, M. H., Farokhi, H., & Gholipour, A. (2017). Oscillations of functionally graded microbeams. *International Journal of Engineering Science, 110*, 35–53.
Ghayesh, M. H. (2018). Dynamics of functionally graded viscoelastic microbeams. *International Journal of Engineering Science, 124*, 115–131.
Gholipour, A., Farokhi, H., & Ghayesh, M. H. (2015). In-plane and out-of-plane nonlinear size-dependent dynamics of microplates. *Nonlinear Dynamics, 79*, 1771–1785.
Gizzi, A., Vasta, M., & Pandolfi, A. (2014). Modeling collagen recruitment in hyperelastic bio-material models with statistical distribution of the fiber orientation. *International Journal of Engineering Science, 78*, 48–60.
Goda, I., & Ganghoffer, J.-F. (2015). 3D plastic collapse and brittle fracture surface models of trabecular bone from asymptotic homogenization method. *International Journal of Engineering Science, 87*, 58–82.
Goda, I., Rahouadj, R., Ganghoffer, J.-F., Kerdjoudj, H., & Siad, L. (2016). 3D couple-stress moduli of porous polymeric biomaterials using μCT image stack and FE characterization. *International Journal of Engineering Science, 100*, 25–44.
Gou, K., & Walton, J. R. (2014). Reconstruction of nonuniform residual stress for soft hyperelastic tissue via inverse spectral techniques. *International Journal of Engineering Science, 82*, 46–73.
Habets, J., van den Brink, R. B., Uijlings, R., Spijkerboer, A. M., Willem, P. T. M., Chamuleau, S. A., et al. (2012). Coronary artery assessment by multidetector computed tomography in patients with prosthetic heart valves. *European Radiology, 22*, 1278–1286.
Haddad, S. M. H., & Samani, A. (2017a). A computational model of the left ventricle biomechanics using a composite material approach. *International Journal of Engineering Science, 111*, 61–73.
Haddad, S. M., & Samani, A. (2017b). A computational model of the left ventricle biomechanics using a composite material approach. *International Journal of Engineering Science, 111*, 61–73.
Hashemi, R. (2016). On the overall viscoelastic behavior of graphene/polymer nanocomposites with imperfect interface. *International Journal of Engineering Science, 105*, 38–55.
Holzapfel, G. A., Sommer, G., Gasser, C. T., & Regitnig, P. (2005). Determination of layer-specific mechanical properties of human coronary arteries with nonatherosclerotic intimal thickening and related constitutive modeling. *American Journal of Physiology-Heart and Circulatory Physiology, 289*, H2048–H2058.
Il'ichev, A., & Fu, Y. (2014). Stability of an inflated hyperelastic membrane tube with localized wall thinning. *International Journal of Engineering Science, 80*, 53–61.
Janela, J., Moura, A., & Sequeira, A. (2010). Absorbing boundary conditions for a 3D non-Newtonian fluid–structure interaction model for blood flow in arteries. *International Journal of Engineering Science, 48*, 1332–1349.
Ji, J., Toubaru, S., Kobayashi, S., Morikawa, H., Tang, D., & Ku, D. N. (2011). Flow and deformation in a multi-component arterial stenosis model. *Journal of Biomechanical Science and Engineering, 6*, 79–88.
Johnston, B. M., Johnston, P. R., Corney, S., & Kilpatrick, D. (2004). Non-Newtonian blood flow in human right coronary arteries: Steady state simulations. *Journal of Biomechanics, 37*, 709–720.
Joshi, S., & Walton, J. R. (2013). Reconstruction of the residual stresses in a hyperelastic body using ultrasound techniques. *International Journal of Engineering Science, 70*, 46–72.
Kachanov, M., & Abedian, B. (2015). On the isotropic and anisotropic viscosity of suspensions containing particles of diverse shapes and orientations. *International Journal of Engineering Science, 94*, 71–85.
Karšaj, I., Sorić, J., & Humphrey, J. D. (2010). A 3-D framework for arterial growth and remodeling in response to altered hemodynamics. *International Journal of Engineering Science, 48*, 1357–1372.
Karimi, A., Shojaei, A., & Razaghi, R. (2017). Viscoelastic mechanical measurement of the healthy and atherosclerotic human coronary arteries using DIC technique. *Artery Research, 18*, 14–21.
Khakalo, S., Balobanov, V., & Niiranen, J. (2018). Modelling size-dependent bending, buckling and vibrations of 2D triangular lattices by strain gradient elasticity models: Applications to sandwich beams and auxetics. *International Journal of Engineering Science, 127*, 33–52.
Li, Z.-Y., & Gillard, J. H. (2007). Simulation of the interaction between blood flow and atherosclerotic plaque. In *Proceedings of the twenty-ninth annual international conference of the IEEE engineering in medicine and biology society* (pp. 1699–1702). IEEE.
Maldonado, N., Kelly-Arnold, A., Vengrenyuk, Y., Laudier, D., Fallon, J. T., Virmani, R., et al. (2012). A mechanistic analysis of the role of microcalcifications in atherosclerotic plaque stability: Potential implications for plaque rupture. *American Journal of Physiology-Heart and Circulatory Physiology, 303*, H619–H628.
Mandal, M. S., Mukhopadhyay, S., & Layek, G. (2012). Pulsatile flow of an incompressible, inhomogeneous fluid in a smoothly expanded vascular tube. *International Journal of Engineering Science, 57*, 1–10.
Mandal, P. K. (2005). An unsteady analysis of non-Newtonian blood flow through tapered arteries with a stenosis. *International Journal of Non-Linear Mechanics, 40*, 151–164.
Mekheimer, K. S., & El Kot, M. (2015). Suspension model for blood flow through catheterized curved artery with time-variant overlapping stenosis. *Engineering Science and Technology, An International Journal, 18*, 452–462.
Perkowska, M., Piccolroaz, A., Wrobel, M., & Mishuris, G. (2017). Redirection of a crack driven by viscous fluid. *International Journal of Engineering Science, 121*, 182–193.
Purves, W. K., Purves, W. K., Orians, G. H., Sadava, D., & Heller, H. C. (2003). *Life: the science of biology: volume III: plants and animals*. Macmillan.
Ramírez-Torres, A., Rodríguez-Ramos, R., Merodio, J., Penta, R., Bravo-Castillero, J., Guinovart-Díaz, R., et al. (2017). The influence of anisotropic growth and geometry on the stress of solid tumors. *International Journal of Engineering Science, 119*, 40–49.
Richardson, P. D., Davies, M., & Born, G. (1989). Influence of plaque configuration and stress distribution on fissuring of coronary atherosclerotic plaques. *The Lancet, 334*, 941–944.
Roelse, M., de Ruijter, N. C. A., Vrouwe, E. X., & Jongsma, M. A. (2013). A generic microfluidic biosensor of G protein-coupled receptor activation—monitoring cytoplasmic (Ca^{2+}) changes in human HEK293 cells. *Biosensors and Bioelectronics, 47*, 436–444.
Ross, R. (1999). Atherosclerosis—an inflammatory disease. *New England Journal of Medicine, 340*, 115–126.
Sevostianov, I., Levin, V., & Radi, E. (2016). Effective viscoelastic properties of short-fiber reinforced composites. *International Journal of Engineering Science, 100*, 61–73.
Seyedkavoosi, S., Zaytsev, D., Drach, B., Panfilov, P., Gutkin, M. Y., & Sevostianov, I. (2017). Fraction-exponential representation of the viscoelastic properties of dentin. *International Journal of Engineering Science, 111*, 52–60.
Shahverdi, H., & Barati, M. R. (2017). Vibration analysis of porous functionally graded nanoplates. *International Journal of Engineering Science, 120*, 82–99.

Shirazi, H. A., & Ayatollahi, M. (2014). Biomechanical analysis of functionally graded biomaterial disc in terms of motion and stress distribution in lumbar spine. *International Journal of Engineering Science, 84*, 62–78.
Soares, J. S., Pasta, S., Vorp, D. A., & Moore Jr, J. E. (2010). Modeling in cardiovascular biomechanics. *International Journal of Engineering Science, 48*, 1563–1575.
Sorof, S. (2004). Intravascular atheroma monitoring: past, present and future of identifying vulnerable plaques. *Applications in Imaging-Cardiac Interventions*, 34–39.
Švihlová, H., Hron, J., Málek, J., Rajagopal, K., & Rajagopal, K. (2016). Determination of pressure data from velocity data with a view toward its application in cardiovascular mechanics. Part 1. Theoretical considerations. *International Journal of Engineering Science, 105*, 108–127.
Švihlová, H., Hron, J., Málek, J., Rajagopal, K., & Rajagopal, K. (2017). Determination of pressure data from velocity data with a view towards its application in cardiovascular mechanics. Part 2. A study of aortic valve stenosis. *International Journal of Engineering Science, 114*, 1–15.
Taelman, L., Degroote, J., Swillens, A., Vierendeels, J., & Segers, P. (2014). Fluid–structure interaction simulation of pulse propagation in arteries: Numerical pitfalls and hemodynamic impact of a local stiffening. *International Journal of Engineering Science, 77*, 1–13.
Tambasco, M., & Steinman, D. A. (2003). Path-dependent hemodynamics of the stenosed carotid bifurcation. *Annals of Biomedical Engineering, 31*, 1054–1065.
Tang, D., Yang, C., Kobayashi, S., & Ku, D. N. (2001). Steady flow and wall compression in stenotic arteries: A three-dimensional thick-wall model with fluid–wall interactions. *Journal of Biomechanical Engineering, 123*, 548–557.
Teng, Z., Feng, J., Zhang, Y., Sutcliffe, M. P., Huang, Y., Brown, A. J., et al. (2015). A uni-extension study on the ultimate material strength and extreme extensibility of atherosclerotic tissue in human carotid plaques. *Journal of Biomechanics, 48*, 3859–3867.
Thomas-Seale, L., Hollis, L., Klatt, D., Sack, I., Roberts, N., Pankaj, P., et al. (2016). The simulation of magnetic resonance elastography through atherosclerosis. *Journal of Biomechanics, 49*, 1781–1788.
Tricerri, P., Dedè, L., Gambaruto, A., Quarteroni, A., & Sequeira, A. (2016). A numerical study of isotropic and anisotropic constitutive models with relevance to healthy and unhealthy cerebral arterial tissues. *International Journal of Engineering Science, 101*, 126–155.
Trofimov, A., Abaimov, S., Akhatov, I., & Sevostianov, I. (2017). Effect of elastic contrast on the contribution of helical fibers into overall stiffness of a composites. *International Journal of Engineering Science, 120*, 31–50.
Versluis, A., Bank, A. J., & Douglas, W. H. (2006). Fatigue and plaque rupture in myocardial infarction. *Journal of Biomechanics, 39*, 339–347.
Wenk, J. F., Papadopoulos, P., & Zohdi, T. I. (2010). Numerical modeling of stress in stenotic arteries with microcalcifications: a micromechanical approximation. *Journal of Biomechanical Engineering, 132*, 091011-1 to 091011-11.
W.H.O. WHO.. *The top 10 causes of death* http://www.who.int/mediacentre/factsheets/fs310/en/.
Wu, W.-T., Aubry, N., Massoudi, M., & Antaki, J. F. (2017). Transport of platelets induced by red blood cells based on mixture theory. *International Journal of Engineering Science, 118*, 16–27.
Xiong, H., Liu, X., Tian, X., Pu, L., Zhang, H., Lu, M., et al. (2014). A numerical study of the effect of varied blood pressure on the stability of carotid atherosclerotic plaque. *Biomedical Engineering Online, 13*, 1–13.
Yang, B., Liu, C., Zheng, W., & Liu, S. (2017). Motion prediction via online instantaneous frequency estimation for vision-based beating heart tracking. *Information Fusion, 35*, 58–67.

Chapter 4

Nonlinear biomechanics of bifurcated atherosclerotic coronary arteries

Statement of Authorship

Title of Paper	Nonlinear biomechanics of bifurcated atherosclerotic coronary arteries
Publication Status	☑ Published ☐ Accepted for Publication ☐ Submitted for Publication ☐ Unpublished and Unsubmitted work written in manuscript style
Publication Details	International Journal of Engineering Science Volume 133, December 2018, Pages 60-83

Principal Author

Name of Principal Author (Candidate)	Alireza Gholipour
Contribution to the Paper	Performed all analyses and wrote the manuscript.
Overall percentage (%)	75
Certification:	This paper reports on original research I conducted during the period of my Higher Degree by Research candidature and is not subject to any obligations or contractual agreements with a third party that would constrain its inclusion in this thesis. I am the primary author of this paper.
Signature	Date 19/8/2019

Co-Author Contributions

By signing the Statement of Authorship, each author certifies that:

i. the candidate's stated contribution to the publication is accurate (as detailed above);

ii. permission is granted for the candidate in include the publication in the thesis; and

iii. the sum of all co-author contributions is equal to 100% less the candidate's stated contribution.

Name of Co-Author	Dr. Mergen H. Ghayesh
Contribution to the Paper	Helped in modelling/simulations, checked the results, and assisted in the preparation of the manuscript.
Signature	Date 19/8/2019

Name of Co-Author	Prof. Anthony Zander
Contribution to the Paper	Checked the results and assisted in the preparation of the manuscript.
Signature	Date 19/08/2019

Please cut and paste additional co-author panels here as required.

International Journal of Engineering Science 133 (2018) 60–83

Contents lists available at ScienceDirect

International Journal of Engineering Science

journal homepage: www.elsevier.com/locate/ijengsci

Nonlinear biomechanics of bifurcated atherosclerotic coronary arteries

Alireza Gholipour, Mergen H. Ghayesh*, Anthony Zander

School of Mechanical Engineering, University of Adelaide, South Australia 5005, Australia

ARTICLE INFO

Article history:
Received 23 July 2018
Revised 11 August 2018
Accepted 11 August 2018
Available online 11 September 2018

Keywords:
Biomechanics
Bifurcated artery
Coronary
Atherosclerosis
Nonlinear

ABSTRACT

One of the most high-risk locations of plaque growth and rupture initiation (and hence occurrence of heart attack) is the first main bifurcation of the left main coronary artery; the aim of this investigation is to analyse the nonlinear three-dimensional biomechanics of bifurcated atherosclerotic left coronary artery. In order to examine the influence of different system parameters, a biomechanical model of a bifurcated coronary artery is developed. Three plaques of varying geometry and material properties inside the three branches of the left main (LM), the left anterior descending (LAD), and the left circumflex (LCx) are modelled incorporating three-dimensionality, nonlinear geometric and material properties, asymmetry, viscosity, and hyperelasticity, and fluid-solid interaction. A finite element method (FEM) is employed to incorporate all of the above-mentioned important features in addition to physiological blood pulsation, heart motion, active media layer contraction, lipid plaque, calcium deposition, three different artery layers, micro-calcification, and non-Newtonian model for blood. Moreover, the effects of different system features such as stenosis, curved shape of the artery, plaque location, and fibrous cap thickness on the stress field (shear and structural) are examined. The developed biomechanical model could be utilised to estimate the risk of the initiation of plaque rupture inside the human coronary artery and the occurrence of heart attack.

1. Introduction

The main causes of death worldwide are ischaemic heart diseases and strokes (W.H.O. WHO 2018). The majority of ischaemic heart diseases can be attributed to atherosclerosis (Tricerri, Dedè, Gambaruto, Quarteroni, & Sequeira, 2016). Plaque formation and obstruction in arteries (Anand, Kwack, & Masud, 2013; Cyron & Humphrey, 2014) are the two consequences of atherosclerosis in human arteries. These plaques grow asymptomatically over a number of years and lead to high risk situations in the critical organs such as the heart and brain. Since imaging techniques are not able to assess the vulnerability of plaques (even though they determine the level of stenosis), the biomechanical (Doraiswamy, Criscione, & Srinivasa, 2016; Goda & Ganghoffer, 2015; Goda, Rahouadj, Ganghoffer, Kerdjoudj, & Siad, 2016; Rubin & Solav, 2016; Švihlová, Hron, Málek, Rajagopal, & Rajagopal, 2016; Švihlová, Hron, Málek, Rajagopal, & Rajagopal, 2017) modelling of the atherosclerosis could be used as an effective tool to determine the risk level associated with plaques inside in the coronary arteries (Haddad & Samani, 2017). This biomechanical (Joshi & Walton, 2013; Shirazi & Ayatollahi, 2014) model can thus be utilised as a preventative tool to estimate the risk of myocardial infarction.

In order to obtain a reliable model of a bifurcated atherosclerotic artery it is essential to incorporate all the parameters of influence in different locations of the arteries. Bifurcations in arteries are known as a high risk location of plaque forming

* Corresponding author.
E-mail address: mergen.ghayesh@adelaide.edu.au (M.H. Ghayesh).

https://doi.org/10.1016/j.ijengsci.2018.08.003
0020-7225/

and rupture. One of the most critical bifurcations in the coronary arteries is bifurcation of LM into LCx and LAD (Doutel, Carneiro, Campos, & Miranda, 2018; Soulis, Farmakis, Giannoglou, & Louridas, 2006).

There are some studies in the literature which developed biomechanical models of bifurcated coronary arteries *in the absence of any stenosis*. Soulis et al. (2006) investigated the wall shear stress (WSS) in the left artery extracted via data from angiographies; they showed that low WSS regions occur at bifurcations. Frattolin, Zarandi, Pagiatakis, Bertrand, and Mongrain (2015) showed the effect of stenosis severity and location on time-dependent WSS of the different shapes of the bifurcated atherosclerotic right coronary artery (RCA). Liu, Wu, Ghista, Huang, and Wong (2015) examined WSS and wall pressure gradient, and studied the influences of curvature and bifurcations on the blood flow; their results showed that low WSS points are prone to plaque formation. Dynamic and quasi-static analyses of bifurcated arteries have been conducted by Weydahl and Moore (2001), who demonstrated that the dynamic geometry effects are essential in mean and oscillating WSS. The left anterior descending coronary artery has been modelled based on realistic data (Prosi, Perktold, Ding, & Friedman, 2004), showing the significance of time-varying curvature on the fluid and WSS. Taking into account the repetitive variation of artery curvature, a three-dimensional fluid analysis of a branched coronary artery was conducted by Pivkin, Richardson, Laidlaw, and Karniadakis (2005); they concluded that the phase difference between arterial motion and blood flow rate could have a significant influence on the flow pulsation and dynamic geometry. Huo et al. (2012) obtained optimal flow patterns based on oscillatory shear index-OSI in a coronary bifurcation for various branching angles and diameter ratios; the optimisation was based on WSS and oscillatory shear index. Fluid properties of coronary bifurcation lesions were investigated considering the lesion configuration and stenosis severity (Pagiatakis, Tardif, L'Allier, & Mongrain, 2015); according to this study the lesion configuration could have substantial effects on the disease progression. Malvè, Garcia, Ohayon, and Martínez (2012) constructed a fluid-solid interaction (FSI) theoretical model of the LCA based on a computerised tomography; they computed the arterial WSS to analyse the correlation between the geometry and WSS. Above-mentioned valuable studies did not consider *diseased bifurcated* coronary arteries; the effects of the *plaque presence* on FSI (El Baroudi, Razafimahéry, & Rakotomanana, 2014) model of the artery (Karšaj, Sorić, & Humphrey, 2010) and blood flow have not been studied yet—*the present paper is the first to do so*.

The biomechanics of the plaques in *non-bifurcated* coronary arteries has been studied in many papers using different numerical techniques; see Refs. (Barretta, Čanađija, Luciano, & de Sciarra, 2018; Dehrouyeh-Semnani, 2018; Farokhi & Ghayesh, 2018a ,b; Ghayesh, 2018; Ghayesh & Farajpour, 2018; Ghayesh & Farokhi, 2018; Ghayesh, Amabili, & Farokhi, 2013; Gholipour, Ghayesh, Zander, & Mahajan, 2018; Jiao and Alavi, 2018; Qi et al., 2018) for more information on different numerical methods. For instance, studies have been conducted based on Magnetic Resonance Imaging (MRI), histology, Intravascular Ultrasound (IVUS), and Optical Coherence Tomography (OCT) of the arteries; they used realistic shape of arteries for their numerical modelling and investigated other features in arteries such as acoustic analysis and prediction of strains (Veress, Weiss, Gullberg, Vince, & Rabbitt, 2002), viscoelastic (Bakhshi Khaniki & Hosseini-Hashemi, 2017; Ebrahimi & Barati, 2016; Farokhi, Ghayesh, Gholipour, & Tavallaeinejad, 2017; Ghayesh, 2018; Liu, Tang, Yu, & Pipes, 2018; Seyedkavoosi et al., 2017) and hyperelastic analysis (Fallah, Ahmadian, & Mohammadi Aghdam, 2017; Galich, Slesarenko, Li, & Rudykh, 2018; Heiland, Forsell, Roy, Hedin, & Gasser, 2013; Il'ichev & Fu, 2014), and non-linear isotropic (Mazloum & Sevostianov, 2018; Ramírez-Torres et al., 2017; Shariff, 2017; Wu, Li, Chen, Kang, & Müller, 2018; Zou & He, 2018) and piecewise homogeneous material modelling (Lu, Duan, & Qiao, 2015). Theoretical and experimental models of fluid micro-hemodynamic and flow reversal of an artificial artery vessel have been examined using a thermal MEMS sensor (Ai et al., 2010). Several investigations have been conducted considering a hyperelastic (Gou & Walton, 2014; Ramírez-Torres et al., 2017) solid and Newtonian fluid models that consider different characteristics such as superficial arterial vessel (Tang, Yang, Kobayashi, Zheng, & Vito, 2003). These studies did not address the prediction of the coupled fluid and solid behaviours since they did not employ FSI analysis considering all the effective parameters when the plaque is present at different locations of coronary arteries.

The investigations of the biomechanics of plaques in *bifurcated coronary* arteries are very limited. Effects of the anatomical features of coronary bifurcation on near-wall and intravascular flow patterns have been studied by Chiastra et al. (2017); their investigation showed that the bifurcation angle affects the hemodynamics slightly and curvature impacts the flow significantly. Influences of different types of plaque in the left coronary artery were examined by Chaichana, Sun, and Jewkes (2013), who showed that the presence of plaques in all three branches is the highest risk situation. Employing a model developed on the basis of in-vivo clinical data of a coronary artery from one patient, Gijsen et al. (2007) examined WSS along the bifurcation. Although these investigations studied atherosclerotic bifurcated coronary artery considering fluid behaviour, however, atherosclerosis is a complex system of coupled interactions of fluid and solid; this gap is filled in the current paper *by developing a fluid-solid interaction (FSI) of* atherosclerotic *bifurcated coronary artery*. Different characteristics of these two regimes can comprehensively affect the accurate system modelling.

1.1. Contributions of the present investigation

This paper is the first to analyse the nonlinear three-dimensional fluid-solid interaction biomechanics of bifurcated atherosclerotic left coronary arteries (i.e. both the bifurcation and plaques are present) with detailed consideration of the shear and structural stresses with the aim of providing a foundation knowledge on plaque rupture (and hence heart attack). Another contribution of this study is to take into account all the following aspects in the model/simulations: (i) solid-fluid interaction; (ii) artery viscoelasticity; (iii) artery hyperelasticity; (iv) blood flow pulsation; (v) non-Newtonian fluid; (vi) effect of different shape of the bifurcated artery; (vii) artery layers; (viii) heart motion; (ix) media-layer active contraction; (x)

calcification and microcalcification; (xi) location and stenosis level of the plaque; and (xii) effect of fibrous cap thickness—it is also the first time that the combination of all of these factors is taken into account for bifurcated coronary arteries. The model and simulations developed (using FEM, Arfaoui, Trifa, Mansouri, Karoui, & Renard, 2018; Fan et al., 2018; Freed & Einstein, 2013; Ganghoffer & Sokolowski, 2014; Goda & Ganghoffer, 2015; Goda et al., 2016; Joshi & Walton, 2013; Khakalo, Balobanov, & Niiranen, 2018; Kolpakov, Andrianov, Rakin, & Rogerson, 2018; Sevostianov, Levin, & Radi, 2016; Shahverdi & Barati, 2017; Shirazi & Ayatollahi, 2014; Švihlová et al., 2016; Trofimov et al., 2017; Trofimov et al., 2018) in the current study is the most comprehensive and complete to date.

2. Model development for bifurcated atherosclerotic left coronary artery

The geometry of an idealised bifurcated artery is adopted based on image from Ref. (Medrano-Gracia et al., 2017), as shown in Figs. 1 and 2. As seen in Fig. 1, the first bifurcation from the left coronary artery into LAD and LCx is considered. Figure 3 shows the geometry dimensions (see Fig. 3 (b)–(d)), blood inlet/outlet, and the plaques. A hyperbolic function is used to incorporate the 3D centreline curvature of the bifurcated artery where for the

Left Main:

$$\begin{aligned} x &= [0 \quad 10] \quad \text{mm}, \\ y &= (\cosh(x/40) - 1)/(\cosh(20/40) - 1) \quad \text{mm}, \\ z &= (\cosh(x/40) - 1)/(\cosh(20/40) - 1) \quad \text{mm}, \end{aligned} \tag{1}$$

Left anterior descending

$$\begin{aligned} x &= [-10 \quad 0] \quad \text{mm}, \\ y &= x\tan(\theta_{LAD}) + 7(\cosh(x/40) - 1)/(\cosh(20/40) - 1) \quad \text{mm}, \\ z &= 7(\cosh(x/40) - 1)/(\cosh(20/40) - 1) \quad \text{mm}, \end{aligned} \tag{2}$$

Left circumflex:

$$\begin{aligned} x &= [-10 \quad 0] \quad \text{mm}, \\ y &= -x\tan(\theta_{LCX}) - 7(\cosh(x/40) - 1)/(\cosh(20/40) - 1) \quad \text{mm}, \\ z &= 7(\cosh(x/40) - 1)/(\cosh(20/40) - 1) \quad \text{mm}. \end{aligned} \tag{3}$$

The stenosis level is defined as

$$\text{Stenosis} = \frac{D_{in} - D_{\min}}{D_{in}} \times 100\,. \tag{4}$$

According to the experimental data adopted from (Medrano-Gracia et al., 2017), the outer diameters of the inlet and outlet are chosen as 4.9 mm and 4.1 mm, respectively. The thickness of each layer (Haddad & Samani, 2017) is set to 0.23 mm, 0.31 mm, and 0.34 mm, for intima, media, and adventitia, respectively (Holzapfel, Sommer, Gasser, & Regitnig, 2005). The length of the artery for each curve in the x direction is set to 10 mm. Other coordinates for the central curve of the artery are obtained based on the normalised curvatures. $\theta_{LAD} = 47.0°$ and $\theta_{LCx} = 46.8°$ (adopted from Medrano-Gracia et al., 2017) are angles of LAD and LCx (Fig. 3), respectively. The thickness of 0.1 mm for fibrous cap and stenosis percentage of 45 are used throughout, unless otherwise mentioned.

2.1. Artery wall and plaque material properties

According to the experimental data obtained from in-vitro testing of different layers of coronary artery given (Holzapfel et al., 2005), a strong nonlinear material behaviour has been observed (the soft material shows exponential stiffening in the presence of large loadings). In order to address this matter, a nonlinear continuum mechanics model of hyperelasticity (Mooney-Rivlin 5-parameter) is used since the system is macroscale, the size effects have been neglected (Ghayesh & Farokhi, 2015; Gholipour et al., 2015; Ghayesh et al., 2013; Ghayesh et al., 2014; Ghayesh & Farokhi, 2015; Farokhi & Ghayesh, 2015; Ghayesh et al., 2013; Ghayesh et al., 2013; Ghayesh, 2018; Ghayesh, 2018). The reason for selecting this model of hyperelasticity over others is that the Mooney-Rivlin 5-parameter model fits well with the experimental data. The material properties of the layers (Tricerri et al., 2016) of a coronary artery have been obtained experimentally in Ref. (Holzapfel et al., 2005); they are adopted for the developed model of this paper. The material properties of the plaques are taken to be the same as those of the intima layer; the properties of the lipid inside the plaques are adopted from Ref. Versluis, Bank, and Douglas (2006). The mass density of all the layers as well as the plaques and lipid are set to 1000 kg/m^3 (Chan, Ding, & Tu, 2007). The hyperelasticity (Bhattacharyya, Sarangi, & Samantaray, 2015; Chebbi, Wali, & Dammak, 2016; Gizzi, Vasta, & Pandolfi, 2014) scheme of Mooney-Rivlin was selected in which because of macro size of the system small size effects (Farokhi & Ghayesh, 2015; Farokhi, Ghayesh, & Amabili, 2013; Farokhi, Ghayesh, Gholipour, & Hussain, 2017; Ghayesh, Farokhi, & Alici, 2016; Ghayesh, Farokhi, & Gholipour, 2017) have been ignored. The material behaviour of the intima, media, adventitia, plaque and lipid are modelled via

$$W = \left(\bar{I}_1 - 3\right)^2 c_{20} + \left(\bar{I}_1 - 3\right)\left(\bar{I}_2 - 3\right) c_{11} + \left(\bar{I}_2 - 3\right)^2 c_{02} + \left(-3 + \bar{I}_1\right) c_{10} + \left(-3 + \bar{I}_2\right) c_{01} + (-1 + J)^2 \frac{1}{d}, \tag{5}$$

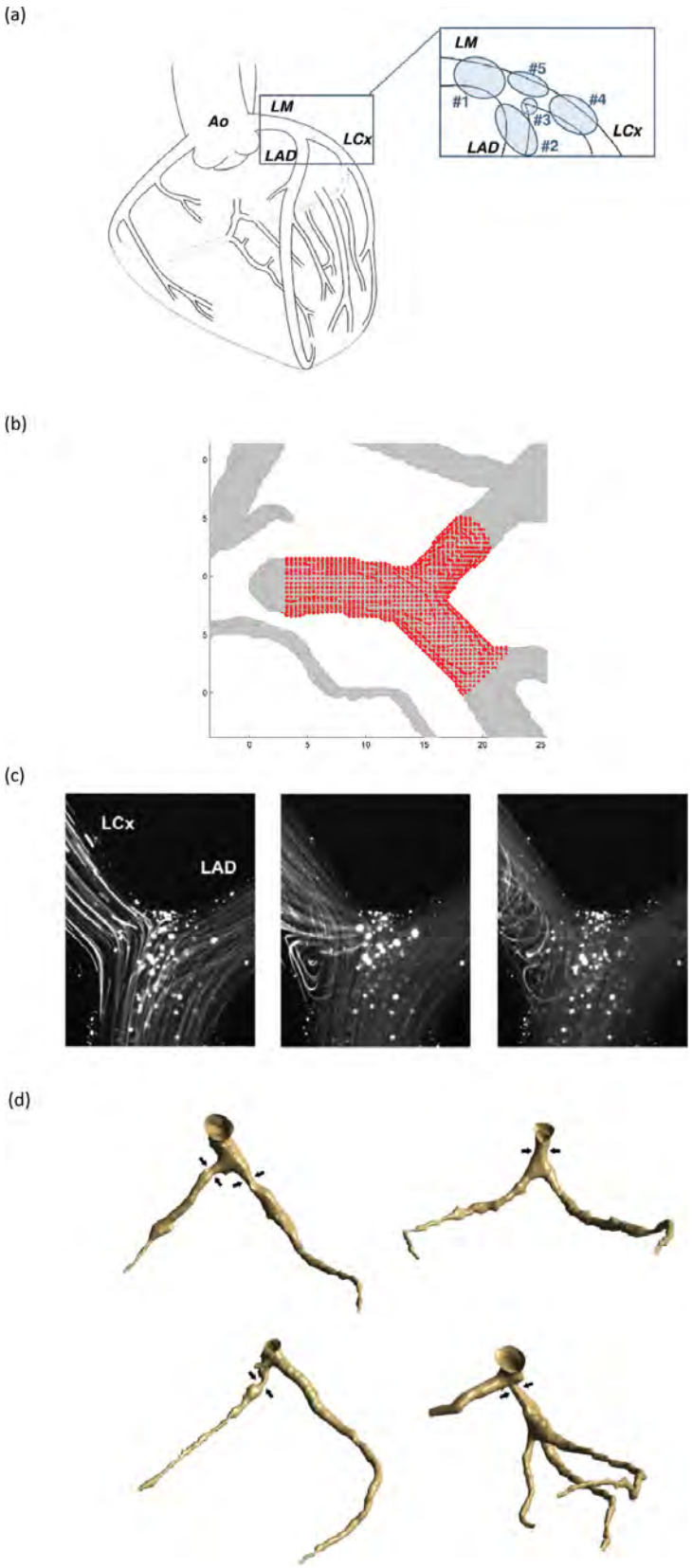

Fig. 1. (a) Plaque sites in the left main coronary bifurcation (Payan & Ohayon, 2017); (b) results from experimental data of bifurcation shape (Medrano-Gracia et al., 2017); (c) flow patterns in the real bifurcation region (Doutel et al., 2018); (d) left coronary models with bifurcation stenosis (Chaichana et al., 2013).

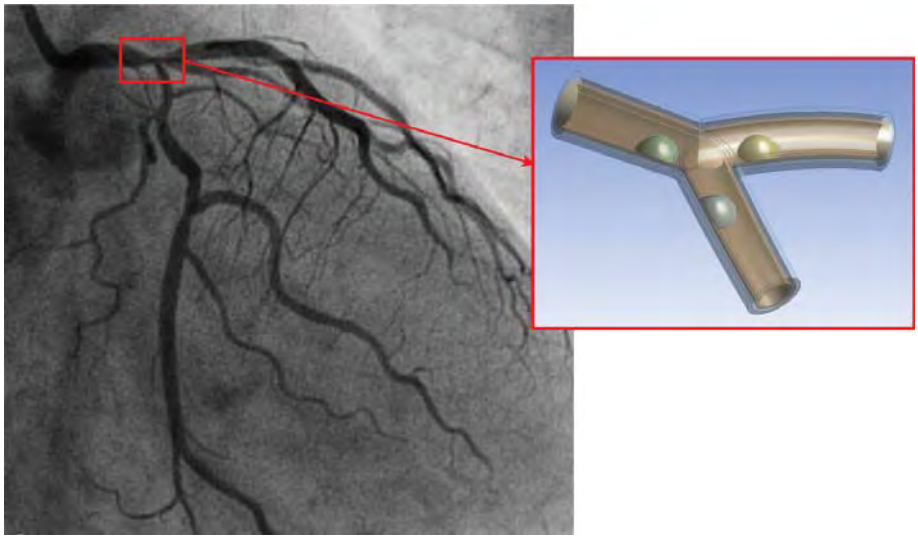

Fig. 2. High level of stenosis at left coronary artery main bifurcation (Kim et al., 2013) and schematic of the extracted geometry.

in which W shows the strain energy; J presents the elastic deformation determinant; d denotes the parameter of material incompressibility; $\bar{I}_1$ is the first deviatoric strain invariant and $\bar{I}_2$ represents the second deviatoric strain invariant; c_{10}, c_{01}, c_{11}, c_{20}, and c_{02} are five material constants (Gholipour et al., 2018).

Another characteristic of the solid phase of the problem is viscoelasticity (Attia & Rahman, 2018; Fallah, Ahmadian, & Aghdam, 2017; Ghayesh, Farokhi, & Hussain, 2016; Hashemi, 2016; Khaniki & Hosseini-Hashemi, 2017) which has been considered by following formulation

$$\sigma = \int_0^t 2G(t-\tau)\frac{de}{d\tau}d\tau + I\int_0^t K(t-\tau)\frac{d\Delta}{d\tau}d\tau, \tag{6}$$

where σ denotes the Cauchy stress, $G(t)$ represents time dependent Prony series shear, t represents time, $K(t)$ represents time dependent Prony series bulk-relaxation moduli, and other parameters are: volumetric strain (Δ), deviatoric strain (e), identity tensor (I). As a result, viscoelasticity is modelled by a five-term relaxation model in ANSYS; the material coefficients of Prony series shear relaxation 5-term model (Gholipour et al., 2018) are used for all of the solid parts of the atherosclerotic artery. In order to define the time dependent nature of $G(t)$ and $K(t)$, the following equations are used

$$G(t) = G_0\left[\alpha_\infty^G + \sum_{i=1}^{n_G}\alpha_i^G \exp\left(-\frac{t}{\tau_i^G}\right)\right], \tag{7}$$

$$K(t) = K_0\left[\alpha_\infty^K + \sum_{i=1}^{n_K}\alpha_i^K \exp\left(-\frac{t}{\tau_i^K}\right)\right], \tag{8}$$

where ${\alpha_i}^G$ and ${\alpha_i}^K$ denote the relative moduli; ${\tau_i}^G$ and ${\tau_i}^k$ are the relaxation time; at $t=0$ G_0 and K_0 represent the relaxation moduli; n_K and n_G define the Prony terms number.

2.2. Heart motion simulation

In order to incorporate the 3D motion of heart, the displacement based on sine waves is assigned to the inlet surface of the all three layers of the artery according to the experimental data in Yang, Liu, Zheng, and Liu (2017), where

$$\begin{Bmatrix} x \\ y \\ z \end{Bmatrix} = \begin{Bmatrix} 0.08\sin(2\pi t/0.8) \\ 0.08\sin(2\pi t/0.8) \\ 0.20\sin(2\pi t/0.8) \end{Bmatrix} \text{mm}, \tag{9}$$

where t is time. The displacement applied to the two outlets are

$$\begin{Bmatrix} x \\ y \\ z \end{Bmatrix} = \begin{Bmatrix} 0.15\sin(2\pi t/0.8) \\ 0.15\sin(2\pi t/0.8) \\ 0.40\sin(2\pi t/0.8) \end{Bmatrix} \text{mm}. \tag{10}$$

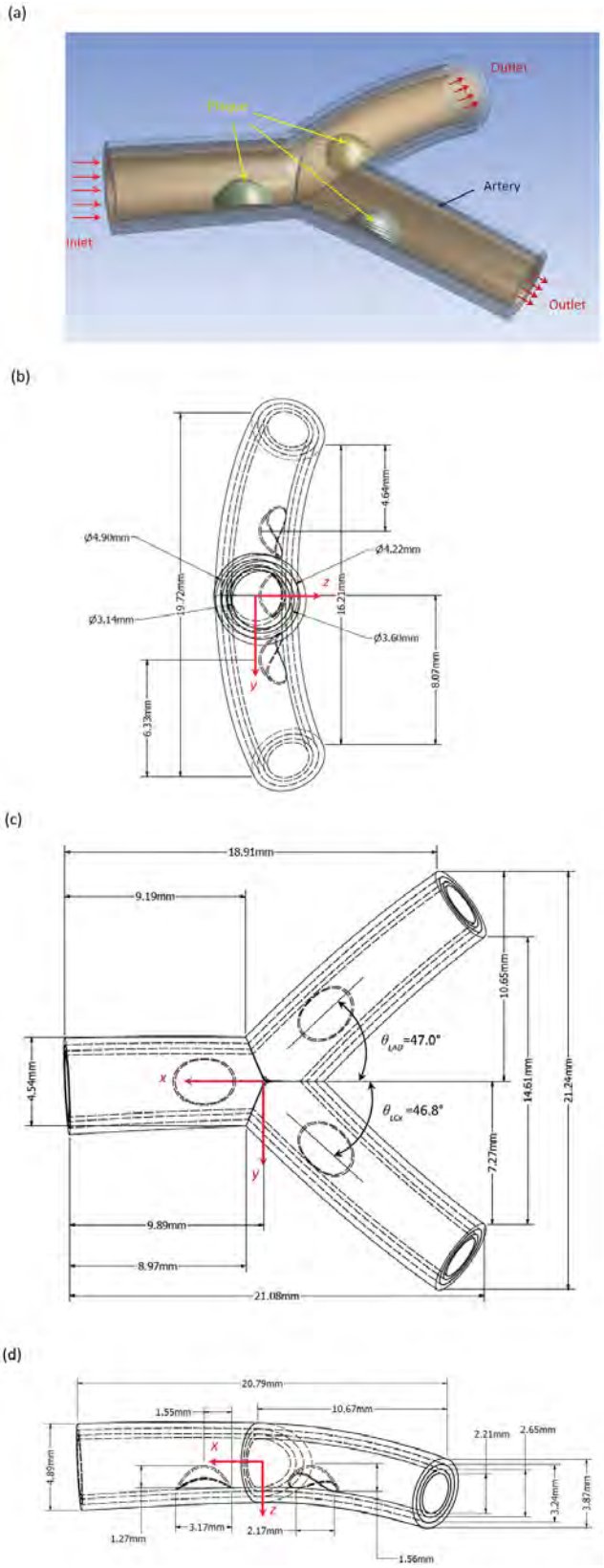

Fig. 3. Artery and plaque model: (a) 3D bifurcated atherosclerotic model with plaque, artery, inlet, and outlet; (b) front view with dimensions; (c) bottom view with dimensions; (d) transverse view with dimensions.

2.3. Contraction of media layer

The media layer of the artery is the muscular layer which pushes the blood. This time-dependent active contraction here as a pressure wave moves in the longitudinal direction of the artery, and is modelled as

$$P = 200\sin(2\pi x/0.02 - t)\text{Pa}, \tag{11}$$

with P being the pressure; x is the longitudinal direction in the LM artery.

2.4. Plaque micro-calcification

The stress concentration in the vicinity of the micro calcification inside the fibrous cap could initiate the rupture process (Maldonado et al., 2012). This is incorporated by modelling different numbers of calcium spheres inside the thickness of the plaque; the radius of 0.02 mm has been set to each sphere.

2.5. Blood characteristics

A non-Newtonian (Janela, Moura, & Sequeira, 2010; Perkowska, Piccolroaz, Wrobel, & Mishuris, 2017), turbulent, and incompressible regime for the blood (Wu, Aubry, Massoudi, & Antaki, 2017) flow is considered. The turbulent model is incorporated to the rotational flow around the asymmetrical plaques. For non-Newtonian flow modelling Carreau constitutive law is used which is given by

$$\eta = \eta_\infty + (-\eta_\infty + \eta_0)\left[\dot{\gamma}^2\lambda^2 + 1\right]^{\frac{-1+n}{2}}, \tag{12}$$

where η denotes the viscosity of the fluid, $\eta_0 = 0.0560$ represents zero shear viscosity, $\eta_\infty = 0.0035$ is infinity shear viscosity, $\dot{\gamma}$ represents the strain rate, $\lambda = 3.3129$ is a time constant, $n = 0.3568$ is the power-law index, and blood density of 1050 kg/m^3 (Cilla, Borrás, Pena, Martínez, & Malve, 2015).

2.6. Physiological blood pulsation

The blood pulsation is incorporated via a time-dependent velocity experimental data for left coronary artery given in Chabi, Champmartin, Sarraf, and Noguera (2015) to investigate the stress field on the artery and plaque (Kachanov & Abedian, 2015; Mandal, Mukhopadhyay, & Layek, 2012; Taelman, Degroote, Swillens, Vierendeels, & Segers, 2014).

3. Numerical integration technique

The 3D asymmetric atherosclerotic bifurcated artery is simulated in ANSYS by means of FEM and finite volume method (FVM) applying fully coupled fluid-solid interaction (FSI).

In order to model the FSI part for the plaque, the outer surface of the plaque which is in contact with the fluid is considered as a FSI surface in Transient Structural mode; the interface of the fluid with the plaque is modelled as a FSI surface in Fluent. In the FSI solution process, a dynamic mesh with remeshing capabilities is employed to model the deformation and interaction between the solid and fluid parts.

For the entire model, involving the three plaques and the coronary artery branches, convergence of the solutions is examined for Transient Structural and Fluid Flow (Fluent). Due to the complex geometry, hexahedral and tetrahedral elements are selected. The system is modelled for $\Delta t = 0.8$ seconds (one heart beat) with the time-step of 0.004 seconds.

4. Results for blood velocity and stress fields

Shown in Fig. 4 is the blood speed variations over one heart-beat period. Panel (a) shows the velocity variation with time for a single heart beat period for the point of maximum velocity (panel (b)). 0.62 m/s is the peak velocity which occurs at $t = 0.42$ s. In each of the branches (LM, LAD, and LCx), the blood flow speed is the largest at an area directly above the plaque, with LM having the largest blood flow speed of all.

Fig. 5 shows the time varying WSS at different locations of the atherosclerotic artery. As seen, the plaque in the left main (LM) artery is subject to the highest WSS compared to the plaques in LAD and LCx and even on the wall of the artery. All the stresses shown in panel (a) have the same time-variation trend. For each branch, the WSS is locally maximum in the vicinity of the plaque with the LM artery having the largest values. Hence, the initiation of plaque rupture (and hence heart attack) is very likely to occur in the LM artery.

The fluid pressure variation on different branches of the bifurcated atherosclerotic artery is depicted in Fig. 6. Depicted in panel (b), the pressure on the wall of the LM artery is maximum. The pressure varies with similar time-pattern of the inlet blood velocity. Due to the viscosity, a pressure drop is observed from upstream to downstream. Moreover, the pressure on the LCx and LAD plaques vary almost the same with time.

In order to examine the von Mises stress (VMS) in the artery, different sections of the diseased artery are selected, presented in panel (b) of Fig. 7; the FEM analysis has been conducted for the entire system and the cross-sections of interest

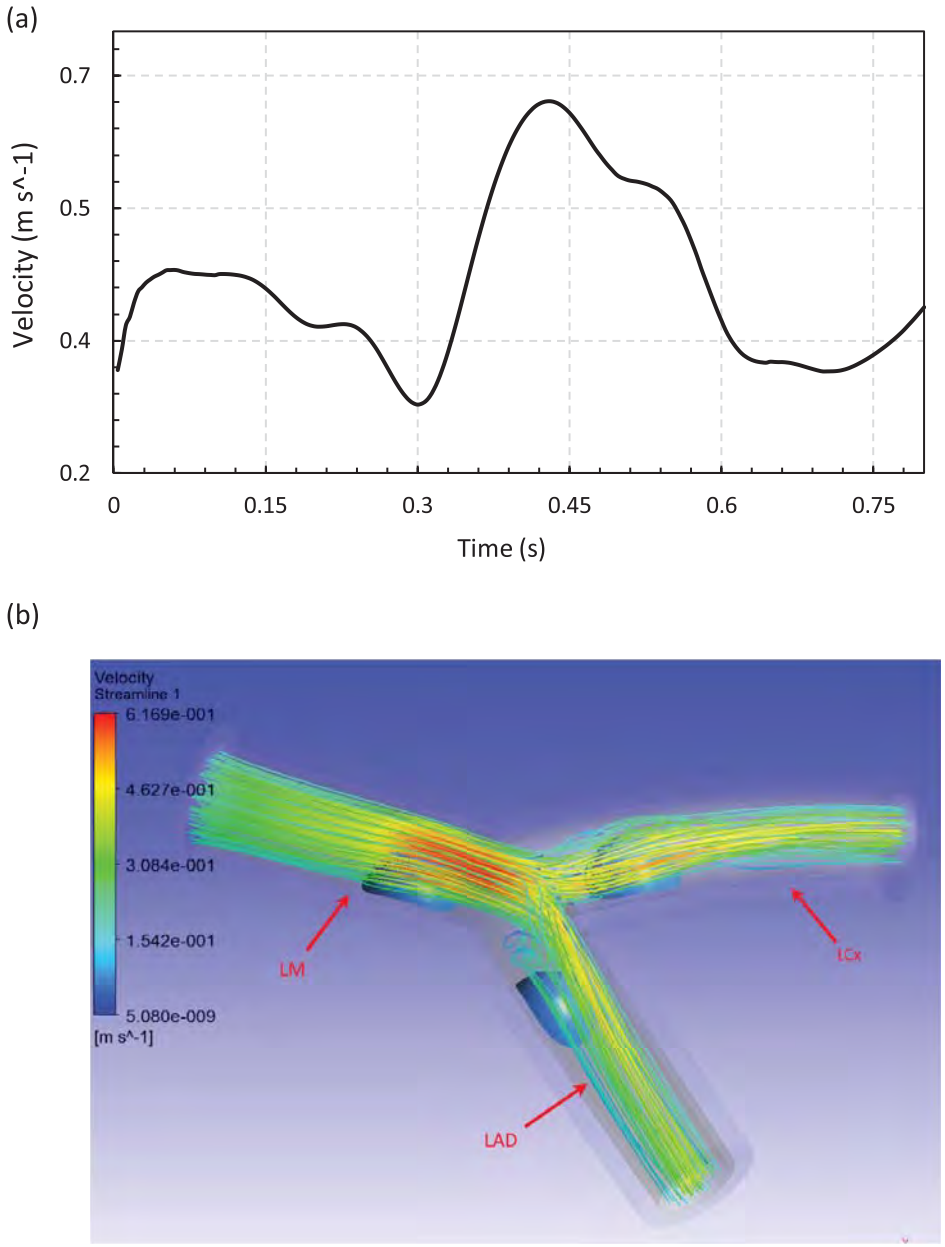

Fig. 4. (a) Time varying velocity of bifurcated artery with three plaques present and (b) the velocity spatial distribution (0.42 s) (the location of maximum velocity is $[x, y, z] = [2.3, 0.2, -0.3]$mm).

are shown. These sections comprise different parallel YZ planes at different x distances from the origin (see Fig. 3). The most vulnerable regions (on the plaques and the walls) are the intima layer of artery at $x = -3$ mm and $x = 7$ mm (Sections A and B, respectively); the first one (section A) corresponds to $x = -3$ mm and the second one (Section B) is for $x = 7$ mm. Regarding the max of the VMS at these locations (panel (b) of Fig. 7) the possibility of a dissection at $x = 7$ mm for the artery and the possibility of rupture at the shoulder area of the plaque at $x = -3$ mm are the highest.

As reported by experiments in Richardson, Davies, and Born (1989), the plaque shoulder (i.e. the intersection of the outer surface of the plaque and the artery wall) is one of the most vulnerable parts. In order to show the variation of both the WSS and VMS at the shoulder, a curvilinear coordinate of S_{index} is defined where the subscript "index" denotes the artery branch (Fig. 8); the origin of this coordinate is placed at the origin of the model (see Fig. 3) for LM, LAD, and LCx, respectively (panel (a)). Panel (b) illustrates the non-dimensionalised stress field variations for the LM artery where there are some regions at which both the WSS and VMS are large; both the stresses are maximum in the middle area of the LM plaque shoulder—this area is prone to rupture. The counterparts for the LCx and LAD are illustrated in panels (c) and (d), respectively. As seen, the maximum values are again almost in the middle region. In conclusion, the middle region of plaque shoulders are the most vulnerable for rupture.

Fig. 9 illustrates the time variation of the maximum of WSS and VMS for different stenosis levels common to each of the three plaques (panels (a)-(c)). As seen in panel (d), an increasing stenosis level increases the maximum value of the WSS

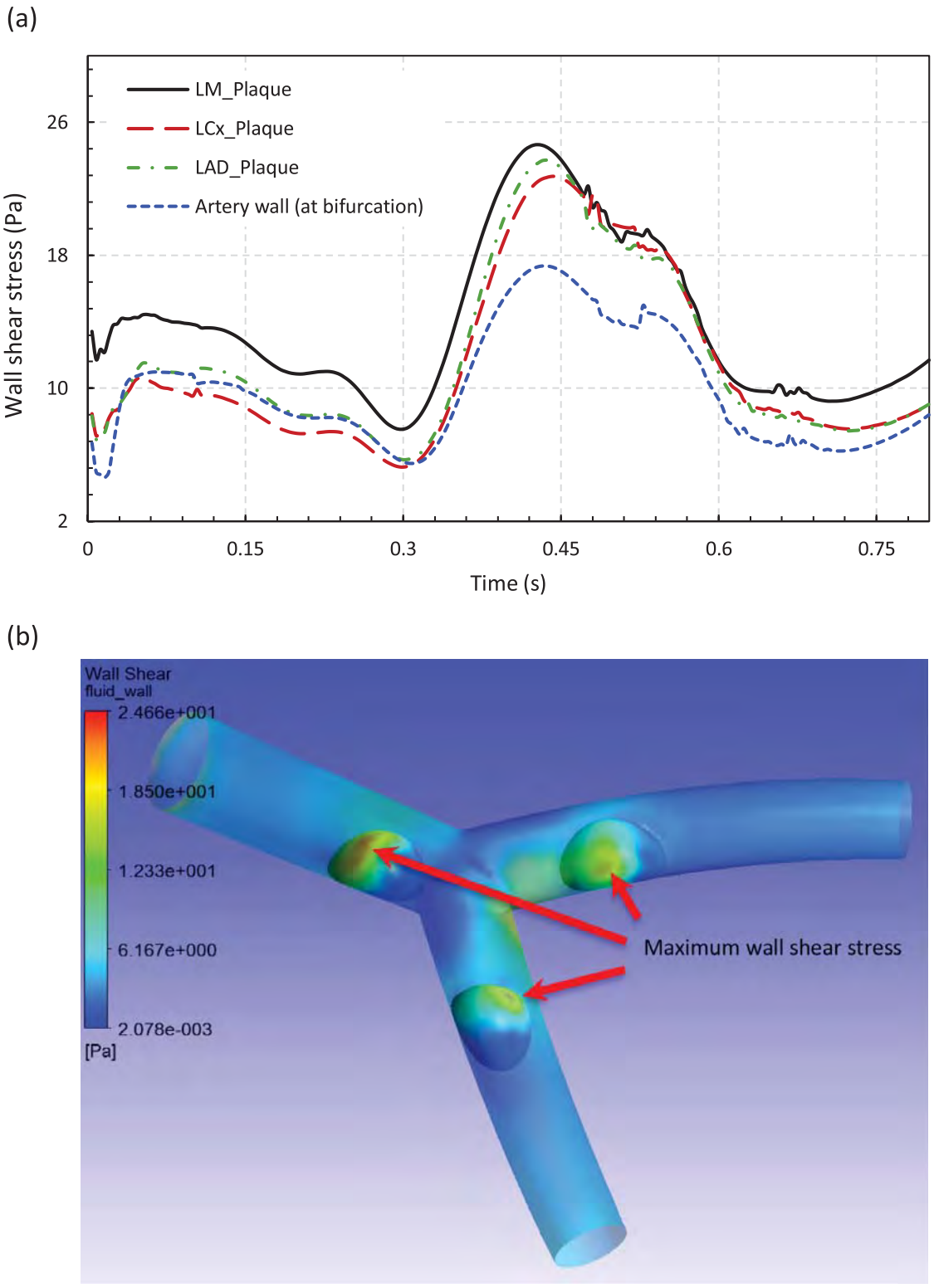

Fig. 5. (a) Time varying WSS of bifurcated artery with three plaques present and (b) the WSS spatial distribution (0.42 s) (the location of maximum WSS is $[x, y, z] = [3.4, 0.1, 0.2]$mm at LM plaque).

on the atherosclerotic plaque, however, the time-variation trend is almost similar for all the stenosis levels. Moreover, the largest value of the WSS happens in the case of 55% stenosis at $t = 0.42$ (s). Panel (e) shows that the time-variation trend of the von-Mises stresses is different from one to another; the maximum value corresponds to the stenosis of 55% at $t = 0.21$ (s). In conclusion, plaque growth in this range of stenosis level increases the risk of plaque rupture.

The bifurcated arteries in the presence of different plaque(s) are presented in Fig. 10 (panels (a)-(d)), where in (a) there is one plaque in the LAD artery; (b) two plaques, one in the LAD and one in the LCx arteries; (c) three plaques, one in each of the branches; (d) two plaques, one in the LM and one in the LAD arteries. Panel (e) shows the variations of the maximum

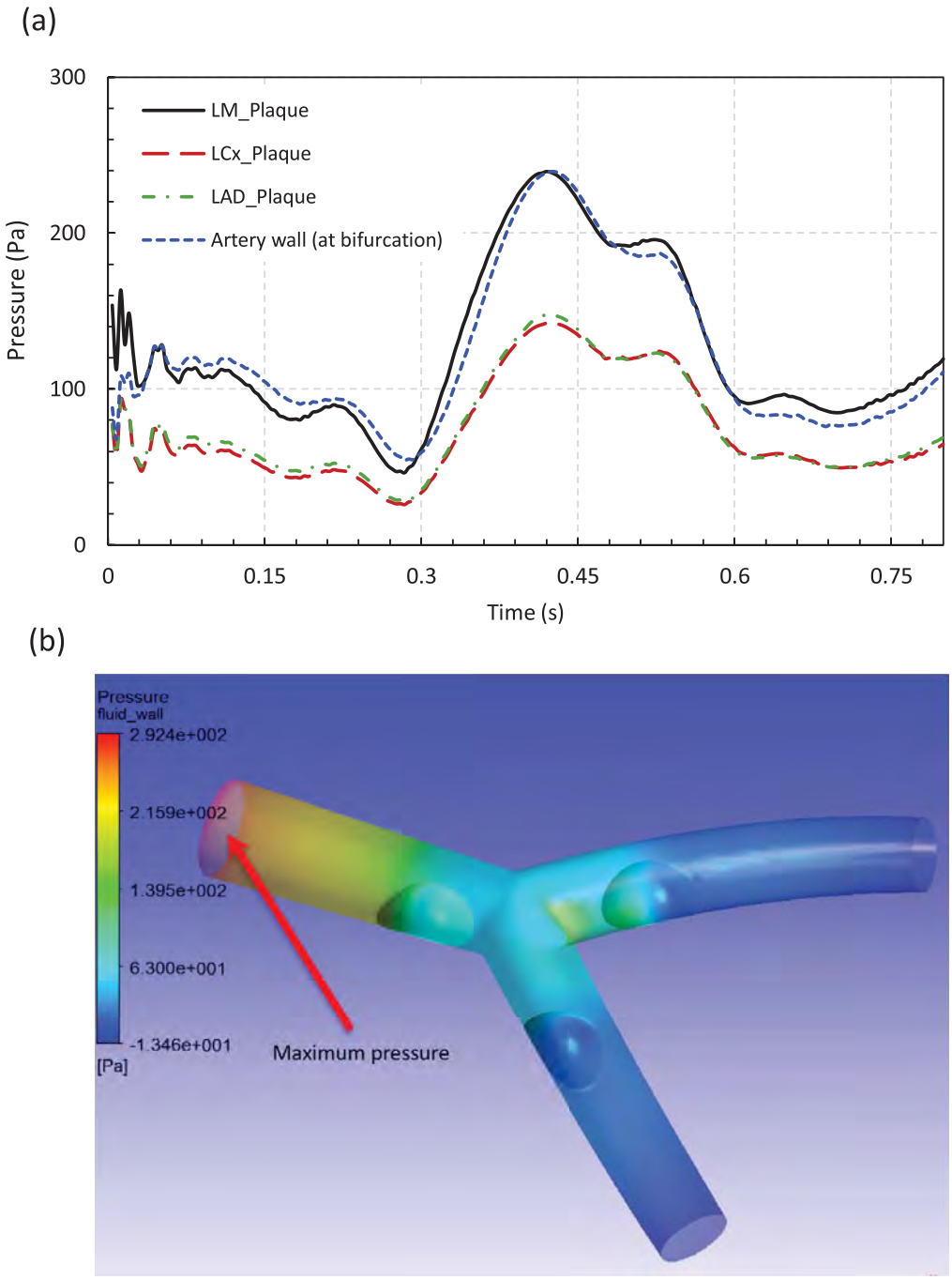

Fig. 6. (a) Time varying pressure of bifurcated artery with three plaques present and (b) the pressure spatial distribution at (0.42 s) (the location of maximum pressure is $[x, y, z] = [10.0, -0.9, -0.9]$mm).

value of the WSS on the surface of the LAD plaque for all four cases of panels (a)-(d); as seen, cases 1–4 possess almost similar trends. The presence of the LM plaque (Case 3) makes the WSS on the LAD plaque jump to the maximum value. The VMS counterparts are shown in panel (f) which show slight variations for the VMS at the maximum value.

As an important feature of the plaque, the fibrous cap thickness could contribute quite extensively in the rupture process. By reducing the thickness of fibrous cap from 0.10 mm to 0.02 mm (panels (a)–(c) of Fig. 11), the VMS increases around 36% (at $t = 0.42$ (s)) which shows the critical role of the fibrous cap in the plaque rupture (panel (e)); panel (d) highlights that the WSS is almost independent of the cap thickness value.

Fig. 12 demonstrates the effect of different plaque shoulder lengths (3.17; 4.17; 5.17; 6.17 mm; see panels (a)–(d), respectively) on the time-varying WSS and VMS; the length of the plaque is considered to be the same for all three plaques. As illustrated in panel (e) the highest WSS on the plaque occurs for the smallest shoulder length. Likewise, the largest VMS takes place for the plaque with the smallest shoulder length. Since the material failure inside the plaque is mainly related to the maximum VMS and the plaque wall failure is mainly due to the WSS, a smaller shoulder length means a higher risk of plaque rupture.

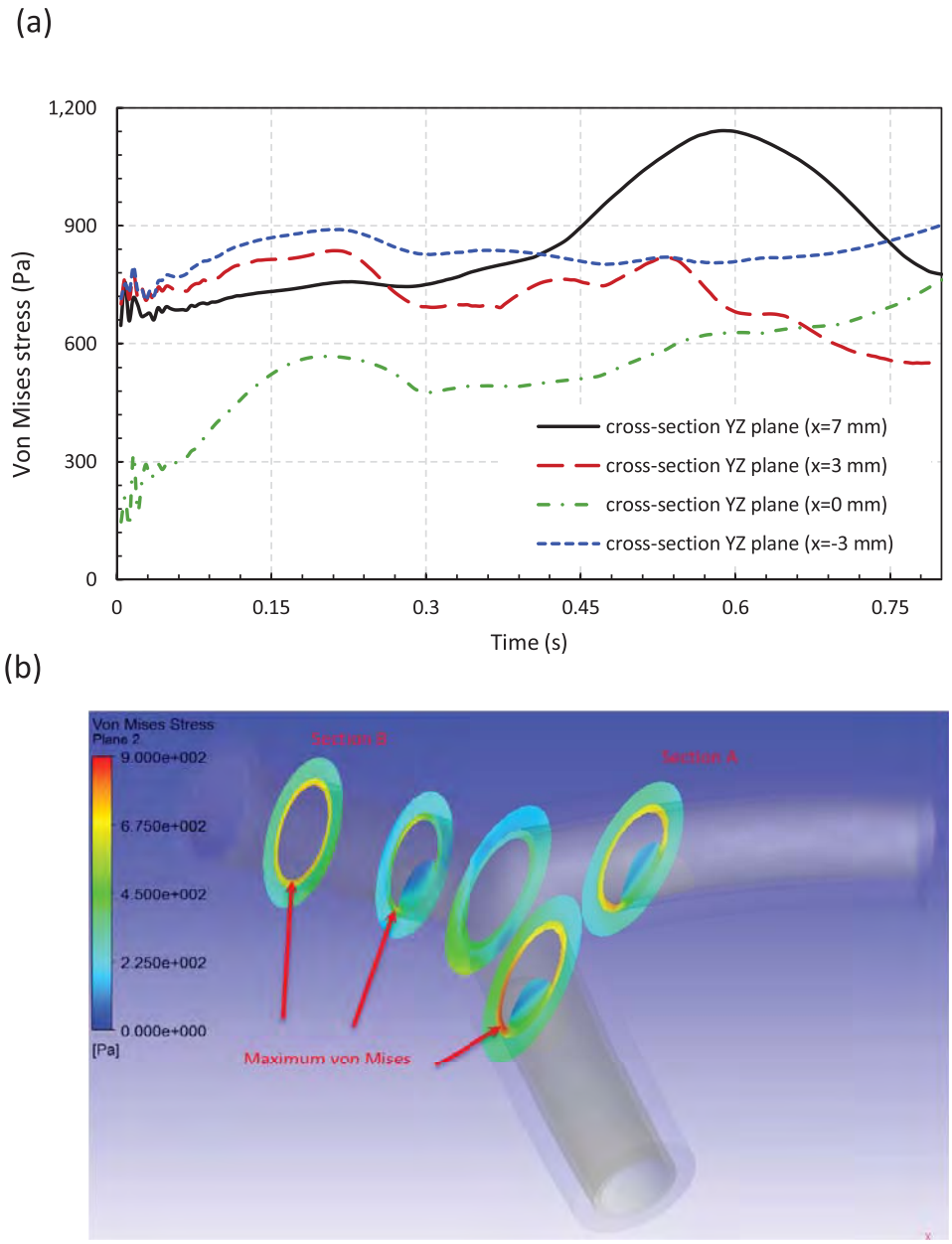

Fig. 7. (a) Time varying VMS of bifurcated artery with three plaques present for various YZ cross-sections and (b) the VMS spatial distribution (0.21 s) for various YZ cross-sections.

The effect of different curvatures of the bifurcated artery (for LAD and LCx branches) on the stress field has been highlighted in Fig. 13. In this comparison, three cases of curvatures, namely Curve 1: flat, Curve 2: slightly curved, and Curve 3: highly curved bifurcated arteries, are considered with the radii (in the XZ plane) of curvatures of ∞, 29.1 mm, and 8.0 mm, respectively. Both WSS and VMS for Curve 3 are maximum between the cases. As a result, the curvature of the bifurcated artery affects the stress distribution inside the plaque and stress distribution on the surface.

According to Ref. Movahed et al. (2008), it is possible for the artery to be calcified and obstructed due to the calcium deposition. In order to model this, three cases of calcified arteries are considered, as shown in Fig. 14; Case 1 with two calcified plaques in LAD and LCx; Case 2 with two plaques made of calcium in LM and LAD; and Case 3 with three plaques made of calcium in the LM, LAD, and LCx branches. As shown in panel (d), the WSS in the calcified artery the Case 3, which has three calcium plaques (in LM, LAD, and LCx), is maximum. In the VMS analysis, the calcified artery Case 3, which has calcium deposition in all branches, has the maximum value.

The angle θ between the LM and LAD arteries is kept constant at 133° and the effect of varying ψ (the angle between the LM and LCx arteries) on the stress field is studied; the results are plotted in Fig. 15. As seen in panel (d), the WSS does not change significantly, however, the largest VMS occurs for $\psi = 127°$.

Micro-calcification, an important factor in plaque rupture, is considered in Fig. 16 which shows results with and without micro-calcification present (seen as 5 spheres in panel (b)). The micro-calcification does not influence the WSS (panel (c)); nonetheless, it increases the VMS to nearly three times larger than that without the micro-calcification.

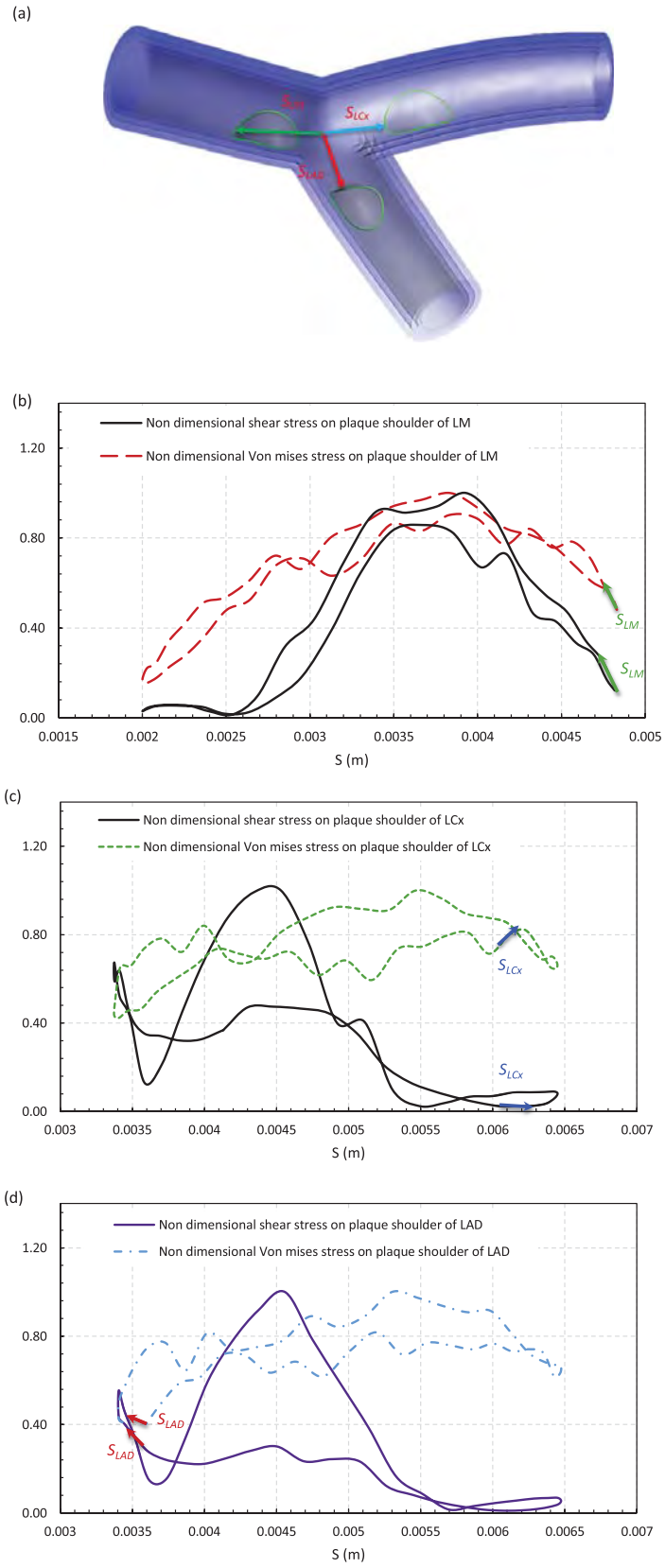

Fig. 8. Comparison of non-dimensional WSS and VMS (normalised to the max stress value of each case) on the plaque shoulder with respect to the curvilinear distance from the coordinate system for (b) LM coronary artery; (c) LCx coronary artery; (d) LAD coronary artery.

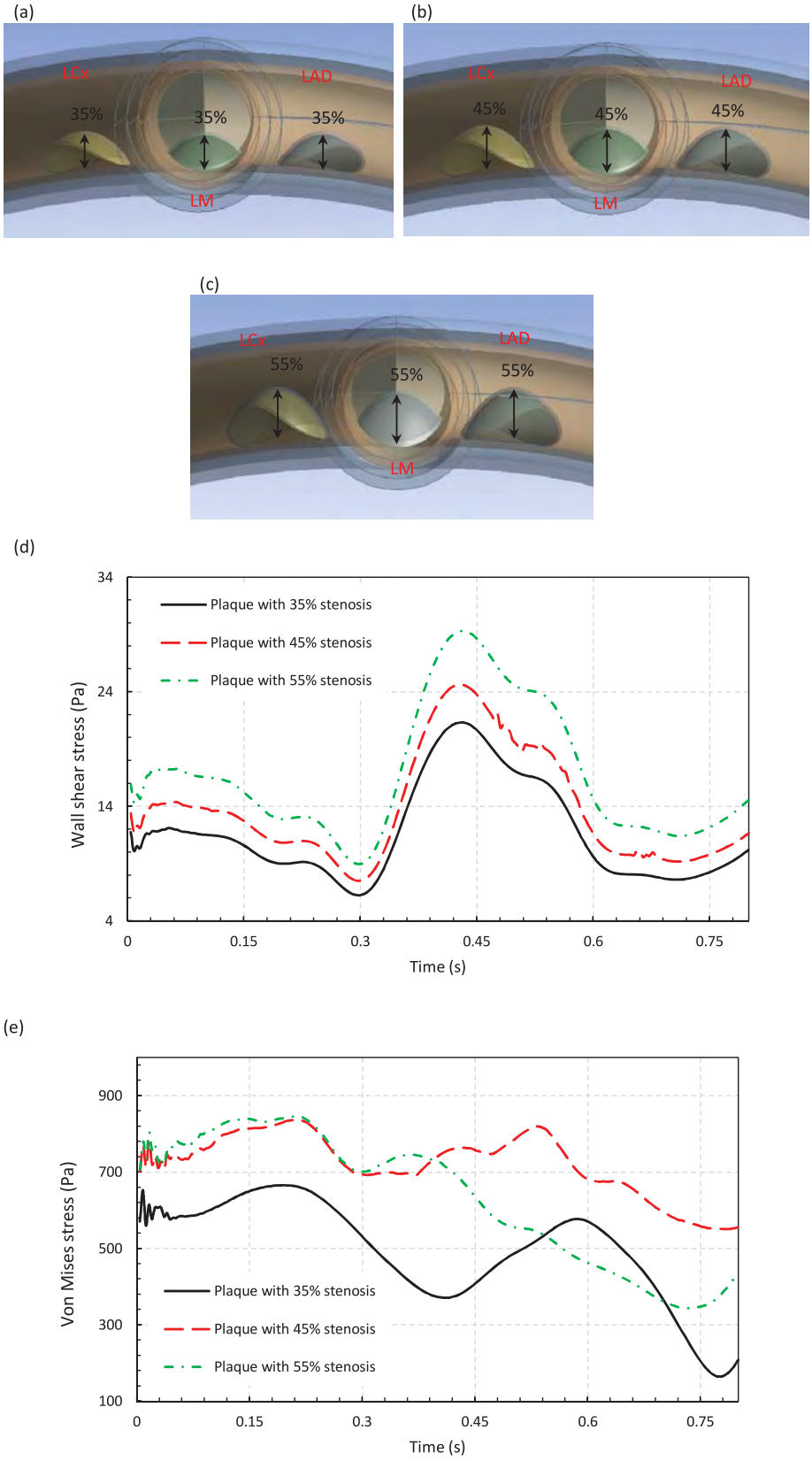

Fig. 9. Effects of various stenosis level on the bifurcated diseased artery: (a) stenosis of 35%; (b) stenosis of 45%; (c) stenosis of 55%; (d) WSS on LM plaque; (e) VMS at LM plaque.

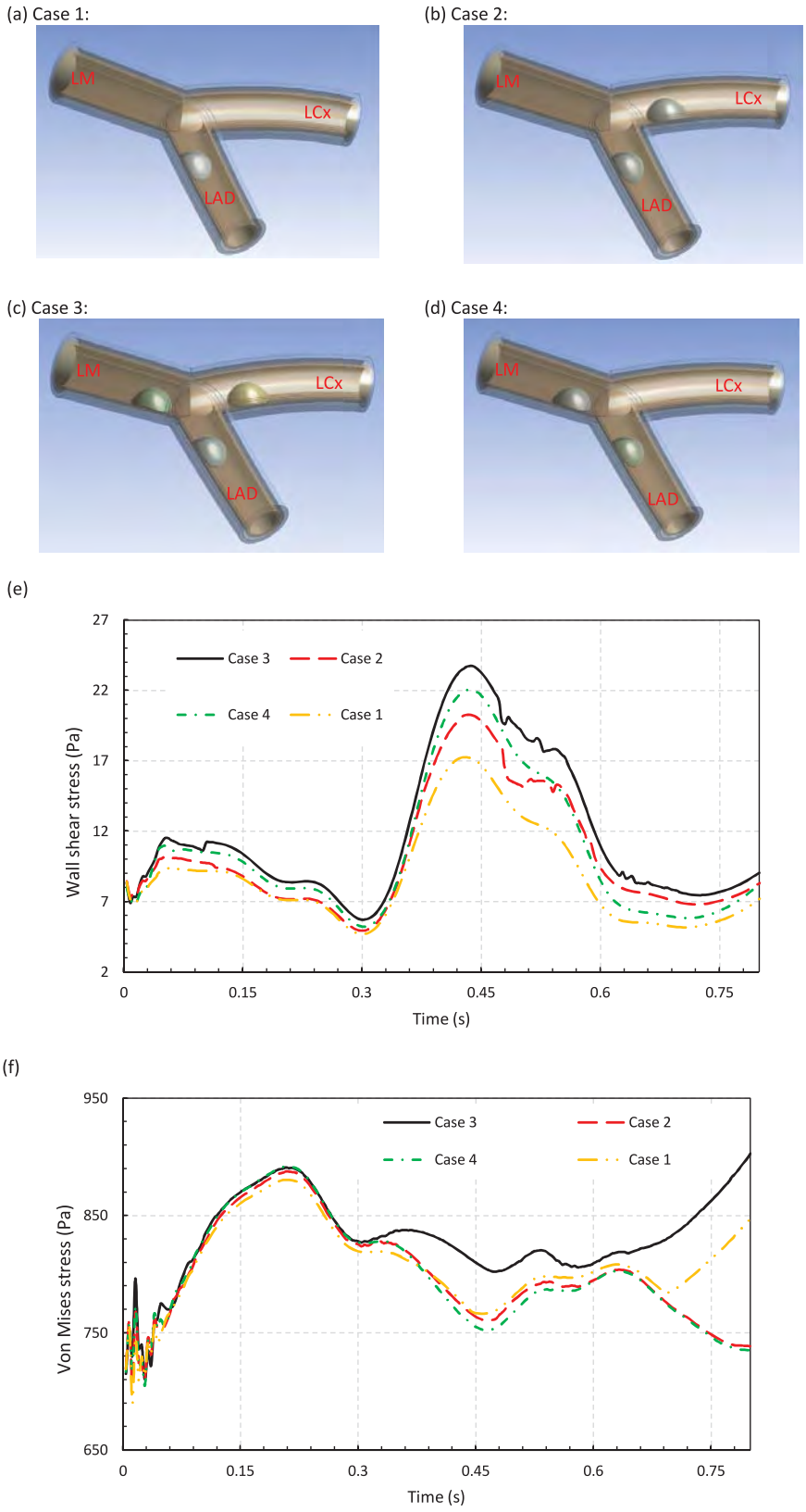

Fig. 10. Effects of plaque presence in each branch (cases 1 to 4) on the stress field: (a) Case 1; (b) Case 2; (c) Case 3; (d) Case 4; (e) WSS on LAD plaque; (f) VMS at LAD plaque.

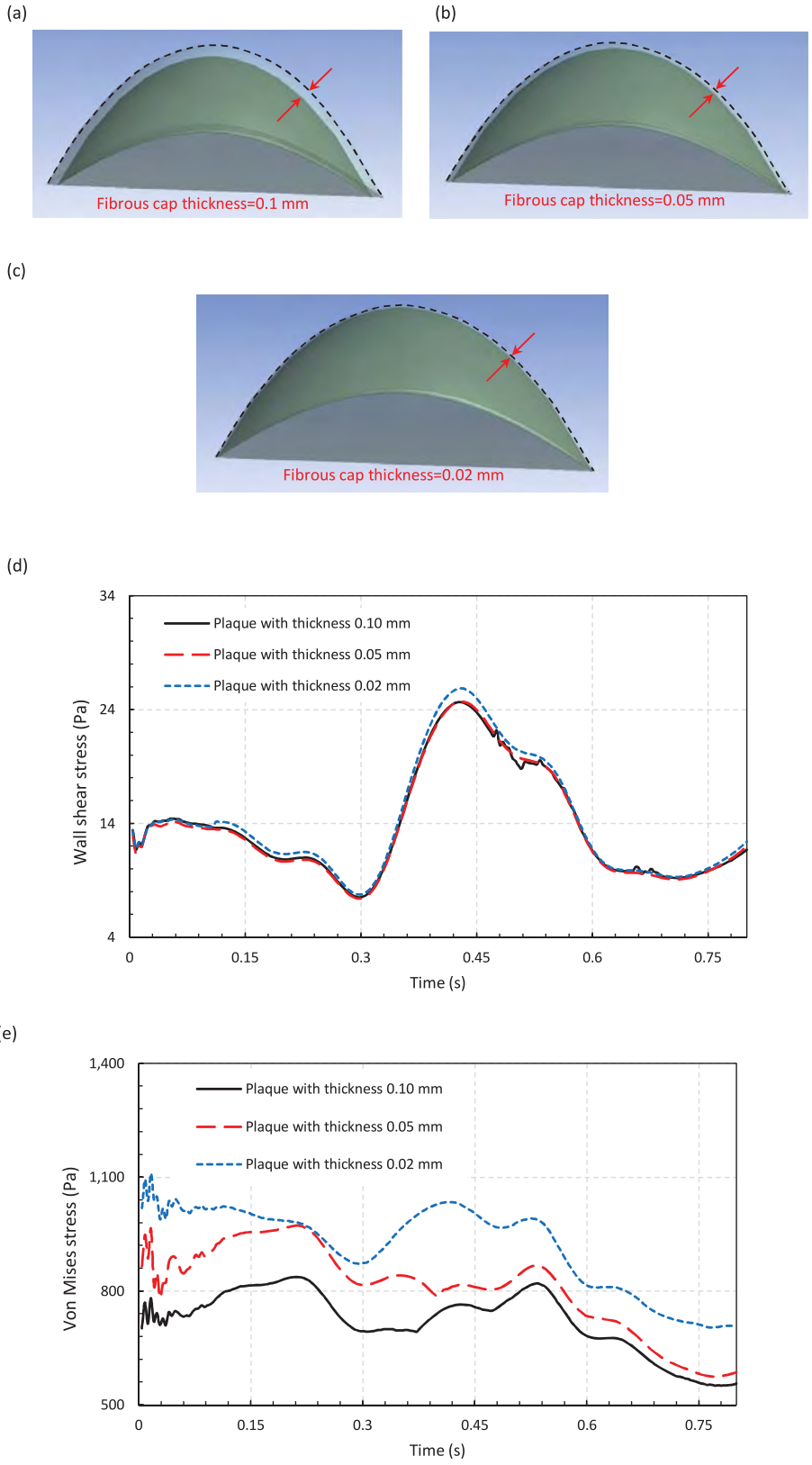

Fig. 11. Effects of different plaque fibrous cap thicknesses: (a) thickness of 0.10 mm for fibrous cap; (b) thickness of 0.05 mm for fibrous cap; (c) thickness of 0.02 mm for fibrous cap; (d) WSS on LM plaque; (e) VMS at LM plaque.

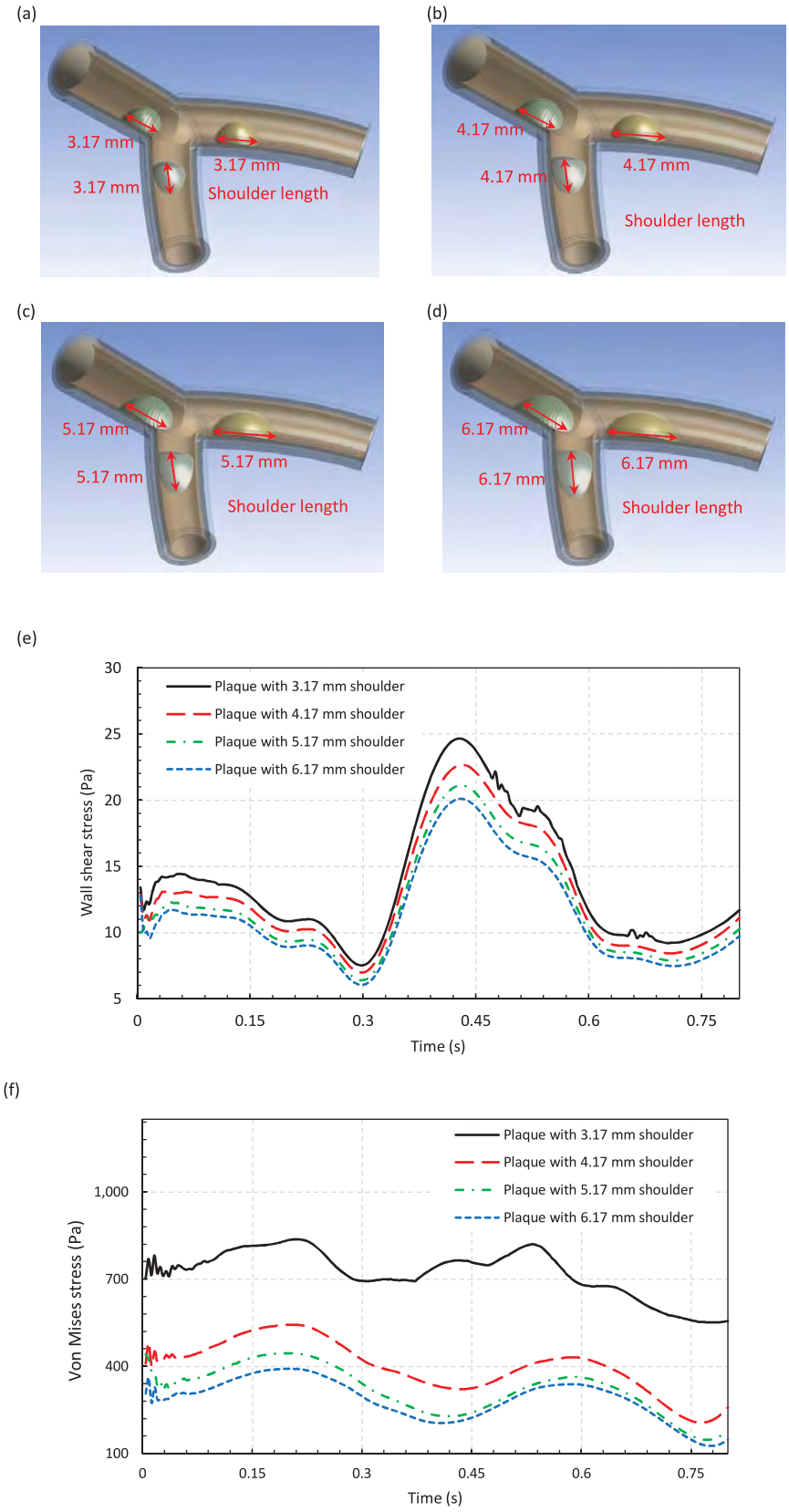

Fig. 12. Effects of various shoulder lengths on the bifurcated atherosclerotic artery stress field: (a) shoulder length of 3.17 mm; (b) shoulder length of 4.17 mm; (c) shoulder length of 5.17 mm; (d) shoulder length of 6.17 mm; (e) WSS on LM plaque; (f) VMS at LM plaque.

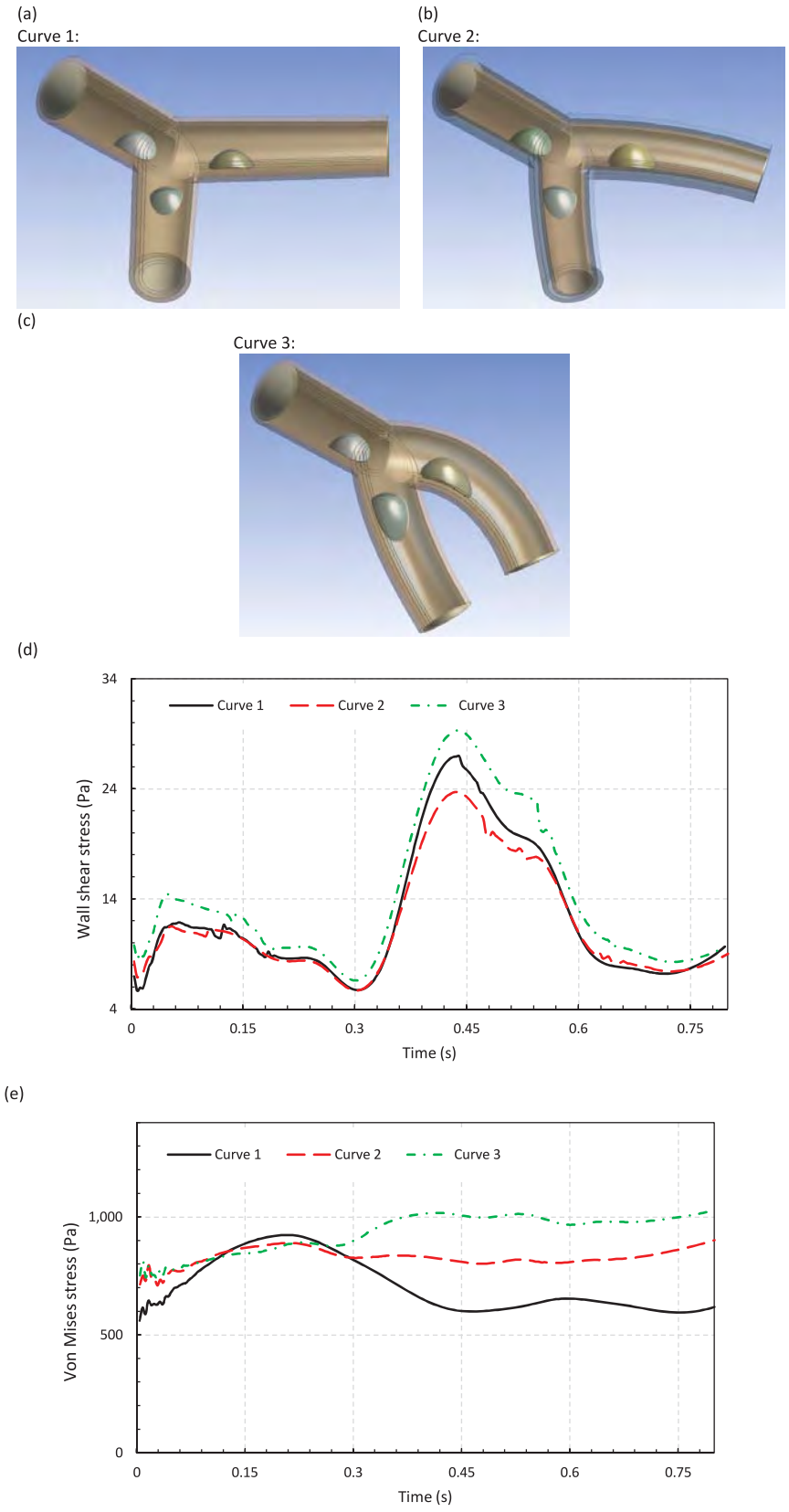

Fig. 13. Effects of curvature on the stress field in a bifurcated atherosclerotic artery: (a) Curvature 1 (∞); (b) Curvature 2 (29.1 mm); (c) Curvature 3 (8.0 mm); (d) WSS on LAD plaque; (e) VMS at LAD plaque.

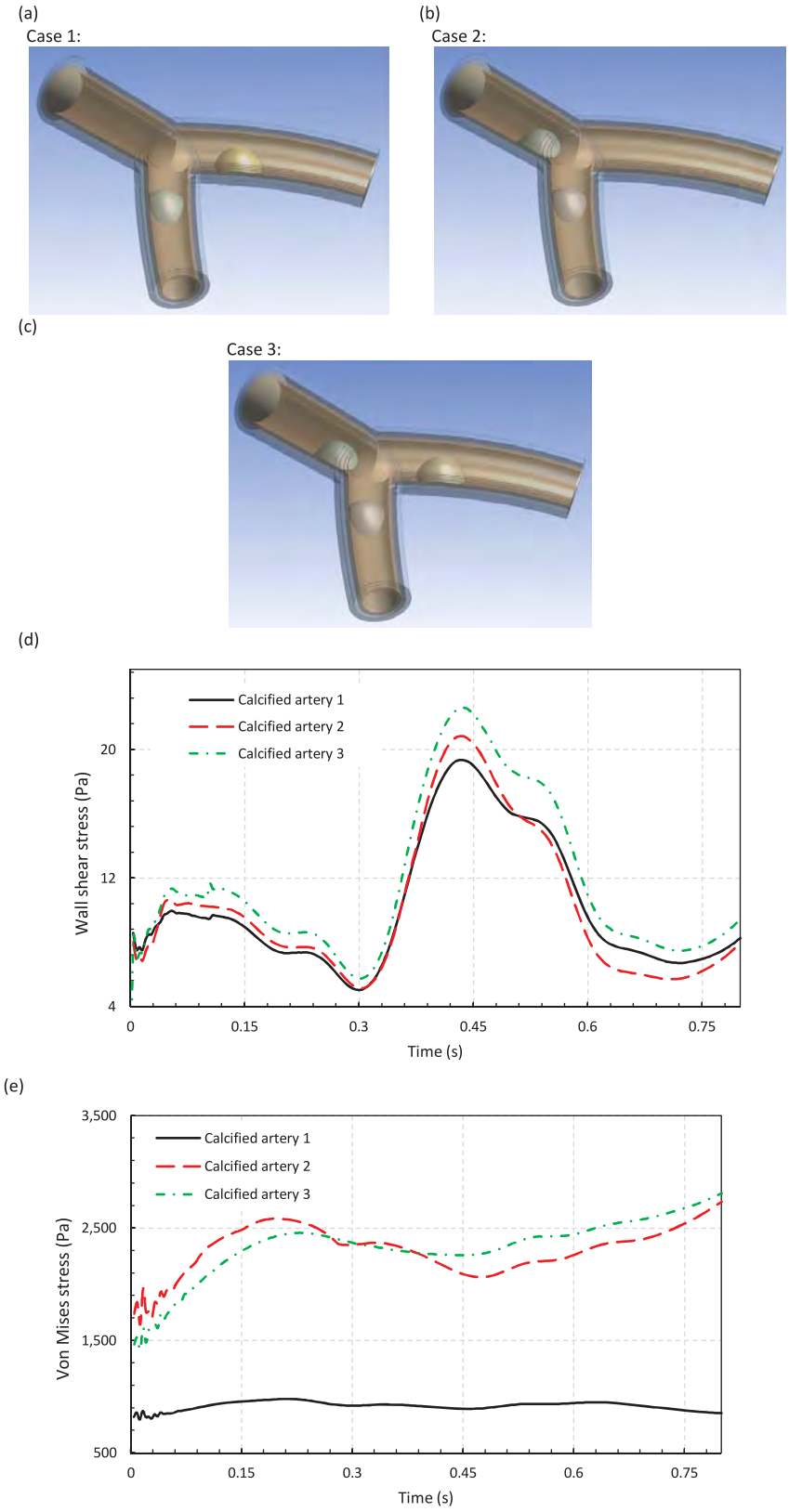

Fig. 14. Effects of calcification on the stress field in a bifurcated atherosclerotic artery: (a) Case 1 with two calcified plaques in LAD and LCx; (b) Case 2 with two calcified plaques in LM and LAD; (c) Case 3 with three calcified plaques in LM, LAD, and LCx branches; (d) WSS on LAD plaque; (e) VMS at LAD plaque.

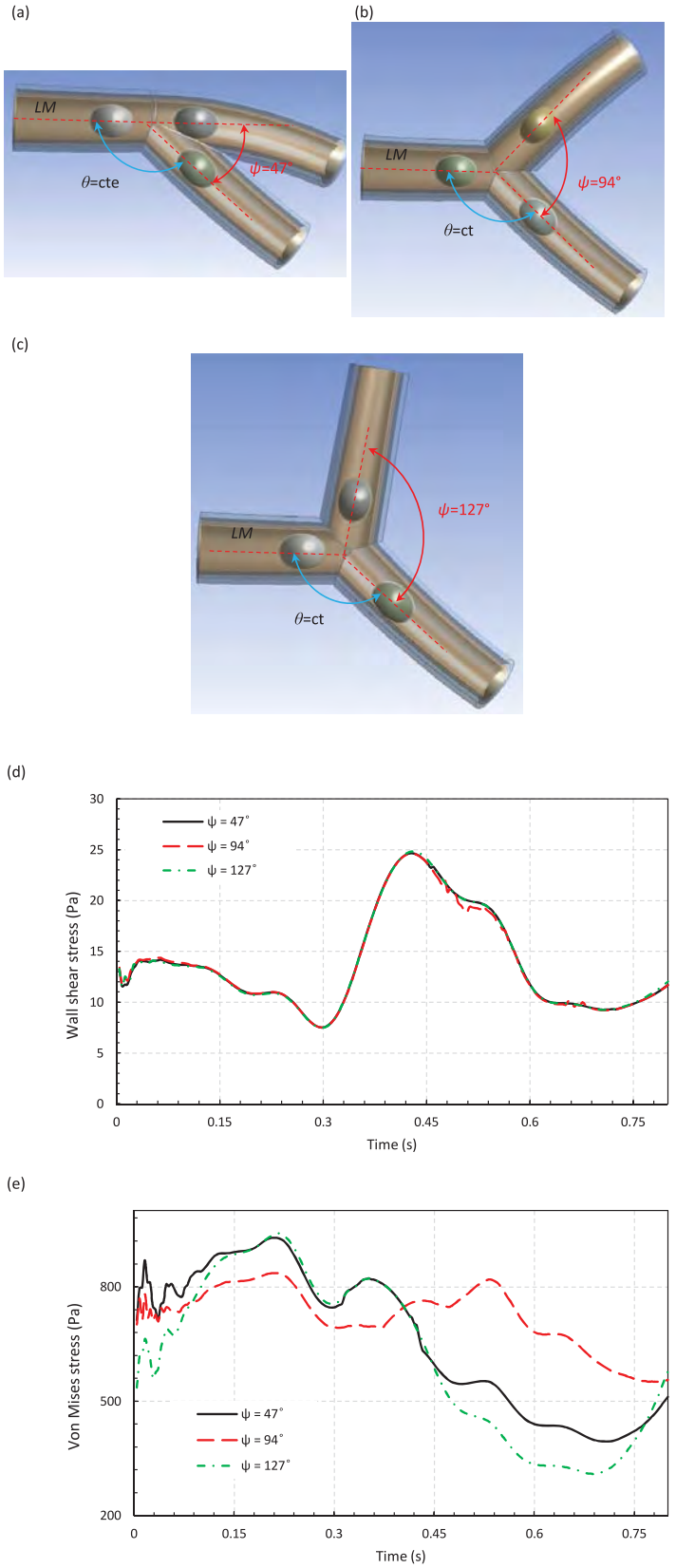

Fig. 15. Effects of angle variations on stress field: (a) $\psi = 47°$; (b) $\psi = 94°$; (c) $\psi = 127°$; (d) WSS on LM plaque; (e) VMS at LM plaque.

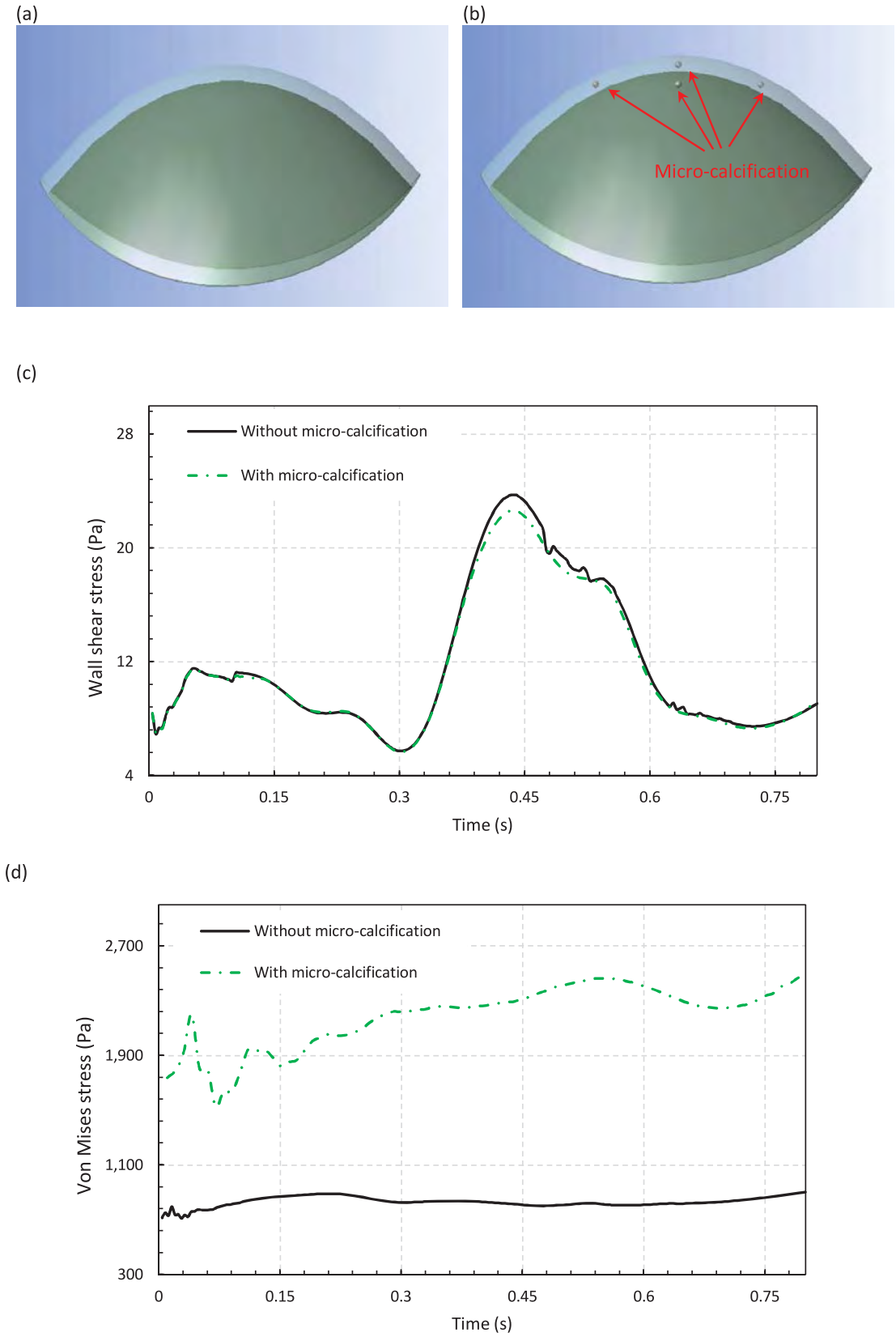

Fig. 16. Effects of micro-calcification: (a) plaque without micro-calcification; (b) plaque with micro-calcification; (c) WSS on LAD plaque; (d) VMS at LAD plaque.

5. Concluding remarks

In the current investigation, a FEM model of the bifurcated atherosclerotic left coronary artery has been established incorporating different features such as nonlinear material and geometry, dynamic time dependent simulation, non-Newtonian fluid model of the blood, hyperelasticity, viscoelasticity artery and plaque, and fluid-solid interaction between these two fields. A reliable predictive model for biomechanical behaviour of the bifurcated atherosclerotic left coronary artery was modelled and simulated and stress fields (as the causes of plaque rupture risks) were determined. All the realistic factors which could affect the problem are modelled in this study; these factors include: bifurcation angle, location of the plaque, level of stenosis, bifurcation curve, blood pulsation, heart motion, three-layered artery, media active muscle contraction, lipid deposition inside the plaque, thickness of fibrous cap, and micro-calcification. This study concludes that:

i. The left main branch has the maximum velocity of all branches which occurs at the top region of the plaque.
ii. In the LM, LAD, and LCx branches, the WSS is maximum at the cap of the plaque in each branch. The low-shear-stress regions for all the plaques are at the shoulders of the plaques; due to this fact, these regions are better candidates for lipid deposition.
iii. A pressure drop is observed from upstream to downstream due to the viscosity. The pressure on the LCx and LAD plaques vary almost with the same pattern in time.
iv. VMS is found to be maximum both at the artery wall and the plaque itself which makes the artery vulnerable to dissention and rupture, respectively.
v. Non-dimensionalised WSS as a fluid/solid interface characteristics and VMS as a solid characteristic in one diagram showed that the middle regions of plaque shoulders are at high risk for rupture; this is in agreement with experimental data in the literature.
vi. As the stenosis level grows, both WSS and VMS increase; this shows that as the plaque height grows, the risk becomes more serious.
vii. The presence of the plaque in the LM branch (regardless of having plaques in LCx and LAD) increases the risk of the rupture. However, having plaques in LM and LAD together is the highest risk.
viii. Fibrous cap thickness highly affects the possibility of the material failure and hence rupture due to stress concentration in the boundary of the intima layer and lipid inside the plaque. A FSI analysis is essential as the VMS can vary significantly with varying thickness.
ix. The larger the shoulder length is the smaller the VMS inside the plaque becomes; similarly, the trend is the same for the WSS in the endothelial layer surface of the artery and the plaque.
x. Different curvatures of the diseased left coronary artery impose different stress distribution inside the plaque and artery. Plaques in highly curved bifurcated arteries are at higher risks of rupture.
xi. Calcified plaques (plaques made from calcium) in the left coronary artery induce higher VMS compared to those made of the regular lipids.
xii. For the original shape of bifurcation angle ($\psi = 94°$), the overall VMS is smaller, however, the WSS is not affected much.
xiii. Presence of micro-calcification increases the level of VMS significantly, however, almost does not change the value of the WSS.

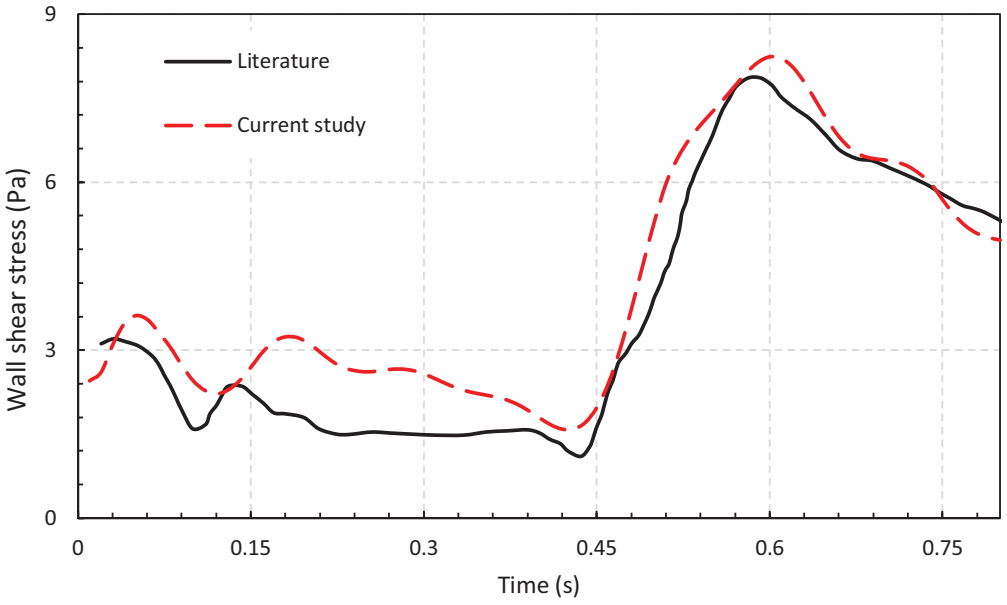

Fig. A-1. Comparison of WSS in coronary artery considering bifurcation from literature (Malvè et al., 2012) and current study.

Appendix A

The following factors are absent in Ref. Malvè et al. (2012): viscoelasticity, non-Newtonian fluid, being three-layered, active media layer contraction, heart motion, presence of plaque, lipid inside the plaque, and micro-calcification. As it is shown in the Fig. A-1, the agreement is excellent.

References

Ai, L., Zhang, L., Dai, W., Hu, C., Shung, K. K., & Hsiai, T. K. (2010). Real-time assessment of flow reversal in an eccentric arterial stenotic model. *Journal of Biomechanics, 43*, 2678–2683.

Anand, M., Kwack, J., & Masud, A. (2013). A new generalized Oldroyd-B model for blood flow in complex geometries. *International Journal of Engineering Science, 72*, 78–88.

Arfaoui, M., Trifa, M., Mansouri, K., Karoui, A., & Renard, Y. (2018). Three-dimensional singular elastostatic fields in a cracked Neo-Hookean hyperelastic solid. *International Journal of Engineering Science, 128*, 1–11.

Attia, M. A., & Rahman, A. A. A. (2018). On vibrations of functionally graded viscoelastic nanobeams with surface effects. *International Journal of Engineering Science, 127*, 1–32.

Bakhshi Khaniki, H., & Hosseini-Hashemi, S. (2017). Dynamic response of biaxially loaded double-layer viscoelastic orthotropic nanoplate system under a moving nanoparticle. *International Journal of Engineering Science, 115*, 51–72.

Barretta, R., Čanađija, M., Luciano, R., & de Sciarra, F. M. (2018). Stress-driven modeling of nonlocal thermoelastic behavior of nanobeams. *International Journal of Engineering Science, 126*, 53–67.

Bhattacharyya, R., Sarangi, S., & Samantaray, A. K. (2015). Effect of stress-softening on the ballooning motion of hyperelastic strings. *International Journal of Engineering Science, 96*, 19–33.

Chabi, F., Champmartin, S., Sarraf, C., & Noguera, R. (2015). Critical evaluation of three hemodynamic models for the numerical simulation of intra-stent flows. *Journal of Biomechanics, 48*, 1769–1776.

Chaichana, T., Sun, Z., & Jewkes, J. (2013). Haemodynamic analysis of the effect of different types of plaques in the left coronary artery. *Computerized Medical Imaging and Graphics, 37*, 197–206.

Chan, W., Ding, Y., & Tu, J. (2007). Modeling of non-Newtonian blood flow through a stenosed artery incorporating fluid-structure interaction. *Anziam Journal, 47*, 507–523.

Chebbi, E., Wali, M., & Dammak, F. (2016). An anisotropic hyperelastic constitutive model for short glass fiber-reinforced polyamide. *International Journal of Engineering Science, 106*, 262–272.

Chiastra, C., Gallo, D., Tasso, P., Iannaccone, F., Migliavacca, F., Wentzel, J. J., et al. (2017). Healthy and diseased coronary bifurcation geometries influence near-wall and intravascular flow: A computational exploration of the hemodynamic risk. *Journal of Biomechanics, 58*, 79–88.

Cilla, M., Borrás, I., Pena, E., Martínez, M., & Malve, M. (2015). A parametric model for analysing atherosclerotic arteries: On the FSI coupling. *International Communications in Heat and Mass Transfer, 67*, 29–38.

Cyron, C., & Humphrey, J. (2014). Vascular homeostasis and the concept of mechanobiological stability. *International Journal of Engineering Science, 85*, 203–223.

Dehrouyeh-Semnani, A. M. (2018). On the thermally induced non-linear response of functionally graded beams. *International Journal of Engineering Science, 125*, 53–74.

Doraiswamy, S., Criscione, J. C., & Srinivasa, A. R. (2016). A technique for the classification of tissues by combining mechanics based models with Bayesian inference. *International Journal of Engineering Science, 106*, 95–109.

Doutel, E., Carneiro, J., Campos, J., & Miranda, J. (2018). Experimental and numerical methodology to analyze flows in a coronary bifurcation. *European Journal of Mechanics-B/Fluids, 67*, 341–356.

Ebrahimi, F., & Barati, M. R. (2016). A nonlocal higher-order refined magneto-electro-viscoelastic beam model for dynamic analysis of smart nanostructures. *International Journal of Engineering Science, 107*, 183–196.

El Baroudi, A., Razafimahéry, F., & Rakotomanana, L. (2014). Fluid–structure interaction within three-dimensional models of an idealized arterial wall. *International Journal of Engineering Science, 84*, 113–126.

Fallah, A., Ahmadian, M. T., & Aghdam, M. M. (2017b). Rate-dependent behavior of connective tissue through a micromechanics-based hyper viscoelastic model. *International Journal of Engineering Science, 121*, 91–107.

Fallah, A., Ahmadian, M. T., & Mohammadi Aghdam, M. (2017a). Rate-dependent behavior of connective tissue through a micromechanics-based hyper viscoelastic model. *International Journal of Engineering Science, 121*, 91–107.

Fan, H., Luo, Y., Yang, F., & Li, W. (2018). Approaching perfect energy absorption through structural hierarchy. *International Journal of Engineering Science, 130*, 12–32.

Farokhi, H., & Ghayesh, M. H. (2015). Nonlinear dynamical behaviour of geometrically imperfect microplates based on modified couple stress theory. *International Journal of Mechanical Sciences, 90*, 133–144.

Farokhi, H., & Ghayesh, M. H. (2015). Thermo-mechanical dynamics of perfect and imperfect Timoshenko microbeams. *International Journal of Engineering Science, 91*, 12–33.

Farokhi, H., & Ghayesh, M. H. (2018b). Nonlinear mechanics of electrically actuated microplates. *International Journal of Engineering Science, 123*, 197–213.

Farokhi, H., & Ghayesh, M. H. (2018a). Nonlinear mechanical behaviour of microshells. *International Journal of Engineering Science, 127*, 127–144.

Farokhi, H., Ghayesh, M. H., & Amabili, M. (2013). Nonlinear dynamics of a geometrically imperfect microbeam based on the modified couple stress theory. *International Journal of Engineering Science, 68*, 11–23.

Farokhi, H., Ghayesh, M. H., Gholipour, A., & Hussain, S. (2017b). Motion characteristics of bilayered extensible Timoshenko microbeams. *International Journal of Engineering Science, 112*, 1–17.

Farokhi, H., Ghayesh, M. H., Gholipour, A., & Tavallaeinejad, M. (2017a). Nonlinear oscillations of viscoelastic microplates. *International Journal of Engineering Science, 118*, 56–69.

Frattolin, J., Zarandi, M. M., Pagiatakis, C., Bertrand, O. F., & Mongrain, R. (2015). Numerical study of stenotic side branch hemodynamics in true bifurcation lesions. *Computers in Biology and Medicine, 57*, 130–138.

Freed, A. D., & Einstein, D. R. (2013). An implicit elastic theory for lung parenchyma. *International Journal of Engineering Science, 62*, 31–47.

Galich, P. I., Slesarenko, V., Li, J., & Rudykh, S. (2018). Elastic instabilities and shear waves in hyperelastic composites with various periodic fiber arrangements. *International Journal of Engineering Science, 130*, 51–61.

Ganghoffer, J.-F., & Sokolowski, J. (2014). A micromechanical approach to volumetric and surface growth in the framework of shape optimization. *International Journal of Engineering Science, 74*, 207–226.

Ghayesh, M. H. (2018). Functionally graded microbeams: simultaneous presence of imperfection and viscoelasticity. *International Journal of Mechanical Sciences, 140*, 339–350.

Ghayesh, M. H. (2018). Nonlinear vibration analysis of axially functionally graded shear-deformable tapered beams. *Applied Mathematical Modelling, 59*, 583–596.

Ghayesh, M. H. (2018). Dynamics of functionally graded viscoelastic microbeams. *International Journal of Engineering Science, 124*, 115–131.

Ghayesh, M. H., Amabili, M., & Farokhi, H. (2013). Nonlinear forced vibrations of a microbeam based on the strain gradient elasticity theory. *International Journal of Engineering Science, 63*, 52–60.

Ghayesh, M. H., Amabili, M., & Farokhi, H. (2013). Three-dimensional nonlinear size-dependent behaviour of Timoshenko microbeams. *International Journal of Engineering Science, 71*, 1–14.
Ghayesh, M. H., & Farajpour, A. (2018). Nonlinear mechanics of nanoscale tubes via nonlocal strain gradient theory. *International Journal of Engineering Science, 129*, 84–95.
Ghayesh, M. H., & Farokhi, H. (2015). Chaotic motion of a parametrically excited microbeam. *International Journal of Engineering Science, 96*, 34–45.
Ghayesh, M. H., & Farokhi, H. (2015). Nonlinear dynamics of microplates. *International Journal of Engineering Science, 86*, 60–73.
Ghayesh, M. H., & Farokhi, H. (2018). On the viscoelastic dynamics of fluid-conveying microtubes. *International Journal of Engineering Science, 127*, 186–200.
Ghayesh, M. H., Farokhi, H., & Alici, G. (2016a). Size-dependent performance of microgyroscopes. *International Journal of Engineering Science, 100*, 99–111.
Ghayesh, M. H., Farokhi, H., & Amabili, M. (2013). Nonlinear dynamics of a microscale beam based on the modified couple stress theory. *Composites Part B: engineering, 50*, 318–324.
Ghayesh, M. H., Farokhi, H., & Amabili, M. (2013). Nonlinear behaviour of electrically actuated MEMS resonators. *International Journal of Engineering Science, 71*, 137–155.
Ghayesh, M. H., Farokhi, H., & Amabili, M. (2014). In-plane and out-of-plane motion characteristics of microbeams with modal interactions. *Composites Part B: engineering, 60*, 423–439.
Ghayesh, M. H., Farokhi, H., & Gholipour, A. (2017). Oscillations of functionally graded microbeams. *International Journal of Engineering Science, 110*, 35–53.
Ghayesh, M. H., Farokhi, H., & Hussain, S. (2016). Viscoelastically coupled size-dependent dynamics of microbeams. *International Journal of Engineering Science, 109*, 243–255.
Gholipour, A., Farokhi, H., & Ghayesh, M. H. (2015). In-plane and out-of-plane nonlinear size-dependent dynamics of microplates. *Nonlinear Dynamics, 79*, 1771–1785.
Gholipour, A., Ghayesh, M. H., Zander, A., & Mahajan, R. (2018). Three-dimensional biomechanics of coronary arteries. *International Journal of Engineering Science, 130*, 93–114.
Gijsen, F. J., Wentzel, J. J., Thury, A., Lamers, B., Schuurbiers, J. C., Serruys, P. W., et al. (2007). A new imaging technique to study 3-D plaque and shear stress distribution in human coronary artery bifurcations in vivo. *Journal of Biomechanics, 40*, 2349–2357.
Gizzi, A., Vasta, M., & Pandolfi, A. (2014). Modeling collagen recruitment in hyperelastic bio-material models with statistical distribution of the fiber orientation. *International Journal of Engineering Science, 78*, 48–60.
Goda, I., & Ganghoffer, J.-F. (2015). 3D plastic collapse and brittle fracture surface models of trabecular bone from asymptotic homogenization method. *International Journal of Engineering Science, 87*, 58–82.
Goda, I., Rahouadj, R., Ganghoffer, J.-F., Kerdjoudj, H., & Siad, L. (2016). 3D couple-stress moduli of porous polymeric biomaterials using µCT image stack and FE characterization. *International Journal of Engineering Science, 100*, 25–44.
Gou, K., & Walton, J. R. (2014). Reconstruction of nonuniform residual stress for soft hyperelastic tissue via inverse spectral techniques. *International Journal of Engineering Science, 82*, 46–73.
Haddad, S. M., & Samani, A. (2017). A computational model of the left ventricle biomechanics using a composite material approach. *International Journal of Engineering Science, 111*, 61–73.
Hashemi, R. (2016). On the overall viscoelastic behavior of graphene/polymer nanocomposites with imperfect interface. *International Journal of Engineering Science, 105*, 38–55.
Heiland, V. M., Forsell, C., Roy, J., Hedin, U., & Gasser, T. C. (2013). Identification of carotid plaque tissue properties using an experimental–numerical approach. *Journal of the Mechanical Behavior of Biomedical Materials, 27*, 226–238.
Holzapfel, G. A., Sommer, G., Gasser, C. T., & Regitnig, P. (2005). Determination of layer-specific mechanical properties of human coronary arteries with nonatherosclerotic intimal thickening and related constitutive modeling. *American Journal of Physiology-Heart and Circulatory Physiology, 289*, H2048–H2058.
Huo, Y., Finet, G., Lefevre, T., Louvard, Y., Moussa, I., & Kassab, G. S. (2012). Which diameter and angle rule provides optimal flow patterns in a coronary bifurcation? *Journal of Biomechanics, 45*, 1273–1279.
Il'ichev, A., & Fu, Y. (2014). Stability of an inflated hyperelastic membrane tube with localized wall thinning. *International Journal of Engineering Science, 80*, 53–61.
Janela, J., Moura, A., & Sequeira, A. (2010). Absorbing boundary conditions for a 3D non-Newtonian fluid–structure interaction model for blood flow in arteries. *International Journal of Engineering Science, 48*, 1332–1349.
Jiao, P., & Alavi, A. H. (2018). Buckling analysis of graphene-reinforced mechanical metamaterial beams with periodic webbing patterns. *International Journal of Engineering Science, 131*, 1–18.
Joshi, S., & Walton, J. R. (2013). Reconstruction of the residual stresses in a hyperelastic body using ultrasound techniques. *International Journal of Engineering Science, 70*, 46–72.
Kachanov, M., & Abedian, B. (2015). On the isotropic and anisotropic viscosity of suspensions containing particles of diverse shapes and orientations. *International Journal of Engineering Science, 94*, 71–85.
Karšaj, I., Sorić, J., & Humphrey, J. D. (2010). A 3-D framework for arterial growth and remodeling in response to altered hemodynamics. *International Journal of Engineering Science, 48*, 1357–1372.
Khakalo, S., Balobanov, V., & Niiranen, J. (2018). Modelling size-dependent bending, buckling and vibrations of 2D triangular lattices by strain gradient elasticity models: Applications to sandwich beams and auxetics. *International Journal of Engineering Science, 127*, 33–52.
Khaniki, H. B., & Hosseini-Hashemi, S. (2017). Dynamic response of biaxially loaded double-layer viscoelastic orthotropic nanoplate system under a moving nanoparticle. *International Journal of Engineering Science, 115*, 51–72.
Kim, T. J., Kim, J. K., Park, B. M., Song, P. S., Kim, D. K., Kim, K. H., et al. (2013). Fatal subacute stent thrombosis induced by guidewire fracture with retained filaments in the coronary artery. *Korean Circulation Journal, 43*, 761–765.
Kolpakov, A. G., Andrianov, I. V., Rakin, S. I., & Rogerson, G. A. (2018). An asymptotic strategy to couple homogenized elastic structures. *International Journal of Engineering Science, 131*, 26–39.
Liu, G., Wu, J., Ghista, D. N., Huang, W., & Wong, K. K. (2015). Hemodynamic characterization of transient blood flow in right coronary arteries with varying curvature and side-branch bifurcation angles. *Computers in Biology and Medicine, 64*, 117–126.
Liu, X., Tang, T., Yu, W., & Pipes, R. B. (2018). Multiscale modeling of viscoelastic behaviors of textile composites. *International Journal of Engineering Science, 130*, 175–186.
Lu, J., Duan, W., & Qiao, A. (2015). Finite element analysis of mechanics of neovessels with intraplaque hemorrhage in carotid atherosclerosis. *Biomedical Engineering Online, 14*, 1.
Maldonado, N., Kelly-Arnold, A., Vengrenyuk, Y., Laudier, D., Fallon, J. T., Virmani, R., et al. (2012). A mechanistic analysis of the role of microcalcifications in atherosclerotic plaque stability: Potential implications for plaque rupture. *American Journal of Physiology-Heart and Circulatory Physiology, 303*, H619–H628.
Malvè, M., Garcia, A., Ohayon, J., & Martínez, M. (2012). Unsteady blood flow and mass transfer of a human left coronary artery bifurcation: FSI vs. CFD. *International communications in heat and mass transfer, 39*, 745–751.
Mandal, M. S., Mukhopadhyay, S., & Layek, G. (2012). Pulsatile flow of an incompressible, inhomogeneous fluid in a smoothly expanded vascular tube. *International Journal of Engineering Science, 57*, 1–10.
Mazloum, A., & Sevostianov, I. (2018). Connections between anisotropic tensors of thermal conductivity and thermal expansion coefficients. *International Journal of Engineering Science, 122*, 1–13.
Medrano-Gracia, P., Ormiston, J., Webster, M., Beier, S., Ellis, C., Wang, C., et al. (2017). A study of coronary bifurcation shape in a normal population. *Journal of Cardiovascular Translational Research, 10*, 82–90.

Movahed, M. R., Kern, K., Thai, H., Ebrahimi, R., Friedman, M., & Slepian, M. (2008). Coronary artery bifurcation lesions: A review and update on classification and interventional techniques. *Cardiovascular Revascularization Medicine, 9*, 263–268.
Pagiatakis, C., Tardif, J.-C., L'Allier, P. L., & Mongrain, R. (2015). A numerical investigation of the functionality of coronary bifurcation lesions with respect to lesion configuration and stenosis severity. *Journal of Biomechanics, 48*, 3103–3111.
Payan, Y., & Ohayon, J. (2017). *Biomechanics of living organs: Hyperelastic constitutive laws for finite element modeling*. World Bank Publications.
Perkowska, M., Piccolroaz, A., Wrobel, M., & Mishuris, G. (2017). Redirection of a crack driven by viscous fluid. *International Journal of Engineering Science, 121*, 182–193.
Pivkin, I., Richardson, P., Laidlaw, D., & Karniadakis, G. (2005). Combined effects of pulsatile flow and dynamic curvature on wall shear stress in a coronary artery bifurcation model. *Journal of Biomechanics, 38*, 1283–1290.
Prosi, M., Perktold, K., Ding, Z., & Friedman, M. H. (2004). Influence of curvature dynamics on pulsatile coronary artery flow in a realistic bifurcation model. *Journal of Biomechanics, 37*, 1767–1775.
Qi, L., Huang, S., Fu, G., Zhou, S., & Jiang, X. (2018). On the mechanics of curved flexoelectric microbeams. *International Journal of Engineering Science, 124*, 1–15.
Ramírez-Torres, A., Rodríguez-Ramos, R., Merodio, J., Penta, R., Bravo-Castillero, J., Guinovart-Díaz, R., et al. (2017). The influence of anisotropic growth and geometry on the stress of solid tumors. *International Journal of Engineering Science, 119*, 40–49.
Richardson, P. D., Davies, M., & Born, G. (1989). Influence of plaque configuration and stress distribution on fissuring of coronary atherosclerotic plaques. *The Lancet, 334*, 941–944.
Rubin, M. B., & Solav, D. (2016). Unphysical properties of the rotation tensor estimated by least squares optimization with specific application to biomechanics. *International Journal of Engineering Science, 103*, 11–18.
Sevostianov, I., Levin, V., & Radi, E. (2016). Effective viscoelastic properties of short-fiber reinforced composites. *International Journal of Engineering Science, 100*, 61–73.
Seyedkavoosi, S., Zaytsev, D., Drach, B., Panfilov, P., Gutkin, M. Y., & Sevostianov, I. (2017). Fraction-exponential representation of the viscoelastic properties of dentin. *International Journal of Engineering Science, 111*, 52–60.
Shahverdi, H., & Barati, M. R. (2017). Vibration analysis of porous functionally graded nanoplates. *International Journal of Engineering Science, 120*, 82–99.
Shariff, M. H. B. M. (2017). On the spectral constitutive modelling of transversely isotropic soft tissue: Physical invariants. *International Journal of Engineering Science, 120*, 199–219.
Shirazi, H. A., & Ayatollahi, M. (2014). Biomechanical analysis of functionally graded biomaterial disc in terms of motion and stress distribution in lumbar spine. *International Journal of Engineering Science, 84*, 62–78.
Soulis, J. V., Farmakis, T. M., Giannoglou, G. D., & Louridas, G. E. (2006). Wall shear stress in normal left coronary artery tree. *Journal of Biomechanics, 39*, 742–749.
Švihlová, H., Hron, J., Málek, J., Rajagopal, K. R., & Rajagopal, K. (2017). Determination of pressure data from velocity data with a view towards its application in cardiovascular mechanics. Part 2. A study of aortic valve stenosis. *International Journal of Engineering Science, 114*, 1–15.
Švihlová, H., Hron, J., Málek, J., Rajagopal, K., & Rajagopal, K. (2016). Determination of pressure data from velocity data with a view toward its application in cardiovascular mechanics. Part 1. Theoretical considerations. *International Journal of Engineering Science, 105*, 108–127.
Taelman, L., Degroote, J., Swillens, A., Vierendeels, J., & Segers, P. (2014). Fluid–structure interaction simulation of pulse propagation in arteries: Numerical pitfalls and hemodynamic impact of a local stiffening. *International Journal of Engineering Science, 77*, 1–13.
Tang, D., Yang, C., Kobayashi, S., Zheng, J., & Vito, R. P. (2003). Effect of stenosis asymmetry on blood flow and artery compression: A three-dimensional fluid-structure interaction model. *Annals of Biomedical Engineering, 31*, 1182–1193.
Tricerri, P., Dedè, L., Gambaruto, A., Quarteroni, A., & Sequeira, A. (2016). A numerical study of isotropic and anisotropic constitutive models with relevance to healthy and unhealthy cerebral arterial tissues. *International Journal of Engineering Science, 101*, 126–155.
Trofimov, A., Abaimov, S., Akhatov, I., & Sevostianov, I. (2017). Effect of elastic contrast on the contribution of helical fibers into overall stiffness of a composites. *International Journal of Engineering Science, 120*, 31–50.
Trofimov, A., Abaimov, S., & Sevostianov, I. (2018). Inverse homogenization problem: Evaluation of elastic and electrical (thermal) properties of composite constituents. *International Journal of Engineering Science, 129*, 34–46.
Veress, A. I., Weiss, J. A., Gullberg, G. T., Vince, D. G., & Rabbitt, R. D. (2002). Strain measurement in coronary arteries using intravascular ultrasound and deformable images. *Journal of Biomechanical Engineering, 124*, 734–741.
Versluis, A., Bank, A. J., & Douglas, W. H. (2006). Fatigue and plaque rupture in myocardial infarction. *Journal of Biomechanics, 39*, 339–347.
W.H.O. WHO. *The top 10 causes of death* http://www.who.int/mediacentre/factsheets/fs310/en/, 2018.
Weydahl, E. S., & Moore, J. E. (2001). Dynamic curvature strongly affects wall shear rates in a coronary artery bifurcation model. *Journal of Biomechanics, 34*, 1189–1196.
Wu, F., Li, X. Y., Chen, W. Q., Kang, G. Z., & Müller, R. (2018). Indentation on a transversely isotropic half-space of multiferroic composite medium with a circular contact region. *International Journal of Engineering Science, 123*, 236–289.
Wu, W.-T., Aubry, N., Massoudi, M., & Antaki, J. F. (2017). Transport of platelets induced by red blood cells based on mixture theory. *International Journal of Engineering Science, 118*, 16–27.
Yang, B., Liu, C., Zheng, W., & Liu, S. (2017). Motion prediction via online instantaneous frequency estimation for vision-based beating heart tracking. *Information Fusion, 35*, 58–67.
Zou, W. N., & He, Q. C. (2018). Revisiting the problem of a 2D infinite elastic isotropic medium with a rigid inclusion or a cavity. *International Journal of Engineering Science, 126*, 68–96.

Chapter 5

Clinical *in vivo* based biomechanics of right and left coronary arteries

Statement of Authorship

Title of Paper	Clinical in vivo based biomechanics of right and left coronary arteries
Publication Status	☐ Published ☐ Accepted for Publication ☑ Submitted for Publication ☐ Unpublished and Unsubmitted work written in manuscript style
Publication Details	

Principal Author

Name of Principal Author (Candidate)	Alireza Gholipour		
Contribution to the Paper	Performed all clinical data collection/analyses and wrote the manuscript.		
Overall percentage (%)	75		
Certification:	This paper reports on original research I conducted during the period of my Higher Degree by Research candidature and is not subject to any obligations or contractual agreements with a third party that would constrain its inclusion in this thesis. I am the primary author of this paper.		
Signature		Date	29/08/2019

Co-Author Contributions

By signing the Statement of Authorship, each author certifies that:

i. the candidate's stated contribution to the publication is accurate (as detailed above);

ii. permission is granted for the candidate in include the publication in the thesis; and

iii. the sum of all co-author contributions is equal to 100% less the candidate's stated contribution.

Name of Co-Author	Dr. Mergen H. Ghayesh		
Contribution to the Paper	Helped in modelling/simulations, checked the results, and assisted in the preparation of the manuscript.		
Signature		Date	30 Aug. 2019

Name of Co-Author	Prof. Anthony Zander		
Contribution to the Paper	Checked the results and assisted in the preparation of the manuscript.		
Signature		Date	2/9/19

Name of Co-Author	A/Prof. Peter Psaltis		
Contribution to the Paper	Helped in clinical data collection, checked the results and assisted in the preparation of the manuscript.		
Signature		Date	2/9/19

Please cut and paste additional co-author panels here as required.

Clinical *in vivo* based biomechanics of right and left coronary arteries

Alireza Gholipour[1], Mergen H. Ghayesh[1,*], Anthony C. Zander[1], Peter J. Psaltis[2, 3]

[1]*School of Mechanical Engineering, University of Adelaide, Adelaide, South Australia 5005, Australia,*
[2]*Adelaide Medical School, University of Adelaide, Adelaide, South Australia 5005, Australia*
[3]*Vascular Research Centre, Lifelong Health Theme, South Australian Health and Medical Research Institute (SAHMRI), Adelaide, South Australia 5000, Australia,*
**Corresponding author: mergen.ghayesh@adelaide.edu.au*

Abstract

A realistic/comprehensive biomechanical model of right/left coronary arteries is developed using the *in vivo* geometric and haemodynamic properties obtained from optical coherence tomography (OCT), angiography, and electrocardiography (ECG). The developed biomechanical model is constructed with the help of an image processing technique and simulated via the finite element method (FEM) for determination of regions with highest shear/von Mises stresses (which determine the potential areas for plaque rupture and initiation of myocardial infarction). A set of simulation results is compared to clinically obtained data to assess the validity of modelling/simulations. The model comprehensively incorporates information relating to three dimensionality, realistic geometry, hyper/viscoelasticity, blood viscosity, heart motion, blood pulsation, and artery bed (i.e. surrounding heart tissue). *In vivo* clinical data from two patients who underwent coronary angiography for clinical indications is used for modelling/simulations, one of whom had a mild (20%) stenosis in the left circumflex (LCx) artery and the other had a right coronary artery (RCA) which was initially 100% occluded in its mid segment (following aspiration thrombectomy to remove clot, the RCA was left with diffuse mild (30-40%) narrowing) and then OCT was used to examine this further and showed proximal thin-capped lipid-rich plaque.

Keywords: Coronary artery; in vivo; biomechanical modelling; optical coherence tomography; angiography; atherosclerosis; plaque rupture.

5.2 Introduction

The primary function of the heart is to pump blood around the body to supply oxygen and vital nutrients to the other organs. It follows that insults to the heart that impair its mechanical pumping function, such as myocardial infarction (or heart attack) carry a high burden of mortality and morbidity. In order to serve its function, the myocardium relies on its own oxygenated blood supply, which is provided by the coronary artery system. Narrowing or obstruction of one or more of the coronary arteries is most commonly caused by a disease process, called atherosclerosis. This entails the build-up of cholesterol-rich inflamed plaques inside the artery wall that pose risk by their flow-limiting nature and their propensity for thrombotic complications that result from plaque rupture or erosion. Plaque rupture is the process by which calcium and lipid inside the plaque release into the blood. Rupture-prone plaques commonly are those with a thin fibrous cap as well as a large lipid-rich core. Despite advances in our understanding of the biological mechanisms that underpin atherosclerosis and its thrombotic complications, there is still much to be learnt about the responsible mechanical and biophysical mechanisms.

Despite the fact that imaging of coronary arteries has been enormously progressed during recent decades, it cannot yet definitively determine the risk of the disease inside the coronary arteries. Nowadays, with the help of advanced imaging techniques, (i.e., Magnetic Resonance Imaging (MRI) together with Computerised Tomography (CT)), it has become possible to investigate coronary arteries non-invasively, although the resolution of images remains imperfect. Better resolution is provided by invasive, intracoronary imaging modalities, most notably Intravascular Ultrasound (IVUS) and OCT that can be utilised to image coronary atherosclerotic plaques as a complement to luminal coronary angiography. Medical imaging techniques have rapidly been improving, especially in recent years, however, alone they are insufficient to provide the critical information required to predict disease initiation, progression and ultimately myocardial infarction. One complementary technique, which (in conjunction with medical imaging techniques) is able to assess the correlations/interactions between the flowing blood and heart structure of the

cardiovascular system is called fluid-structure interaction (FSI) technique in biomechanics, which finally improves our understanding of the biomechanical behaviour of the cardiovascular system and hence the progression/initiation of coronary artery disease (CAD).

In the case of analysing the whole domain of coronary arteries and examining high risk locations of plaque rupture, biomechanical fluid/solid coupled modelling/simulations of the coronary arteries is one promising solution, which can incorporate all the relevant conditions of the problem. Due to the nature of the problem, there are many influential parameters and conditions in the coronary artery system which cause many nonlinearities. Modelling/simulations these nonlinearities and finding their effects are the key factor in obtaining high risk locations inside coronary arteries; biomechanical modelling of the coronary arteries uses the fluid stress field (e.g. wall shear stress (WSS)) and the solid stress field (e.g. von Mises stress (VMS)) to inform about high risk sites and lesions inside the coronary vasculature. Biomechanical modelling can be employed based on different approaches. These include: 1) pure theoretical modelling, where the simplified shape of the coronary arteries is considered; 2) *in vitro* modelling, where the modelling/simulations is based on characteristics obtained via testing on arteries when they are outside a living body; and 3) *in vivo* modelling, where characteristics of coronary arteries when working inside a living body are considered. As the working conditions of the artery and the blood need to be realistic for a reliable analysis, *in vivo* simulation is considered to be the most desirable and accurate one. The following literature review considers studies based upon *in vivo* data in two parts: solid and FSI.

5.2.1 Literature review on solid (FEM) models based on clinical in vivo measurements

In the following studies, *in vivo* images were used to model the coronary artery without considering the blood contained inside; i.e. they analysed the biomechanics of only the artery wall in the absence of blood. This is intended to be only a brief review; an interested reader is referred to Ref. [1] for more information.

Liang et al. [2], for example, analysed the 2D radial and circumferential strains on the coronary artery wall based on IVUS from the LAD coronary artery, where they could obtain the strain field incorporating cardiac motion; they demonstrated the use of *in vivo* clinical IVUS data for measurement of strain field. Using elastography from IVUS, Baldewsing et al. [3] obtained heterogonous material elasticity of the coronary artery to estimate plaque stability. They modelled thin cap fibroatheroma from *in vivo* IVUS images and assessed rupture by measuring strain. Moreover, twelve patients were examined by shear strain elastography (SSE) to find vulnerable plaques in coronary arteries. Keshavarz-Motamed et al. [4] found good correlation between soft plaque content and SSE; they also showed that high-level-inflammation plaques display higher values of SSE.

The first investigation which used OCT images was performed by Chau et al. [5], who estimated the 2D stress and strain distributions in coronary arteries; they compared OCT and histology-based geometry and analysed sensitivity of the stress and strain distributions. Both the OCT and histology-based results showed the same stress and strain distributions on the coronary artery.

Biomechanical properties, such as cross-sectional compliance and dispensability, were studied by Shaw et al. [6] for diseased coronary and normal coronary arteries; they found that plaque composition had a correlation with cross-sectional compliance when patients had atheroma. Dynamic optimisation of IVUS-based segmentation was conducted by Floc'h et al. [7] to reconstruct atherosclerotic coronary plaque elasticity; they applied their method to seven IVUS images and obtained Young's modulus of arteries and plaques. Arterial wall strain and stress caused by myocardial contraction were investigated by Ohayon et al. [8], who examined the stiffness of the bifurcated coronary artery and its correlation with plaque location. MRI and CT techniques were also used to obtain the geometry and motion of the coronary artery; they concluded that local coronary wall stiffness is important for the initiation of atherosclerosis.

5.2.2 Literature review on FSI models based on clinical in vivo measurements

Due to the inherent nonlinearity of the problem, it is vital to consider both the solid and fluid parts of the coronary arteries and their interactions as well. The following studies examined the FSI behaviour of the coronary arterial vasculature.

Liu et al. [9] studied the plaque progression inside a coronary artery based on CT angiographies taken at baseline and of a 12-month of follow-up; VMS, WSS, and lumen area were obtained through FSI simulations; they found that negative remodelling in the coronary artery was associated with areas of low VMS and expansive remodelling with regions of high VMS. Coupled FSI of the left main (LM) bifurcation was studied by Dong et al. [10]; they examined the effect of bifurcation angulation on the stress field using a CT based *in vivo* model of the left coronary bifurcation. It was concluded that angulation significantly changes the mechanical stress distribution. Asanuma et al. [11] developed an IVUS-based FSI model of a coronary artery to examine both tissue and shear stresses; they found that the location of the peak shear stress is different from that of the tissue stress in the coronary artery. Moreover, they discovered that plaque rupture may occur due to tissue stress while being triggered by shear stress.

Fan et al. [12] studied the correlation between the thickness of the plaque and wall stresses on the plaque using IVUS-based simulations for 10 patients; they found that a larger thickness of plaque's wall increases flow shear stress and decreases the plaque wall stress. *In vivo* IVUS-based patient follow-up was conducted by Wang et al. [13] in order to analyse coronary plaque wall strain and WSS; they examined different factors such as wall thickness, the depth of lipid, and cap thickness in correlation with shear and plaque wall stress. Tang et al. [14] defined an index of plaque vulnerability in atherosclerotic coronary arteries; they examined the 2D MRI images of coronary arteries to find a stress-based computational index for the plaque. Guo et al. [15] developed an IVUS-based computational model of coronary arteries to examine the stress and strain of plaque and arteries; they analysed the effect of material stiffness variation on stress and strain variation and compared *ex vivo* and *in vivo* data and showed that material properties obtained from *in vivo* vessels shows they are significantly softer than *ex vivo* vessels.

5.2.3 Contributions of the present study

This paper is the *first* to develop a more realistic/comprehensive biomechanical model of the right and left coronary arteries based on geometric and haemodynamic properties measured from OCT, angiography and ECG; this fully 3D nonlinear FSI model has been applied in simulations for the first time to determine the artery and plaque stress fields to enable predictions of plaque rupture and therefore myocardial infarction. Clinical data were obtained from two patients. Patient 1 presented with a non-ST elevation myocardial infarction (NSTEMI) and had OCT imaging performed of the non-dominant left circumflex (LCx) artery which contained a mild 20% luminal stenosis in its 176 segment of OCT measurement. Patient 2 had presented with an ST-segment elevation myocardial infarction (STEMI) and was found to have a severe, 70% luminal stenosis of the 255 OCT segment of the dominant right coronary artery (RCA). The developed model has incorporated the influences of three dimensionality, hyper viscoelasticity, realistic geometry, heart motion, blood viscosity, blood pulsation, and surrounding heart tissue.

5.3 Clinical data measurement using OCT, angiography, and ECG

Clinical data were obtained from patients who were admitted to the Royal Adelaide Hospital (RAH) and underwent clinically indicated coronary angiography. These clinically measured data were then analysed at the South Australian Health and Medical Research Institute (SAHMRI) and the School of Mechanical Engineering, the University of Adelaide in order to obtain realistic geometries of the coronary arteries, heart deformation measurements, and corresponding heart beat characteristics. Ethics approval has been obtained from the Central Adelaide Local Health Network Human Ethics Research Committee (HREC ref: HREC/18/CALHN/781) to use the clinical data for the purpose of biomechanical modelling/simulations.

Patient 1: male patient (age 64) presented with an NSTEMI and was found at coronary angiography to have the following: LM had a mild distal plaque (20% stenosis); left anterior descending (LAD) had a severe mid-vessel stenosis of 70-80% with hyperaemic fractional flow reserve (FFR) value of 0.79; LCx showed

mild mid vessel irregularity causing only 20% narrowing; RCA showed atheroma with irregular severe mid vessel stenosis and moderate distal long plaque (50%) (**Figure 5-1**). For this patient, we used angiographic and OCT image processing to model the LCx which had mild mid luminal irregularity causing only 20% angiographic stenosis. Shown in **Figure 5-1** are the angiogram images of the LCx artery where sub-figure (a) represents the angiogram image with primary angle = 27.4° and a secondary angle = 22.3° and sub-figure (b) is that with primary angle = -0.7° and secondary angle = -34.5°. Primary and secondary angles were for the two angles obtained from angiograms, namely Left Anterior Oblique (LAO)/Right Anterior Oblique (RAO) and Caudal (CAU)/Cranial (CRA), respectively (RAO and CAU were assumed to be positive). The start (distal) and the end (proximal) of the pull-back image from OCT of the LCx are also shown in **Figure 5-1**.

Patient 2: male patient (age 80) who presented with an inferior STEMI, complicated by hypotension; angiography revealed the following: LM was angiographically normal; LAD had a mild (40-50%) stenosis in the mid vessel; LCx had a minor irregularities; RCA was initially 100% occluded in its mid segment. Following aspiration thrombectomy to remove clot, the RCA was left with diffuse mild (30-40%) narrowing. OCT was used to examine this further and showed a thin-capped lipid-rich plaque. The patient had an irregular heartbeat due to ventricular ectopy at the time of imaging. Orthogonal angiographic images are depicted in **Figure 5-2**; the first plane of the image has primary angle = 44.2° and a secondary angle = 25.5° and the second plane is directed with primary angle = -0.3° and secondary angle = 34.7°. OCT pullback start point (distal) and end point (proximal) on the artery are also shown.

For each patient, three different measurements were conducted, namely OCT, angiogram, and ECG. In order to model the unsteady time-dependent biomechanics of the coronary artery, ECG data of the patient were used at the time of the procedure to obtain the heart rate which was used in the modelling. The other aspect of the clinical measurement in this study is x-ray angiogram images; the angiogram was used to assess the coronary artery conditions by injecting dye contrast and detecting it with x-ray. Due to the critical situation of both patients and in order to appreciate the 3-D nature of the arteries for each

patient, we made sure to take orthogonal views of angiography. In the case of ambiguity of the situation, either FFR or OCT was conducted. For each patient, OCT measured the cross-sections of their coronary arteries. A combination of these clinical measurements was used to develop biomechanical model/simulation of the coronary arteries.

5.4 In vivo realistic 3D geometry, 3D motion and heart rate

It is crucial to use clinically obtained *in vivo* characteristics of coronary arteries in the model development and simulations as even small variations in geometric and haemodynamic conditions may alter the shear and VMSs substantially. Based on the clinical data obtained using angiography, OCT, and ECG (see Section 2), the development of the artery models detailed in this section.

The planar angiograms were used to construct the 3D position curve of the catheter; namely angiogram angles of RAO/LAO and CAU/CRA point coordinates have been employed; see **Figures 5-1** and **5-2** for patients 1 and 2, respectively.

Having 2D coordinates of all the desired points and their origin, which is the tip of the catheter, the 3D coordinates were calculated using MATLAB (version 2016a, Mathworks, Natick, MA, US) based on angiogram angles assuming

$$A = (x_A, y_A), \tag{5.1}$$

for the position of point *A*. The RAO/LAO axis was assumed as the *x*-axis and the CAU/CRA was assumed as the *y*-axis. *Primary_angle* is the value of RAO or LAO obtained by assuming RAO positive. *Secondary_angle* is the value of CAU or CRA assuming CAU positive. Defining rotation vectors of

$$Rotation_x = \begin{bmatrix} 1 & 0 & 0 \\ 0 & \left[\cos(primary\_angle)\right] & -\left[\sin(primary\_angle)\right] \\ 0 & \left[\sin(primary\_angle)\right] & \left[\cos(primary\_angle)\right] \end{bmatrix}, \tag{5.2}$$

$$Rotation_y = \begin{bmatrix} [\cos(secondary\ \_angle)] & 0 & [\sin(secondary\ \_angle)] \\ 0 & 1 & 0 \\ -[\sin(secondary\ \_angle)] & 0 & [\cos(secondary\ \_angle)] \end{bmatrix}, \quad (5.3)$$

and applying the rotation to the catheter points, the following 3D positon was obtained.

$$A_{3D} = Rotation_x Rotation_y \begin{bmatrix} x_A \\ y_A \\ 0 \end{bmatrix}. \quad (5.4)$$

The position vectors were then normalised and the 3D curve of the catheter was obtained (**Figures 5-3** and **5-4**).

Points were then obtained from the OCT sequence for two closed lines of the inner lumen of the intima and the outer shape of the adventitia for each cross-section (**Figure 5-5**). The point extracted from each loop was then transferred to the catheter point which had already been obtained from the angiogram. The geometry was developed for every 1 mm length of OCT catheter cross-sections (**Figure 5-6**). All these coordinates were imported to ANSYS® (version 19.0, ANSYS Inc., Canonsburg, PA, US) to develop the geometry.

As the cardiac cycle has different phases, it is important to take these into account in the biomechanical modelling/simulations. By synchronising the clinically obtained ECG with the angiogram images, it was possible to ensure that the model was replicating the exact same stage of the cardiac cycle. Moreover, since the coronary artery is mounted on the heart and in each cycle due to the motion of the different areas of the heart such as left and right atrium and ventricle, the walls of the coronary artery experience large deflections; this dynamic motion was determined using consecutive angiographic image frames. Using anatomical marks, such as branches, the motion of these points was calculated based on the ECG. The same procedure of obtaining the 3D position of the points was employed here as a function of time. For each time point there were three different planes of information according to the phase of the cardiac cycle on ECG to synchronise them as one point in time. Then, the 3D motion

variation of the point with respect to time was obtained. For each case study, the motion at the beginning and end of the artery was obtained.

Due to the nonlinear behaviour of the coronary arteries, the Mooney-Rivlin 5-parameter hyperelastic model (best fitted curves to the experimental data) was considered based on *in vitro* testing [16] to take into account this important feature of the artery. The Prony Shear Relaxation 5-term material viscoelastic model was considered to model the damping of the coronary artery [17]. It is also important to incorporate the nonlinear relation for the change of the blood viscosity with the strain rate of the blood in order to obtain more realistic WSS; this was considered via a non-Newtonian blood model via a nonlinear change in viscosity with the strain rate of Carreau type [18]. The pulsatile blood flow inlet velocity was modelled by applying an eight-term sin-function which appropriately fitted the experimental data [19]. As the coronary artery is mounted on the heart, it is important to consider the surrounding soft tissue to achieve a more complete model; **Figure 5-7** shows the part of the artery embedded inside the heart tissue; the catheter curve was used to determine the area of the foundation. This figure also shows the different parts of the LCx model of Patient 1: sub-figure (a) illustrates the coronary artery bed and upper part; sub-figure (b) represents the blood component of the model; sub-figure (c) shows the FSI surface between the artery and the blood (FSI coupling area). **Figure 5-8** and its sub-figures are similar to those in **Figure 5-7**, but for the RCA of Patient 2. The elastic support with the stiffness of 100 N/m^3 used for the shown area of the coronary artery bed; this value was obtained from a deflection validation for Patient 1 and was used for Patient 2 as well.

5.5 Numerical simulations via Finite Element / Finite Volume Methods

The nonlinear unsteady 3D model of the coronary arteries was implemented by using the FEM in ANSYS for the solid component and the finite volume method (FVM) for the fluid with a fully-coupled solution between these two domains (i.e. FSI). Due to the flexible nature of tissues, performing an FSI analysis is essential; in the biomechanical modelling of the coronary artery, the

interaction between solid (plaque and artery) and fluid (blood) parts highly influences the behaviour of each.

The interface between the blood and the artery was considered as a coupling surface. Due to the dynamic nature of the biosystem, a dynamic mesh (or remeshing technique) was employed to incorporate the changes at every time step. For both domains, tetrahedral elements with the same element size around the coupling interface were used; all the points from the coupling surface of the fluid were mapped onto that of the solid part. In the coupling process, the displacement of the coronary artery wall as (a source) was transferred to the blood as a target and the pressure of the blood boundary condition (as a source) was transferred to the coronary artery wall as a target (two-way coupling). The convergence of each domain as well as transferring process was obtained throughout the solution.

5.6 Results for shear/body stresses

5.6.1 Patient 1: Left circumflex coronary artery

Figure 5-9 shows WSS distribution imposed by blood viscosity to the intima layer of the LCx coronary artery. The WSS is maximum at the outer surface of the plaque. There are also few local maxima which are considered to be potential high risk areas; these local maxima cannot be determined using solely imaging techniques. A local peak of WSS may cause damage to the intima layer of the coronary artery and contribute to formation of a plaque. On the other hand, a local minimum is also important, since it can be a potential site for low-density-lipoprotein (LDL) deposition; these features cannot be determined solely by means of clinical images. Variation of the WSS with time over one pulsation period is shown in sub-figure (b), highlighting the maximum value around the half-way point with time of the pulse.

The VMS distribution and the variation of the maximum value as an indicator of the effective stress inside the artery are shown in **Figure 5-10**. The VMS distribution around the plaque shows a local maximum in the area of the plaque; this local maximum value occurs toward the proximal side of the shoulder of the plaque. Sub-figure (b) also shows that the maximum value of the VMS occurs at *t*

= 0.17s; the heart motion seems to be the dominant reason for time-dependent variation of VMSs, as the pattern follows the heart motion rather than the heart pulse.

Different quantities, such as VMS, von Mises strain, stiffness, and 3D shear stress inside the artery, along the intersection curve of the artery bed and the upper part of the artery are shown in **Figure 5-11**; i.e. along curves 1, 2, 3, and 4 (see sub-figures (a) and (b)). Curve 1 is the intersection between the outer surface of the adventitia layer with the artery bed for the outer curvature of the artery; Curve 2 shows the intersection between the intima layer of the artery with the bed on the same side of Curve 1; Curve 3 is the counterpart of Curve 2 but for the inner curvature; Curve 4 is the counterpart of Curve 1, but for the outer curvature. Point 1 (in sub-figures (a) and (b)) shows the origin for the curvilinear length and Point 2 shows the end of the curve. Sub-figure (c) shows the VMS distribution on Curves 2 and 3, illustrating that the VMSs are smaller near the plaque area (around half-way of the artery length); sub-figure (d) is the counterpart of (c) for the strains. According to sub-figure (c), in general, the intima effective stress on the side of the plaque (Curve 3) is larger than that on the other side; this makes the plaque side at higher risk of intima-layer failure. The same scenario takes place for the von Mises strain as well (sub-figure (d)). Another interesting point to note in sub-figure (c) is that the effective VMS for both Curves 2 and 3 is larger near the proximal and distal areas when compared to the plaque area; the same conclusion can be drawn for the strain (sub-figure (d)). The stiffness of the artery, which approximates a fraction of the stress over strain at each point, is shown in sub-figure (e). Generally speaking, the stiffness of the artery on the side of the plaque (Curve 3) is larger, which means the other side (Curve 2), suffers more from (high) blood pressure as it is more flexible than the plaque side. Sub-figure (f) highlights that, in general, the local stiffness does not change significantly through the thickness of the artery. The maximum shear stress can be considered as one criteria to assess the failure of the material; sub-figure (g) represents the shear stress variation on Curve 3 on different planes of *XY*, *YZ*, and *ZX* (see **Figure 5-7** for the planes); the reason to choose Curve 3 is that it is for the intima larger on the plaque side where the shear can be responsible for plaque rupture.

The shear stress on the *ZX* plane is the greatest of all and the value of the overall shear stress decreases as the distal area is approached. Sub-figure (h) also shows the *ZX* shear stress on Curves 2 and 3, which are both on the intima layer of the artery; Curve 3, which is on the side of the plaque, has a higher value for the shear stress prior to the plaque location. This implies a higher chance for the initiation of plaque rupture at the shoulder of the plaque closer to the proximal. Nevertheless, beyond the plaque location, the value of the shear stress on the two curves is almost equal towards the end of the artery.

5.6.2 Patient 2: Right coronary artery with arrhythmia

The WSS distribution and its time variation on the RCA are shown in **Figure 5-12** for Patient 2; as the stenosis level is higher compared to the first patient, and as a result the WSS maximum caused by the blood flow is almost tripled (see **Figure 5-9** (b) for comparison). Moreover, for both patients the WSS is maximum in the vicinity of the plaque, regardless of this fact that Patient 1 has one plaque and Patient 2 has three plaques. However, the trend of the time variation is similar to that of Patient 1.

The VMS distribution and the time variation for Patient 2 are presented in **Figure 5-13**. Comparing the plot of **Figure 5-13** (b) with **Figure 5-10** (b), i.e. for Patient 1, highlights that the trends are different; this could be the result of the different deflection trend for the RCA. Also, the peak value occurs later (around t = 0.47 s) for Patient 2 as compared to Patient 1 (around t = 0.17 s).

Figure 5-14 shows the counterpart of **Figure 5-11** for Patient 2. As seen in sub-figure (c), closer to the proximal area prior to plaque 1, the VMS on Curve 2 (plaque 1 side) is larger than that of Curve 3; this phenomenon can be attributed to the fact that plaque rupture takes place at the proximal shoulder of the plaque. Sub-figure (d) illustrates the strain on the intima layer of the artery; the strain variation prior to the plaque area is larger on the side of the plaque. This reveals the mechanism for compensation of plaque presence upstream of it.

Figure 5-14 also shows that the pattern of the stiffness with time fluctuates significantly along the artery length (sub-figure (e)); these fluctuations differ on either side of the artery. This highlights that due to the complex situation, there

are many local sites considered to be high risk for plaque rupture or dissection of the artery. Sub-figure (f) shows that the local stiffness on either side of the artery wall is different at each arc-length and vary with different patterns along the length of the artery. Normally the stiffness of the outer (adventitia; here Curve 4) layer of the artery is expected to be higher; however, when both the intima and the adventitia have almost the same stiffnesses, the artery is not flexible to sudden changes due to blood pressure or heart motion. In general, the stiffness for Patient 2 is larger than that of Patient 1; this means Patient 1 is at a lower rupture risk. The shear stresses on different planes for Patient 2 are almost the same, however, the shear stress values increase as the distal of the artery is approached (sub-figures (g) and (h)). Also, the absolute value of shear stress for Patient 2 is larger than that of Patient 1.

5.6.3 Model/simulation validation

In order to validate the developed model of the artery, the deflection of the distal of the artery in 3D space was compared to the 3D motion extracted from angiogram (**Figure 5-15**); in other words, 3D deflection of the distal artery for the *x*, *y*, and *z* directions was compared to the experimental/clinical data obtained from the angiogram. As depicted in **Figure 5-15**, the trend and the amplitude of the motion were very close illustrating very good agreement. The minor differences between modelling/simulation results and the clinical data may be due to the material properties used [16].

5.7 Concluding remarks

In this paper, a realistic and comprehensive *in vivo* based modelling and simulations of coronary arteries of one patient with NSTEMI and another one with an inferior STEMI/ectopy were conducted based on geometric and haemodynamic properties obtained from OCT, angiography, and ECG. LCx of Patient 1 with minor stenosis was modelled and simulated and RCA of Patient 2 with a thin-capped lipid-rich plaque was modelled and simulated. In order to determine and examine the dynamic stress fields of coronary arteries, a nonlinear

FSI biomechanical model based on the FEM was developed using ANSYS. Realistic characteristics of this highly coupled biomechanical system such as artery hyperelasticity, artery viscoelasticity, physiological blood pulsation, non-Newtonian viscosity of the blood, the artery elastic bed (heart soft tissue), and heart motion were taken into account in the model. WSSs, VMSs, von Mises strains, and shear stresses inside the artery were obtained and analysed for the detection of possible plaque formation/rupture and dissection.

This investigation concludes that for Patient 1 that the WSS is maximum on the outer surface of the plaque; however, there are a few local maxima locations which can be considered as potential high-risk areas. The local minimum shear areas were shown to be present; determination of these sites was important as they were potential locations for LDL deposition and hence plaque formation. A time domain analysis also showed that the largest value of the shear stress occurs half-way through a heartbeat. Regarding the VMS for Patient 1, it was found that the maximum value occurs near the proximal area, however, a local maximum occurs in the vicinity of the plaque and at the shoulder which is closer to the proximal. It was also found that the time-variation pattern of the VMS follows more that of heart motion rather than its pulse. Another interesting finding was that the local maximum value on the plaque side is larger than that of the area opposite to the plaque, hence, the plaque side is at a higher risk of intima-layer failure. Also, a general conclusion on the stiffness was that the plaque side is stiffer than the area opposite to the plaque.

It was found for Patient 2 that, as the stenosis level is higher than that of Patient 1, the maximum WSS is much larger. Moreover, regardless of the number of plaques (i.e. one for Patient 1 and three for Patient 2), the plaque regions possess the maximum of the WSS. Moreover, time variation patterns of shear for both patients are almost the same; however, they are different for the VMSs. It was also found for Patient 2 that the plaque shoulder on the proximal side of Plaque 1 is at the highest risk for rupture. Moreover, for some areas of the artery, the values of the stiffnesses of the intima and the adventitia layers are close to each other which implies that the artery may not be sufficiently flexible to sudden

strains due to high blood pressure or heart motion, which increase the risk of dissection and rupture.

Acknowledgement

We acknowledge the assistance provided by Dr. Daisuke Shishikura and Mr. Giuseppe Di Giovanni from the Atherosclerosis Imaging Core Laboratory at SAHMRI, Mrs Trudy Patrick from Abbott Pty Ltd and doctors and nurses from the Cardiovascular Investigation Unit at the RAH. The support provided for this investigation from The University of Adelaide, RAH, and SAHMRI are highly acknowledged. P.JP. is supported by research fellowships from the National Heart Foundation of Australia (Future Leader Fellowship FLF102056) and National Health and Medical Research Council of Australia (CDF1161506).

I acknowledge the support I have received for my research through The University of Adelaide and Faculty of Engineering, Computer & Mathematical Sciences, The University of Adelaide.

References

[1] L. Cardoso, S. Weinbaum, Changing views of the biomechanics of vulnerable plaque rupture: a review, Annals of biomedical engineering, 42 (2014) 415-431.
[2] Y. Liang, H. Zhu, T. Gehrig, M.H. Friedman, Measurement of the transverse strain tensor in the coronary arterial wall from clinical intravascular ultrasound images, Journal of Biomechanics, 41 (2008) 2906-2911.
[3] R.A. Baldewsing, M.G. Danilouchkine, F. Mastik, J.A. Schaar, P.W. Serruys, A.F. van der Steen, An inverse method for imaging the local elasticity of atherosclerotic coronary plaques, IEEE Transactions on Information Technology in Biomedicine, 12 (2008) 277-289.
[4] Z. Keshavarz-Motamed, Y. Saijo, Y. Majdouline, L. Riou, J. Ohayon, G. Cloutier, Coronary artery atherectomy reduces plaque shear strains: An endovascular elastography imaging study, Atherosclerosis, 235 (2014) 140-149.
[5] A.H. Chau, R.C. Chan, M. Shishkov, B. MacNeill, N. Iftimia, G.J. Tearney, R.D. Kamm, B.E. Bouma, M.R. Kaazempur-Mofrad, Mechanical analysis of atherosclerotic plaques based on optical coherence tomography, Annals of Biomedical Engineering, 32 (2004) 1494-1503.
[6] J.A. Shaw, B.A. Kingwell, A.S. Walton, J.D. Cameron, P. Pillay, C.D. Gatzka, A.M. Dart, Determinants of coronary artery compliance in subjects with and without angiographic coronary artery disease, Journal of the American College of Cardiology, 39 (2002) 1637-1643.
[7] S. Le Floc'h, J. Ohayon, P. Tracqui, G. Finet, A.M. Gharib, R.L. Maurice, G. Cloutier, R.I. Pettigrew, Vulnerable atherosclerotic plaque elasticity reconstruction based on a segmentation-driven optimization procedure using strain measurements: theoretical framework, IEEE Transactions on Medical Imaging, 28 (2009) 1126-1137.
[8] J. Ohayon, A.M. Gharib, A. Garcia, J. Heroux, S.K. Yazdani, M. Malvè, P. Tracqui, M.-A. Martinez, M. Doblare, G. Finet, Is arterial wall-strain stiffening an additional process responsible for atherosclerosis in coronary bifurcations?: an in vivo study based on dynamic CT and MRI, American Journal of Physiology-Heart and Circulatory Physiology, 301 (2011) H1097-H1106.
[9] X. Liu, G. Wu, C. Xu, Y. He, L. Shu, Y. Liu, N. Zhang, C. Lin, Prediction of coronary plaque progression using biomechanical factors and vascular characteristics based on computed tomography angiography, Computer Assisted Surgery, 22 (2017) 286-294.
[10] J. Dong, Z. Sun, K. Inthavong, J. Tu, Fluid–structure interaction analysis of the left coronary artery with variable angulation, Computer Methods in Biomechanics and Biomedical Engineering, 18 (2015) 1500-1508.
[11] T. Asanuma, Y. Higashikuni, H. Yamashita, R. Nagai, T. Hisada, S. Sugiura, Discordance of the Areas of Peak Wall Shear Stress and Tissue Stress in Coronary Artery Plaques as Revealed by Fluid-Structure Interaction Finite Element Analysis, International heart journal, 54 (2013) 54-58.
[12] R. Fan, D. Tang, C. Yang, J. Zheng, R. Bach, L. Wang, D. Muccigrosso, K. Billiar, J. Zhu, G. Ma, Human coronary plaque wall thickness correlated positively with flow shear stress and negatively with plaque wall stress: an IVUS-based fluid-structure interaction multi-patient study, Biomedical Engineering Online, 13 (2014) 32.

[13] L. Wang, Z. Wu, C. Yang, J. Zheng, R. Bach, D. Muccigrosso, K. Billiar, A. Maehara, G.S. Mintz, D. Tang, IVUS-based FSI models for human coronary plaque progression study: components, correlation and predictive analysis, Annals of Biomedical Engineering, 43 (2015) 107-121.
[14] D. Tang, C. Yang, J. Zheng, P.K. Woodard, J.E. Saffitz, J.D. Petruccelli, G.A. Sicard, C. Yuan, Local maximal stress hypothesis and computational plaque vulnerability index for atherosclerotic plaque assessment, Annals of Biomedical Engineering, 33 (2005) 1789-1801.
[15] X. Guo, J. Zhu, A. Maehara, D. Monoly, H. Samady, L. Wang, K.L. Billiar, J. Zheng, C. Yang, G.S. Mintz, Quantify patient-specific coronary material property and its impact on stress/strain calculations using in vivo IVUS data and 3D FSI models: a pilot study, Biomechanics and Modeling in Mechanobiology, 16 (2017) 333-344.
[16] G.A. Holzapfel, G. Sommer, C.T. Gasser, P. Regitnig, Determination of layer-specific mechanical properties of human coronary arteries with nonatherosclerotic intimal thickening and related constitutive modeling, American Journal of Physiology-Heart and Circulatory Physiology, 289 (2005) H2048-H2058.
[17] A. Gholipour, M.H. Ghayesh, A. Zander, R. Mahajan, Three-dimensional biomechanics of coronary arteries, International Journal of Engineering Science, 130 (2018) 93-114.
[18] A. Gholipour, M.H. Ghayesh, A. Zander, Nonlinear biomechanics of bifurcated atherosclerotic coronary arteries, International Journal of Engineering Science, 133 (2018) 60-83.
[19] F. Chabi, S. Champmartin, C. Sarraf, R. Noguera, Critical evaluation of three hemodynamic models for the numerical simulation of intra-stent flows, Journal of biomechanics, 48 (2015) 1769-1776.
[20] S.J. MEDICAL, https://www.abbott.com/abbott-stjudemedical-en-uk.html, (2019).

(a)

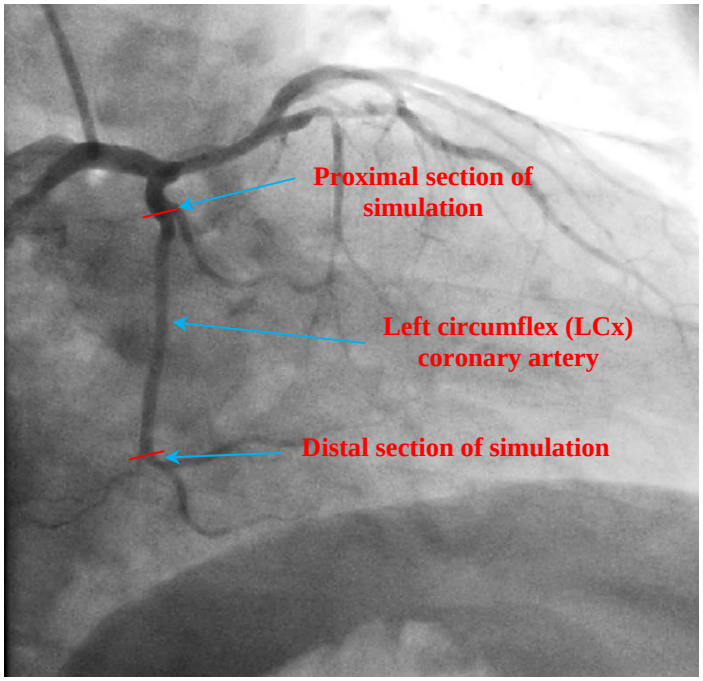

(b)

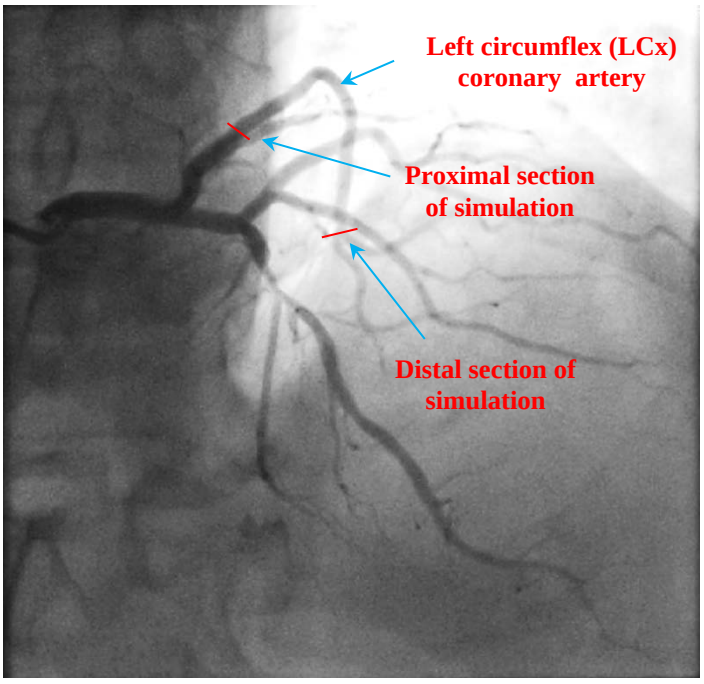

Figure 5-1. Patient 1 angiograms for the LCx coronary artery: (a) with primary angle =27.4° and secondary angle = 22.3°; (b) with primary angle = -0.7° and secondary angle = -34.5°; these angiograms were performed at the RAH.

(a)

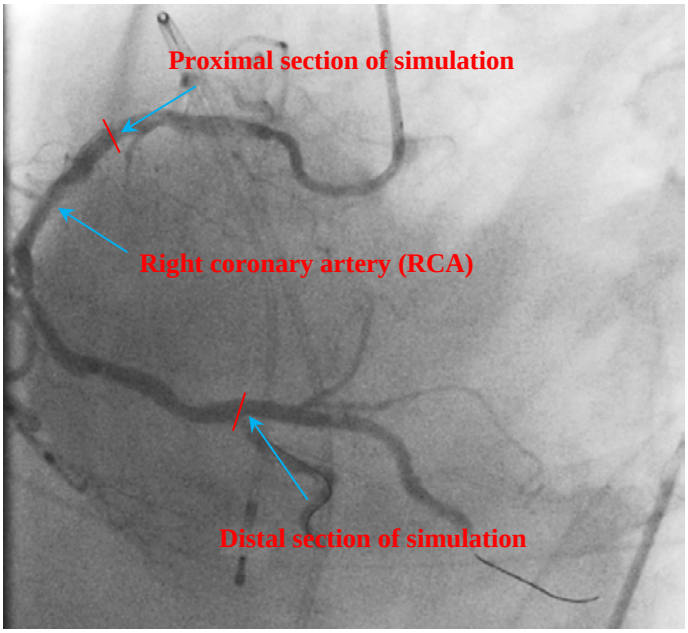

(b)

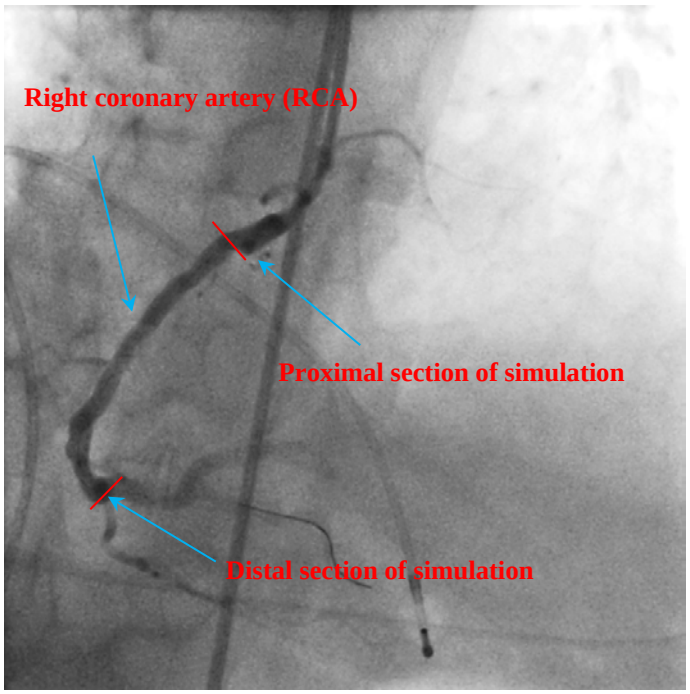

Figure 5-2. Patient 2 angiograms for the RCA (a) with primary angle = 44.2° and secondary angle = 25.5°; (b) with primary angle = -0.3° and secondary angle = 34.7°; these angiograms were performed at the RAH.

(a)

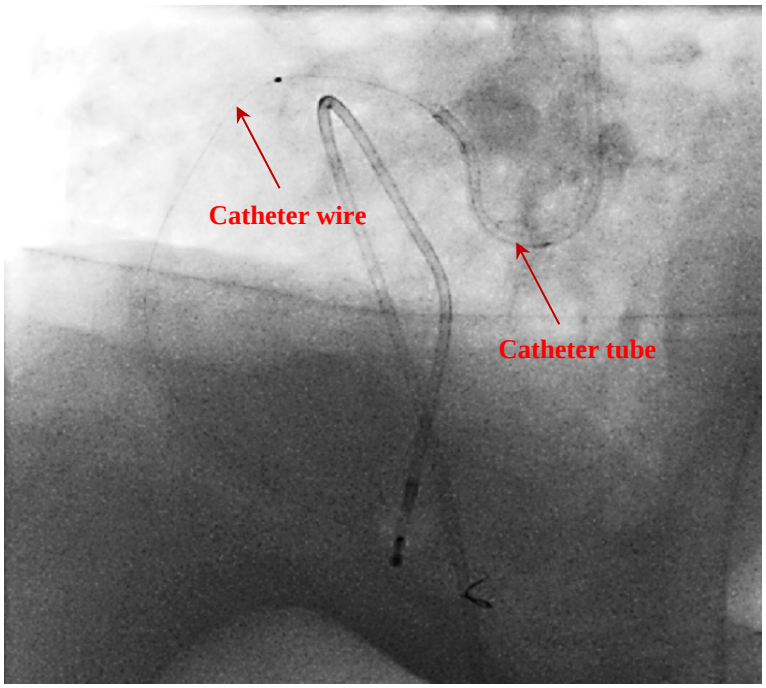
Catheter wire
Catheter tube

(b)

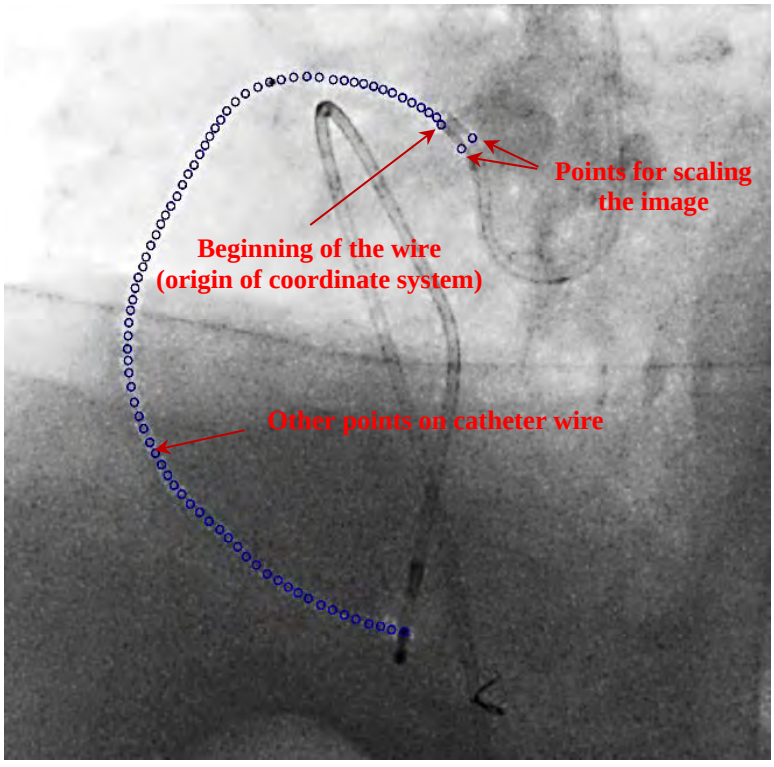
Points for scaling the image
Beginning of the wire (origin of coordinate system)
Other points on catheter wire

(c)

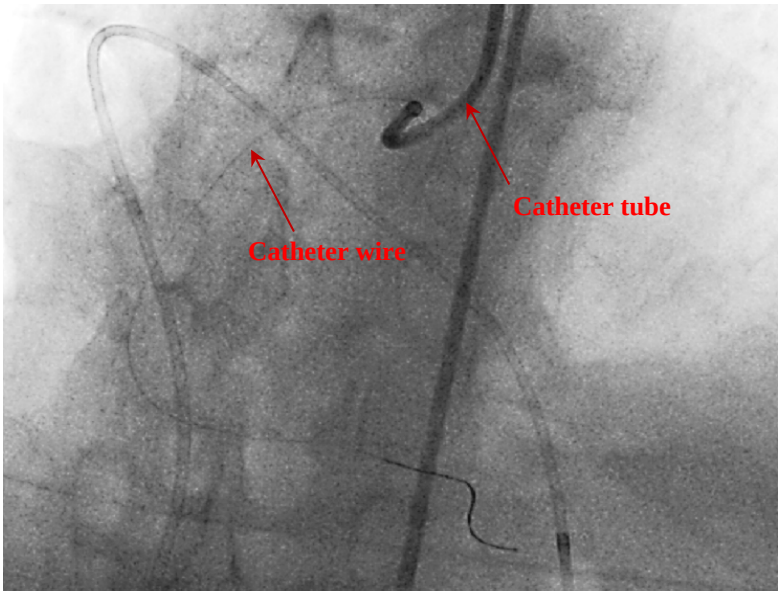

(d)

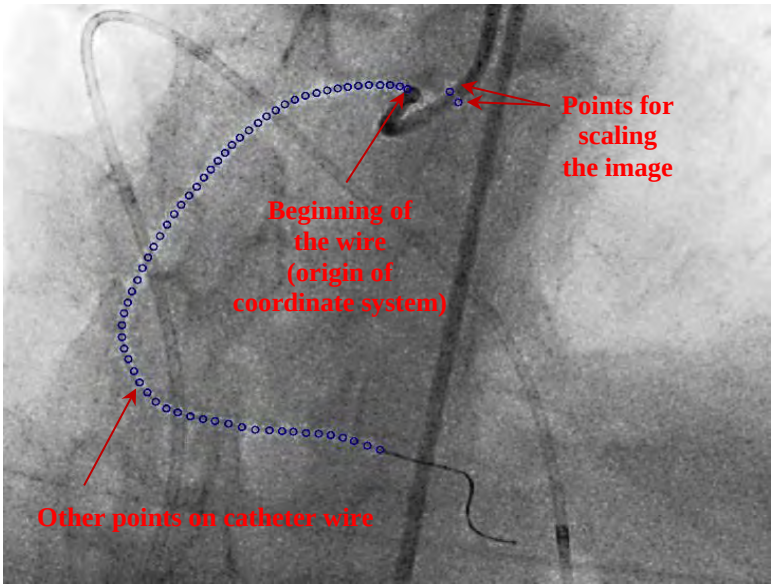

Figure 5-3. Construction of the 3D position curve of catheter based on the angiograms obtained at the RAH: (a, b) where (a) shows angiogram with primary angle = -35.4° and secondary angle = -0.1°; (b) points on (a) image for calibration and position extraction; (c, d) where (c) shows angiogram with primary angle = -0.2° and secondary angle = -29.7°; (d) points on (c) image for calibration and position extraction.

(a)

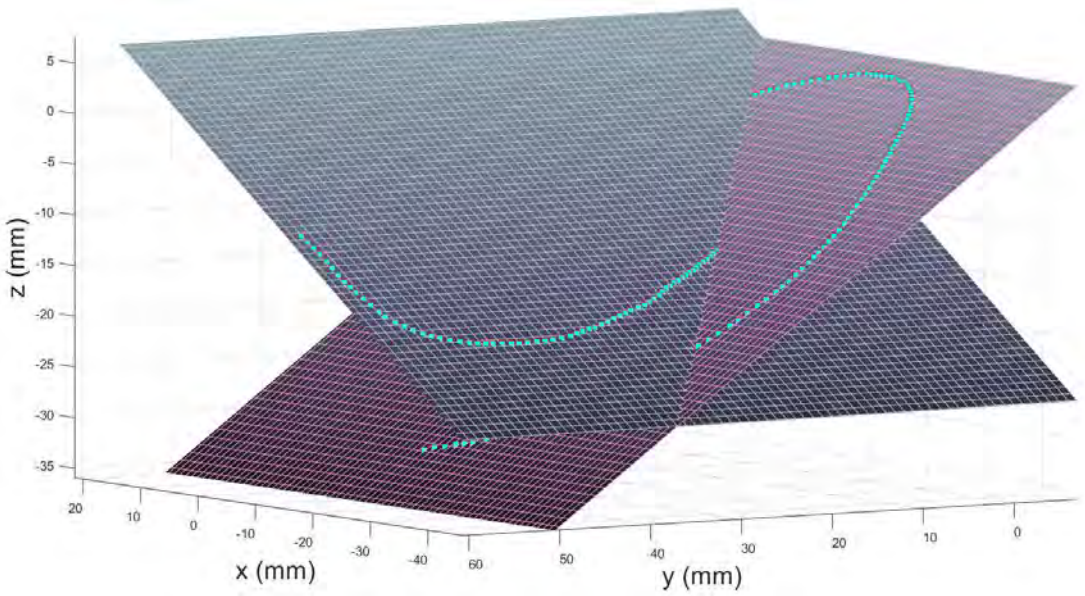

(b)

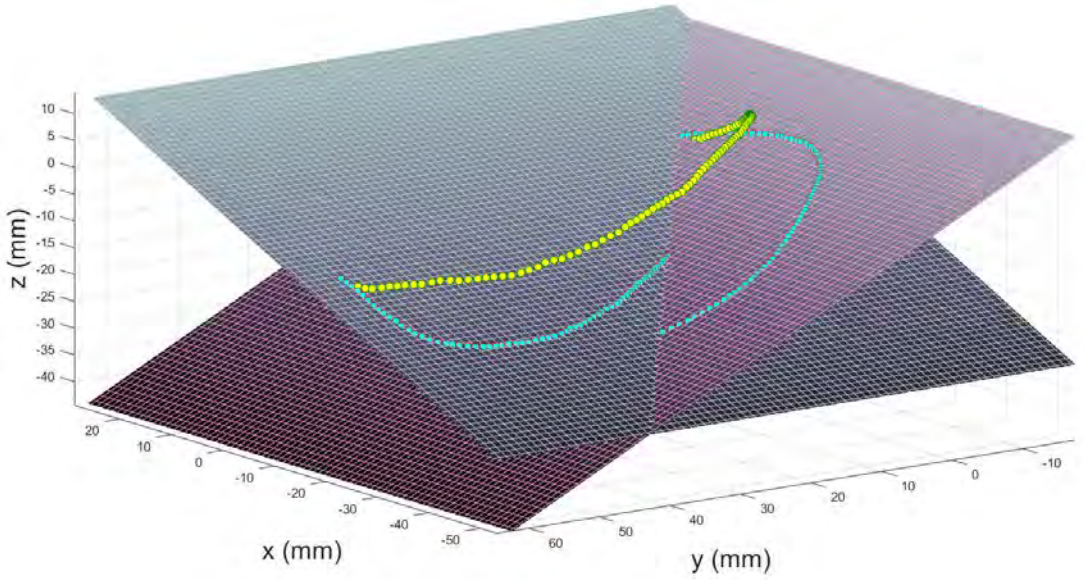

(c)

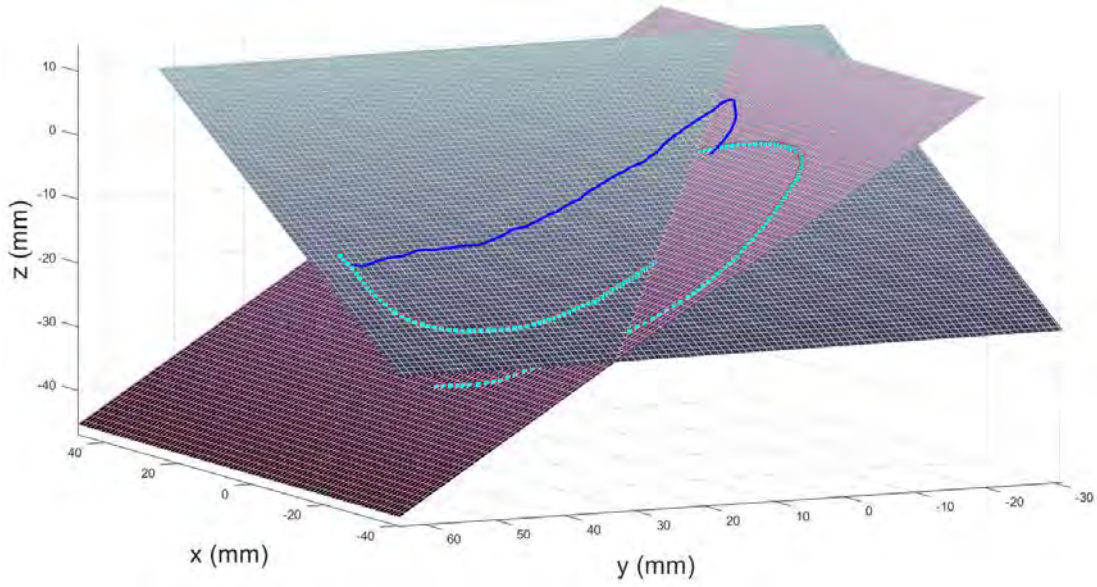

Figure 5-4. Steps for constructing 3D curve of catheter in MATLAB: (a) plotted 2D points obtained from each angiogram plane (blue points); (b) plot 3D points which are the 3D position of the catheter (yellow points); (c) 3D curve of the catheter by connecting the extracted points.

(a)

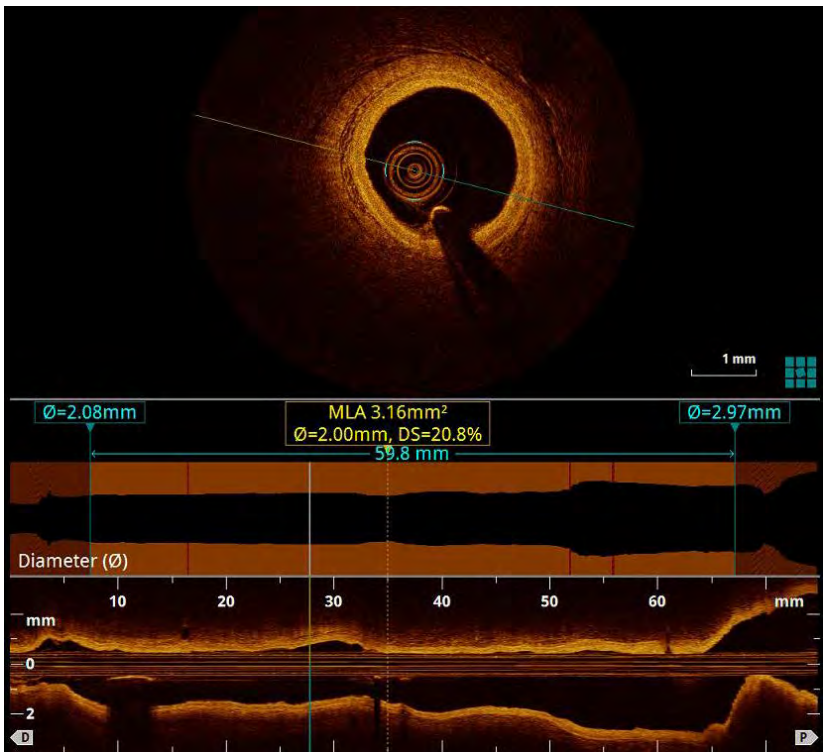

(b)

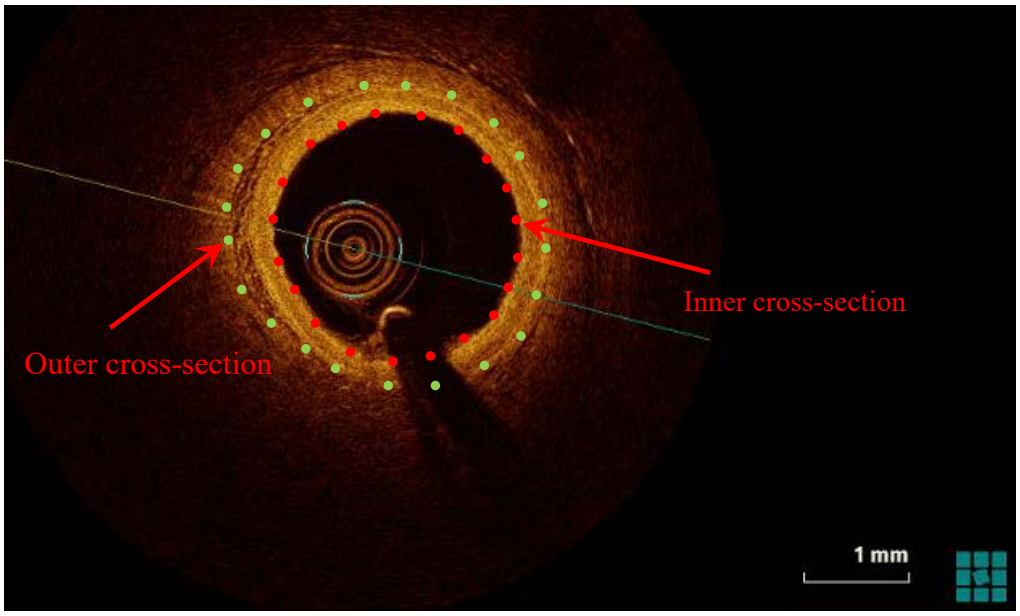

Figure 5-5. (a) In-vivo OCT images used to construct the inner and outer cross-sections of the artery around the 3D catheter position; (b) schematic point selection in the 2D plane for constructing inner (red points) and outer (green points) cross-sections (ST. JUDE MEDICAL software [20]).

(a)

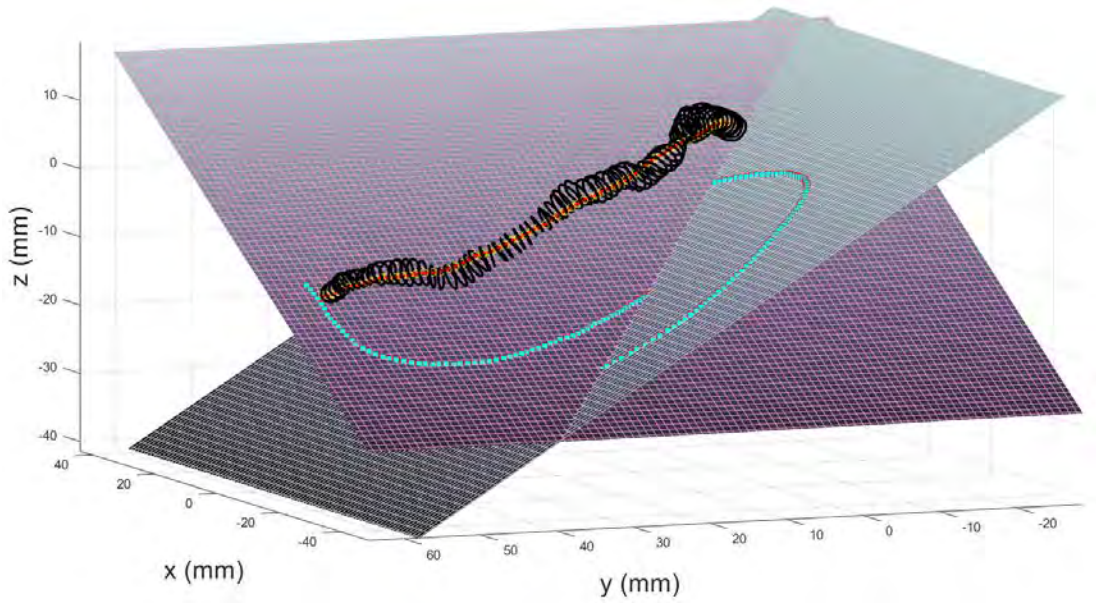

(b)

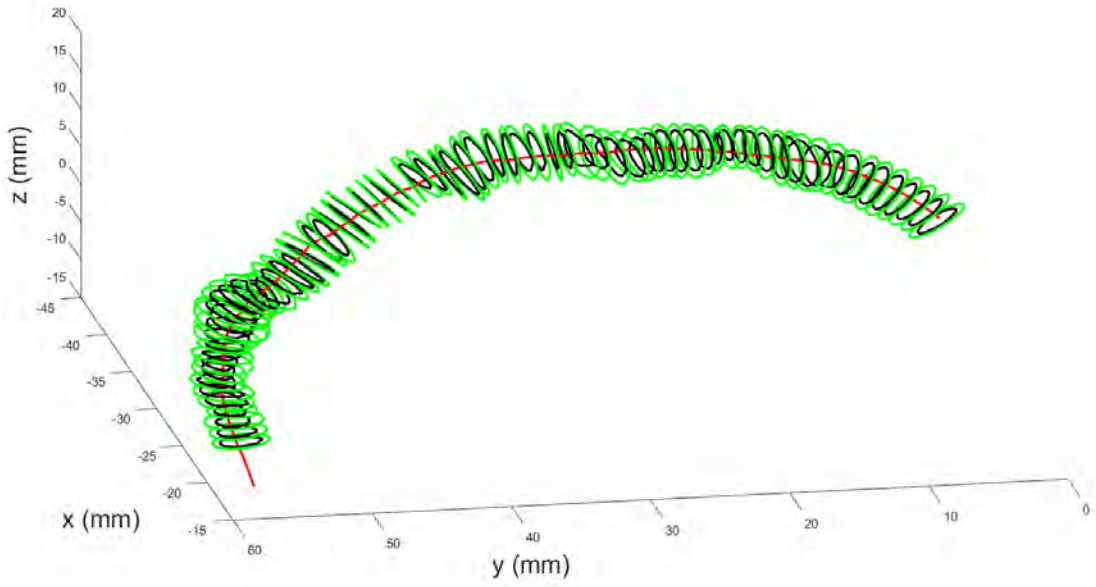

Figure 5-6. Inner and outer cross-sections of the artery based on OCT in-vivo images along the catheter curve (a) inner cross-sections; (b) inner and outer cross-sections together.

(a)

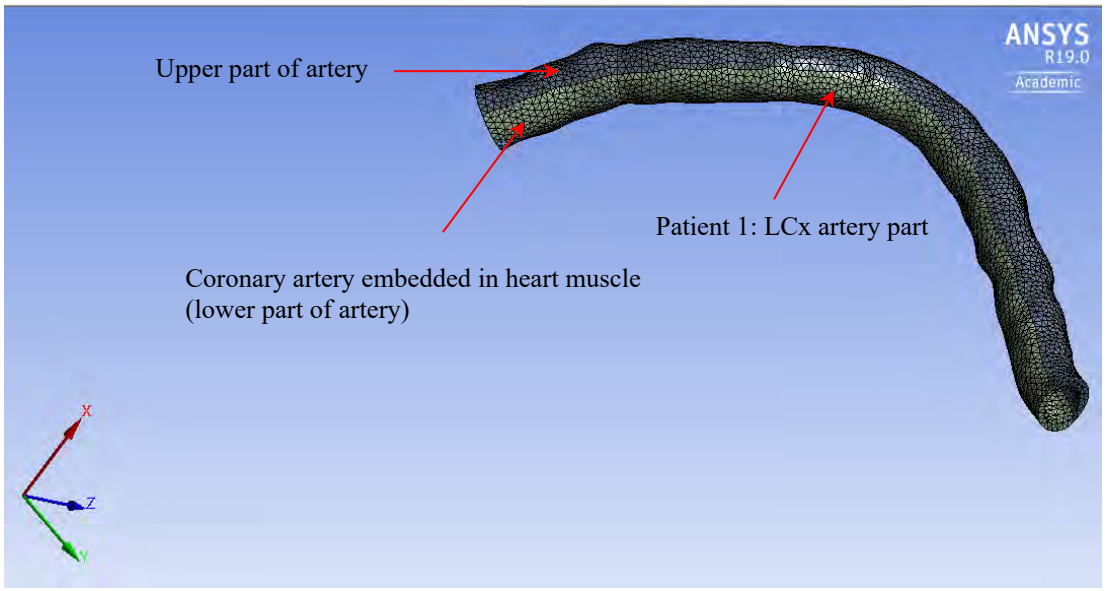
Upper part of artery
Patient 1: LCx artery part
Coronary artery embedded in heart muscle
(lower part of artery)
ANSYS
R19.0
Academic
X
Z
Y

(b)

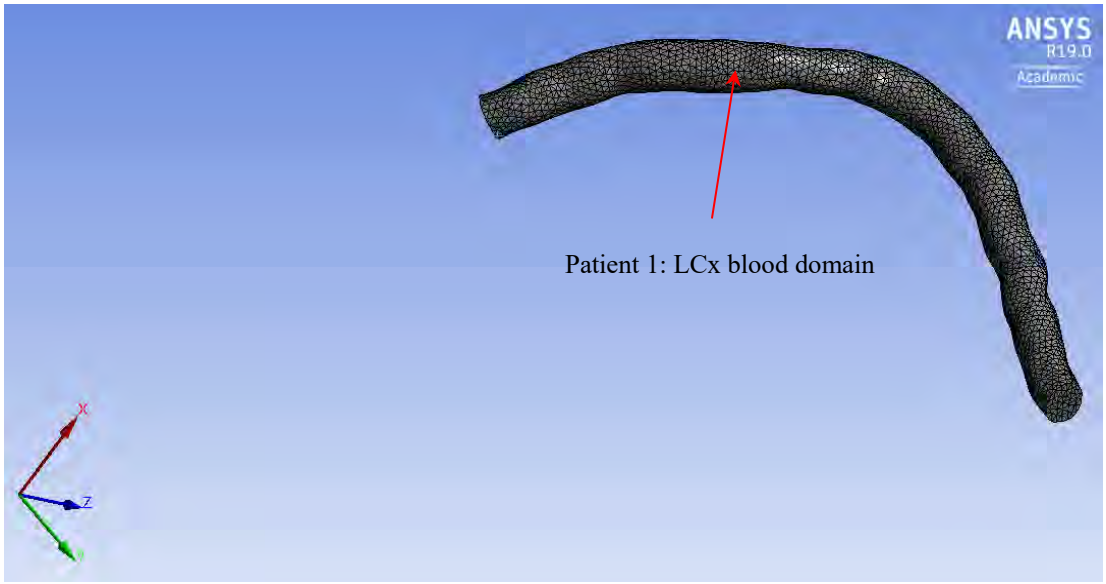
Patient 1: LCx blood domain
ANSYS
R19.0
Academic
X
Z
Y

(c)

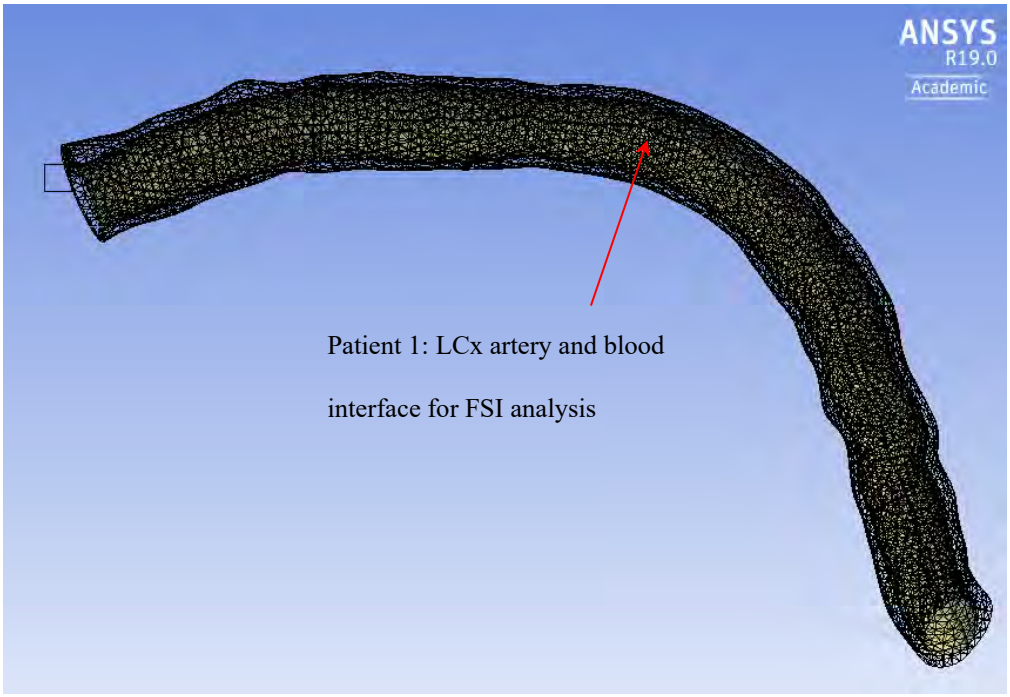

Figure 5-7. Patient 1: 3D realistic model of LCx coronary artery for Patient 1 with 20% stenosis: (a) artery itself (lower part, shown in green colour, is embedded inside the heart tissue); (b) blood inside the artery; (c) FSI surface between the two domains (i.e., the yellow surface).

(a)

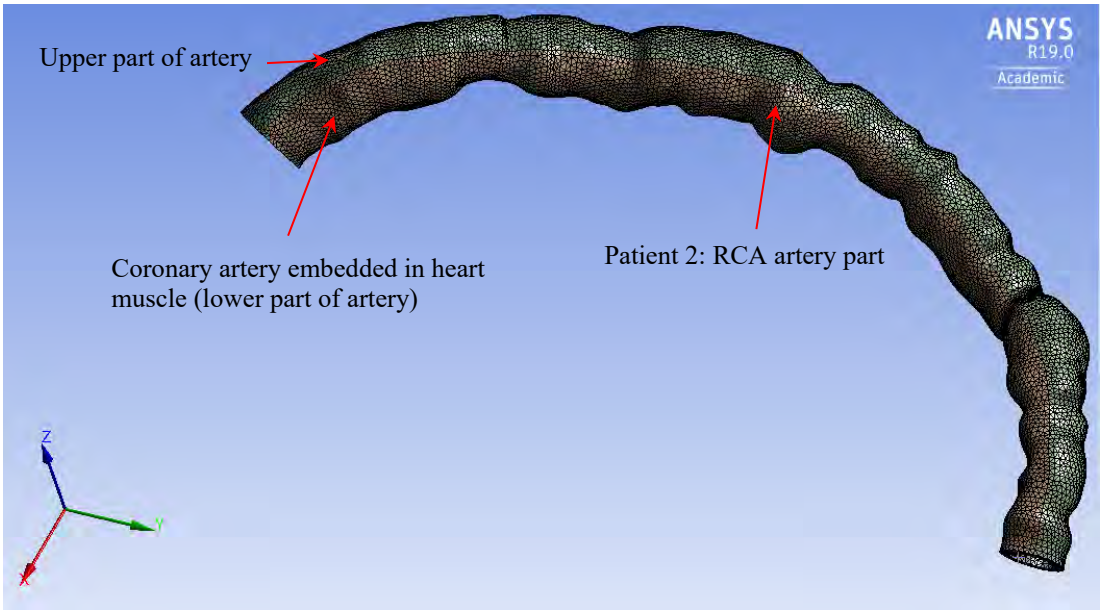
Upper part of artery
Coronary artery embedded in heart muscle (lower part of artery)
Patient 2: RCA artery part
ANSYS
R19.0
Academic
Z
Y
X

(b)

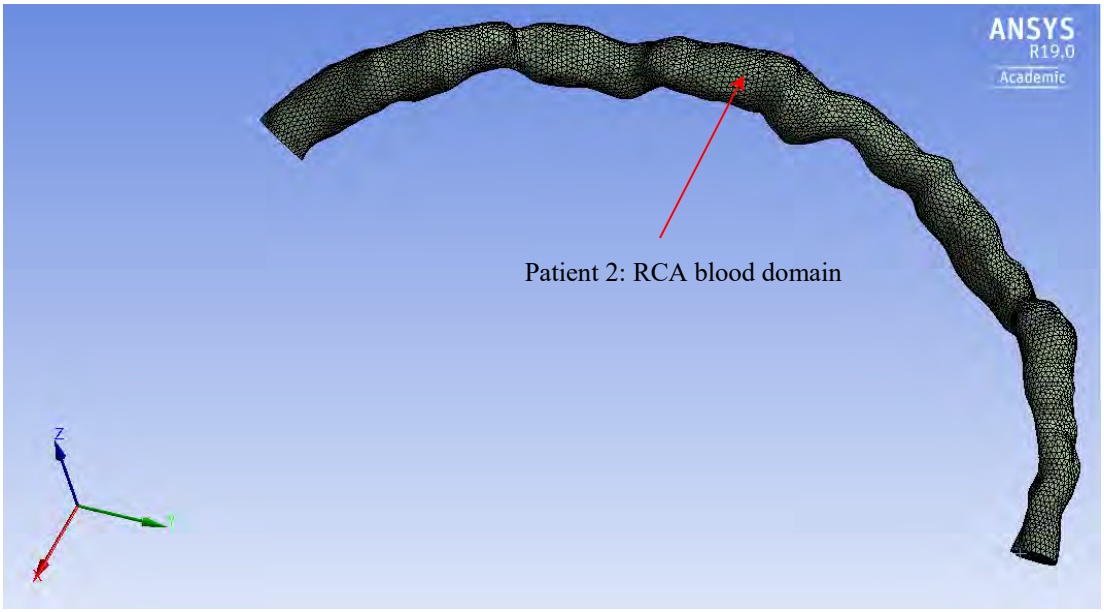
Patient 2: RCA blood domain
ANSYS
R19.0
Academic
Z
Y
X

(c)

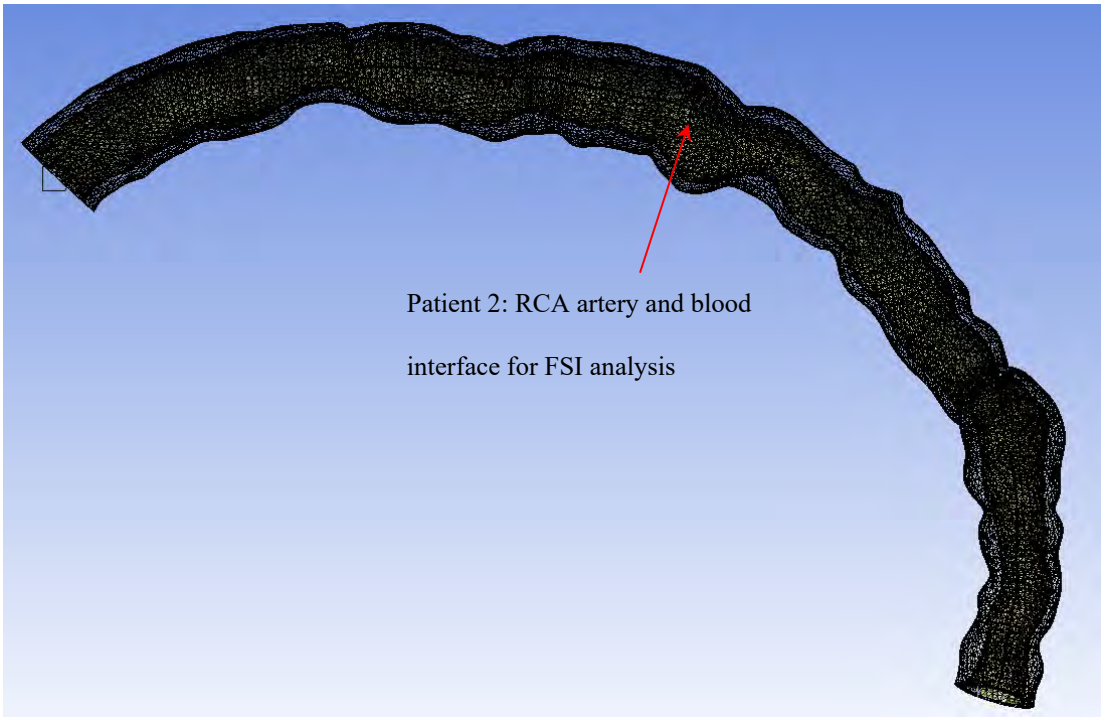

Figure 5-8. Patient 2: 3D realistic model of RCA coronary artery for Patient 2: (a) artery itself (lower part, shown in red colour, is embedded inside the heart tissue); (b) blood inside the artery; (c) FSI surface between the two domains (i.e., the yellow surface).

(a)

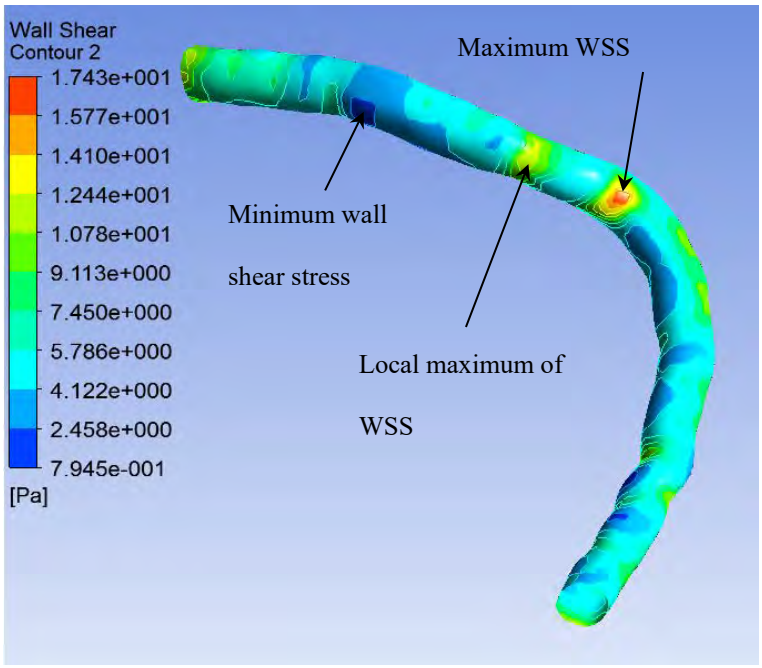

(b)

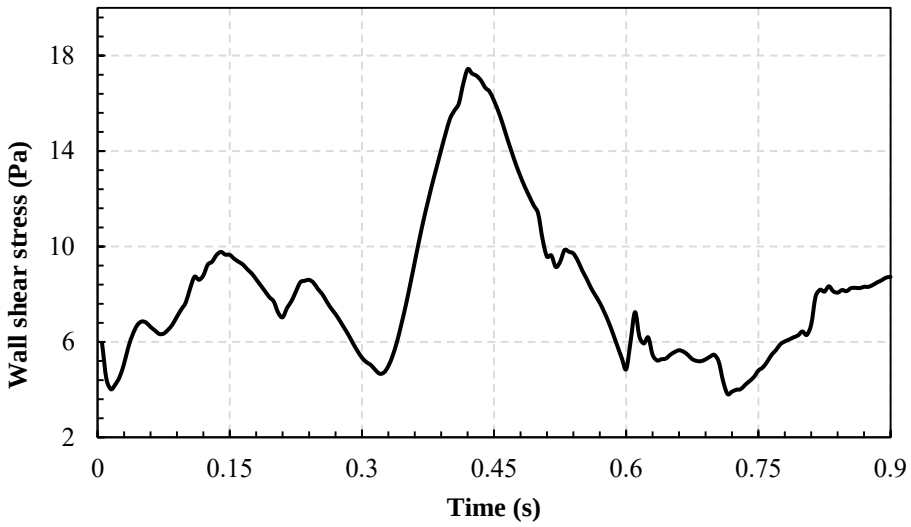

Figure 5-9. Patient 1: WSS of LCx coronary artery: (a) WSS spatial distribution; (b) time-dependent variation at the location of the maximum value of (a).

(a)

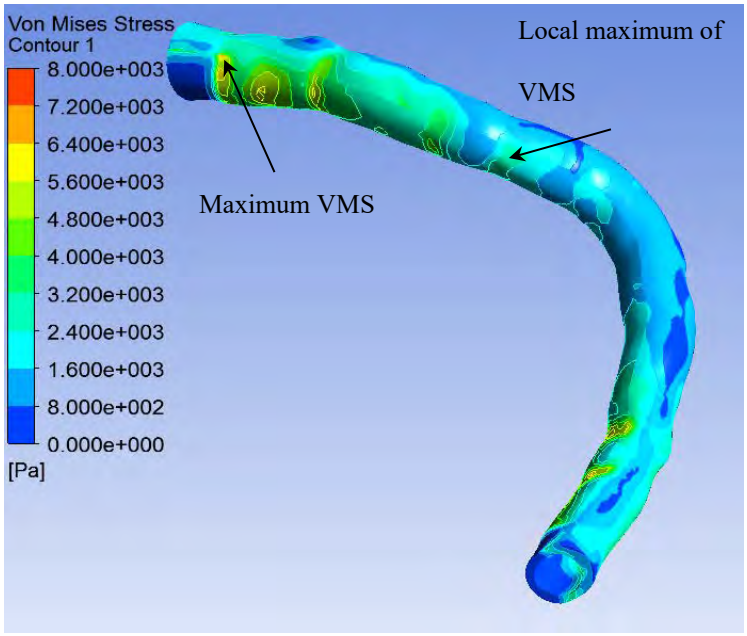

(b)

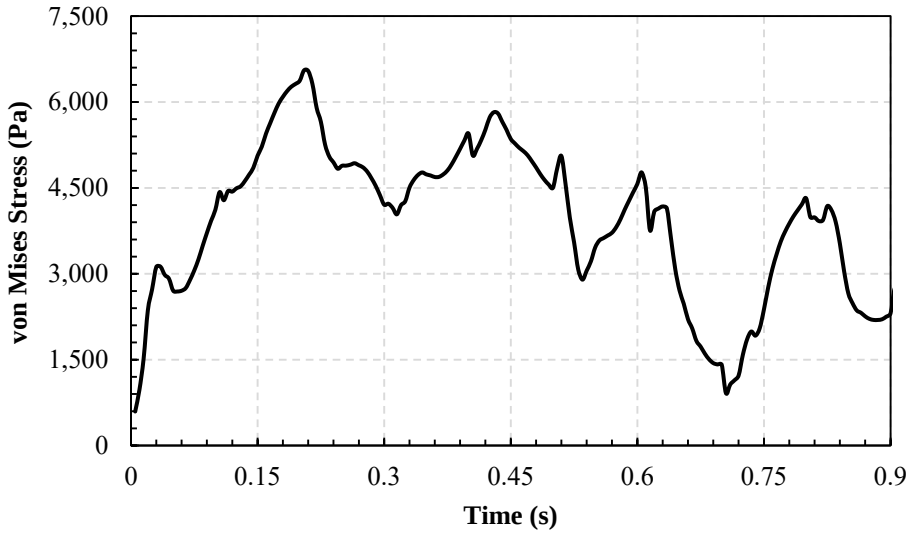

Figure 5-10. Patient 1: VMS of LCx coronary artery: (a) VMS spatial distribution; (b) time-dependent variation at the location of the maximum value of (a).

(a)

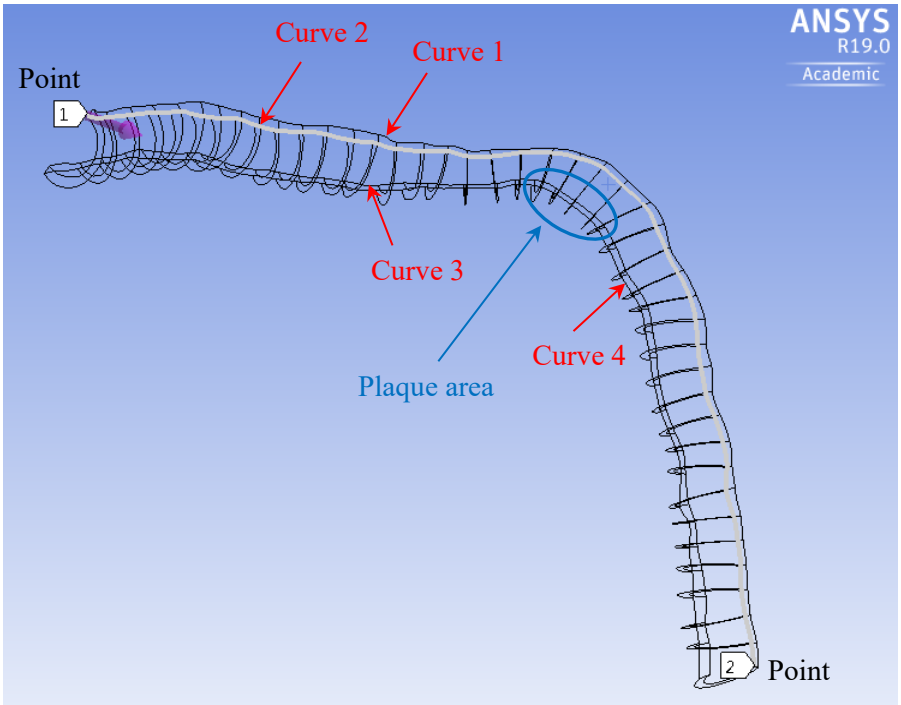
ANSYS
R19.0
Academic
Point
1
Curve 2
Curve 1
Curve 3
Plaque area
Curve 4
2
Point

(b)

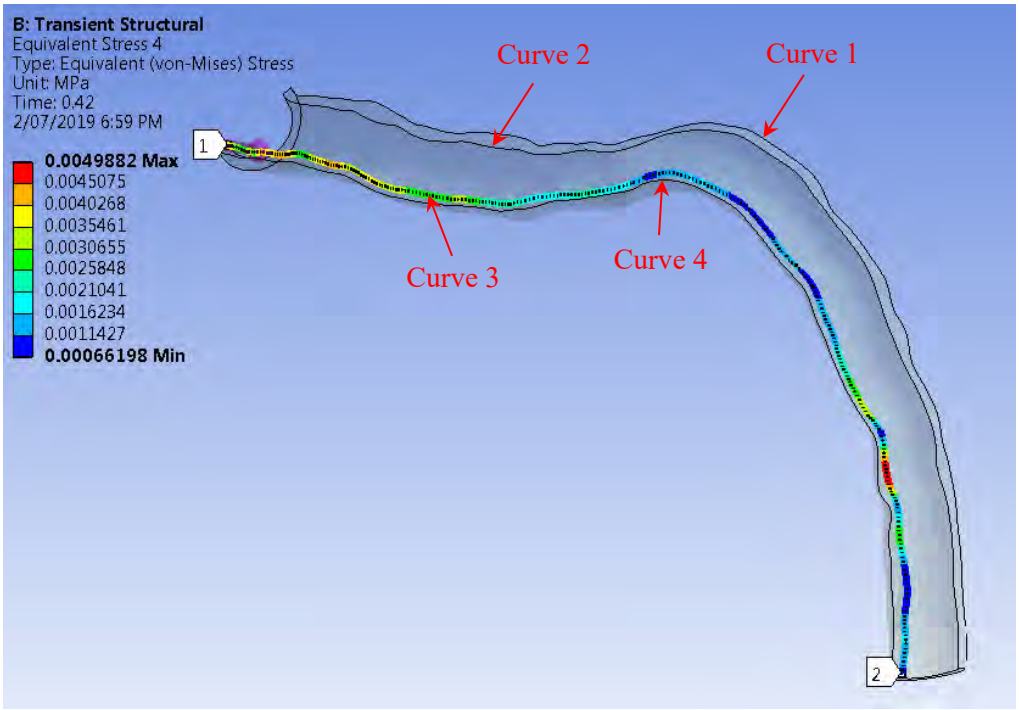
B: Transient Structural
Equivalent Stress 4
Type: Equivalent (von-Mises) Stress
Unit: MPa
Time: 0.42
2/07/2019 6:59 PM
0.0049882 Max
0.0045075
0.0040268
0.0035461
0.0030655
0.0025848
0.0021041
0.0016234
0.0011427
0.00066198 Min
1
Curve 2
Curve 1
Curve 3
Curve 4
2

(c)

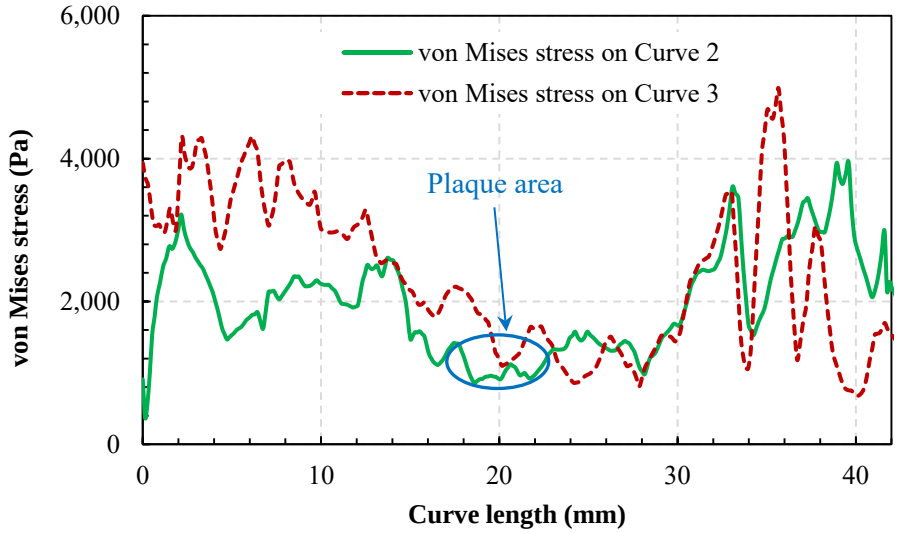
6,000
4,000
2,000
0
von Mises stress (Pa)
von Mises stress on Curve 2
von Mises stress on Curve 3
Plaque area
0
10
20
30
40
Curve length (mm)

(d)

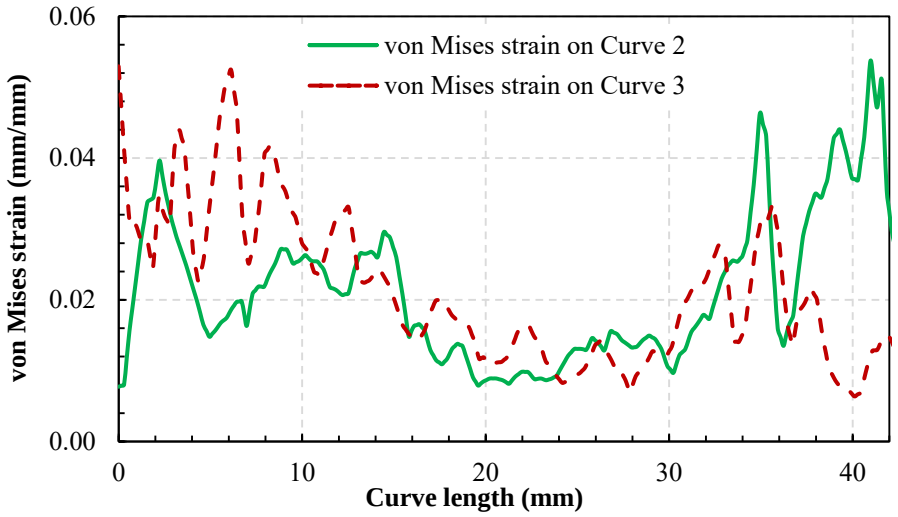
0.06
0.04
0.02
0.00
von Mises strain (mm/mm)
von Mises strain on Curve 2
von Mises strain on Curve 3
0
10
20
30
40
Curve length (mm)

(e)

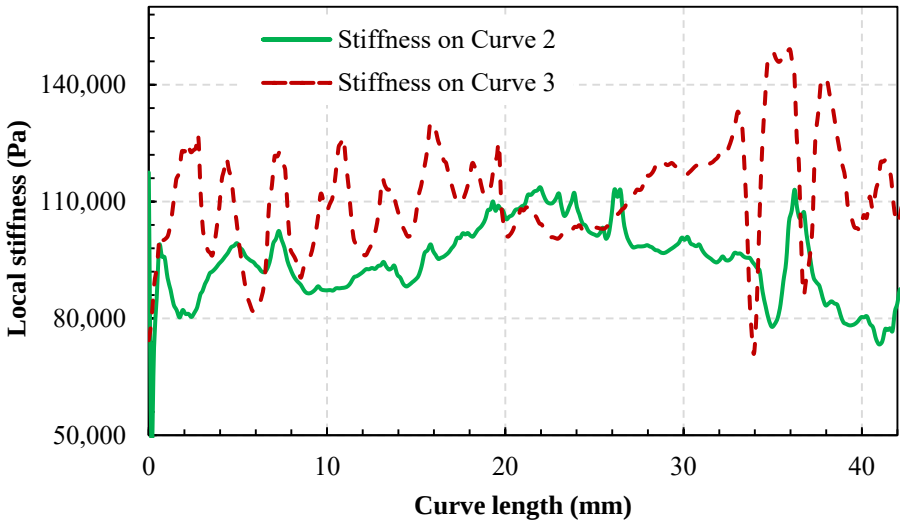
Stiffness on Curve 2
Stiffness on Curve 3
140,000
110,000
80,000
50,000
Local stiffness (Pa)
0
10
20
30
40
Curve length (mm)

(f)

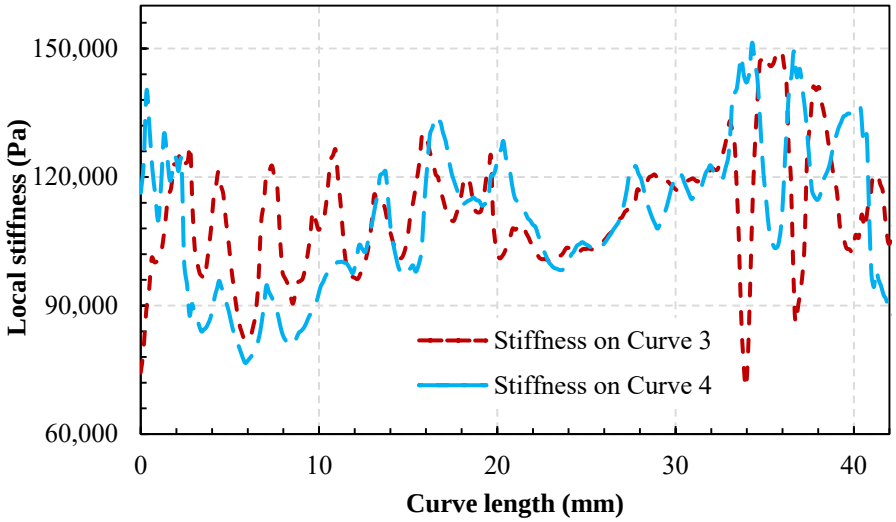
150,000
120,000
90,000
60,000
Local stiffness (Pa)
Stiffness on Curve 3
Stiffness on Curve 4
0
10
20
30
40
Curve length (mm)

(g)

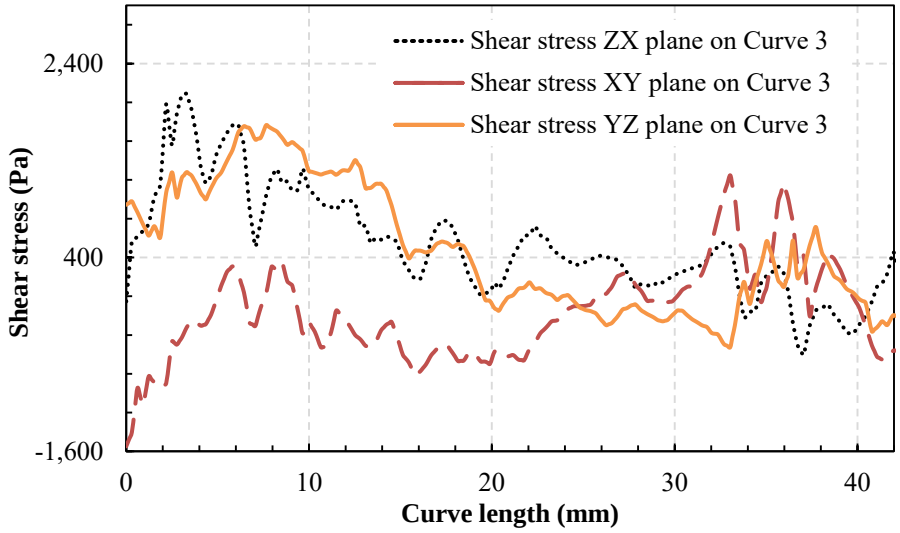

(h)

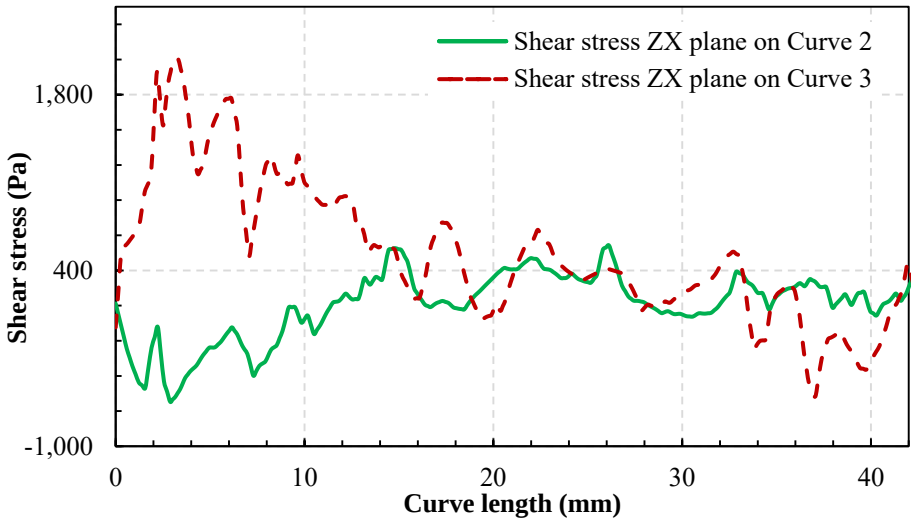

Figure 5-11. Patient 1: Imaginary longitudinal cross at the intersection of the LCx artery and heart muscle which gives a better vision of stress/strain distributions on four different curves (i.e., curves 1-4, see subfigures (a, b)); time is set to 0.42 s when the shear stress is maximum; (c) VMS for Curve 2 and Curve 3 along the length; (d) VMS and von Mises strain for Curve 2 and Curve 3; (e) stiffness for Curve 2 and Curve 3 along the length; (f) stiffness for Curve 3 and Curve 4 along the length; (g) shear stress on Curve 3 for different planes: XY, ZY, and ZX; (h) shear stress of ZX for Curve 2 and Curve 3.

(a)

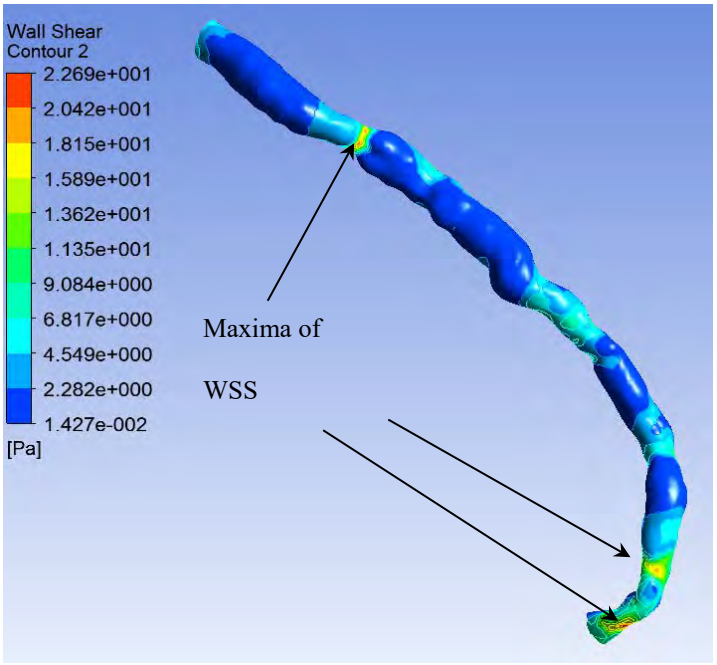

(b)

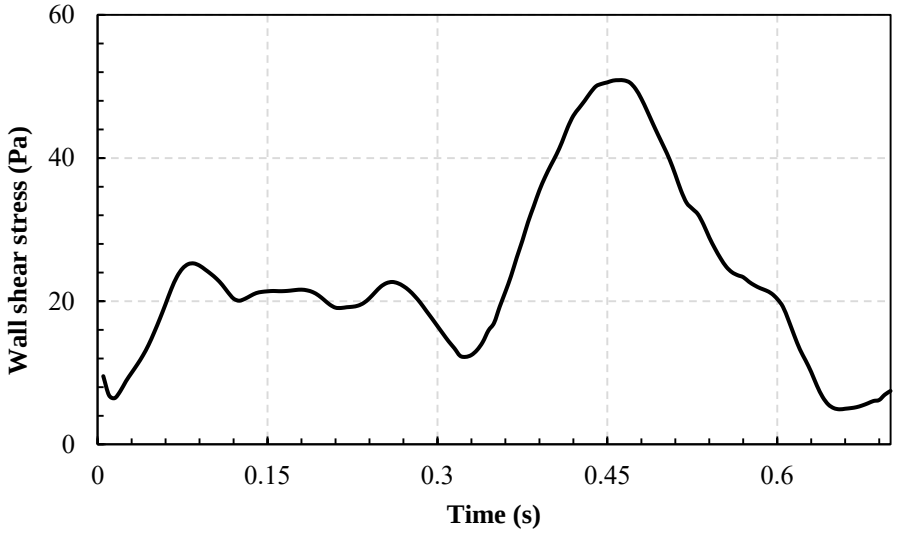

Figure 5-12. Patient 2: WSS of RCA coronary artery: (a) WSS spatial distribution; (b) time-dependent variation at the location of the maximum value of (a).

(a)

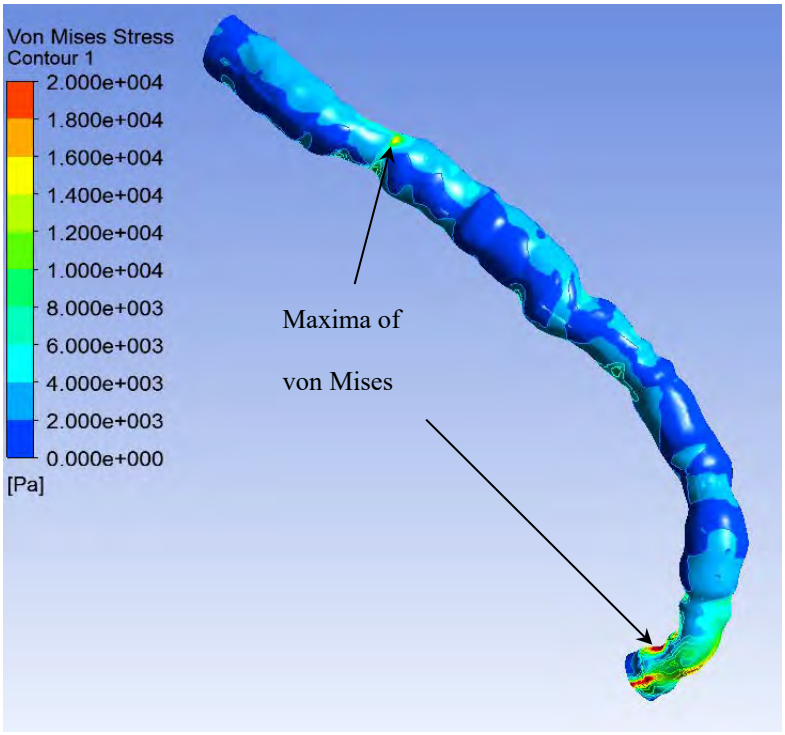

(b)

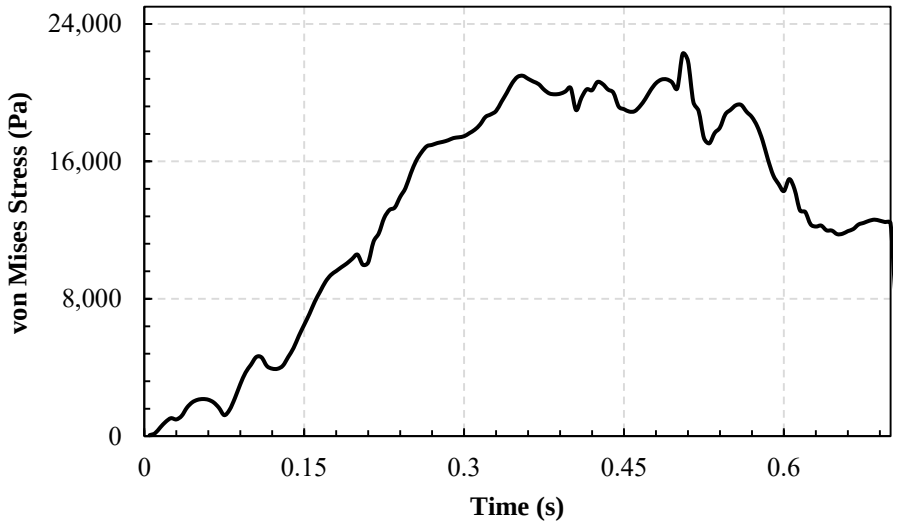

Figure 5-13. Patient 2: VMS of RCA coronary artery: (a) VMS spatial distribution; (b) time-dependent variation at the location of the maximum value of (a).

(a)

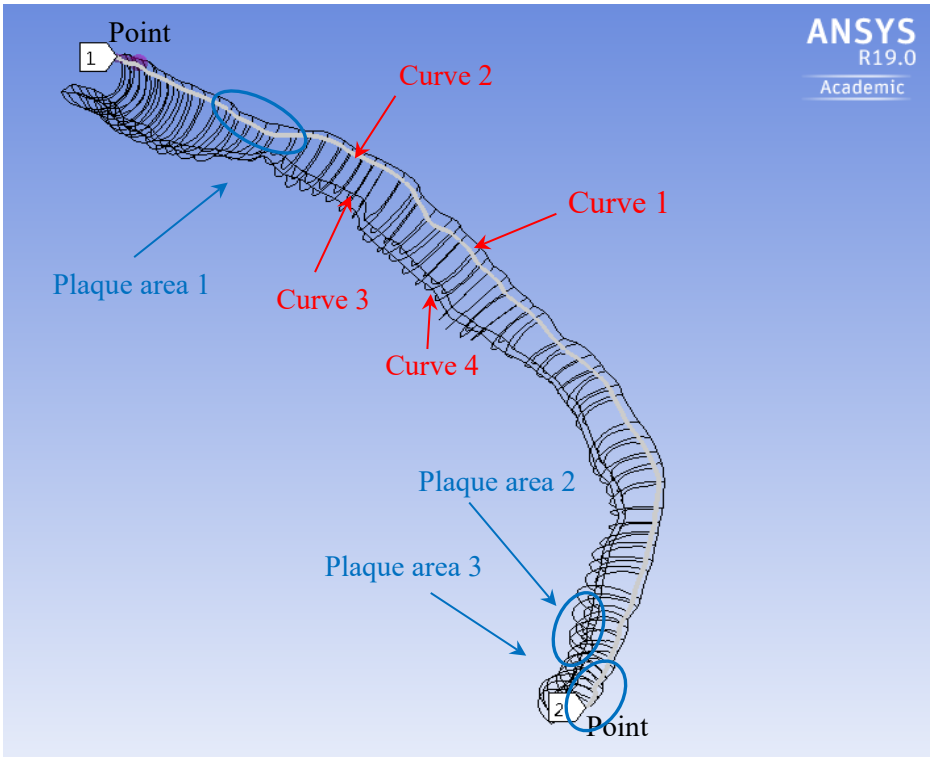
Point
1
Curve 2
Curve 1
Plaque area 1
Curve 3
Curve 4
Plaque area 2
Plaque area 3
2
Point
ANSYS
R19.0
Academic

(b)

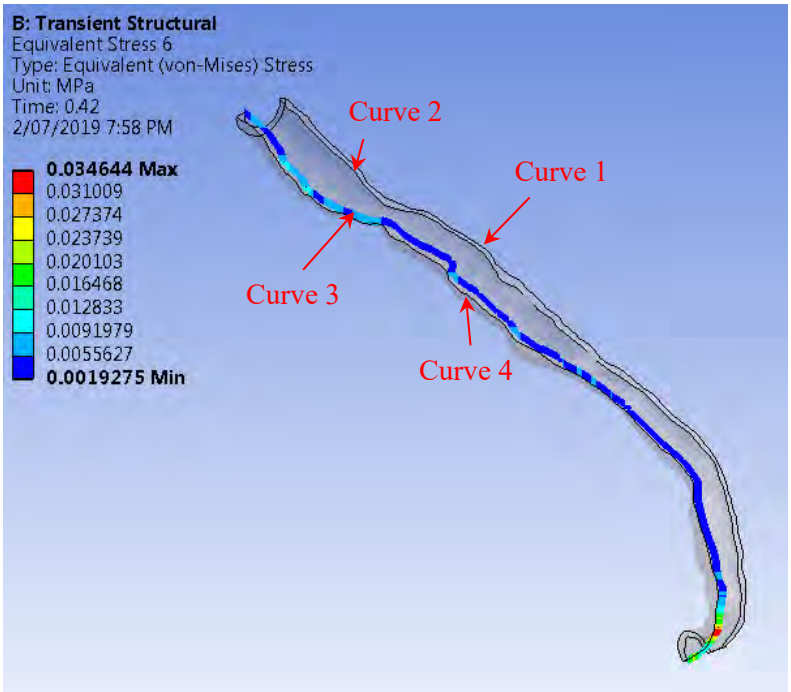
B: Transient Structural
Equivalent Stress 6
Type: Equivalent (von-Mises) Stress
Unit: MPa
Time: 0.42
2/07/2019 7:58 PM
0.034644 Max
0.031009
0.027374
0.023739
0.020103
0.016468
0.012833
0.0091979
0.0055627
0.0019275 Min
Curve 2
Curve 1
Curve 3
Curve 4

(c)

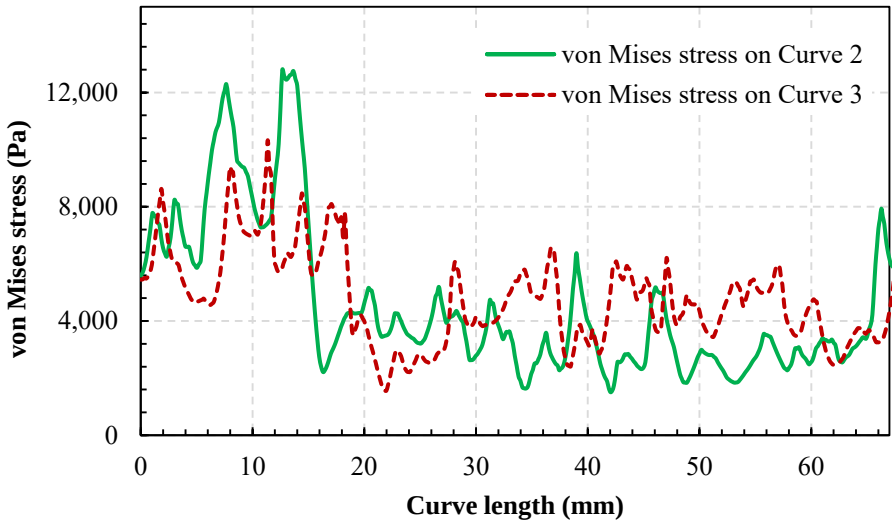
von Mises stress on Curve 2
von Mises stress on Curve 3
12,000
8,000
4,000
0
von Mises stress (Pa)
0
10
20
30
40
50
60
Curve length (mm)

(d)

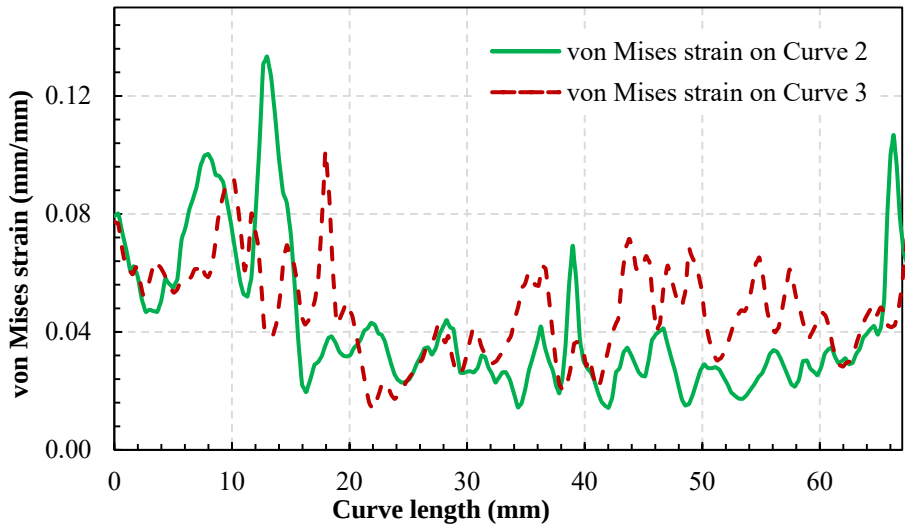
von Mises strain on Curve 2
von Mises strain on Curve 3
0.12
0.08
0.04
0.00
von Mises strain (mm/mm)
0
10
20
30
40
50
60
Curve length (mm)

(e)

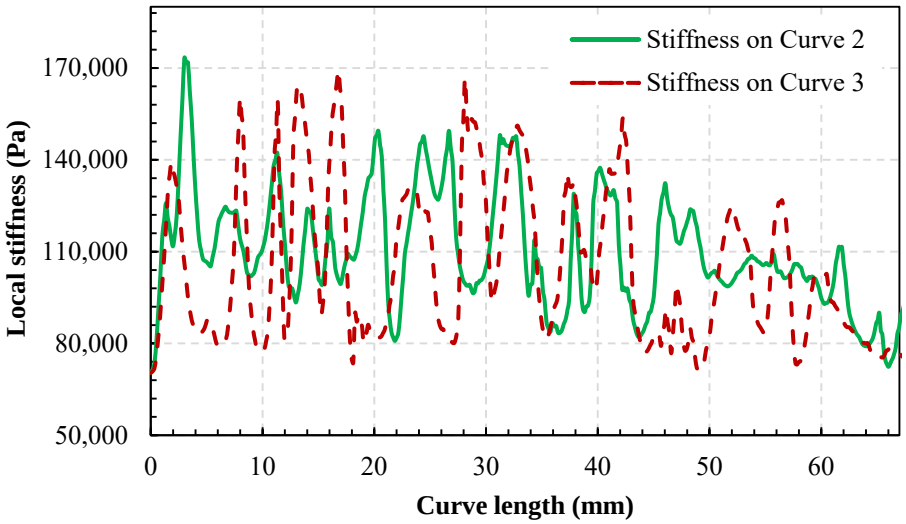
Stiffness on Curve 2
Stiffness on Curve 3
Local stiffness (Pa)
170,000
140,000
110,000
80,000
50,000
0
10
20
30
40
50
60
Curve length (mm)

(f)

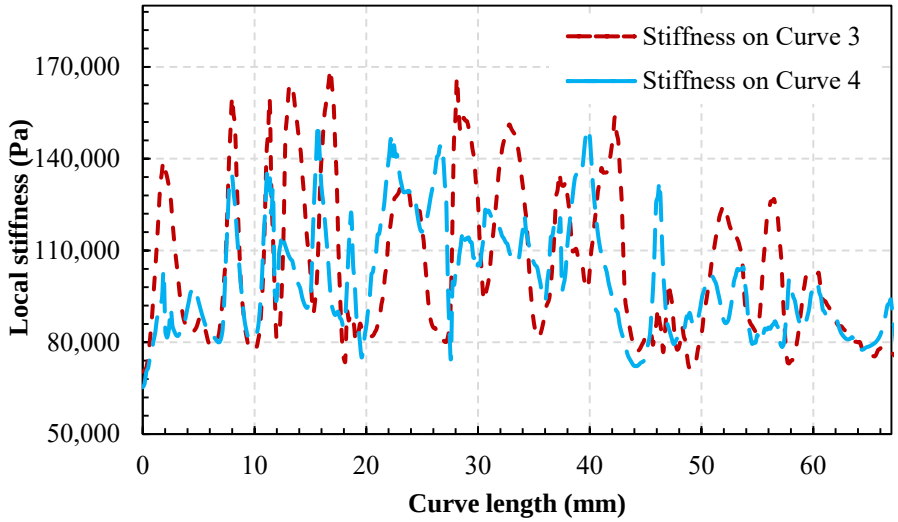
Stiffness on Curve 3
Stiffness on Curve 4
Local stiffness (Pa)
170,000
140,000
110,000
80,000
50,000
0
10
20
30
40
50
60
Curve length (mm)

(g)

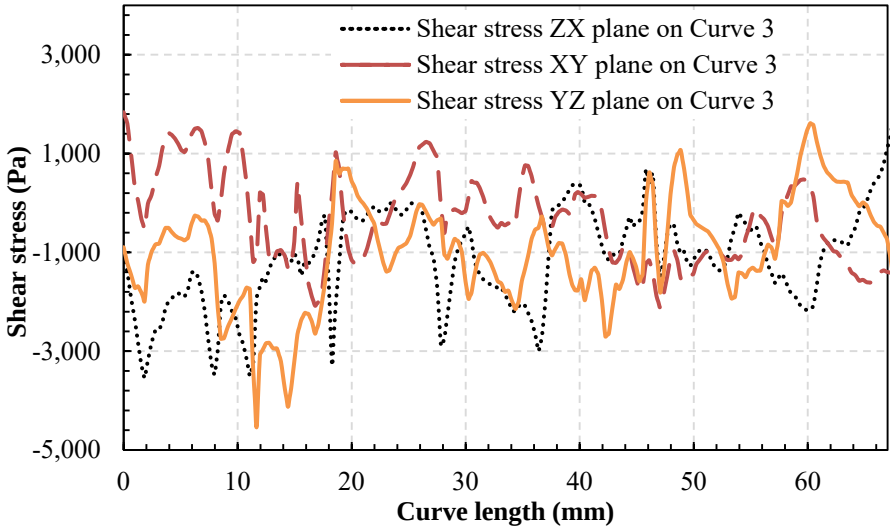

(h)

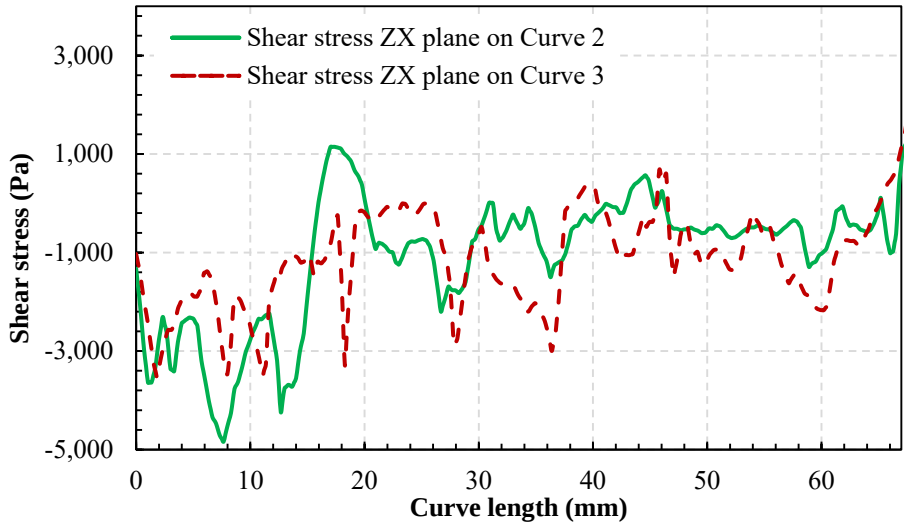

Figure 5-14. Patient 2: Imaginary longitudinal cross at the intersection of the RCA artery and heart muscle which gives a better vision of stress/strain distributions on four different curves (i.e., curves 1-4, see subfigures (a, b)); time is set to 0.42 s when the shear stress is maximum; (c) VMS for Curve 2 and Curve 3 along the length; (d) VMS and von Mises strain for Curve 2 and Curve 3; (e) stiffness for Curve 2 and Curve 3 along the length; (f) stiffness for Curve 3 and Curve 4 along the length; (g) shear stress on Curve 3 for different planes: XY, ZY, and ZX; (h) shear stress of ZX for Curve 2 and Curve 3.

(a)

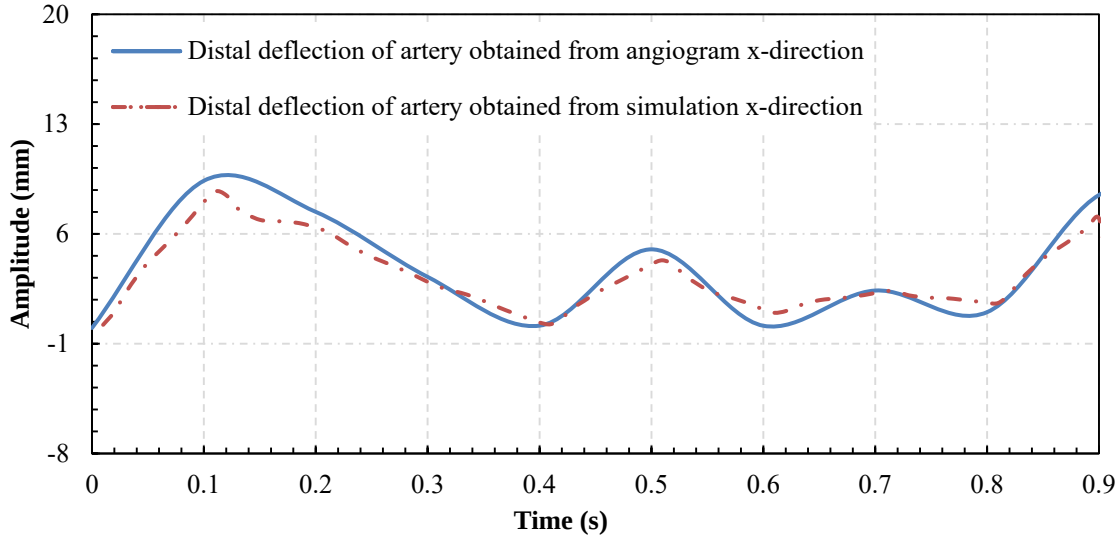
Distal deflection of artery obtained from angiogram x-direction
Distal deflection of artery obtained from simulation x-direction
Amplitude (mm)
20
13
6
-1
-8
0
0.1
0.2
0.3
0.4
0.5
0.6
0.7
0.8
0.9
Time (s)

(b)

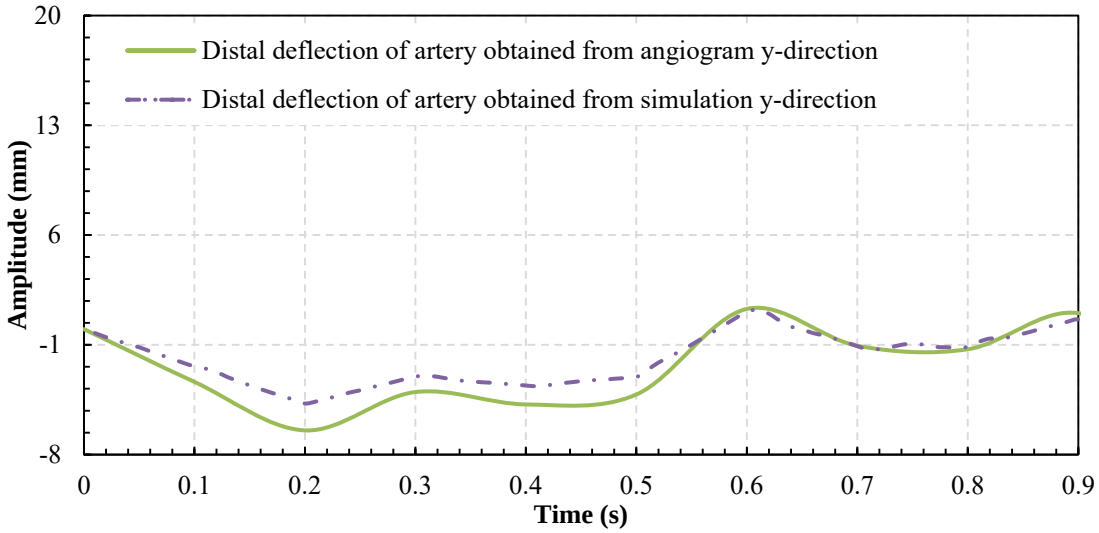
Distal deflection of artery obtained from angiogram y-direction
Distal deflection of artery obtained from simulation y-direction
Amplitude (mm)
20
13
6
-1
-8
0
0.1
0.2
0.3
0.4
0.5
0.6
0.7
0.8
0.9
Time (s)

(c)

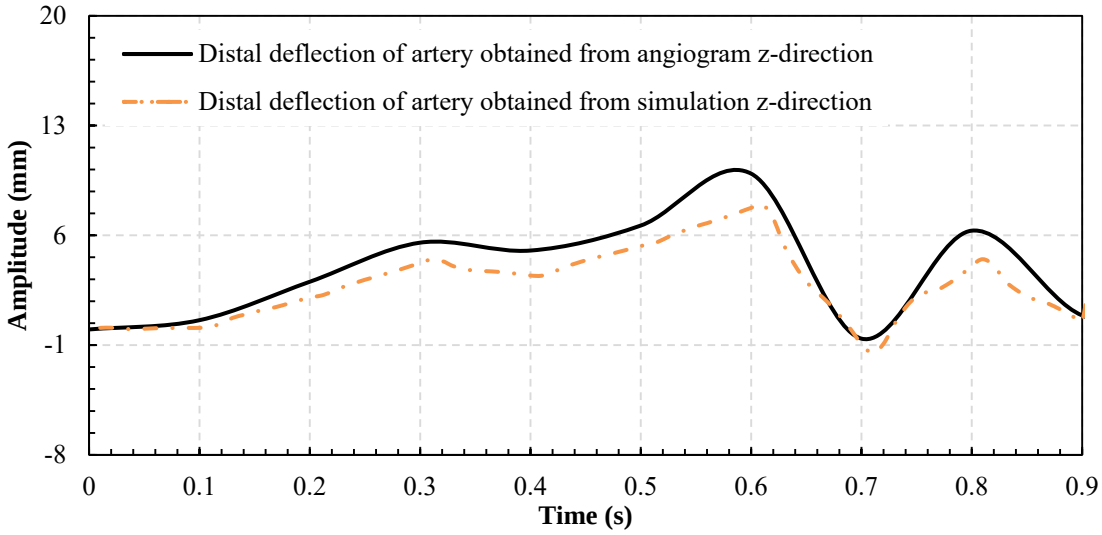

Figure 5-15. Model validation with clinical data: Distal deflections in the x (a), y (b), and z (c) directions for the LCx coronary artery versus time for Patient 1.

Chapter 6

Plaque rupture prediction for an atherosclerotic coronary artery via use of *in vivo* clinical data

Statement of Authorship

Title of Paper	Plaque rupture prediction for an atherosclerotic coronary artery via use of *in vivo* clinical data
Publication Status	☐ Published ☐ Accepted for Publication ☑ Submitted for Publication ☐ Unpublished and Unsubmitted work written in manuscript style
Publication Details	

Principal Author

Name of Principal Author (Candidate)	Alireza Gholipour
Contribution to the Paper	Performed all clinical data collection, modelling, simulations, and wrote the manuscript.
Overall percentage (%)	75
Certification:	This paper reports on original research I conducted during the period of my Higher Degree by Research candidature and is not subject to any obligations or contractual agreements with a third party that would constrain its inclusion in this thesis. I am the primary author of this paper.
Signature	Date 12/09/2019

Co-Author Contributions

By signing the Statement of Authorship, each author certifies that:

i. the candidate's stated contribution to the publication is accurate (as detailed above);

ii. permission is granted for the candidate in include the publication in the thesis; and

iii. the sum of all co-author contributions is equal to 100% less the candidate's stated contribution.

Name of Co-Author	Dr. Mergen H. Ghayesh
Contribution to the Paper	Helped in modelling/simulations, checked the results, and assisted in the preparation of the manuscript.
Signature	Date 13/09/2019

Name of Co-Author	Prof. Anthony Zander
Contribution to the Paper	Checked the results and assisted in the preparation of the manuscript.
Signature	Date 16/09/19

Name of Co-Author	A/Prof. Peter Psaltis		
Contribution to the Paper	Helped in clinical data collection, checked the results and assisted in the preparation of the manuscript.		
Signature		Date	16/9/19

Please cut and paste additional co-author panels here as required.

Plaque rupture prediction for an atherosclerotic coronary artery via use of *in vivo* clinical data

Alireza Gholipour[1], Mergen H. Ghayesh[1,*], Anthony C. Zander[1], Peter J. Psaltis[2, 3]

[1]*School of Mechanical Engineering, University of Adelaide, Adelaide, South Australia 5005, Australia,*
[2]*Adelaide Medical School, University of Adelaide, Adelaide, South Australia 5005, Australia,*
[3]*Vascular Research Centre, Lifelong Health Theme, South Australian Health and Medical Research Institute (SAHMRI), Adelaide, South Australia 5000, Australia,*

**Corresponding author: mergen.ghayesh@adelaide.edu.au*

Abstract

The three-dimensional (3D) fracture biomechanics of an atherosclerotic coronary artery is analysed by the development of a finite element model via use of *in vivo* clinical data and conducting a fatigue analysis for plaque rupture based on smart crack growth. Three dimensional *in vivo* modelling/simulation of the coronary artery is developed based on angiography, optical coherence tomography (OCT), electrocardiography (ECG), and time-dependent pressure measurement conducted at the Royal Adelaide Hospital (RAH). An image processing technique is applied to the clinical data to develop a realistic 3D model of the coronary artery. A biomechanical simulation is then conducted using the finite element method (FEM) incorporating fully coupled fluid-structure interaction (FSI) to determine high-risk regions in the artery by examining stress fields for both blood and artery where high stress areas are recognised as potential locations for plaque rupture (crack) initiation. Finally plaque crack extension and the life cycle of the artery are investigated based on Paris' law. The developed model/simulation is comprehensive, incorporating the effect of fluid/solid couplings, non-Newtonian blood viscosity, three-dimensionality, physiological blood pressure pulsation, and surrounding heart tissue.

Keywords: atherosclerotic coronary artery, crack propagation, smart crack growth, OCT, plaque rupture prediction

6.2 Introduction

Heart diseases and stroke, as the largest causes of death globally and hence economic and social burdens, are responsible for the death of 15.2 million people globally per annum [1]; among these two causes of death, heart diseases are almost double in size to stroke. The primary cause for myocardial infarction (or in general heart attack) is artery occlusion due to plaque disruption. Even though medical imaging techniques continue to rapidly improve, they alone are insufficient to assess the interactions between the flowing blood and the heart structure and hence are not capable of predicting the disease initiation and progression which may lead to myocardial infarction. One promising method to complement medical imaging technology is to employ biomechanical analysis techniques for the cardiovascular system, where by *in vivo* clinical data is used with FSI (here blood and heart structure interaction) analysis for further improvement of our understanding of initiation/progression of heart diseases with the final aim of preventing myocardial infarction.

In order to use biomechanical analysis techniques for plaque rupture prediction/progression (and hence preventing heart attack), the first step is to identify the high risk locations inside atherosclerotic coronary arteries; once this is accomplished, the analysis for plaque rupture and crack growth is conducted to develop further understanding and to extract the critical information necessary to predict disease initiation/progression. Different *in vitro* studies [2-4] showed that atherosclerotic human arteries generally start to fracture at certain values of stress; it is, therefore, reasonable to use maximum stress as a predictor for plaque rupture initiation.

Propagation of cracks inside coronary arteries has been studied in the following investigations: Bank *et al*. [5] discussed fatigue failure as a mechanism causing plaque rupture; they showed that this hypothesis is in agreement with physiologic and epidemiologic data. Versluis *et al*. [6] considered a 2D idealised cross-section of the diseased artery and analysed the fatigue mechanism for different blood pressures, anatomy, and tissue properties; they showed that the crack starts at stress concentration on the lumen wall of the artery and fatigue occurs at low stress levels. Using cohesive surfaces, Ferrara *et al*. [7] modelled a

crack in a 3D regime based on *in vitro* magnetic resonance images using cohesive fracture mechanics which allows a crack to extend along solid boundaries; their findings showed that crack development starts at the internal wall of the artery which was in agreement with experimental findings. Furthermore, they claimed that the possibility of plaque rupture in high levels of stenosis is less. In another study, Paritala *et al*. [8] employed an extended FEM in addition to OCT to develop a 2D model of plaque rupture; they demonstrated that high pulse pressure is equivalent to low plaque life. Histological images of eight atherosclerotic coronary cross-sections were analysed by Rezvani‐Sharif *et al*. [9], who found that lipid pool presence facilitates crack propagation rate.

Plaque rupture has also been investigated in carotid arteries; the following literature review, even though not directly related to the topic of this paper, may inform us more about crack imitation/progression in biological systems. The phenomenon of carotid atherosclerotic plaque rupture was investigated based on MRI by Huang *et al*. [10], who used a modified Paris law to compare crack propagation from numerical data and *in vivo* fibrous cap defects. The effect of calcification on fatigue rupture has been analysed for a diseased artery in 2D space by Wu *et al*. [11], who concluded that the presence of calcium inside the plaque does not enhance the risk of plaque rupture. Davis *et al*. [12] conducted experimental *in vitro* testing to obtain the fracture behaviour of atherosclerotic plaques; they illustrated that the degree of crack tip opening and collagen content have an inverse relation.

Contributions of the present paper to the field: This paper is the *first* to study the fracture biomechanics of an atherosclerotic coronary artery in 3D space via development of an FEM model development and simulations via *in vivo* clinical data; the plaque rupture and smart crack growth are examined via a fatigue analysis. In the first step, the clinical data obtained from angiography, OCT, blood pressure measurement, and ECG (conducted at the RAH) were used to develop the geometric (using image processing techniques) and haemodynamic characteristics of the LAD coronary artery. An FEM analysis of FSI has then been conducted to determine high-risk regions for plaque rupture initiation in the artery via examination of the obtained shear and stress fields. The plaque crack

extension/propagation and life cycles were then investigated. The model and simulations incorporated fully fluid/solid couplings, three dimensionality, non-Newtonian blood viscosity, blood pressure pulsation, and surrounding heart tissue.

6.3 Clinical measurements: angiography, pressure variation, OCT and ECG

The required clinical data for the geometric/haemodynamic characteristics have been obtained at the RAH ("Central Adelaide Local Health Network" research office; HREC ref: HREC/18/CALHN/781). Results obtained from post-processing of the clinical data, which was conducted at the South Australian Health and Medical Research Institute (SAHMRI) and the School of Mechanical Engineering, The University of Adelaide, were used as *in vivo* realistic geometry, physiological pressure pulsation, and heart rate in the biomechanical modelling/simulations.

In order to perform fatigue analysis and crack propagation modelling/simulations, clinical data of a specific patient were used. The characteristics of the patient: coronary angiogram for a patient (52-year-old male) presenting with a NSTEMI (non-ST-elevation myocardial infarction) and past medical history of acquired brain injury; LAD had mild proximal disease, resulting in 30-40% angiographic stenosis (47% stenosis in its 224 segment of OCT measurement); LCx had a focal 20% lesion in the proximal region; the right coronary artery (RCA) had a 50-60% lesion in the mid vessel and focal 20-30% stenosis in the distal vessel. Angiography images of the LAD are shown in **Figure 6-1**. Specifications of the four angiogram planes are shown in sub-figures (a), (c), (e), and (g), where sub-figure (a) represents an angiogram with primary angle = 30.1° and secondary angle = 20.0°; sub-figure (c) represents that of primary angle = -1.1° and secondary angle = -38.5°; sub-figure (e) represents that of primary angle = -44.9° and secondary angle = -30.3°; sub-figure (g) represents angiogram with primary angle = -44.5° and secondary angle = 29.7°; panels (b), (d), (f), and (h) show corresponding images for the calibration and position extraction for panels (a), (c), (e), and (g), respectively. The right anterior oblique (RAO)/left anterior oblique (LAO) is named primary angle and caudal (CAU)/cranial (CRA)

is named secondary angle (RAO and CAU are considered to be positive). In these figures the starting point (distal) and ending point (proximal) of OCT pull back are also shown.

To construct a biomechanical model of the LAD, four different clinical measurements were performed; namely OCT, time-dependent pressure at the entrance of left coronary artery, ECG, and angiograms. *In vivo* cross-sectional images of the LAD were obtained from OCT whilst the artery was operating; the different layers, lumen, fibrous cap, lipid, and calcification of the artery are all aspects which the OCT can reveal. Angiogram images were obtained using x-ray and dye contrast in which the narrowing and the level of the diseased artery were determined. Due to the complex 3D shape of the artery, it is essential to obtain angiogram images from different angles and combine them. Using angiogram images from different angles, the 3D position of the catheter was obtained. Using simultaneous ECG data made it possible to match the images of the heart from different angles in the same stage of the cardiac cycle. The time-dependent blood pressure at the entrance of the left main (LM) was obtained and used in the simulations as a representative boundary condition of the biomechanical system.

6.4 Realistic *in vivo* 3D model development

Due to the inherent existence of different geometric and material properties nonlinearities as well as fluid/solid couplings of coronary arteries, developing clinically based *in vivo* modelling/simulation of the coronary artery is essential, as neglecting even small aspects of the haemodynamic and geometric conditions could result in significant change in the stress field or plaque rupture situation of the coronary artery. In the following, the procedures for 3D reconstruction of *in vivo* coronary artery and applying haemodynamic conditions to a realistic biomechanical model are explained.

In order to develop the 3D position locus of the catheter, images from four angiogram planes have been used (**Figure 6-1**). Each angiogram plane was specified based on two angles: the CAU/CRA and the LAO/RAO. In this study, the RAO/LAO axis was considered to be the *x*-axis; the *primary angle* was the rotation around the *x* axis with RAO positive. CAU/CRA axis was considered as

the *y*-axis; the *secondary angle* was the rotation around the *y* axis with CAU positive.

The tip of the angiogram tube was chosen as an origin which was common in all angiogram images. Then, in order to scale all the obtained points, the tube diameter was used (6 French = 2 mm). Bifurcation branches were used as the biological markers to construct the 3D geometry. In the image processing procedure, synchronising the different stages of the cardiac cycles was important to ensure that every angiogram image was at the same point in the cardiac cycle, such that their combination produced the correct geometry for the patient-specific LAD model. ECG matching with the angiography procedure provided accurate stages for the coronary artery 3D *in vivo* modelling/simulations. Using rotation matrices given in [13] and image processing code developed for this study in MATLAB (version 2018a, Mathworks, Natick, MA, US), the 3D position of the LAD was obtained.

Only the lumen of an artery (blood) can be detected from the angiogram images, since the dye contrast only shows the blood flow inside the artery. In order to model/simulate the coronary artery, fibrous cap, and lipid geometry, OCT images have been obtained whilst the LAD was operating. **Figure 6-2** illustrates OCT cross-section of the atherosclerotic LAD coronary artery of the patient with a lipid pool inside (sub-figure (a)). In sub-figure (b), different areas of atherosclerotic LAD are shown with schematic points, namely adventitia (i.e., outer cross-section; green points), intima (i.e., inner cross-section; red points), and lipid pool (i.e., blue points). These 2D points were then reconstructed in ANSYS® (version 19.0, ANSYS Inc., Canonsburg, PA, US) (sub-figure (c)). Different stages of creating the realistic *in vivo* 3D geometry of patient-specific LAD is shown in **Figure 6-3**. Sub-figure (a) represents the 3D points extracted from each of the angiogram planes (red points) and the 3D position of the LAD (green points), constructed using the image processing method. Sub-figure (b) shows the blue curve, constructed from OCT images spanning on the beginning (distal) and ending (proximal) of the coronary artery. Sub-figure (c) illustrates the inner cross-section, obtained from OCT, which have been located at the appropriate location of the 3D catheter curve (where the light blue colour is the

lumen of the patient-specific LAD). In sub-figure (d), both the inner and outer cross-sections (light blue and black curves, respectively) of the patient-specific LAD are shown, or in other words, the *in vivo* realistic 3D geometry of the LAD was developed using angiogram images, ECG, and OCT.

Additional clinical data obtained during the operation at RAH are the blood pressure variation at the entrance of the LM; this pressure was applied at the inlet of the *in vivo* realistic model. Similar to the synchronisation utilised for determination of different stages of the cardiac cycle using ECG, the time-dependent pressure variation was applied in the beginning of the heart cycle accordingly. **Figure 6-4** shows the pressure variation profile at the entrance of left coronary artery during one cardiac cycle.

Figure 6-5 represents the constructed *in vivo* 3D realistic patient-specific coronary artery with a lipid pool. Sub-figure (a) shows the inlet, outlet, and the lipid pool within the thickness of the LAD. Another important boundary condition of the coronary artery which has been incorporated in the model is the surrounding heart tissue. Since a segment of the outer surface of the coronary artery is mounted inside the heart tissue, the 3D curve of the catheter was assumed to be the divider between the outer surface of the coronary artery embedded inside heart tissue (sub-figure (b)); the elastic support value of 1 N/mm^3 has been used.

In order to conduct the smart crack growth and the fatigue analysis, the material specification has been adopted from Ref. [8]. Another essential characteristic of haemodynamic condition of the coronary artery is the blood viscosity [14].

6.5 Numerical simulations for fatigue analysis and smart crack growth

The 3D dynamical stress field of the patient-specific LAD for both artery (solid part) and blood (fluid part) and their interactions (FSI) were obtained using the FEM. FSI modelling was utilised to determine accurate stress fields for each part of the biomechanical system. A two-way fully coupled FSI simulation of patient-specific LAD was conducted with the coupling surface interface chosen between the blood and artery. During the solution process for the dynamical response of the biomechanical system, remeshing of the solid and fluid parts was

incorporated based on the dynamic mesh configuration. A tetrahedral mesh type was chosen for creating elements during analysis. Once the stress fields (von Mises stress (VMS) and wall shear stress (WSS)) for both parts was obtained, a fatigue analysis and smart crack growth were performed to predict rupture.

The distribution of the VMS on the artery was used to determine the locations on atherosclerotic coronary artery at high risk of rupture. Crack initiation was applied to specific areas and smart crack propagation and fatigue life analysis were performed. As a result, critical areas of plaque rupture and the rupture progression and duration were predicted.

Plaque rupture initiation has been considered via an introduced crack on the fibrous cap area of the atherosclerotic LAD. In this paper, crack initiation is achieved in FEM by removal of 3D prism; therefore, the ruptured area has a tip line at crack tip. By solving the FSI of the biomechanical system, the stress at the tip of the crack became infinity which showed that classical strength of materials is unable to predict material failure and crack propagation; therefore, fracture mechanics theory was used to solve for plaque rupture progression (crack growth). Moreover, it is interesting to note that fracture mechanics criteria can be considered as a small-scale yielding. In fracture mechanics, due to stress concentration at crack's tip, the stress value is correlated with $1/\sqrt{r}$ (r is the radius of a circle around the crack tip) [15]. Using fracture mechanics, tip's stress singularity was considered; however, the stress was not be used as a criteria to determine the failure of the material [16]. According to fracture mechanics, the stress around the crack tip is given by

$$\sigma_{ij} = \frac{K_I}{\sqrt{2\pi r}} h_{ij}(\theta), \tag{6.1}$$

where σ_{ij} is the stress, K_I is the stress intensity factor (SIF) (which depends on geometry and loading of the system), $h_{ij}(\theta)$ is a specific function for each direction, and (r, θ) are the polar coordinates around the crack tip [16]. Based on experimental observations in the fracture mechanics field, a crack grows as the SIF reaches its critical value (here, K_{Ic} is called fracture toughness) [17].

Crack propagation in any structure can either be due to a static or a dynamic loading. In solid mechanics field, when the dynamic loading is of a

harmonic/periodic type, the analysis to determine changes in the stress/strain fields inside the structure is called *fatigue* analysis. Hence, for the artery problem, as the blood pressure is by nature periodic, the crack growth was conducted via a fatigue analysis. Fatigue analysis has been performed using Paris' law, where correlation between the crack extension da and the number of cycles dN with SIF was used [18]

$$\frac{\mathrm{d}a}{\mathrm{d}N} = C\left(\Delta K_I\right)^m, \tag{6.2}$$

in which C and m are the material properties; these were adopted from [15] for the artery problem considered.

Conducting a fatigue analysis once the plaque rupture initiates (i.e., crack extension) the number of cycles corresponding to that extension was calculated, then by having the heart rate, the life of the plaque was calculated via

$$Life\ \ of\ \ plaque\ \ \left[minute\right] = \frac{N\ \left[beats\right]}{Heart\ Beat\ Rate\left[bpm\right]}. \tag{6.3}$$

As a result, the time required for the plaque rupture propagation was predicted using the heart rate, as well as geometry, and haemodynamic conditions.

6.6 Results for stresses and fatigue analysis

Figure 6-6 (a) shows the spatial distribution of VMS on the LAD coronary artery. The local maximum of the VMS is located in the vicinity of the plaques, highlighting that these are vulnerable spots. Based on the OCT data, the plaque in the proximal area is lipid-rich (and has the highest stenosis) compared to the other plaques where they are not lipid-rich. It was shown in the literature that a lipid-rich plaque is more prone to rupture as the lipid itself has very low mechanical strength [9, 19]. The proximal plaque has been recognised as a location where cracks initiate, as the material strength is the lowest (due to lipid presence) and local VMS is higher. A cross-section at the proximal plaque (sub-figure (b)) confirms the globally highest VMS as well; hence, once again this location is the most likely candidate for plaque initiation and progression.

Material failure of the fibrous cap can be considered as the plaque rupture initiation; in **Figure 6-7** the process of fatigue analysis and crack extension is depicted. As shown previously in **Figure 6-6** (b), the VMS at the intima layer is a maximum on the shoulder of the plaque. In order to analyse the rupture initiation and extension of the crack (i.e., rupture initiation and progression) a segment of the artery with thickness of 0.5 mm has been selected (sub-figures (a) and (b) in **Figure 6-7**). Rupture initiation is assumed to be at the proximal shoulder of the plaque as it was found to be the most vulnerable area (see **Figure 6-6**). The first noticeable finding observed is that the rupture extends (propagates) (follow sub-figures (c)-(f) of **Figure 6-7**); this is important from a mechanics of structures perspective as not all cracks in a structure propagate under certain loadings due to the mechanical strength and plastic relaxation of the material and structure. Sub-figures (c)-(f) show the different stages of crack growth in the fatigue analysis: in sub-figure (c) the crack extension is 0.03 mm for the number of cycles of 7827 (104 min); in sub-figure (d) crack extension is 0.39 mm for 28588 cycles (381 min); in sub-figure (e) it is 0.67 mm for 39805 cycles (531 min); in sub-figure (f) it is 0.90 mm for 45405 cycles (605 min). In conclusion, for a rupture initiation at the proposed location, it would take around 2 hours for the rupture to start and 10 hours to reach the end of the artery layer (the adventitia). Sub-figure (g) shows the rupture extension (crack extension) with the number of cycles. In general, occlusion occurs when the crack progresses deep enough to permit the calcium and lipid to be released into the blood, which leads to thrombus and hence occlusion; however, if the amount of crack progression (extension) is small enough or it occurs at a sufficiently large number of fatigue cycles (due to various geometric/strength/haemodynamic reasons) the artery has sufficient time to defuse the situation by repairing the crack area and preventing a complete occlusion.

In the process of crack propagation inside the artery, the crack extension starts when the SIF reaches its critical value. Usually the critical value of SIF is determined via experiment. Since there are no experimental data for the critical SIF value of coronary arteries, the values of the SIF obtained from Paris' law (see Equation 2) are used; the corresponding results are depicted in **Figure 6-8**. Panel (a) shows the distribution of the SIF values on the crack tip when the crack starts

growing after 104 minutes from the initiation of the plaque (7827 cycles); as illustrated the crack starts to grow when the SIF reaches the minimum value of 0.016 MPa·mm$^{0.5}$ which is a critical SIF obtained from Paris' law analysis; this sub-figure indicates that in the middle of the crack the SIF has larger values with the maximum of 0.026 MPa·mm$^{0.5}$. Therefore, in the 3D analysis of crack growth in the LAD segment under cyclic heart pressure, crack growth starts in the middle of the thickness. In sub-figure (b) SIF variation with thickness (length of crack) of the artery, for different contours around the crack are shown. As explained in Section 4, SIF is calculated for different radii around the crack (Contour 1 by 0.05 mm, Contour 2 by 0.10 mm, Contour 3 by 0.15 mm radii around the crack tip). Sub-figure (c) shows the distribution of the SIF at the end of the extension period in which the side of the segment has a maximum value of SIF. The general conclusion hence is that in this situation of geometry and haemodynamic properties, if plaque rupture initiates for the LAD coronary artery it will continue until the whole fibrous cap tears and consequently complete occlusion and hence heart attack occurs.

By employing the analyses described here it is possible to find the high risk locations for which plaque rupture can be predicted. In the beginning of the crack growth (sub-figure (b)), all the contours have nearly the same value of SIF; however, by the end of the period of crack extension, the value of the SIF has converged for Contours 2 and 3, considering the fact that the value of SIF has changed significantly (three times larger) compared to the start of the crack growth.

The aim of the analysis and results plotted in **Figure 6-9** is to develop a relation between the minimum fatigue cycle required for the initiation of plaque-rupture extension and the angle of crack orientation; see sub-figure (a) for the definition of crack angle. Sub-figure (b) highlights that, for the lipid core area, the minimum cycle required for start of rupture progression is max, however, the plaque shoulder regions require the minimum number of cycles for the plaque rupture propagations to commence. This is in agreement with the clinical data reported in Ref. [19] for the critical location of plaque rupture growth.

A question that may be raised is how we can ensure that the segment of the coronary artery chosen for fatigue and crack propagation analyses is the proper one in the plaque area. In order to answer this question, the total proximal plaque area is considered (**Figure 6-10** (a)) and a crack tip along the artery length between Points 1 and 2 is focused on. **Figure 6-10** (b) shows the SIF as a function of the length, where Point 1 is located at length = 0 mm and Point 2 at length = 3.6 mm; as seen, the area closer to Point 2 possesses larger vales for SIF. This also confirms that the chosen segment is the appropriate one for crack propagation analysis.

6.7 Concluding remarks

This paper investigated for the first time the 3D fracture biomechanical behaviour of an atherosclerotic coronary artery. *In vivo* clinical data from angiography, ECG, OCT, and time-dependent pressure measurement (obtained at RAH) were used to develop an FEM based FSI model of the biomechanical system so as to analyse plaque rupture (crack) initiation and progression. An image processing technique was developed to post-process the clinical data and obtain information related to the geometry and haemodynamic conditions which were employed to construct the FEM model. The comprehensive model/simulations included FSI, non-Newtonian blood viscosity, physiological blood pressure pulsation, surrounding heart tissue, and three-dimensionality. Results for rupture initiation and progression showed that: (i) the vulnerable areas, with local maxima of VMS, are in the vicinity of the plaques; (ii) of all the plaque areas investigated, the proximal one with lipid-rich core was found to be the most vulnerable for rupture initiation; (iii) for the proximal plaque, the plaque shoulders are the most vulnerable areas for the initiation of rupture; (iv) the most vulnerable area for plaque propagation (extension) is again the shoulders of the proximal plaque; (v) for the shoulder of the proximal plaque, the rupture (crack) *does* propagate under the physiological/geometric conditions of the artery investigated which indicates that the patient is at risk of artery occlusion (hence heart attack) as soon as crack develops at the shoulders of the proximal plaque; (vi) in the presence of a crack (in they infinitesimally small), it takes approximately 2 hours

for the start of rupture propagation and another 8 hours until the rupture reaches adventitia; (vii) the rupture growth starts in the middle of the crack tip as this is the location where the SIF value is the largest.

Acknowledgement

We acknowledge assistance provided by Dr. Daisuke Shishikura and Mr. Giuseppe Di Giovanni from the Atherosclerosis Imaging Core Laboratory at SAHMRI, Mrs Trudy Patrick from Abbott Pty Ltd and doctors and nurses from the Cardiovascular Investigation Unit at the RAH. The support provided for this investigation from The University of Adelaide, RAH, and SAHMRI are highly acknowledged. P.JP. is supported by research fellowships from the National Heart Foundation of Australia (Future Leader Fellowship FLF102056) and National Health and Medical Research Council of Australia (CDF1161506).

I acknowledge the support I have received for my research through The University of Adelaide and Faculty of Engineering, Computer & Mathematical Sciences, The University of Adelaide.

Reference

[1] World Health Organisation (WHO), The top 10 causes of death, https://www.who.int/en/news-room/fact-sheets/detail/the-top-10-causes-of-death, (2019).
[2] C.L. Lendon, M. Davies, G. Born, P.D. Richardson, Atherosclerotic plaque caps are locally weakened when macrophages density is increased, Atherosclerosis, 87 (1991) 87-90.
[3] H. Huang, R. Virmani, H. Younis, A.P. Burke, R.D. Kamm, R.T. Lee, The impact of calcification on the biomechanical stability of atherosclerotic plaques, Circulation, 103 (2001) 1051-1056.
[4] G.C. Cheng, H.M. Loree, R.D. Kamm, M.C. Fishbein, R.T. Lee, Distribution of circumferential stress in ruptured and stable atherosclerotic lesions. A structural analysis with histopathological correlation, Circulation, 87 (1993) 1179-1187.
[5] A. Bank, A. Versluis, S. Dodge, W.H. Douglas, Atherosclerotic plaque rupture: a fatigue process?, Medical Hypotheses, 55 (2000) 480-484.
[6] A. Versluis, A.J. Bank, W.H. Douglas, Fatigue and plaque rupture in myocardial infarction, Journal of Biomechanics, 39 (2006) 339-347.
[7] A. Ferrara, A. Pandolfi, Numerical modelling of fracture in human arteries, Computer Methods in Biomechanics and Biomedical Engineering, 11 (2008) 553-567.
[8] P.K. Paritala, P.K. Yarlagadda, J. Wang, Y. Gu, Z. Li, Numerical investigation of atherosclerotic plaque rupture using optical coherence tomography imaging and XFEM, Engineering Fracture Mechanics, 204 (2018) 531-541.
[9] A. Rezvani-Sharif, M. Tafazzoli-Shadpour, D. Kazemi-Saleh, M. Sotoudeh-Anvari, Stress analysis of fracture of atherosclerotic plaques: crack propagation modeling, Medical & Biological Engineering & Computing, 1-12.
[10] Y. Huang, Z. Teng, U. Sadat, J. He, M.J. Graves, J.H. Gillard, In vivo MRI-based simulation of fatigue process: a possible trigger for human carotid atherosclerotic plaque rupture, Biomedical Engineering online, 12 (2013) 36.
[11] B. Wu, X. Pei, Z.-Y. Li, How does calcification influence plaque vulnerability? Insights from fatigue analysis, The Scientific World Journal, 2014 (2014).
[12] L.A. Davis, S.E. Stewart, C.G. Carsten III, B.A. Snyder, M.A. Sutton, S.M. Lessner, Characterization of fracture behavior of human atherosclerotic fibrous caps using a miniature single edge notched tensile test, Acta Biomaterialia, 43 (2016) 101-111.
[13] B. Siciliano, L. Sciavicco, L. Villani, G. Oriolo, Robotics: modelling, planning and control, Springer Science & Business Media, 2010.
[14] A. Gholipour, M.H. Ghayesh, A. Zander, Nonlinear biomechanics of bifurcated atherosclerotic coronary arteries, International Journal of Engineering Science, 133 (2018) 60-83.
[15] X. Pei, B. Wu, Z.-Y. Li, Fatigue crack propagation analysis of plaque rupture, Journal of Biomechanical Engineering, 135 (2013) 101003.
[16] C.T. Sun, Fracture mechanics, Butterworth-Heinemann/Elsevier, Waltham, Mass., 2012.
[17] G.R. Irwin, Analysis of stresses and strains near the end of a crack traversing a plate, Journal of Applied Mechanics, 24 (1957) 361–364.

[18] P. Paris, F. Erdogan, A critical analysis of crack propagation laws, Journal of Basic Engineering, 85 (1963) 528-533.
[19] P.D. Richardson, M. Davies, G. Born, Influence of plaque configuration and stress distribution on fissuring of coronary atherosclerotic plaques, The Lancet, 334 (1989) 941-944.
[20] ST. Jude. Medical, https://www.abbott.com/abbott-stjudemedical-en-uk.html, (2019).

(a)

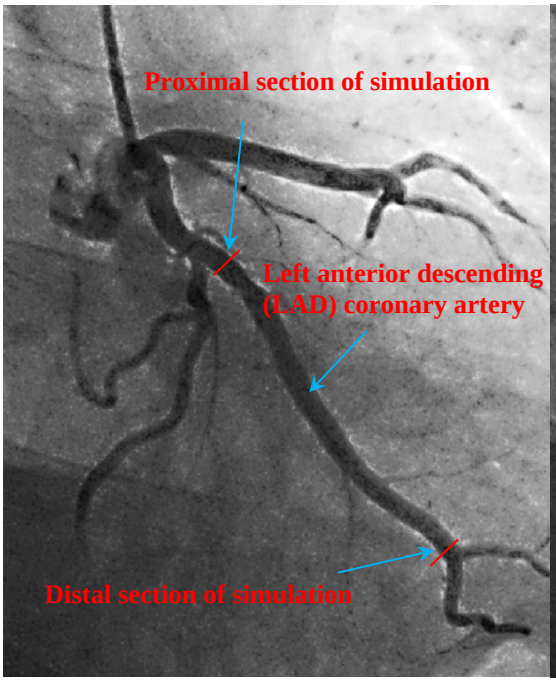
Proximal section of simulation
Left anterior descending
(LAD) coronary artery
Distal section of simulation

(b)

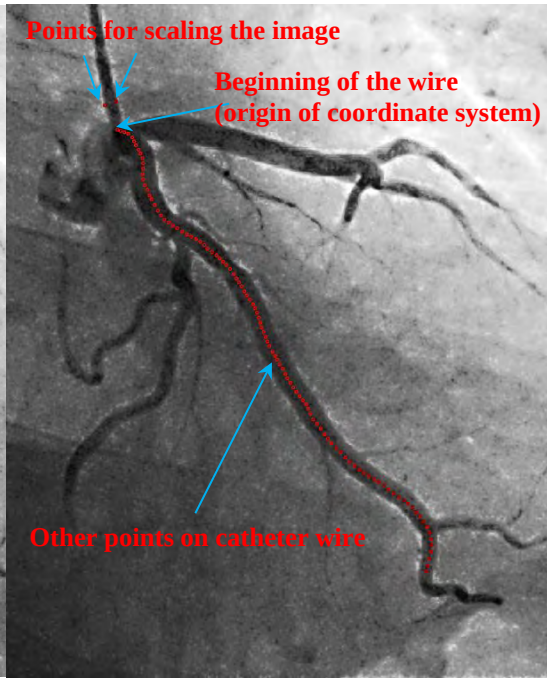
Points for scaling the image
Beginning of the wire
(origin of coordinate system)
Other points on catheter wire

(c)

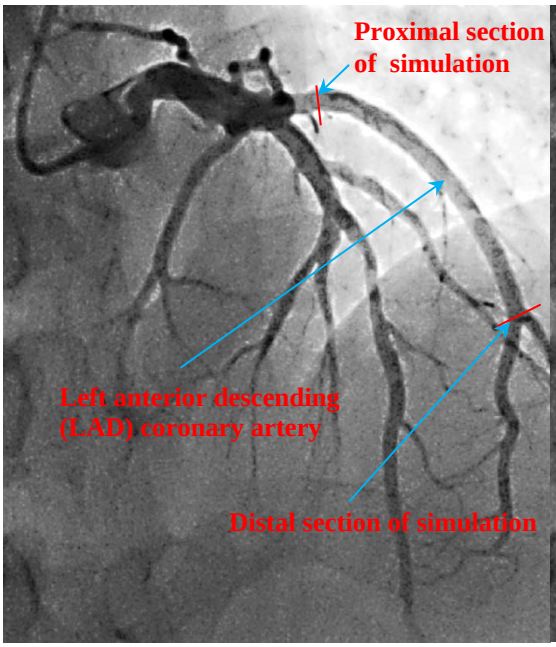
Proximal section
of simulation
Left anterior descending
(LAD) coronary artery
Distal section of simulation

(d)

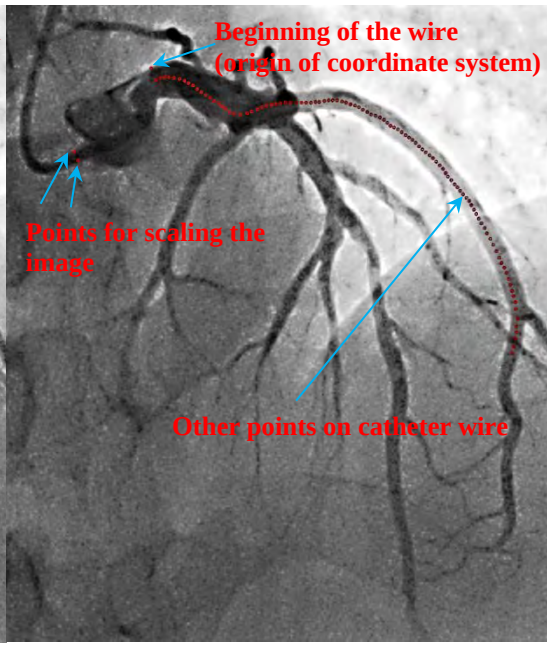
Beginning of the wire
(origin of coordinate system)
Points for scaling the
image
Other points on catheter wire

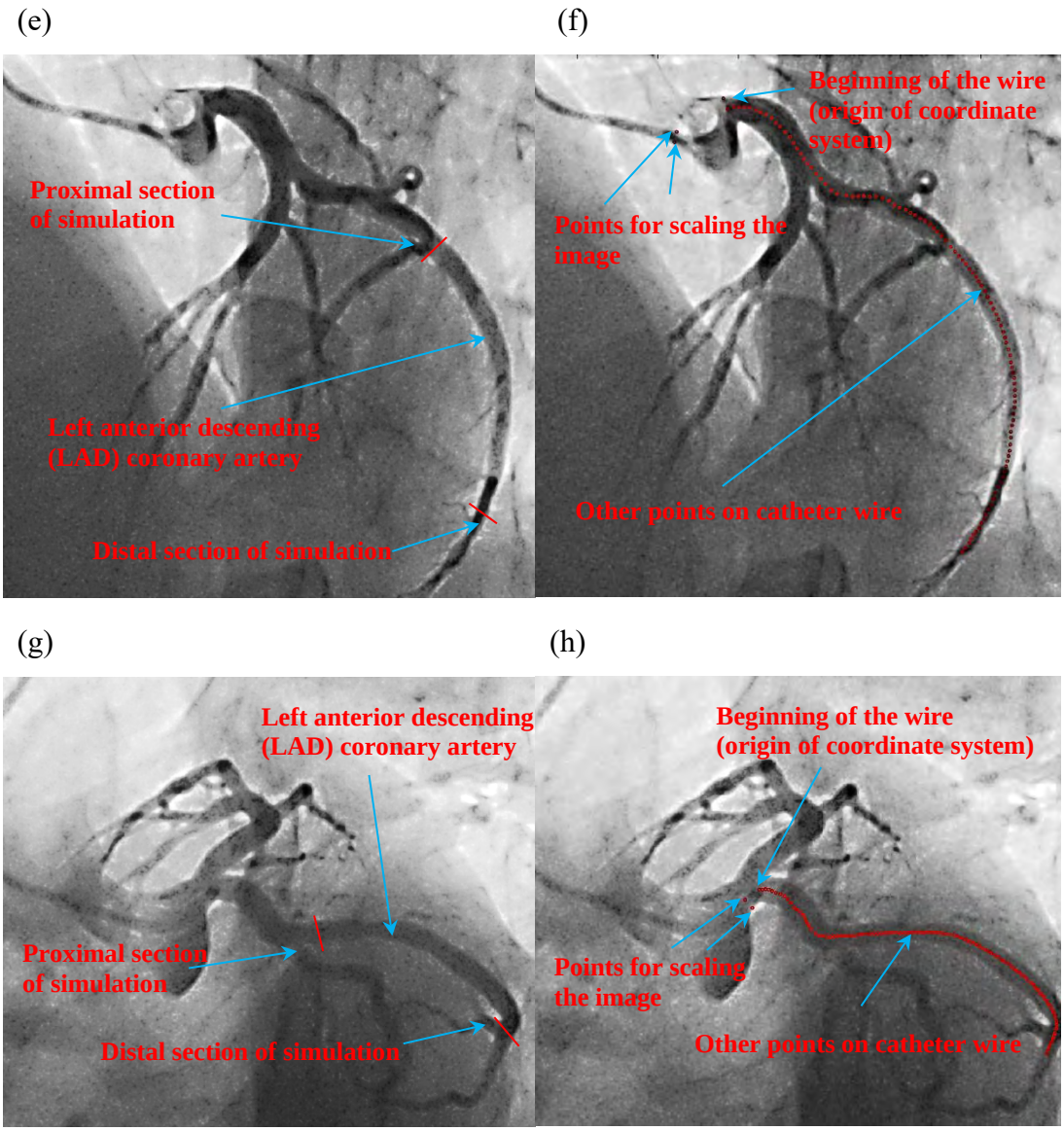

Figure 6-1. Angiograms for the LAD coronary artery: (a, b) where (a) shows angiogram with primary angle = 30.1° and secondary angle = 20.0°; (b) points on (a) image for calibration and position extraction; (c, d) where (c) shows angiogram with primary angle = -1.1° and secondary angle = -38.5°; (d) points on (c) image for calibration and position extraction; (e, f) where (e) shows angiogram with primary angle = -44.9° and secondary angle = -30.3°; (f) points on (e) image for calibration and position extraction; (g, h) where (g) shows angiogram with primary angle = -44.5° and secondary angle = 29.7°; (h) points on (g) image for calibration and position extraction; these angiograms have been obtained at the RAH.

(a)

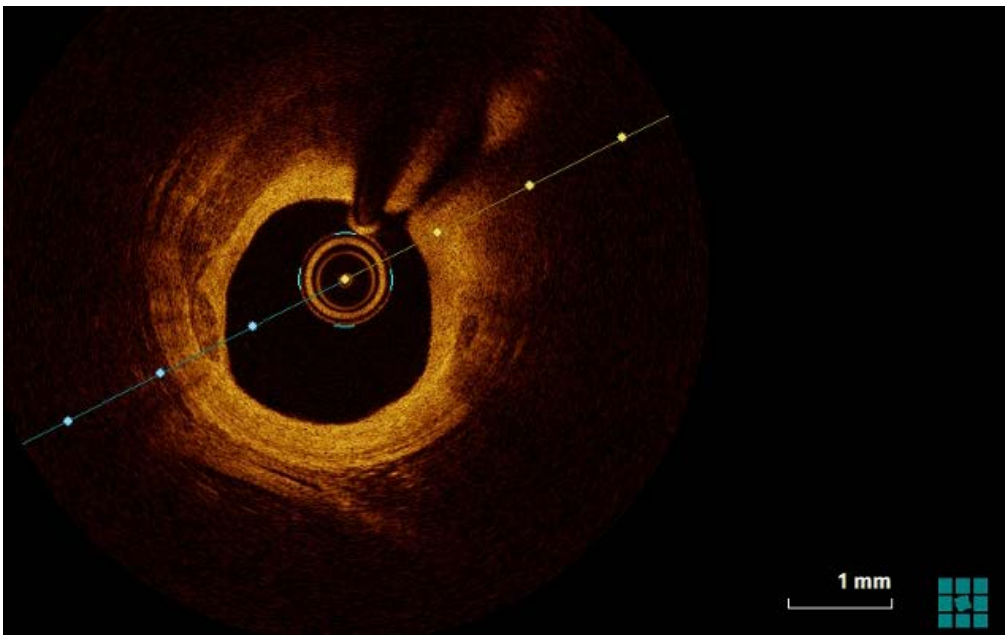

(b)

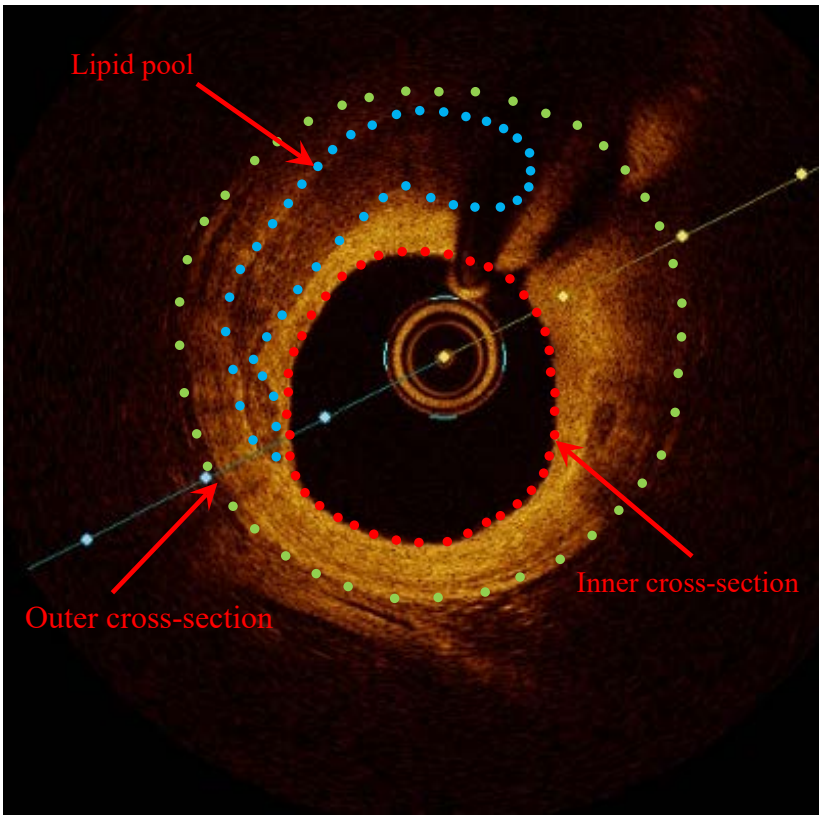

(c)

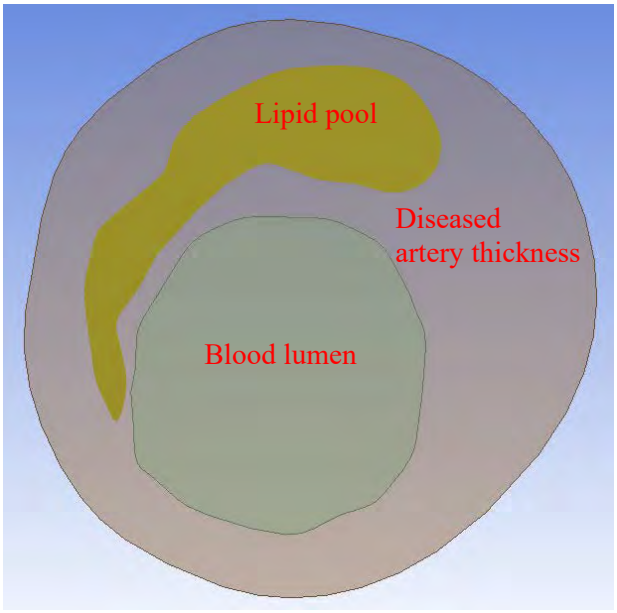

Figure 6-2. (a) *In vivo* OCT images used to construct the inner and outer cross-sections of the artery around the 3D catheter position; (b) schematic point selection in the 2D plane for constructing inner (red points) and outer (green points) cross-sections and lipid (blue points) region (ST. JUDE MEDICAL software [20]); (c) constructed cross-section in ANSYS.

(a)

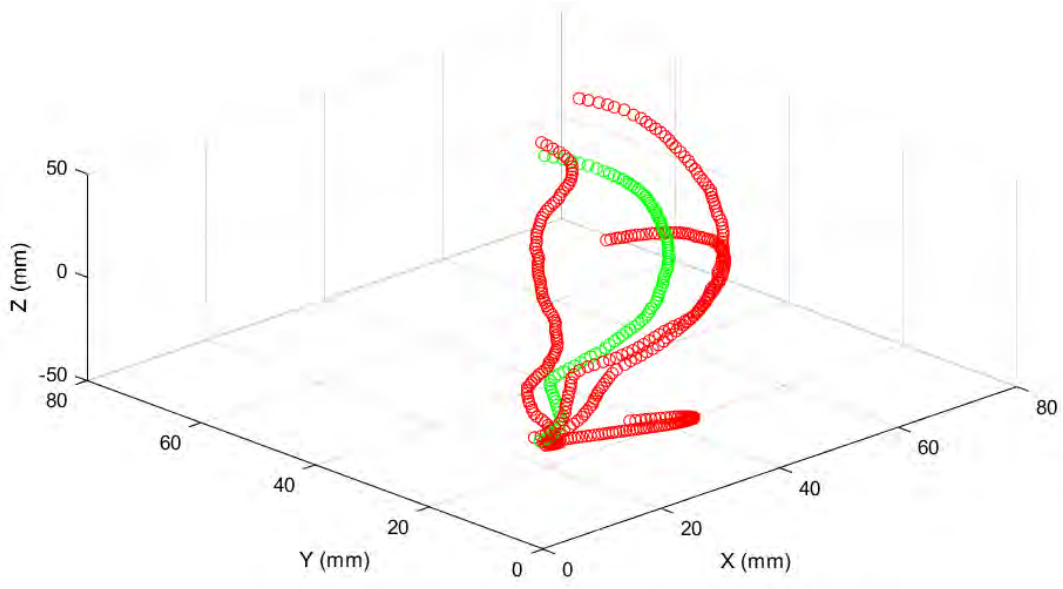
50
0
-50
Z (mm)
80
60
40
20
0
Y (mm)
0
20
40
60
80
X (mm)

(b)

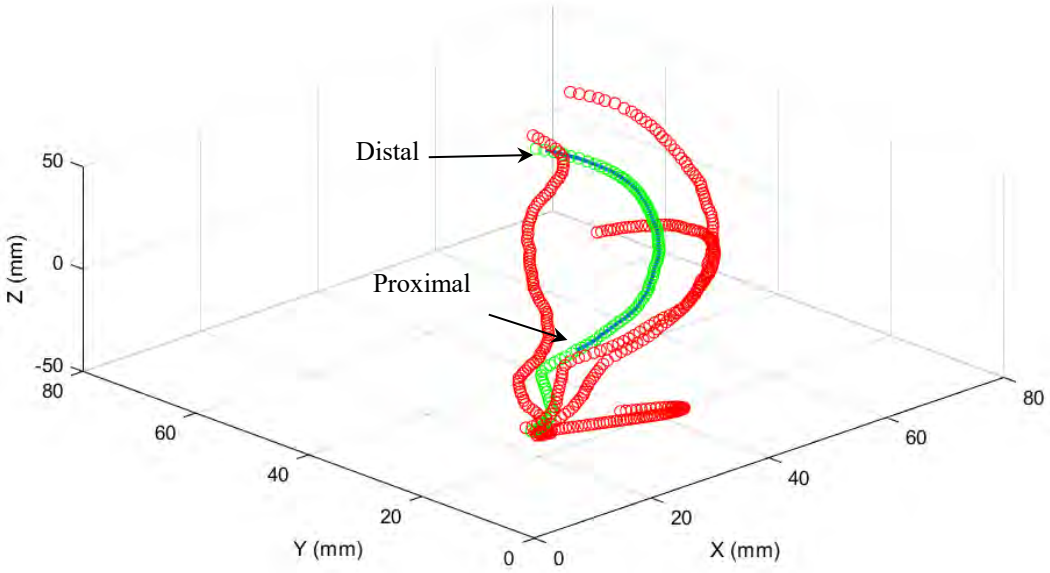
Distal
Proximal
50
0
-50
Z (mm)
80
60
40
20
0
Y (mm)
0
20
40
60
80
X (mm)

(c)

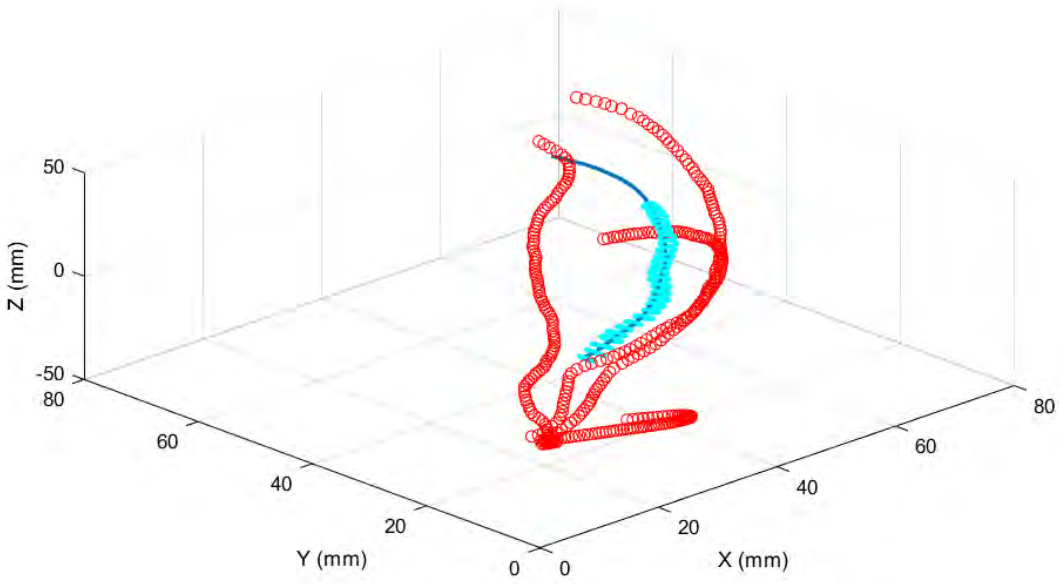

(d)

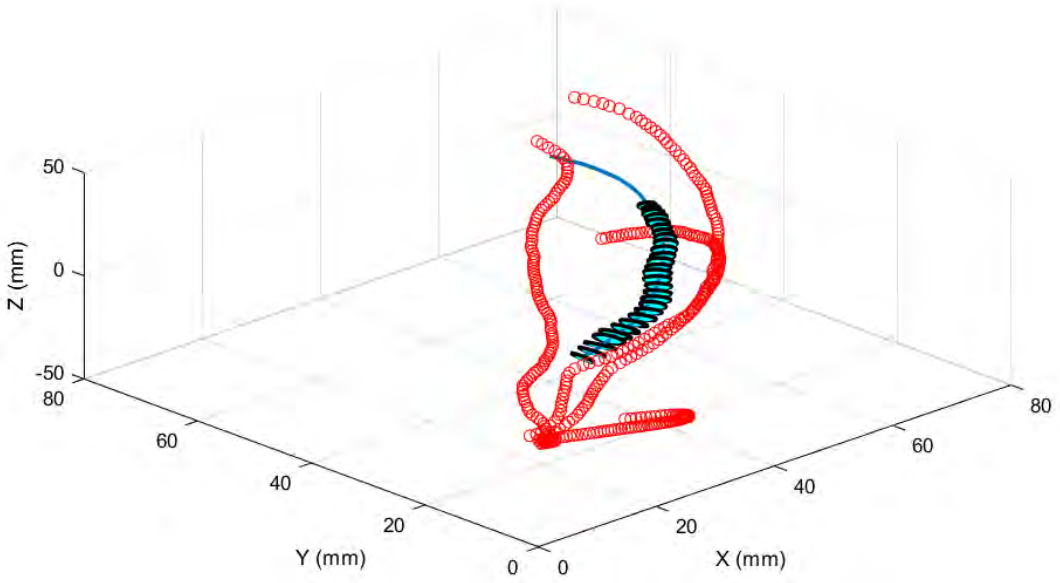

Figure 6-3. Steps for constructing 3D curve of the catheter and the cross-sections of the artery in MATLAB: (a) plotted 2D points extracted from each angiogram plane (red circles) together with the 3D position of the catheter (green circles); (b) 3D blue curve of the start (distal) and the end (proximal) of the OCT procedure; (c) adding the inner cross-sections (light blue curves); (d) adding the outer cross-sections (black curves).

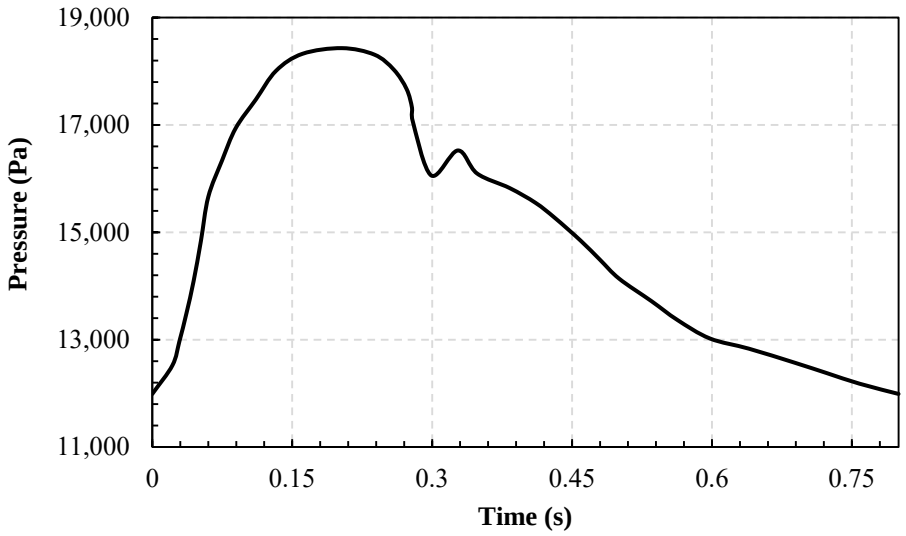

Figure 6-4. Pressure variation with time at the entrance of the LM artery.

(a)

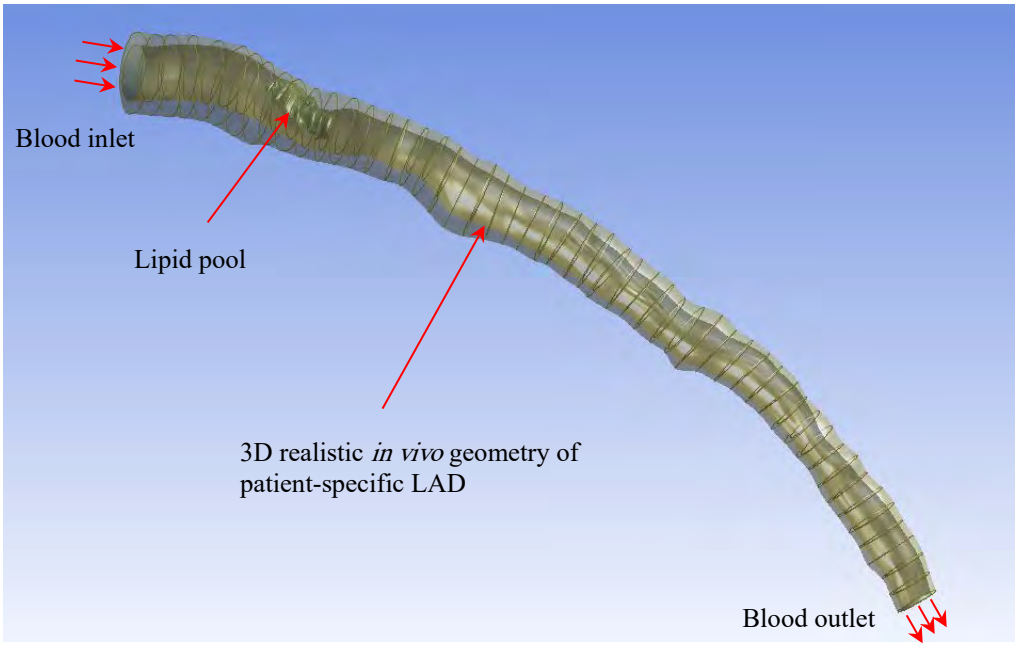

(b)

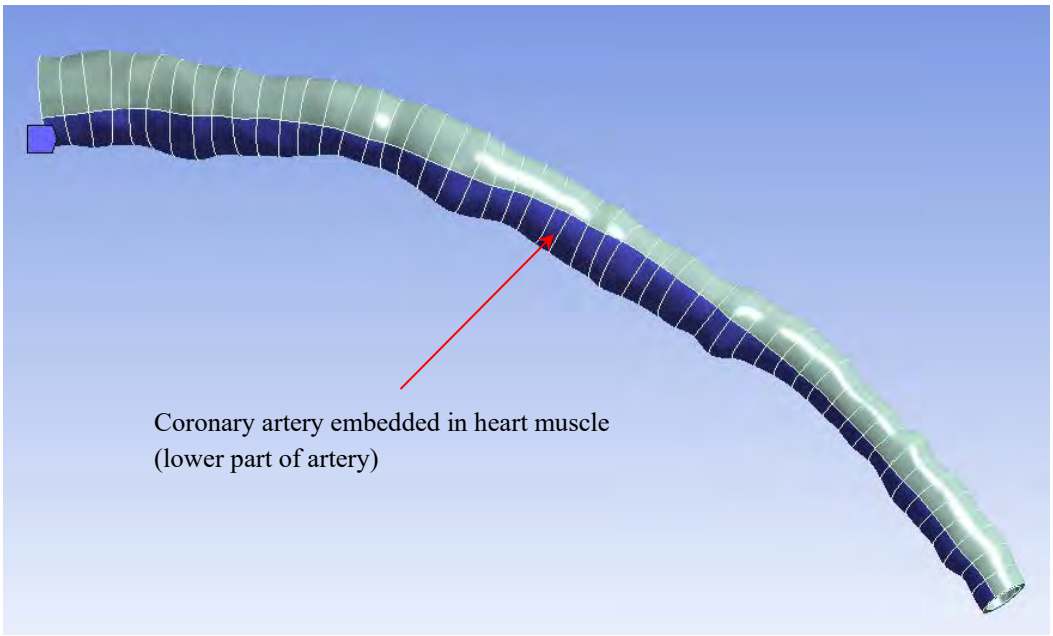

Figure 6-5. 3D realistic model of the LAD coronary artery: (a) blood inlet and outlet with lipid pool inside; (b) artery itself (lower part, shown in blue, is embedded in the heart tissue).

(a)

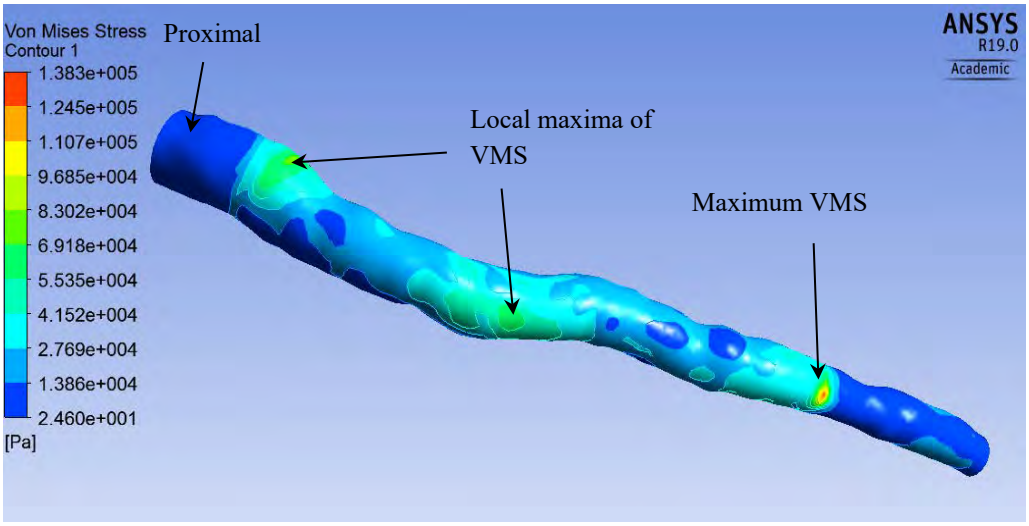

(b)

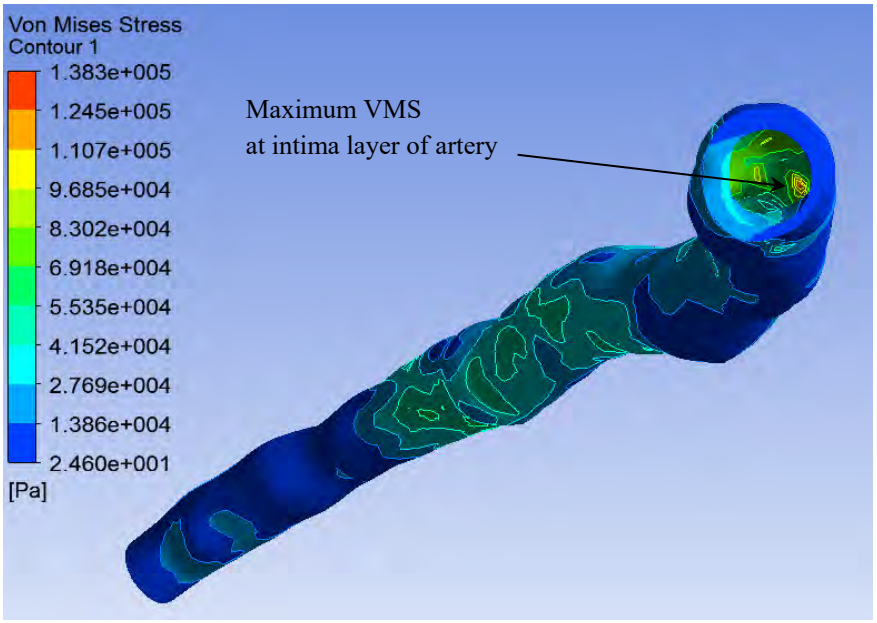

Figure 6-6. Spatial distribution of the VMS for the realistic LAD coronary artery, highlighting the local/global maximum values (t = 0.23s) (a) view 1; (a) view 2.

(a)

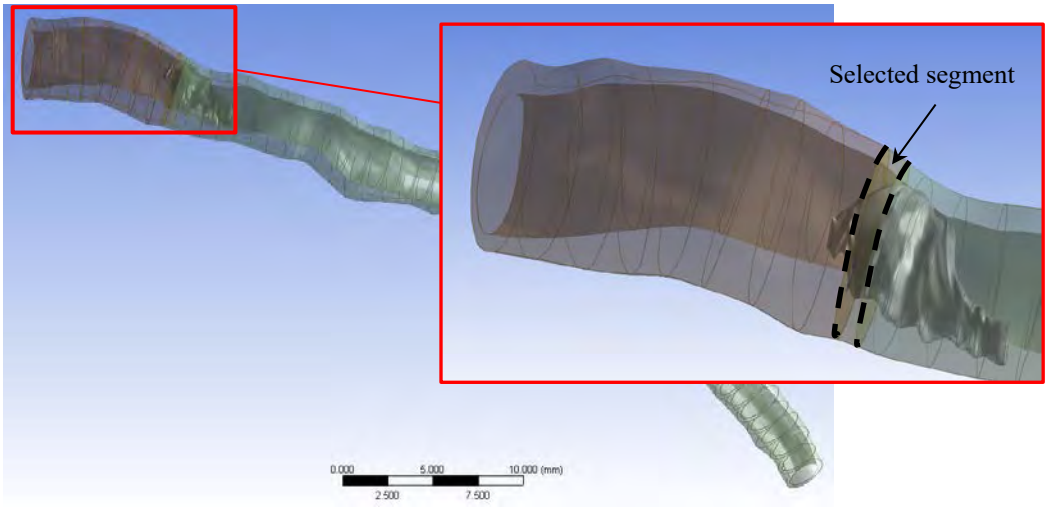
Selected segment
0.000
5.000
10.000 (mm)
2.500
7.500

(b)

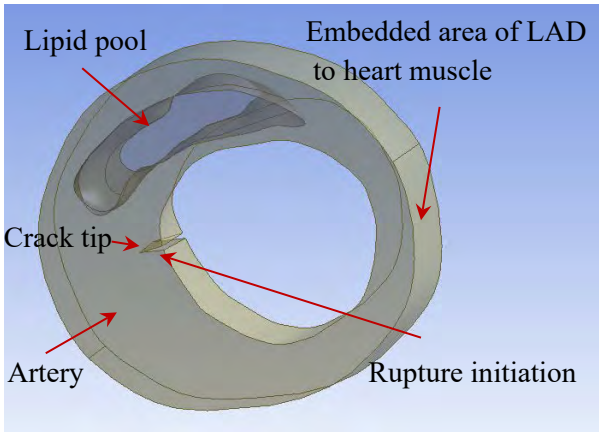
Lipid pool
Embedded area of LAD
to heart muscle
Crack tip
Artery
Rupture initiation

(c)

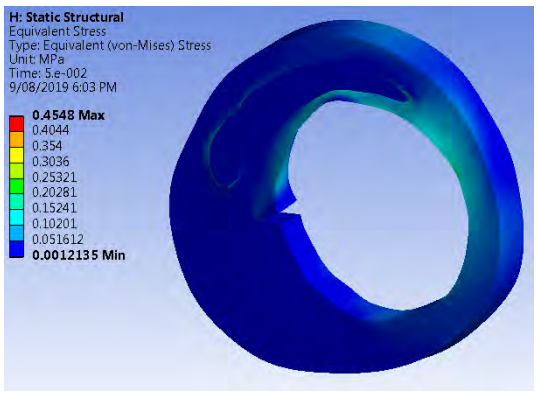
H: Static Structural
Equivalent Stress
Type: Equivalent (von-Mises) Stress
Unit: MPa
Time: 5.e-002
9/08/2019 6:03 PM
0.4548 Max
0.4044
0.354
0.3036
0.25321
0.20281
0.15241
0.10201
0.051612
0.0012135 Min

(d)

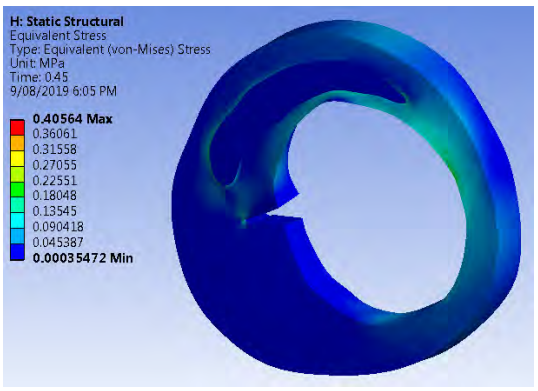
H: Static Structural
Equivalent Stress
Type: Equivalent (von-Mises) Stress
Unit: MPa
Time: 0.45
9/08/2019 6:05 PM
0.40564 Max
0.36061
0.31558
0.27055
0.22551
0.18048
0.13545
0.090418
0.045387
0.00035472 Min

(e) (f)

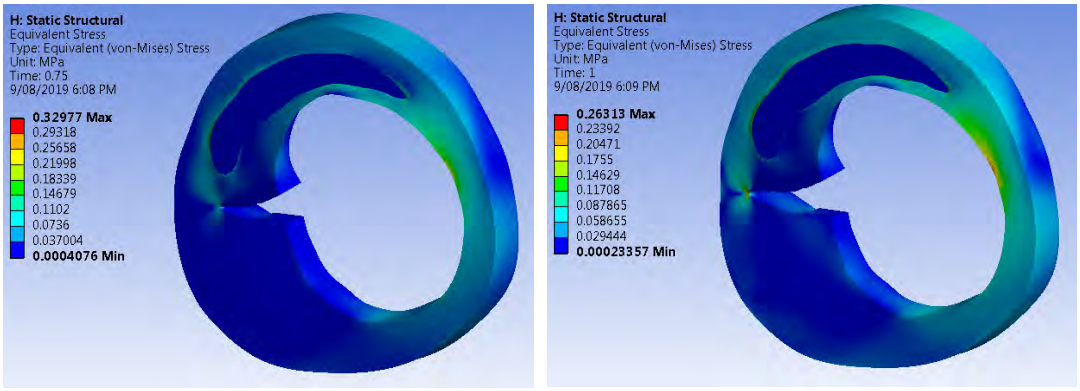

(g)

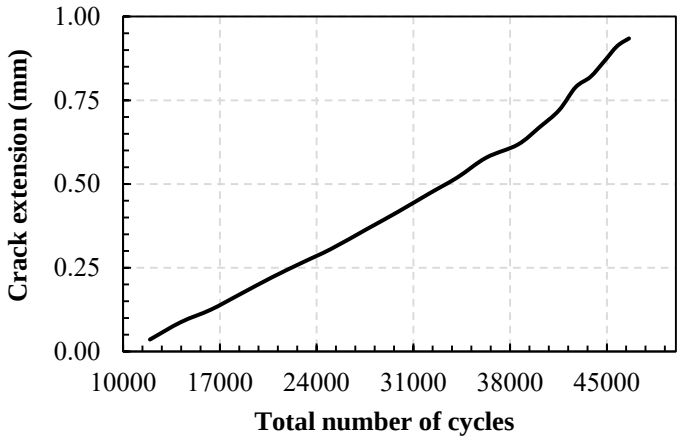

Figure 6-7. (a) segmentation of the LAD coronary artery for crack propagation analysis; (b) a segment of the artery with a crack; (c)-(f) different stages of crack growth in the fatigue analysis: (c) crack extension is 0.03 mm for the number of cycles: 7827 (104 min); (d) crack extension is 0.39 mm for the number of cycles: 28588 (381 min); (e) crack extension is 0.67 mm for the number of cycles: 39805 (531 min); (f) crack extension is 0.90 mm for the number of cycles: 45405 (605 min); (g) life cycles of the fatigue analysis.

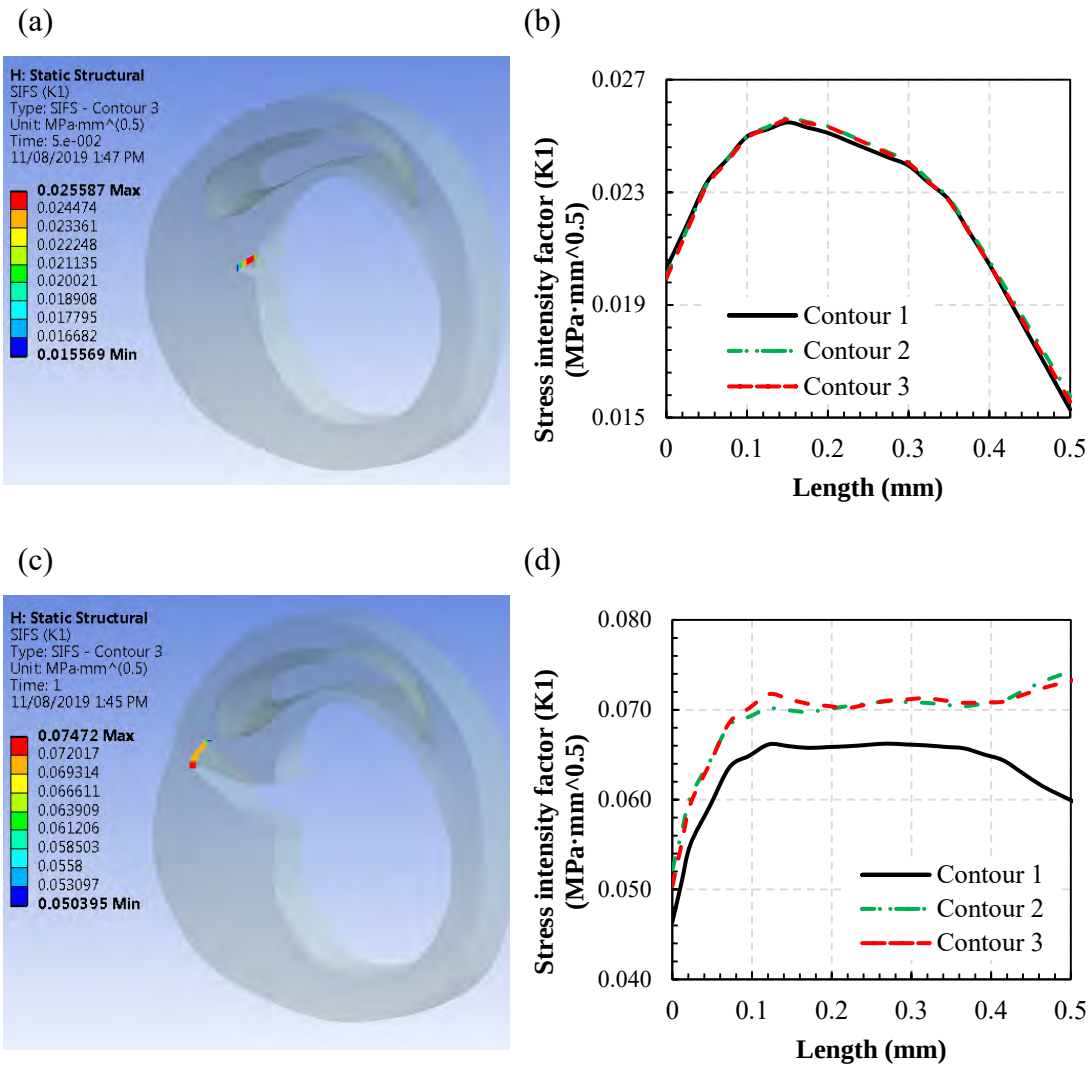

Figure 6-8. (a) 3D SIF distribution for the crack tip for crack growth commencement; (b) different contours of SIF around the crack tip for crack growth commencement; (c) spatial SIF distribution for the end of the crack growth period; (d) different contours of SIF around the crack tip for the end of the crack growth period, highlighting a convergence for Contours 2 and 3.

(a)

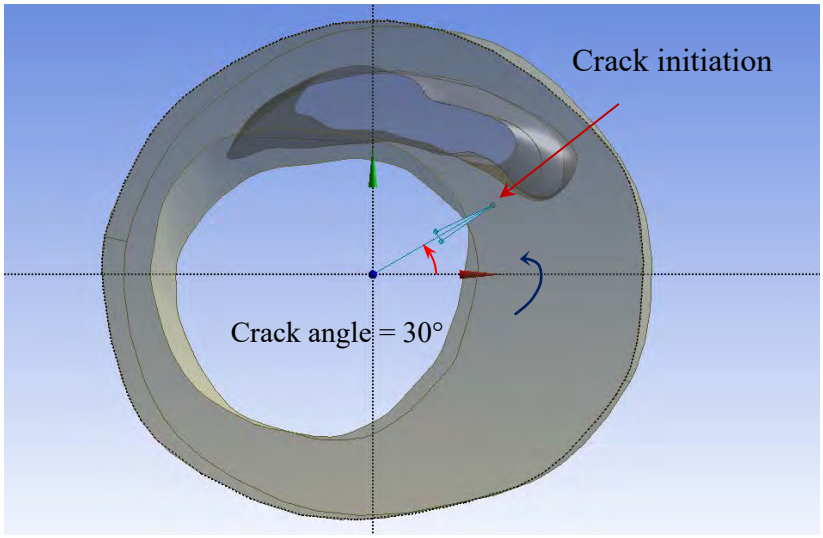

(b)

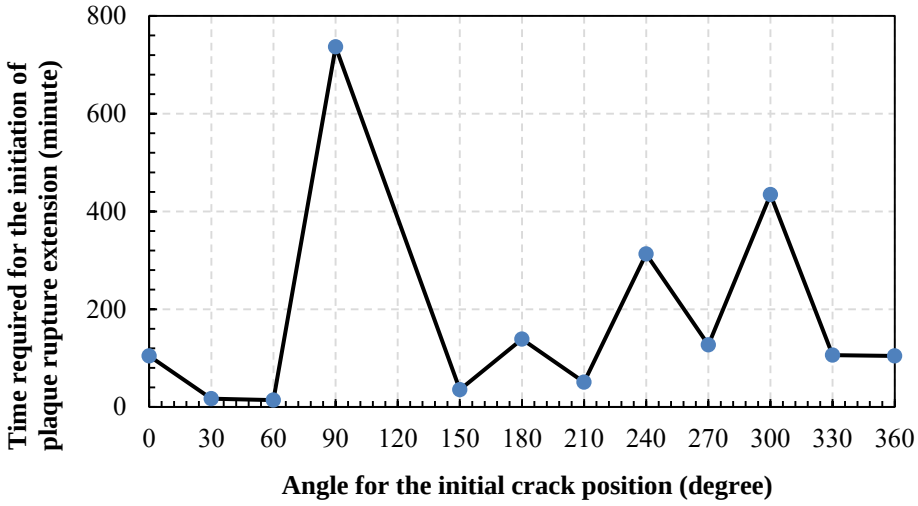

Figure 6-9. (a) crack initiation for different angles around the plaque; (b) crack extension start time for different angles.

(a)

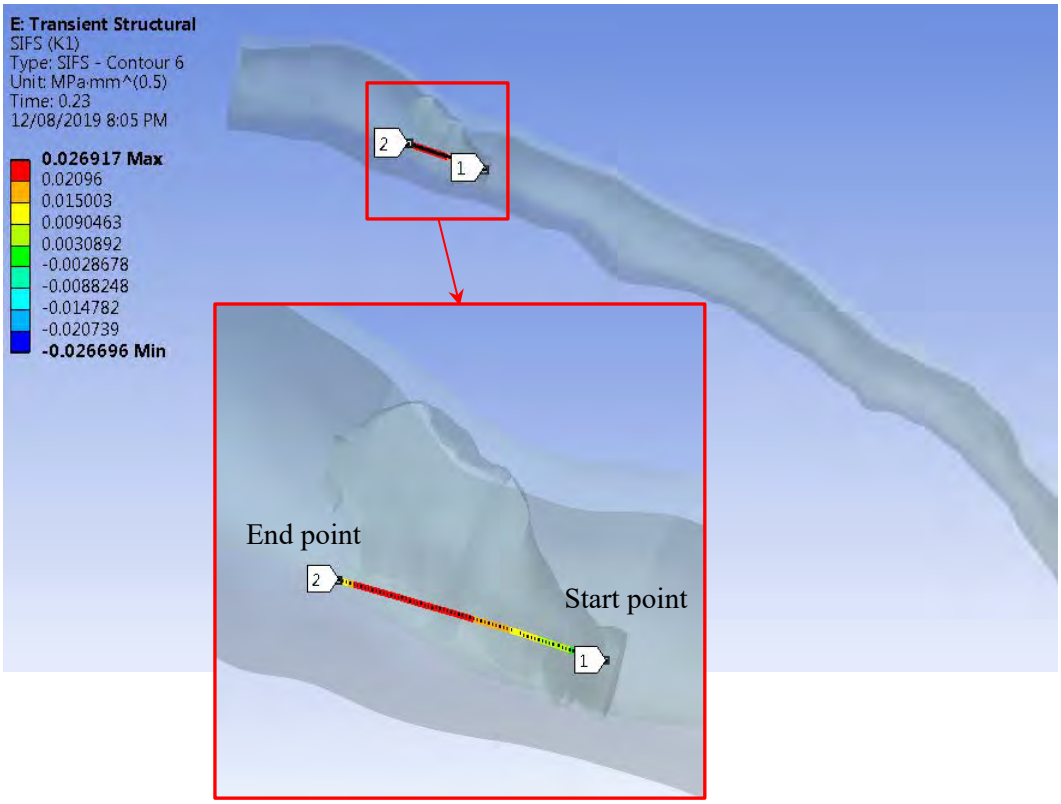

(b)

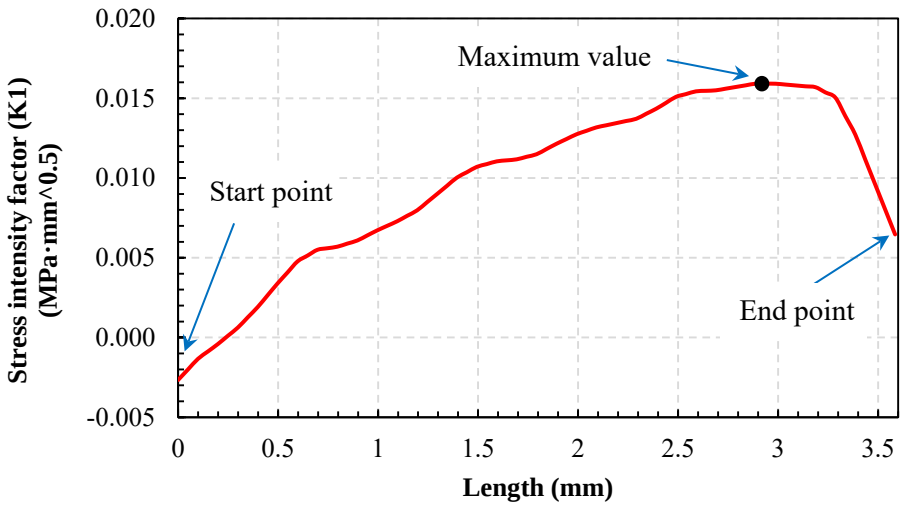

Figure 6-10. Dynamic analysis of SIF for an *extended* crack during one heart rate: (a) crack tip and the corresponding SIF distribution at t = 0.23s; (b) contour of (a).

Chapter 7

Summary and recommendations

7.1 Summary of main outcomes and achievements

In this thesis, the nonlinear, fluid-structure interaction (FSI) dynamics of atherosclerotic coronary arteries have been modelled/simulated, based on clinical data obtained at the Royal Adelaide Hospital (RAH), as a tool to predict the initiation/progression of plaque rupture and hence heart attack. With over 15 million deaths reported globally each year due to coronary heart disease (CAD) and stroke, as well as 18,000 deaths annually in Australia alone, developing the ability to predict plaque rupture, and hence heart attack ,could save lives. While there are valuable reported investigations in the literature, the effects of FSI in the coronary vasculature has been investigated inadequately; this has been shown to impact stress and strain results as well as the prediction of disease initiation. Due to the complex nature of the coronary vasculature, omitting any factors can drastically impact results, hence, including all important factors from *in vivo* data and imagery is necessary for the accurate prediction of disease initiation or plaque

rupture. The capability to accurately model/simulate the coronary arteries has been developed in this thesis to include key parameters such as: (1) the blood physiological pulsation, (2) tapered shape of the artery, (3) the motion of the artery due to the heart motion, (4) media layer muscle contraction, (5) the lipid pool inside the plaque, (6) non-Newtonian flow for the blood, (7) the three layers of the artery wall, i.e. adventitia, media, and intima, (8) the micro-calcification, and (9) hyperelastic/viscoelastic material properties. More specifically each of the papers comprising the main body of work of this thesis has contributed new knowledge as follows.

Chapter Three (Paper 1): A theoretical model for the left main (LM) coronary artery was developed to investigate the effects of various factors influencing disease and plaque rupture. All aforementioned parameters were included in the dynamic model, with these parameters considered the most realistic representation of the LM coronary artery and the plaque behaviour to date; it is intended this will provide an accurate and reliable method of plaque rupture prediction. Results showed that considering the interaction of the fluid and structure is essential for plaque rupture risk prediction, with computational fluid dynamics (CFD) and finite element method (FEM) alone insufficient to accurately describe the complex interactions. It was also shown that considering heart motion, the tapered shape of arteries, active media layer contraction, the three layers, pulsatile blood flow, plaque lipid core and viscoelastic material properties results in accurate stress field predictions and, hence, accurate plaque rupture prediction. The presence of a plaque increased wall shear stress (WSS), blood velocity, blood pressure and structural stress on the artery with increasing stenosis 25-55% (high risk stenosis levels) resulting in increasing shear and von Mises stress (VMS), a result corroborated by clinical data. Increasing plaque shoulder length led to increased structural stress and reduced WSS; meanwhile, the inclusion of 3D heart motion led to an increase in structural stress of 265%. The inclusion of all three artery layers resulted in a decrease in structural stress, although shear stress variation was minimal. Microcalcification inclusions resulted in stress concentrations which could lead to rupture from the microcalcification location, whilst the inclusion of non-Newtonian blood models resulted in a 483% increase

in shear stress on the plaque in comparison with Newtonian blood models. VMS only showed marginal increases in the change of non-Newtonian blood models. Artery taper also resulted in slight increases in shear stresses and no phase lag was seen between straight and tapered artery geometries. This was the first time that all of the aforementioned parameters have been included simultaneously in the same model, producing the most comprehensive and reliable biomechanical model/simulations of coronary arteries and plaques to date. These results have been published in the International Journal of Engineering Science (Q1; Impact Factor = 9.052; journal rank: 1 out of 88 in Multidisciplinary Engineering).

Chapter Four (Paper 2): This chapter details the developed three-dimensional, nonlinear, finite element model of *bifurcation* in the LM coronary artery. The parameters incorporated into the dynamic, time dependent model, include: nonlinear hyperelastic/viscoelastic material, non-Newtonian fluid model, blood pulsation, heart motion, artery taper, active media layer contraction, three artery layers, plaque lipid core, fibrous cap thickness, microcalcification and plaque stenosis level. To reliably simulate the stress fields and, hence, determine the risk of plaque rupture in the artery bifurcation, the biomechanical model also included the influence of variation in the bifurcation angle, bifurcation curve and the location of the plaque. The main findings show that in all artery branches, WSS magnitude is a maximum at the top of each plaque whilst it is lowest at the shoulders, suggesting the shoulders as more at risk of lipid deposition. The left circumflex (LCx), left anterior descending (LAD), and LM coronary artery segments show almost identical pressure patterns over time, with downstream segments resulting in lower pressure than upstream sections. The maximum values of VMS resulted at both the artery wall and plaque itself, suggesting vulnerability to dissection and rupture respectively; the middle regions of plaque shoulders were identified as the most at risk region for rupture due to the combination of both the solid characteristics of VMS and the fluid-solid characteristics of the non-dimensionalised WSS. This is in agreement with experimental data from the literature which shows plaque shoulder as a most high risk location of the plaque. Plaque presence in the LM coronary artery section increases the risk of rupture, regardless of the plaque location or severity in the

downstream sections, however, the combination of LM and LAD plaques together produced the largest rupture risk. In particular, the plaque fibrous cap thickness influences rupture risk by concentrating stress at the intima layer and plaque lipid core boundary. Both decreasing VMS within the plaque and WSS at the endothelial surface where the plaque meets the artery seen as the plaque shoulder length increases. Furthermore, calcified plaques produced higher VMS when compared to lipid plaques in the left coronary artery and microcalcification resulted in a significant increase in VMS, but little variation in WSS. Variations in stress distributions were also seen with varying artery curvatures, with larger curvatures suggesting a higher risk of rupture whereas the original bifurcation angle resulted in lower VMS but no change in WSS. This is the first time that all aforementioned parameters have been included simultaneously in the same model of an artery *bifurcation*; results have been published in the International Journal of Engineering Science (Q1; Impact Factor = 9.052; journal rank: 1 out of 88 in Multidisciplinary Engineering).

Chapter Five (Paper 3): With the previous two chapters developing the theoretical biomechanical model, this chapter presents the most comprehensive, *patient-specific* model of coronary arteries, based on *in vivo* imaging and data measured at the RAH from two patients; the first with non-ST segment elevation myocardial infarction (NSTEMI) and another one with an inferior STEMI/ectopy conducted. Geometric and haemodynamic properties were extracted through the use of Optical Coherence Tomography (OCT), Angiography and Electrocardiography (ECG) at the RAH with the first patient showing a single minor stenosis of the LCx and the second patient showing three thin-capped, lipid rich plaques in the right coronary artery (RCA), both of which were modelled. Including all important parameters such as three dimensionality, hyper viscoelasticity, realistic geometry, heart motion, blood viscosity, blood pulsation, and surrounding heart tissue were assessed using the biomechanical model based on the FEM using ANSYS, with WSS, VMS, as well as shear and von Mises strains analysed to detect plaque rupture/artery dissection; more specifically:

Patient One: Results showed maximum WSS over the outer surface of the plaque but few areas of low WSS, significant for the deposition of

low-density lipoproteins (LDL) and, hence, high-risk disease regions. The maximum value of VMS occurred at the proximal region of the artery, while a local maximum resulted at the plaque shoulder region, closest to the proximal direction. The largest WSS magnitude was found via a time domain analysis, occurring half-way through the cardiac cycle (heart rate), while the VMS time-variation was seen to follow the motion of the heart rather than the blood profile. Furthermore, the local maximum was also found to be located on the plaque side of the artery rather than opposite it, highlighting a larger risk of intimal-layer failure at the plaque while the plaque side of the artery was also found to be stiffer than the opposing area.

Patient Two: This patient showed a higher stenosis than patient one, hence, the maximum WSS produced was larger. The number of plaques within the model did not affect the distribution of WSS, with all plaque areas possessing local maximum values. Similarities were seen between the time-variation patterns from Patient One and Patient Two, however, VMS was seen to vary whilst the proximal side of the plaque shoulder of the first plaque was the most at risk of rupture. The stiffness of the adventitia and intima layers were seen to closely match in some artery sections, suggesting reduced flexibility and the potential for increased dissection and rupture risk under sudden strains imposed by the high blood pressure or heart motion.

These results have highlighted the potential for developing patient specific biomechanical models of coronary arteries; this paper has been submitted for publication.

Chapter Six (Paper 4): For the first time, the three-dimensional, fracture and fatigue-life behaviour of a realistic atherosclerotic coronary artery have been assessed using smart crack growth. Constructed from *in vivo* clinical imaging obtained from a patient at the RAH, including Angiography, ECG, OCT and time-dependent pressure measurements, the biomechanical, FSI model based on the FEM was used to analyse plaque rupture (crack) initiation/progression. Clinical data was post-processed by developing an image processing technique with the haemodynamic and geometric information used to construct the model. All

critical aforementioned parameters were included along with the surrounding heart tissue. Results showed that the most vulnerable areas for rupture, with largest local VMS, were around plaque locations, with the proximal, lipid-rich plaque shown to be the most at risk of rupture initiation. The shoulders of this plaque were the most at risk location for both rupture and plaque propagation/extension. An assessment of rupture showed that the crack propagates under the physiological/geometric conditions of the artery; this patient is hence at risk of artery occlusion and heart attack if an infinitesimal crack develops at the shoulder of the proximal plaque. If an infinitesimal crack develops, rupture propagation begins after only approximately two hours, with maximum stress intensity factor (SIF) and hence rupture growth starting in the middle of the crack tip. After a further eight hours, the rupture reaches the adventitia later, leading to artery dissection. These results showed the ability to predict the location and initiation of plaque rupture and, hence, could predict heart attack.

In summary, this thesis outlined the development of an accurate, patient-specific, nonlinear, biomechanical *in vivo* based model/simulations, capable of assisting in the prediction of the initiation of plaque rupture and hence heart attack. All critical parameters have been included: three dimensionality, physiological blood pulsation, non-Newtonian blood flow, motion of the artery due to the heart, surrounding heart tissue, tapered shape of the artery, the three layers of the artery wall, bifurcation angle and artery curvature, media layer muscle contraction, the lipid pool inside the plaque, surrounding heart tissue, micro calcification and hyperelastic/viscoelastic material properties. This is the first time that all these parameters have been considered in the same biomechanical model of coronary arteries. The three-dimensional fracture and fatigue-life behaviours of the arteries and plaques within the FSI model were then assessed to determine the time required to rupture as a function of crack location. By developing an image processing technique to post-process *in vivo* imaging data, patient-specific models were constructed with all the aforementioned parameters and, hence, accurate prediction of plaque rupture/artery dissection has been made. These results predicted the time to artery dissection/plaque rupture and hence time to a heart attack, which has the potential to assist diagnosis and treatment and save millions

of lives globally while reducing the morbidity and economic burden created by coronary heart disease.

7.2 Recommendations for future work

The focus of this thesis was on modelling the dynamical behaviour of atherosclerotic coronary as well as their stress/strain fields and fatigue-life and crack progression based on *in vivo* clinical data, which were obtained at the RAH, and then predicting plaque rupture in diseased arteries. This work could assist clinicians in preventing heart attack and, hence, deaths and morbidity. The numerical nonlinear model/simulation developed using clinical measurements and including both the blood and artery/plaque domain and their interactions is the most accurate and reliable to date. The work presented in the current thesis can further be pursued and extended into many areas, including the following:

i. Obtaining mechanical properties of fracture life-cycles and SIF for healthy and atherosclerotic arteries, especially when the parameters vary with time.
ii. Modelling and simulations of a patient with different diseases such as diabetes and different high risk habits such as smoking to examine the effect of these diseases and habits on coronary artery systems before and after coronary artery diseases; a system sensitivity to these effects can further be studied.
iii. Examining the effect of different medicine by modelling and simulating the biomechanical analysis of coronary arteries.
iv. Using the obtained model to develop virtual fractional flow reserve (FFR) to examine the physiological effect of coronary stenosis.
v. Modelling the 3D motion of the heart based on the *in vivo* clinical measurements.
vi. Obtaining mechanical properties based on *in vivo* dynamical behaviour of the bio-system.
vii. Modelling the heart tissue and wall of different parts of the heart to obtain the effect of them on coronary artery dynamics.
viii. Modelling and simulation of atherosclerotic coronary arteries before and after plaque rupture based on clinical data.